DAMAGE DETECTION OF LOCALIZED DEFECTS IN SPUR GEAR PAIRS AND GEARED TRANSMISSIONS USING DAMAGE-INDUCED DYNAMIC RESPONSE

by

SUHAS GUPTA THUNUGUNTLA

A dissertation submitted in partial fulfillment of the
requirements for the degree of

DOCTOR OF PHILOSOPHY IN MECHANICAL ENGINEERING

2025

Oakland University
Rochester, Michigan

Doctoral Advisory Committee:

Christopher Cooley, Ph.D., Chair
Adrian Hood, Ph.D.
Randy Gu, Ph.D.
Brian Dean, Ph.D.

ACKNOWLEDGMENTS

I would like to express my deepest gratitude to my advisor, Dr. Christopher Cooley, for his guidance, support, and continuous encouragement throughout the research process. I acquired immense knowledge from Dr. Cooley's courses Experimental Vibration Analysis, Mechanical Vibrations, and Non-Linear Vibrations which helped in carry out my research. I have also received vast amounts of technical talk tips from Dr. Cooley, encouraging feedback for technical presentations and always pushing me to present at various conferences.

I would also like to thank my committee member, Dr. Adrian Hood, for giving his expert feedback based on his in-field knowledge of rotorcraft transmissions testing at DEVCOM ARL. My research work was successfully furthered with the help of Dr. Hood's inputs from the discussions in the weekly ARL-OU meetings. I also would like to appreciate Dr. Hood's help in managing the manuscripts, and presentations getting reviewed from ARL personnel (OPSEC process).

I would also like to thank my other committee members, Dr. Randy Gu and Dr. Brian Dean for their input in completing this research. Finite Element course teachings by Dr. Gu gave me an alternate perspective on the subject and helped me in completing my research. I thank Dr. Sandeep Vijayakar at Advanced Numerical Solutions, LLC for providing the Calyx Transmission3D software used in this work.

I am sincerely grateful to Dr. Cooley for acquiring funds for my tuition fee and research assistant role which helped me to steer towards reaching my goals without any financial concerns. Also, I would like to thank the Army Research Laboratory and Dr. Hood for funding my research. Additionally, I would like to thank the board members of the American Gear Association for providing me with a scholarship for the academic year 2023-2024 to further my career in the field of gears.

I am extremely grateful to my wife, Akhila for always pushing me towards reaching my goal, and keeping my health in check. Also, I am very thankful to my family for always supporting me and motivating me. I would like to thank my friends, and cousins for helping me when I am in need and guiding me to pick the right choices.

SUHAS GUPTA THUNUGUNTLA

ABSTRACT

DAMAGE DETECTION OF LOCALIZED DEFECTS IN SPUR GEAR PAIRS AND GEARED TRANSMISSIONS USING DAMAGE-INDUCED DYNAMIC RESPONSE

by

SUHAS GUPTA THUNUGUNTLA

Adviser: Christopher Cooley, Ph.D.

Geared transmissions are important systems, especially in the aerospace and rotorcraft industry. Loss of power from gearbox failure due to damaged tooth poses reliability and safety issues. Health and Usage Monitoring Systems (HUMS) are used in rotorcraft vehicles to monitor the performance of their transmissions and other critical components. Condition monitoring systems use measured vibrations from geared transmissions to detect damage to the gears and other components inside them. A major challenge for damage detection systems is identifying damage from otherwise normal changes in vibrations that may occur.

In this dissertation, the analysis of the damage-induced dynamic response of geared transmission is carried out by understanding the dynamic response on the spur gear pair and applying it to the geared transmission accelerations. For the accurate damage-induced dynamic response of the spur gear pair, accurate tooth mesh interface parameters are derived utilizing the finite element/contact mechanics (FE/CM) method. Tooth mesh characterization involves determining the static transmission error and the mesh stiffnesses when the teeth have either root cracks or surface pitting damage. The damage cases considered include tooth root cracks or surface pits localized to a single gear tooth. The FE/CM method accurately predicts the tooth mesh stiffnesses of the unity-ratio gear pair when it is healthy without damage, and when the teeth have root cracks and surface pitting. The static transmission error

increases and the tooth mesh stiffness decreases with increasing size of pits and increasing lengths of cracks. The distinct differences in duration observed between tooth surface pit and root cracks may permit their detection from static transmission error measurements.

Dynamic transmission error is calculated using the lumped-parameter model and shown to compare well with dynamic response calculations from the FE/CM gear pair model. Larger damage on the gear pair generally causes higher vibrations to result. Quasi-static responses are observed at speeds less than one-third of the natural frequency, while above that, the damage-induced dynamic response shows impulse-like behavior. The damage-induced dynamic response of high-speed spur gear pairs with localized defects shows that the response is oscillatory with decaying amplitudes, a linear oscillator, and based on these, a phenomenon-based model is proposed for approximating the damage-induced dynamic response which is determined solely by an amplitude (dependent on damage severity), damping ratio, and natural frequency (properties of gear pair). The simplicity of the phenomenon-based model permits analytical closed-form expressions of several condition indicators used in damage detection and the ability to predict condition indicators for varying gear pair properties.

Geared transmission vibrations are determined using the FE/CM model to detect damage. When damage (i.e., tooth root cracks or tooth surface pits) occurs on the individual gears of the planetary stage, additional transient vibrations occur that meaningfully alter the resulting vibrations and their spectrum. The ability to calculate condition indicators (CI) for detecting damage is explored and it appears to be sensitive to the input vibration signal used in the CI calculation. Tooth root cracks with lengths less than 50 percent through the tooth thickness generally do not lead to substantial increases in the individual CIs. Calculating the damage-induced dynamic response or the exact difference signal effectively detects even smaller crack length damages in the space-fixed or rotating gears of the planetary stage, utilizing the calculation of CIs. These will enable reliable damage detection techniques for geared transmissions, improving safety, reliability, vehicle readiness, and vehicle performance.

TABLE OF CONTENTS

TABLE OF CONTENTS - Continued

LIST OF TABLES

LIST OF FIGURES

CHAPTER ONE

INTRODUCTION

1.1 Background and Motivation

Geared transmission is a mechanical system that utilizes the meshing of gear teeth to transmit power from a source to other components while adjusting speed, torque, and direction of rotation as needed. The primary function of a geared transmission is to match the specific requirements of the driven components, ensuring optimal performance and efficiency. Some of the primary applications of geared transmissions include automobiles, aerospace (rotorcraft and fixed-wing aircraft), industrial machinery, wind turbines, and many others. In rotorcraft, geared transmissions convert the high-speed rotational energy of the engine into the lower rotational speeds required to drive the main and tail rotors. These transmissions are designed to handle significant torque loads. The main rotor transmission reduces engine speed to the lower speed necessary for rotor operation, while the tail rotor transmission is responsible for adjusting the power sent to the tail rotor, which controls the aircraft's yaw. The design of rotorcraft transmissions typically incorporates various types of gears, such as planetary, bevel, and helical gears, to achieve the required reduction ratios and power distribution. These systems must operate reliably under extreme conditions, such as high power demands during takeoff and low-speed operation during hover while maintaining smooth and responsive control. The key components of the geared transmissions are gears, bearings, shafts, housing, and lubrication. Gears are the central components that transmit power and torque between shafts. Different types of gears are Spur gears, helical gears, bevel gears, and planetary gears. Figure 1.1 shows the OH-58 (Bell 206) rotorcraft transmission and the rotating spur gears (sun and planet gears) used in the planetary stage of the rotorcraft transmission.

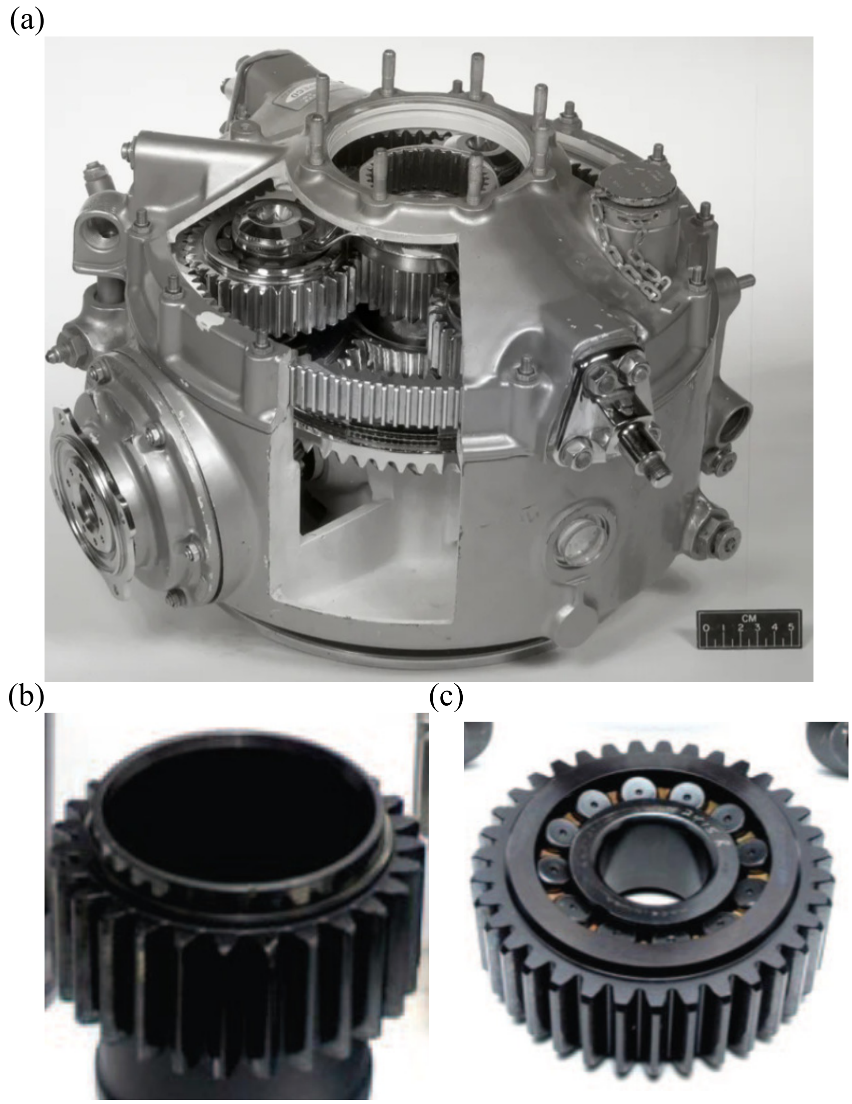

Figure 1.1: (a) The OH-58 rotorcraft transmission, which contains gears, shafts, bearings, and housing is shown in the image. A portion of the transmission housing has been removed to provide a detailed view of the internal components. This image is sourced from Ref. [2]. The rotating spur gears in the planetary stage of the OH-58 rotorcraft transmission: (b) sun and (c) planet gears. These images are taken from Ref. [3].

Gears are critical components in geared transmissions, as power is transmitted between components through the interlocking of gear teeth. Gears can exhibit different types of damage as a result of the stresses they encounter during operation. The two most common types of damage to the gear tooth are tooth root crack and tooth surface pitting damage. Figure 1.2 shows the tooth root crack and tooth surface pitting damage to the gear tooth. The tooth root crack damage typically occurs due to excessive bending stresses at the root of the tooth. This crack can initiate from surface imperfections or fatigue, overload, misalignment, or improper lubrication. The tooth root crack damage leads to tooth breakage or failure of the gear. Tooth surface pitting damage is a fatigue failure that generally occurs after many load and unload cycles of the teeth. Pitting is caused by fluctuating tooth forces generating alternating surface stresses on the teeth. Although pitting occurs in precisely manufactured and accurate gears after many cycles, it can occur in much fewer cycles when manufacturing or assembly errors (e.g., misalignment) cause the gear tooth surfaces not to mate properly. Lubrication failures can contribute to pitting damage when sufficient film thicknesses do not develop, and metal-to-metal contact occurs between mating gear teeth. Tooth root cracks and surface pitting are significant contributors to gear failure, requiring careful monitoring and maintenance to ensure the reliable performance of geared systems.

(a) (b)

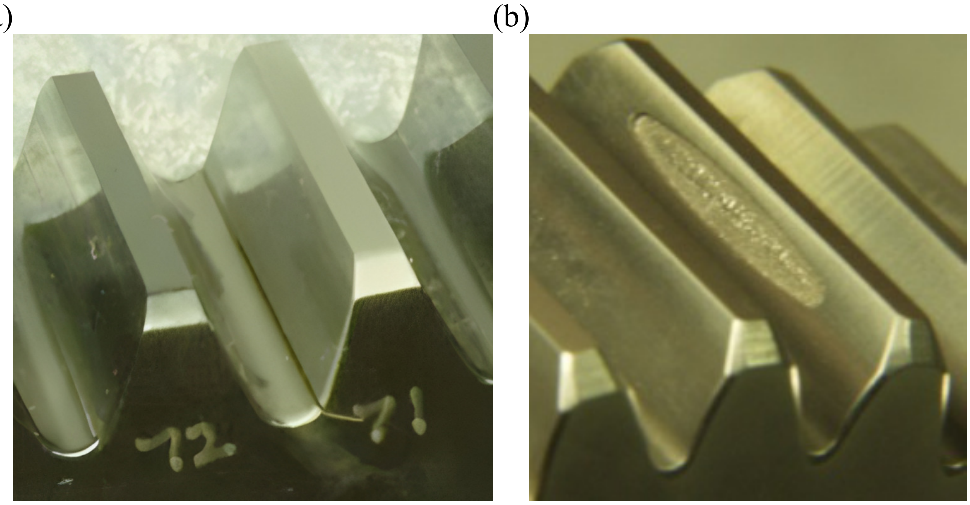

Figure 1.2: (a) Tooth root crack damage on the ring (space-fixed) gear tooth and (b) tooth surface pitting damage on the rotating planet gear tooth in the planetary stage of the transmission. These images are taken from Ref. [4]. The root crack and surface pitting damages were produced as part of seeded fault experiments in Ref. [4].

Tooth root cracks and surface pitting damage on the gear teeth of rotorcraft transmiss-//ions can lead to catastrophic failures affecting flight safety. These failures, which compromise the integrity of the gear teeth responsible for transmitting power to the rotors, can result in mechanical breakdowns that cause loss of control, power loss, and potentially total failure of the transmission system. For rotorcrafts, gearbox failures are particularly dangerous, as they can lead to an immediate loss of rotor speed or torque, disrupting flight stability and control. Figure 1.3 shows the history of accidents and accidents with fatalities involved according to the U.S Helicopter Safety Team (USHST) from the year 2000 to 2024. A notable example of gearbox failure due to tooth root crack damage occurred in 2011 when a gear tooth breakage in a rotorcraft gearbox resulted in a catastrophic failure that led to the deaths of 16 individuals. This tragic incident highlights the extreme consequences of gear tooth failures, underscoring the importance of rigorous maintenance, monitoring, and the use of technologies to detect and mitigate such issues before they result in a total failure of the rotorcraft transmission system. The ability to maintain the integrity of the gearbox, through early detection of cracks or pitting, is therefore critical not only for the efficient operation of rotorcraft but for ensuring the safety of both the aircraft and its occupants.

Health and Usage Monitoring Systems (HUMS) are used in rotorcraft vehicles to monitor the performance of the rotorcraft transmissions and other critical components [5, 6]. Operations of HUMS include data acquisition, data manipulation, condition monitoring, and health assessment. Data acquisition is used to acquire the sensor signals placed across the rotorcraft. Figure 1.4 shows the OH-58 or Bell 206 rotorcraft, which is equipped with gearbox condition monitoring sensors as part of the HUMS installed throughout the aircraft. Vibration measurements are one input used by these systems to detect damage. The data manipulation and condition monitoring of HUMS modifies the raw signals like averaging techniques and calculates the condition indicator values to assess the health of

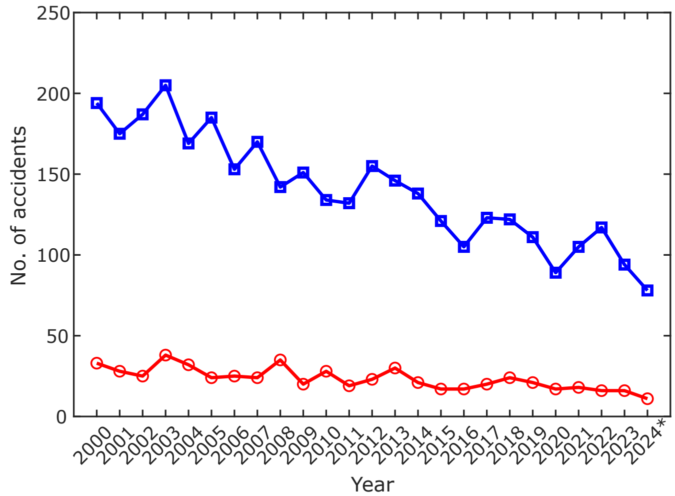

Figure 1.3: History of US rotorcraft accidents 2000 to 2024, based on the reports available in USHST database. The solid (blue) line with square markers represents rotorcraft accidents, while the solid (red) line with circle markers represents accidents involving fatalities. The asterisk (*) next to the year 2024 indicates that data is based on reports available up to the present.

transmission. Further analyzing the characteristics of the vibration signatures generated by damage and quantifying their impact on detection could improve the performance of HUMS and improve rotorcraft vehicle readiness, reliability, and safety. The detection of damage from the measured vibrations of transmissions has been a long-standing challenge for condition monitoring systems. Periodic maintenance based on the HUMS enables failures to be identified in advance to make flight operations safe and reliable. This research advances the development of HUMS for early damage detection.

Statistical condition indicators are the measure of the statistical features of the vibration signals acquired from different sensors. The condition indicators are calculated using raw accelerations, time-synchronous averaging (TSA) accelerations, difference signal accelerations, and residual signal accelerations. Raw accelerations are directly acquired from the sensors without any data manipulation. TSA accelerations are the raw accelerations with the time-synchronous averaging technique applied, which helps to filter out unwanted

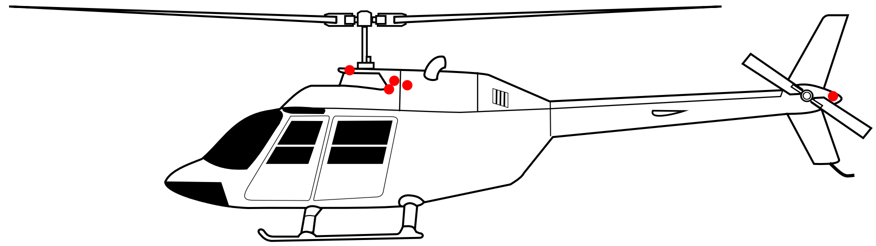

Figure 1.4: OH-58 or Bell 206 rotorcraft with gear condition monitoring sensors (red circle markers) placed across rotorcraft. This drawing is sourced from Ref. [7].

noise and asynchronous vibrations from the signal. Difference signal accelerations are obtained by modifying the spectral content of the TSA-averaged accelerations; specifically, the mesh frequency component and first-order sideband amplitudes at all harmonics are removed, and the inverse Fourier transform of the resulting spectrum gives the difference signal accelerations. For residual signal accelerations, only the mesh frequency amplitudes at all harmonics are removed. These accelerations are computed from the vibrations of a single transmission. The condition indicators evaluated in this work include root mean square (RMS), crest factor, energy operator, and kurtosis, with raw or TSA accelerations as their input. Additionally, RMS difference, FM4, M8A, and energy ratio are evaluated using difference signal accelerations as their input. These condition indicators are explained in detail in Appendix. A.

Transmission error is the main source of noise and vibration in the geared transmission. The unsteady forces are raised due to the transmission error, which is the difference between the actual position of the gear pair and the position it would if everything is ideal. This error is the linear motion error observed along the line of action, at the tooth mesh interface which corresponds to the rotational vibration of the gears. There are three types of transmission errors. **No-load transmission error** is the error that is calculated at vanishing torque. This error is zero for gear pairs without modifications and nonzero for gear pairs with tooth modifications. **Static transmission error** is the error that is calculated at the nominal torque of the gear pair. The speed at which the gear pair rotates while calculating this error is very low. **Dynamic transmission error** is the error calculated when the gears are dynamically rotating at high speeds. The local slope tooth mesh stiffness of the gear pair is evaluated using static transmission error and forces calculated at torques greater and lower than nominal torque. The average slope mesh stiffness of the gear pair is evaluated from the force generated at the mesh to the static transmission error. The tooth mesh stiffnesses and static transmission error are used in the calculation of gear pair dynamic response.

1.2 Literature Review

The research work in this dissertation is carried out in different steps to detect damage in the geared transmissions. The different steps are tooth mesh characterization of spur gear pairs with localized defects, analysis of the dynamic response of the spur gear pairs with localized defects, and damage detection in geared transmission with defects on space-fixed/rotating gears. This section presents a review of the literature on spur gear pairs with localized defects, their dynamic response, and damage detection in transmission systems, highlighting how the existing research differs from the focus of this study.

Gears vibrate because of static transmission error excitation and fluctuations in tooth mesh stiffness [8–10]. Near resonance, these vibrations can become so large that tooth contact loss occurs [11–15]. Tooth contact loss has been confirmed experimentally in Refs. [16, 17]. Accurate representations of the tooth mesh (e.g., the static transmission errors and mesh stiffness fluctuations) are important parameters for gear dynamic models. This has motivated a number of methods for calculating the static transmission errors and tooth mesh stiffnesses of individual gear pairs. These methods primarily center on analytical models [18–29], conventional finite element formulations [30–32], experiments [33–40], and combined finite element/contact mechanics formulations [14, 17, 41]. Damage to the gear teeth alter the usual fluctuations in static transmission error and tooth mesh stiffness, which can lead to increased vibrations and dynamic response. The mesh stiffness of gear pairs with tooth surface pitting damage was analyzed in Refs. [1, 42–57] used the potential energy method, approximated the shape of the pitting damage using regular geometrical shapes, performed experiments to capture the accurate pitting damage shape, evaluated with multiple pits in the gear pair, evaluated for micro-sized pits distributed on the tooth surface, and evaluated using shape independent approach. The mesh stiffness of the gear pairs with tooth root crack damage are analyzed in Refs. [44–46, 53, 58–71] which used the strain energy formulation, the potential energy method, evaluated for gears with thin webbed blanks, evaluated for carburized gears, and evaluated for spatial crack lengths. In this research work, the FE/CM model is validated with the results published in the literature and it is used to systematically analyze the effects of tooth root crack and tooth surface pitting damage on the characteristics of spur gear tooth mesh interfaces through various parametric studies for varying damage severity.

The damage detection in spur gear pair requires accurate calculation of the condition indicators which depends on accurate evaluation of damaged dynamic response. The dynamic response of gear systems has been extensively studied to understand how different types of damage affect the overall vibration characteristics. Several models exist for deriving the dynamic response of a gear pair with consideration for tooth root crack and tooth surface pitting damage. The dynamics are derived utilizing a lumped-parameter model with different numbers of degrees of freedom, experiments, finite elements, and hybrid methods in Refs. [1, 8–13, 42, 43, 45, 47, 50, 62, 64, 66, 68, 69, 71–85]. Many studies used unity-ratio gear pair, in this dissertation, we are calculcating the dynamic response for nonunity-ratio spur gear pair with varying lengths of tooth root crack damage and varying amounts of tooth surface pitting damage using the lumped-parameter model and the FE/CM model. Several analyses of the dynamic responses of the gear pair with localized defects are performed and the dependence of gear pair dynamic properties and damage severity on condition indicator values is shown.

The damage in geared transmissions alters the vibrations and identifying or isolating the vibrations due to damage from the normal meshing vibrations is the main component in detecting damage. The vibrations are evaluated using the statistical condition indicators to determine the presence of damage in the transmission. A number of other methods for detecting damage to geared transmissions have been proposed, which can be found in the bibliographies of the review articles in Refs. [5, 6, 59, 86–96]. The techniques used in the detection of the damage on the gearbox are analyzed in the Refs. [4, 97–125, 125, 126, 126–129] used the amplitude, phase demodulation, incorporated and analyzed time-frequency methods, used path independent modulation like vibration separation, and develpoed new diagnostic method like Constrianed Adaptive Lifting (CAL) algorithm, wavelet neural network, synchro-squeezing transform and systematic scheme to explore the motion periods. The majority of these works assess condition indicators using measured vibrations from experiments. We analyze the vibrations of transmission using a finite element/contact mechanics (FE/CM) model that accurately captures the gear tooth mesh excitations accounting for the kinematic motion of the planets, changing contact conditions at the gear teeth, tooth bending and rim deformation, vibration, and damage and determine the condition indicators that positively identify the presence of damage by isolating its content from the normal meshing vibrations.

1.3 Scope

This work investigates the effects of damage on the gear mesh characteristics and dynamic response of spur gear pairs and rotorcraft transmissions using a finite element/contact mechanics (FE/CM) approach. Initially, the study examines tooth surface pitting damage in a unity-ratio spur gear pair, considering three locations for the pitting: at the pitch, in the approach, and in the recess. Parametric studies assess static transmission error, tooth contact forces, and tooth pair stiffness for various pit sizes and locations, comparing these results with healthy gears to quantify the impact of pitting. The FE/CM method is then applied to analyze both unity-ratio and nonunity-ratio gear pairs, with tooth surface pitting and tooth root crack damage. Static transmission errors and tooth mesh stiffnesses are compared with studies in the literature to validate the methodology. The analysis explores the effects of damage on the magnitude, location, and duration of transmission error and tooth mesh stiffness, comparing the impacts of surface pitting and root cracks.

The tooth mesh interface parameters are incorporated into a lumped-parameter gear model to calculate the dynamic response under different damage conditions. The lumped-parameter model is further used to analyze the dynamic response of a nonunity-ratio gear pair at various speeds, investigating nonlinear dynamic behavior and the transition from quasi-static to impulse-like dynamics with damage. A simplified phenomenon-based model that captures the damage-induced dynamic behavior of gear pairs with localized tooth root crack and surface pitting damage is derived to investigate the relationship between the condition indicators, damage severity, and gear dynamic proprieties.

The FE/CM model of a rotorcraft transmission, including input spiral bevel and output planetary stages with associated mechanical coupling (shafts, bearings, carrier, and housing), is used to quantify the effects of damage on vibrations generated in the housing. Vibrations from healthy transmissions and those with a localized tooth root crack in the space-fixed (ring) gear are compared, and various difference signal calculation methods are explored to isolate damage-induced vibrations. This study also examines the sensitivity of the FM4 condition indicator to damage severity, sensor location, and damaged tooth location, providing insights into the performance of condition monitoring techniques. The FE/CM transmission model is used to study tooth root crack damage in the rotating (sun) gear of the planetary stage, comparing vibrations and frequency spectra between damaged and undamaged transmissions. The FM4 condition indicator is calculated for different damage scenarios, and the best methodologies for detecting damage in rotating gears are identified based on varying sensor locations and damage lengths. This work contributes to the development of HUMS condition monitoring systems to detect damage in the early stage of failure.

CHAPTER TWO

TOOTH MESH CHARACTERIZATION OF UNITY-RATIO SPUR GEAR PAIRS WITH SURFACE PITTING DAMAGE

2.1 Introduction

Damaged gear teeth impact the noise, vibration, and durability of transmission systems. Tooth surface pitting damage is a fatigue failure that generally occurs after many load and unload cycles of the teeth. Pitting is caused by fluctuating tooth forces generating alternating surface stresses on the teeth. Although pitting occurs in precisely manufactured and accurate gears after many cycles, it can occur in much fewer cycles when manufacturing or assembly errors (e.g., misalignment) cause the gear tooth surfaces not to mate properly. Lubrication failures can contribute to pitting damage when sufficient film thicknesses do not develop, and metal-to-metal contact occurs between mating gear teeth.

Tooth surface pitting, as well as other types of damage, cause changes to the contact pressure distribution on the gear teeth that alters the deformations resulting from meshing. Tooth pitting damage causes portions of the gear surface to lose contact and not carry load. Near damage, the contact pressures on the gear teeth increase with sharp changes. The static transmission error, tooth contact forces, and tooth pair stiffnesses change with pitting damage on the teeth. The pitting damage results in additional excitation that drives larger dynamic response compared to cases when undamaged, healthy teeth are in mesh. Because teeth with surface pits have more dynamics, they often generate more noise, cause damage to progress on already-damaged teeth, and drive damage to spread to additional teeth or other components. Therefore, the ability to predict when damage has occurred to gears has become important for applications.

Gears vibrate because of static transmission error excitation and fluctuations in tooth mesh stiffness [8–10]. Near resonance, these vibrations can become so large that tooth contact loss occurs [11–15]. Tooth contact loss has been confirmed experimentally in Refs. [16, 17]. The tooth mesh characteristics, which include the loaded and unloaded transmission errors and tooth mesh stiffnesses, are used as inputs to dynamic models used to predict dynamic response.

A number of methods have been proposed for the calculation of tooth meshing stiffnesses. Kasuba and Evans [18] determined the mesh stiffnesses of gear pairs and used them to calculate the resulting dynamic response. Chang et al. [31] determined mesh stiffnesses using finite element methods and local contact analyses of elastic bodies. Cooley et al. [41] compared mesh stiffness calculations using two common formulations. They found the different calculations give meaningfully different mesh stiffnesses when the gear teeth have modifications. Less prominent differences occurred for unmodified gears. Liang et al. [23] proposed three models for accurate mesh stiffness calculations. Comparisons were made to finite element results. Sun et al. [22] developed a method to calculate mesh stiffnesses for spur gear pairs with tooth modifications. Raghuwanshi and Parey experimentally determined gear mesh stiffness using digital image correlation in Ref. [36] and laser displacement sensors in Ref. [37]. They compared their results to finite element and analytical methods. Xiong et al. [25] studied the effect of backlash on mesh stiffness using a potential energy method. Miguel et al. [26] presented an analytical model for calculating tooth characteristics for spur gears with modifications and non-nominal load conditions. Dai et al. [27] compared an analytical mesh stiffness model to experiments. Further studies related to gear mesh stiffness calculations can be found in the review article by Marafona et al. [130]. These analyses focused on the fluctuating mesh stiffnesses of healthy gears without damage. The stiffness fluctuations resulting from gears with pitting damage on the teeth are a focus of this research work.

The impact of tooth surface pit damage on the gear tooth mesh interface of mating gears has been studied by a number of investigators. Choy et al. [42] determined the mesh stiffnesses of gear pairs with surface pitting wear and partial tooth fracture. Chaari et al. [43] determined the time-varying mesh stiffness of spur gear pairs with rectangular-shaped pitting damage. Rincon et al. [46] modeled elliptical pitting damage and determined the resulting mesh stiffnesses using finite element and analytical formulations. Ma and Chen [45] investigated the effect of surface pits and root crack failures on mesh stiffness. The dynamic response was determined using numerical simulations. Jiang et al. [47] studied rectangular tooth spalling on helical gear pairs. Liang et al. [49] studied the pitting damage on external spur gears with different severity levels and its influence on mesh stiffness. Saxena et al. [48] compared the mesh stiffnesses of gear teeth with rectangular-, circular-, and V-shaped pits. Liang et al. [50] investigated pitting damage distributed over multiple teeth. Lei et al. [51] investigated the mesh stiffness of spur gears with micro-sized pitting damage distributed across the tooth surface. Luo et al. [52] evaluated the effects of pitting damage on tooth mesh stiffness including accurate pit depth geometry. Luo et al. [54] discussed a shape-independent approach to modeling pits in gear pairs. Huangfu et al. [1] studied the meshing characteristics and dynamics of the pit by accurately capturing the pit geometry on the gear tooth. Yousfi et al. [55] used double discretization tooth surface to identify pit depth variation in width and height directions, and used the potential energy method to determine mesh stiffnesses. We analyze the effects of tooth surface pit damage using a finite element/contact mechanics model that has been demonstrated to accurately predict the dynamics of healthy teeth without damage. Because the contact on mating gear teeth is calculated at each gear configuration accounting for elastic deformations of the gears and damage to the tooth surfaces, we are able to investigate a wide range of damage not previously considered. This includes cases where the pitting damage covers a majority of the active tooth surface.

Tooth root cracks are another type of damage that alters the deflections and mesh stiffnesses of the gear tooth mesh interface [44, 61, 63, 67]. Whereas tooth root cracks affect gear tooth contact through local compliance changes to the gear tooth and blank, tooth surface pits directly change how contact is distributed on the gear teeth. The mesh stiffnesses may differ meaningfully for different damage types.

This research work analyzes the effects of tooth surface pitting damage on the gear tooth mesh characteristics of a unity ratio spur gear pair from the literature using a finite element/contact mechanics (FE/CM) approach. Three cases of pitting damage are considered: (i) pits centered at pitch, (ii) pits centered in the approach, and (iii) pits centered in the recess. The static transmission error, tooth contact forces, and tooth pair stiffnesses are determined using parametric studies for a wide range of pit sizes. The results are compared to those for healthy teeth to quantify the effect of tooth pitting on the gear tooth mesh interface.

2.2 Tooth Mesh Characterization of Healthy Spur Gear Pair

A combined finite element/contact mechanics (FE/CM) approach is used in this work. The details of the elastic contact formulation and how it couples to the finite element approach are given by Vijayakar [131]. Parker et al. [14] described the formulation for the dynamics of two-dimensional gear pairs. It was extended by Cooley et al. [132] for three-dimensional gears, as part of an efficient frequency-domain approach for dynamics calculations. The FE/CM method has been shown to accurately predict the nonlinear dynamic response of spur gear pairs compared to experiments when the teeth are unmodified

[14] and have tooth profile modifications [17]. The FE/CM was shown to accurately predict tooth root stresses in planetary gears [133] and spur gear pairs [134]. The method leverages the small size of the contact zone (i.e., the location where two mating gear teeth interface) compared to the overall dimensions of the gear teeth. It is assumed that beyond a certain distance from contact, the deformations of gear teeth are accurately predicted using the finite element approach. At locations near the contact zone, relative deflections are accurately captured using an analytical formula derived using elastic half-space approximations. When these two solutions are paired, it is possible to obtain accurate full-field approximations of the total displacements anywhere on the tooth surface, including those in the vicinity of the contact zone. The FE/CM formulation uses high-precision finite elements along the involute tooth surfaces, which are captured using specialized finite elements that have high nodal resolution along the tooth profile and continuous shape functions so that local curvatures are accurately captured. Not needed are highly refined finite element meshes interior to the tooth surface. When the contact problem is approached with conventional finite element approaches, excessively refined finite element meshes interior to the tooth surface are generally needed for convergence. Computational efficiency is sacrificed. The FE/CM approach avoids this issue. The FE/CM approach permits the calculation of the elastic contact pressure distribution and elastic deformations accounting for changing contact conditions due to gear positioning within the mesh cycle, elastic deformations throughout the gear, and damage.

The unity-ratio spur gear pair analyzed in this research work is from Ref. [1]. The finite element model of the gear pair is shown in Figure 2.1. The gears have 25 teeth, 6 mm module, and 20 degrees pressure angle. Their pitch, root, and outer diameters are 150, 135, and 162 mm, respectively. The gear facewidths are 16 mm. A 200 N-m torque is applied to the inner diameter of the output gear. The theoretical contact ratio is 1.61 for this gear pair.

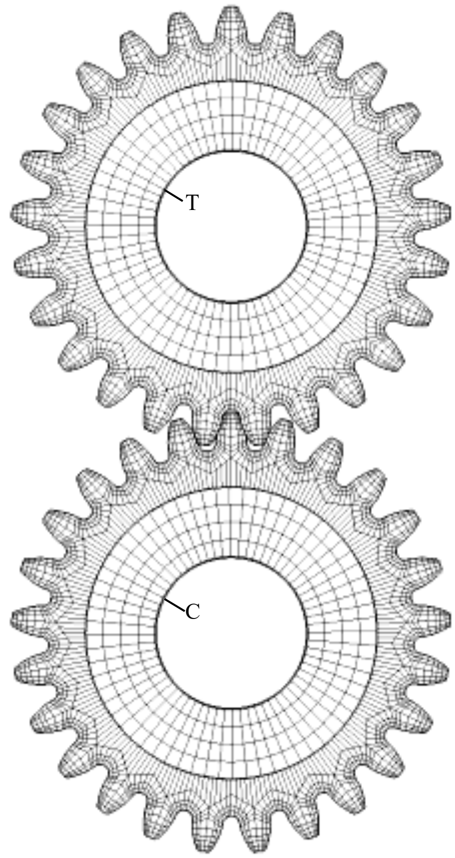

Figure 2.1: Finite element/contact mechanics model of the spur gear pair analyzed in this study. A torque is applied to the output gear inner diameter "T". The input pinion inner diameter is constrained to have no deformation ("C").

The (loaded) static transmission error is calculated from $\delta_0 = r_{b_i}\theta_i + r_{b_o}\theta_o - \varepsilon$, where r_{b_i} and r_{b_o} are base radii of the input and output gears. θ_i and θ_o are the rotational deflections of the input and output gears calculated from the rigid body rotational degrees-of-freedom of the FE/CM model. The no-load transmission error ε is generally calculated by analyzing the gear pair at a sufficiently low nominal load that the elastic deformations are much smaller than the deformations resulting from tooth surface modifications. The no-load transmission error $\varepsilon \to 0$ in this research work on unmodified gear teeth. The static transmission error for the unity-ratio spur gear pair with all teeth healthy is shown in Figure 2.2 for three mesh cycles. The static transmission error is larger when only a single pair of teeth are in contact. For these instances in the mesh cycle, all load is applied to a single tooth, which results in it experiencing large bending deformations. The static transmission error decreases when two pairs of teeth are in contact and the load is shared. These are well-known and expected results.

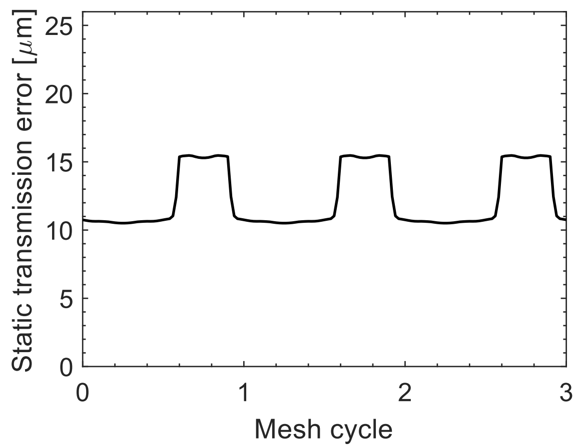

Figure 2.2: FE/CM calculation of static transmission error for the healthy spur gear pair at 200 N-m torque.

Figure 2.3(a) shows the tooth contact forces for the gear pair over three mesh cycles. A complete load and un-load cycle is shown for tooth i (solid line). The tooth that comes into contact immediately before is shown by a dashed line. The dash-dotted line shows the loads on the next tooth that comes into contact. The loads on other teeth are not shown for brevity. The load on tooth i (solid line) vanishes until it enters mesh near 0.88 mesh cycle. After 0.88 mesh cycle, the gear pair has two different pairs of teeth in contact simultaneously with the load on tooth i increasing and the load on tooth $i-1$ decreasing with increasing mesh cycle. At mesh cycle 1.62, tooth $i-1$ leaves mesh and only tooth i carries the load. Tooth i carries the maximum load in this region. At 1.88 mesh cycle, tooth $i+1$ comes into contact causing the load on tooth i to decrease. This is the expected loading and unloading cycle for healthy spur gear pairs. Tooth pitting damage will be shown to alter this behavior.

The stiffness of tooth i with its mating tooth on the output gear is calculated from $k_i = F_i/\delta_0$, where $F_i = \int_{S_i} p_i dS_i$ is the total load on tooth i at a given instant in the mesh cycle, p_i is the contact pressure distribution on the tooth surface S_i, and δ_0 is the corresponding static transmission error of the gear pair. The tooth pair stiffness calculation uses an average slope approach where the total tooth load is divided by the total mesh deflection. Because the gear teeth are un-modified with perfect involutes, the resulting calculations do not differ substantially from those of the local slope method, where the tooth stiffnesses are determined by finding the slope of the force-deflection curve for the gear teeth at a given nominal load.

The calculated tooth pair stiffnesses for the unity-ratio gear pair (Figure 2.1) are shown in Figure 2.3(b). The tooth pair stiffnesses have similar load and un-load behavior as shown for the tooth contact forces in Figure 2.3(a). The tooth mesh stiffness is determined by summing the stiffnesses of the individual tooth pairs in contact $k_m = \sum k_i$. For instances in the mesh cycle when only a single pair of teeth are in contact the tooth pair stiffnesses are identical to the tooth mesh stiffnesses. When multiple pairs of teeth are in contact, the mesh stiffness is larger than when only one pair of teeth are in mesh. The tooth mesh stiffness obtained from the individual tooth pair stiffnesses is identical to that which would be obtained by calculating the mesh stiffness directly. We use tooth pair stiffnesses in this research work because pitting damage results in local changes at the mesh that are generally confined to a single tooth pair. With these tooth pair stiffnesses, the overall effects caused by damage can be easily determined.

The static transmission errors (Figure 2.2) and tooth pair stiffnesses (Figure 2.3) are used as excitations to dynamic models. The dynamic mesh force for a pair of gears in contact is given by $f_m(\delta,t) = \sum_i k_i(t)(\delta - \delta_0)$, where δ is the dynamic mesh deflection that depends on the kinematic variables of the dynamic model used and the sum is over all pairs of teeth in contact. The dynamic response in gears results from two sources: parametric excitation arising from fluctuating changes to the tooth pair stiffnesses $k_i(t)$ and direct forcing $\sum_i k_i(t)\,\delta_0(t)$ from static transmission error excitation. For many gear pairs $\sum_i k_i(t)\,\delta_0(t) \approx k_0\delta_0(t)$, where k_0 is the average tooth mesh stiffness calculated over one complete tooth mesh cycle. Because of their importance to dynamic modeling and the dynamic response predicted from models, we investigate the static transmission error and tooth pair stiffnesses of spur gears with pitting damage.

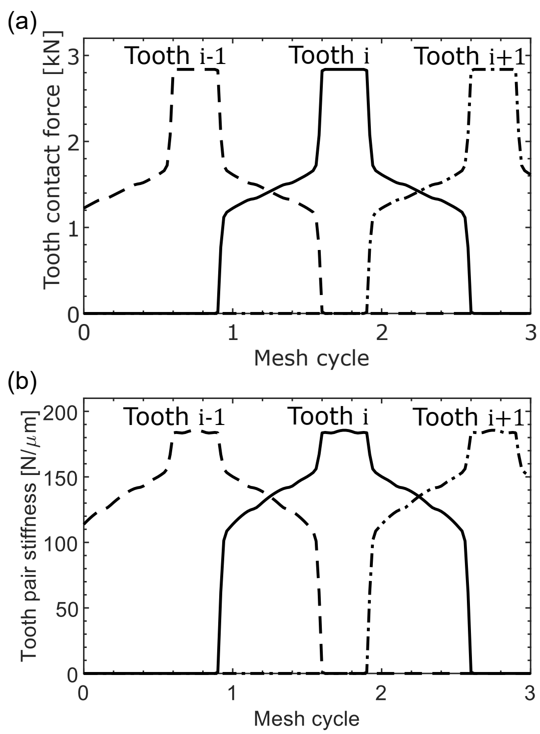

Figure 2.3: FE/CM calculation of (a) tooth contact force and (b) tooth pair stiffness for the healthy spur gear pair at 200 Nm torque. The dashed, solid, and dotted lines denote three successive teeth in contact.

2.3 Tooth Mesh Characterization with Surface Pitting Damage

Tooth surface pitting damage is incorporated into the FE/CM model by introducing an initial separation into each cell in the contact grid where damage is prescribed. In this research work, pits with elliptical shapes are considered (Figure 2.4). The pit is defined by its center location along the facewidth t_c and profile s_c of the tooth. Their sizes are defined by a width (along the tooth face) and a height (along the tooth profile). Higher contact grid resolution is necessary for damaged teeth to accurately capture the sharp changes in contact pressures. Because certain user-defined cells do not carry the load within a prespecified damaged region of the tooth surface, the contact pressure distribution on the teeth changes, causing the deflections of the teeth to differ from healthy. Pitting damage can be applied to teeth on the input or output gears. Multiple pits can be applied on a single gear tooth. This research work evaluates pitting damage on only the input gear teeth, and we apply just one pit on the tooth surface.

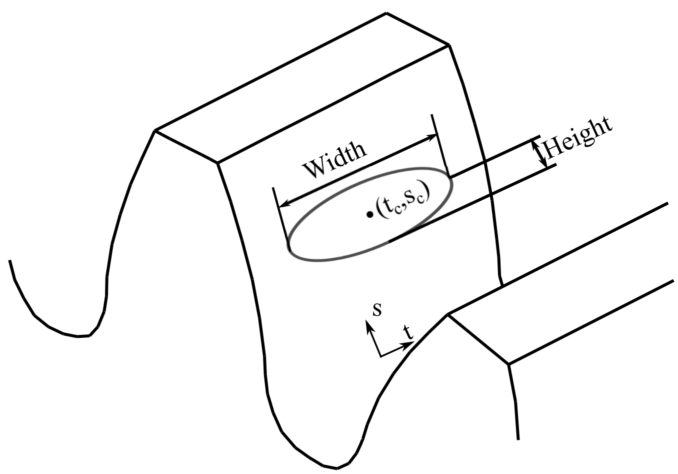

Figure 2.4: Schematic of a spur gear tooth with pit damage having an elliptical shape. The pit center is located at t_c along the facewidth and s_c along the profile.

The effect of pitting damage on the tooth mesh characterization is determined numerically through parametric studies on the gear pair shown in Figure 2.1. The parametric study simultaneously varies the size of the pit (i.e., both the width and height) so that the effects can be seen as the damaged area grows. Three different center locations along the profile are considered. Small damage that covers relatively little of the facewidth and large damage that covers nearly the entire tooth flank are analyzed. The following sections show the results of these parametric studies.

2.3.1 Pits Centered at the Pitch

Figure 2.5(a) shows pits of varying sizes that are centered at the midface of the tooth ($t_c = 0$) at the pitch point ($s_c = 28.38$). The pit is applied to the input gear of the gear pair, although, because the gears are identical, the results that follow would be the same if it were applied to the output gear. The depth is 0.01 mm for all pits considered. The pit widths are 4 mm, 8 mm, 12 mm, and 16 mm, respectively. Their heights are 1.43 mm, 4.75 mm, 8.08 mm, and 14.72 mm, respectively. The percentages of the pit damage area to the total active area of the tooth surface are 2% (blue), 13% (red), 33% (green), and 79% (orange). The pits analyzed here have dimensions much larger than those in Refs. [43, 46]. Our focus is damage on a single tooth.

The static transmission errors corresponding to the pits in Figure 2.5(a) are shown in Figure 2.5(b). The static transmission error increases in amplitude as the pit damage area increases and fewer cells on the tooth surface carry the load. The duration of the mesh cycle where the static transmission error deviates from healthy depends on the height of the pit (measured along the tooth profile). When the damaged area is just 2% (blue curve), the static transmission error only deviates from healthy when a single pair of teeth are in contact. For larger pits like those for 13% and 33% damaged area, the static transmission error deviates from healthy for a much wider range of mesh cycle, including locations where two pairs of teeth are in contact. When the damage covers 79% of the tooth surface area, the range of mesh cycles where the static transmission error differs is nearly equal to the contact ratio of the gear pair (1.61). These increases in static transmission error are expected to increase the gear's dynamic response. Because the damage is on a single tooth the duration that the STE in Figure 2.5(b) is affected is less than two mesh cycles. Damage on multiple consecutive teeth leads to extended regions of the mesh cycle being affected [1].

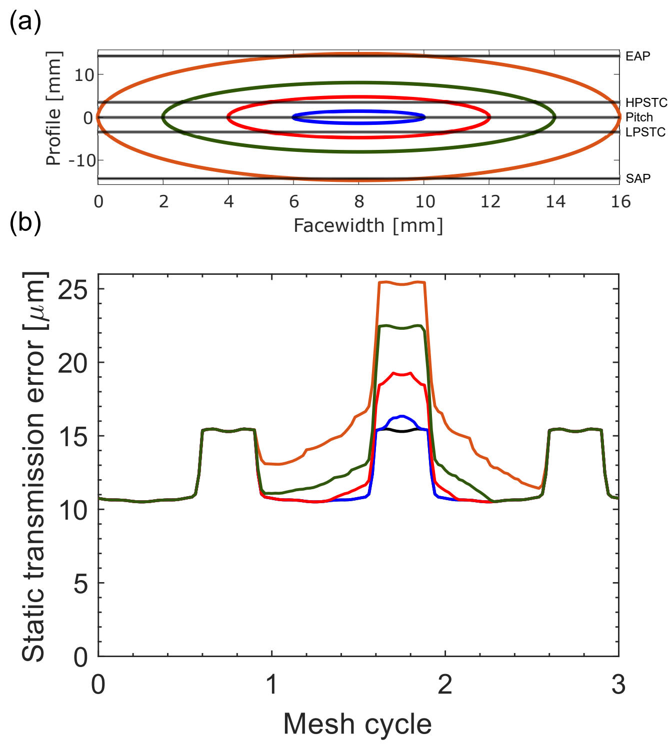

Figure 2.5: (a) Schematic of the gear tooth surface with pitting damage centered midway through the gear face at the pitch point. (b) FE/CM calculation of static transmission error for varying mesh cycle. The black line is for healthy teeth without damage. The blue, red, green, and orange lines correspond to pits that cover 2%, 13%, 33%, and 79% of the tooth surface, respectively. In (a) SAP, LPSTC (HPSTC), and EAP denote the start of active profile, lowest (highest) point of single tooth contact, and end of active profile, respectively.

Table 2.1 provides percentage differences between damaged and healthy calculations of static transmission error at three different instants of the mesh cycle. The first instant is selected at 1.4 mesh cycle when two pairs of teeth are in contact. The second instant occurs for single pair of teeth in contact at 1.74 mesh cycle. The third instant occurs when two pairs of teeth are in contact at 2.08 mesh cycle. The percentage difference for the smallest pit area (i.e., 2%) vanishes whenever two pairs of teeth are in contact because the pit height is so small that it is only active in the region of single tooth pair contact. The other size pits affect the static transmission errors at all three instants. All pit damages analyzed have largest deviations from healthy when only a single pair of teeth are in contact. Interestingly, the results in Table 2.1 and Figure 2.5(b) show that the effect of the pit damage is slightly asymmetric about the pitch point.

Table 2.1: Percentage difference of damaged gear pair static transmission error compared to when the teeth are healthy at different instants in mesh cycle. The pit damage is shown schematically in Figure 2.5 STC (DTC) denotes single (double) tooth contact.

Pitting Damage Area	Mesh cycle 1.4 (DTC)	Mesh cycle 1.74 (STC)	Mesh cycle 2.08 (DTC)
2%	0	6.56%	0
13%	3.03%	22.36%	0.11%
33%	13.89%	37.32%	12.27%
79%	33.97%	49.27%	34.49%

Tooth contact forces for the pitting damage shown in Figure 2.5(a) are shown in Figure 2.6(a). When the damage is just 2% of the total surface area of the tooth, the tooth loads are nearly identical to those for healthy, undamaged teeth. This is because this small pit damage only impacts the tooth contact distribution when a single pair of teeth are in contact. In this case, the contact pressure distribution changes, but the total contact force remains the same for the gears to maintain equilibrium. Even at larger damaged areas, the total contact force on the tooth with the region of single tooth contact does not change. For all pits, the maximum tooth contact force is 2.8 kN at 1.78 mesh cycle, which occurs when only a single pair of teeth are in contact. For damage areas 13% and higher meaningful differences between the contact loads for damaged teeth and healthy teeth occur, but only when multiple pairs of teeth carry the load. As seen in Figure 2.6(a), the load generally increases on healthy teeth and decreases on the damaged tooth. The large pit that covers 79% of the tooth surface area has local maxima of 0.7 kN at 1.1 mesh cycle and 0.98 kN at 2.4 mesh cycle.

The tooth pair stiffnesses for the gear pair with pits centered at the pitch are shown in Figure 2.6(b). Although the gear tooth loads do not change for small damage like 2% (Figure 2.6(a)), the tooth pair stiffness decreases noticeably due to the pit. The pit with 13% area decreases further when only a single pair of teeth are in contact. For pit areas of 2% and 13%, the tooth pair stiffnesses with damage have local minima at the pitch point where only a single pair of teeth are in contact. The duration of the mesh cycle where differences are seen also increases with increasing damaged area. Whereas the pit with 2% area had differences confined to the single contact region, pits of larger areas have differences that extend into the regions of double tooth contact both below and above the pitch. The decrease in mesh stiffness of the damaged tooth is substantial. The amount that the mesh stiffness increases for the other healthy pair of teeth in contact is much less. For the pits with 33% and 79% area, the stiffnesses are nearly constant in the single tooth contact region. For the pit that covers 79% of the tooth surface, the tooth pair stiffness has a local maximum on the healthy pair of teeth in contact. This occurs only for this large amount of damage. Like the tooth contact forces in Figure 2.6(a), the tooth pair stiffnesses in Figure 2.6(b) are asymmetrical about the pitch point even though the pit is placed symmetrically along the profile (see Figure 2.5(a)). Because damage creates additional fluctuations in the tooth pair stiffnesses the gear pair is expected to have more vibrations than it would if all gear teeth were healthy.

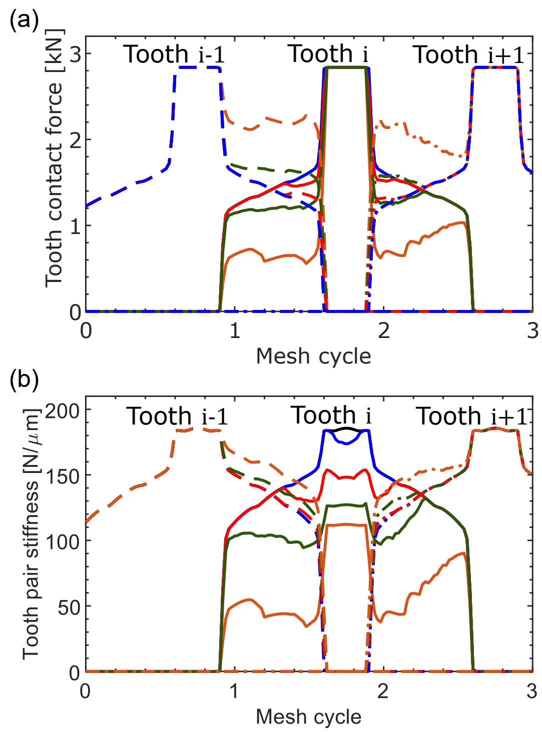

Figure 2.6: FE/CM calculation of (a) tooth contact force and (b) tooth pair stiffnesses of the spur gear pair with varying sizes of pit damage located at the pitch. The black line is for healthy teeth without damage. The blue, red, green, and orange lines are for pit damage that covers 2%, 13%, 33%, and 79% of the tooth surface, respectively. The tooth with damage is shown by solid lines. The tooth that engages immediately before (after) is shown by dashed (dash-dotted) lines.

2.3.2 Pits Centered in the Approach

This section analyzes pits that are centered within the approach of the gear pair. Figure 2.7(a) shows pits of varying sizes that are centered at the midface of the tooth and the midpoint of the approach length. The depth is fixed at 0.01 mm for all pits. The pit widths are 4 mm, 8 mm, 12 mm, and 16 mm. Their heights are 0.71 mm, 2.32 mm, 3.93 mm, and

7.14 mm respectively. The percentages of the pit damage area to the total active area of the tooth surface are 1% (blue), 6% (red), 16% (green), and 39% (orange). These pits have smaller areas than those considered at the pitch.

The static transmission errors for the pits in Figure 2.7(a) are shown in Figure 2.7(b). The effect of pit damage occurs earlier in the mesh cycle because of the location of the pit. As for the case when the pit center was at the pitch, the static transmission error increases with increasing amount of damage. Pits with 1% and 6% area only affect the static transmission error within the region of double tooth contact. The largest static transmission error occurs near the location of the pit (i.e., 1.38 mesh cycle) when two pairs of teeth are in contact. Pits with 16% and 39% area have local maxima near the pit location at 1.38 mesh cycle. These pits impact the deformations in both the double and single tooth contact regions. The largest differences in static transmission error for these large pits occur near the LPSTC, which is where the number of tooth pairs in contact change from two to one. The pit with 39% area damaged is so large that the static transmission error deviates from that of the healthy teeth for the entire region of single tooth contact.

Table 2.2 provides percentage differences between damaged and healthy calculations of static transmission error at two instants of the mesh cycle. The first instant is selected when two pairs of teeth are in contact at 1.36 mesh cycle, and the second instant is in the transition region where the number of teeth in contact changes at 1.62 mesh cycle. The percentage difference for 1% pit and 6% pit vanishes when single pair of teeth are in contact because their dimensions are small and only impact the results for a narrow range of mesh cycles. The other two pits affected the static transmission error at both instants. The highest amplitude differences are observed to occur at 1.62 mesh cycle when contact occurs near the LPSTC.

(a)

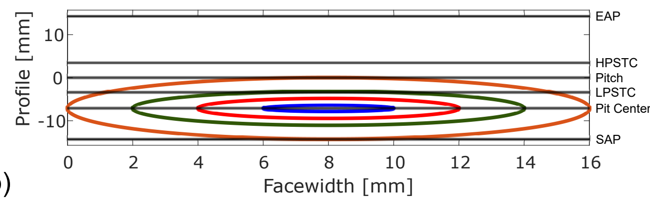

(b)

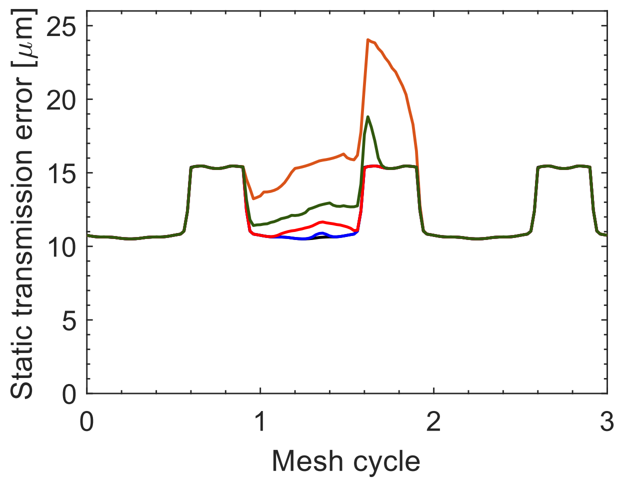

Figure 2.7: (a) Schematic of the gear tooth surface with pitting damage centered in the approach at the midface of the gear. (b) FE/CM calculation of static transmission error for varying mesh cycle. The black line is for healthy teeth without damage. The blue, red, green, and orange lines correspond to pits that cover 1%, 6%, 16%, and 39% of the tooth surface, respectively. In (a) SAP, LPSTC (HPSTC), and EAP denote the start of active profile, lowest (highest) point of single tooth contact, and end of active profile, respectively.

Table 2.2: Percentage difference of damaged gear pair static transmission error compared to when the teeth are healthy at different instants in mesh cycle. The pit damage is shown schematically in Figure 2.7 STC (DTC) denotes single (double) tooth contact.

Pitting Damage Area	Mesh cycle 1.36 (DTC)	Mesh cycle 1.62 (DTC-STC)
1%	2.57%	0
6%	9.30%	0
16%	19.00%	19.76%
39%	39.56%	43.67%

The tooth contact forces are shown in Figure 2.8(a). For increasing pit area, the force on the damaged tooth decreases and that on the healthy tooth increases, but only within the region where two pairs of teeth are in contact. The load on the damaged tooth does not change when only the damaged tooth is in contact, similar to that found for pits centered at the pitch. The tooth loads on the next tooth $i+1$ are not affected by the pit.

The tooth pair stiffnesses for the pits in Figure 2.7(a) are shown in Figure 2.8(b). Differences in mesh stiffness due to pitting damage are largest within the range of mesh cycles where two pairs of teeth are in contact. For small pit areas of 1% and 6%, the mesh stiffnesses only change within the region of double tooth contact. The pits with larger areas have differences that extend into the region of single tooth contact. The tooth pair stiffnesses for the healthy teeth immediately after damage are not affected. They are identical to those for healthy teeth.

2.3.3 Pits Centered in the Recess

The recess region occurs when the input gear has contact between pitch and the end of the active profile. Figure 2.9(a) shows the pits considered in this section; all pits are centered at the midface of the tooth and the midpoint of the recess length. The pits have the same dimensions as those analyzed in the approach.

Figure 2.9(b) shows the static transmission error for the pits in Figure 2.9(a). Pits with 16% damaged areas and below have increases in static transmission error near 2.2 mesh cycle when two pairs of teeth are in contact. Even though the pit with 16% damage area begins at the highest point of single tooth contact (Figure 2.9(a)), its effect on static transmission error is observed to occur in a region where two pairs of teeth are in contact. The pit with 39% damaged area impacts the static transmission error for a wider range of mesh cycles including those when only a single pair of teeth are in contact. The static transmission error is largest for this large pit near the HPSTC. The effect of the pit is seen to occur for nearly the entire range of mesh cycles when the damaged tooth is in contact.

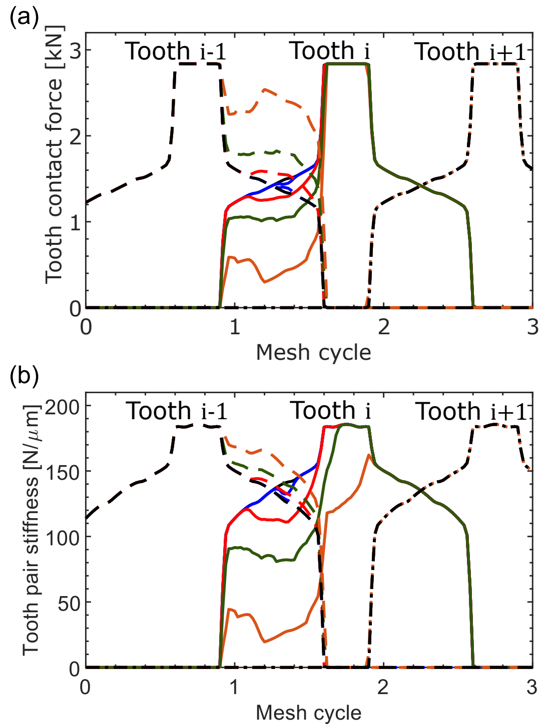

Figure 2.8: FE/CM calculation of (a) tooth contact force and (b) tooth pair stiffnesses of the pit damaged spur gear pair with varying sizes of pit damage located in the approach. The pit is shown schematically in Figure 2.7 The black line is for healthy teeth without damage. The blue, red, green, and orange lines are for pit damage that covers 1%, 6%, 16%, and 39% of the tooth surface, respectively. The tooth with damage is shown by solid lines. The tooth that engages immediately before (after) is shown by dashed (dash-dotted) lines.

Table 2.3 provides percentage differences between damaged and healthy calculations of static transmission error at 1.88 (near the HPSTC) and 2.14 (region of double tooth contact) mesh cycle. The percentage differences vanish for pits with 1%, 6%, and 16% damaged area at 1.88 mesh cycle because the effects of damage do not extend to this region (see Figure 2.9(b)). When the damaged area increases to 39%, the percentage difference increases dramatically. At mesh cycle 2.14, the percentage difference increases monotonically with increasing damage area.

Figure 2.10(a) shows the tooth contact forces for the pits centered within the recess. Damage only affects the tooth loads when two pairs of teeth are in contact. Like the prior

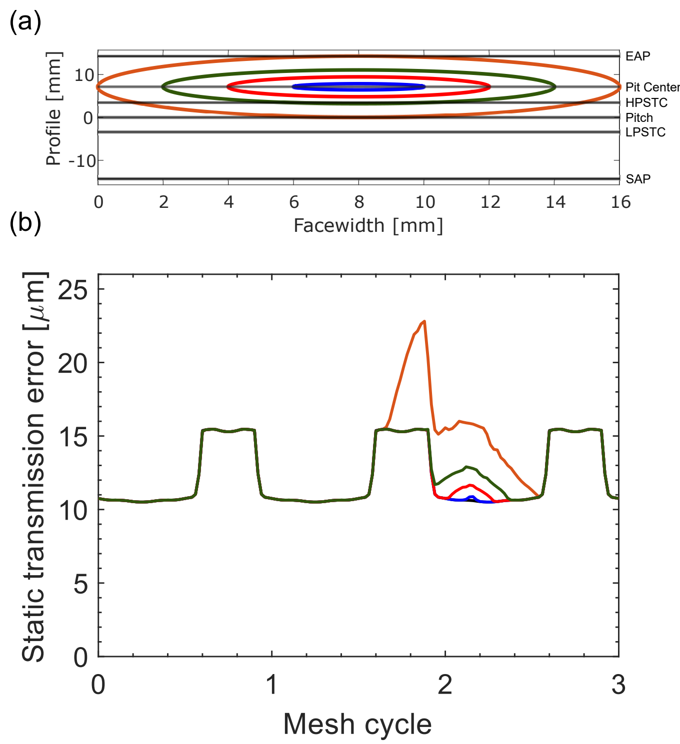

Figure 2.9: (a) Schematic of the gear tooth surface with pitting damage centered in the recess at the midface of the gear. (b) FE/CM calculation of static transmission error for varying mesh cycle. The black line is for healthy teeth without damage. The blue, red, green, and orange lines are for pit damage that covers 1%, 6%, 16%, and 39% of the tooth surface, respectively. In (a) SAP, LPSTC (HPSTC), and EAP denote the start of active profile, lowest (highest) point of single tooth contact, and end of active profile, respectively.

Table 2.3: Percentage difference of damaged gear pair static transmission error compared to when the teeth are healthy at different instants in mesh cycle. The pit damage is shown schematically in Figure 2.9 STC (DTC) denotes single (double) tooth contact.

Pitting Damage Area	Mesh cycle 1.88 (STC-DTC)	Mesh cycle 2.14 (DTC)
1%	0	2.37%
6%	0	9.46%
16%	0	19.15%
39%	38.59%	39.72%

cases when the pits were located at the pitch and approach, the damaged tooth carries less load, and the next healthy tooth carries more load. Interestingly, the tooth loads shown in Figure 2.10(a) differ from those shown in Figure 2.8(a) even though the amount and geometry of damage are identical.

Figure 2.10(b) shows the tooth pair stiffnesses corresponding to the pitting damage shown in Figure 2.9(a). The pits with damaged areas equal to 1%, 6%, and 16% only affect the tooth pair stiffness when two pairs of teeth are in contact. The pit with 39% damaged area meaningfully alters the stiffnesses in both single and double tooth contact regions. Similar to the tooth loads, the tooth pair stiffnesses for pits in the recess (Figure 2.10(b)) differ from those in the approach (Figure 2.8(b)), even though the damage has the same size.

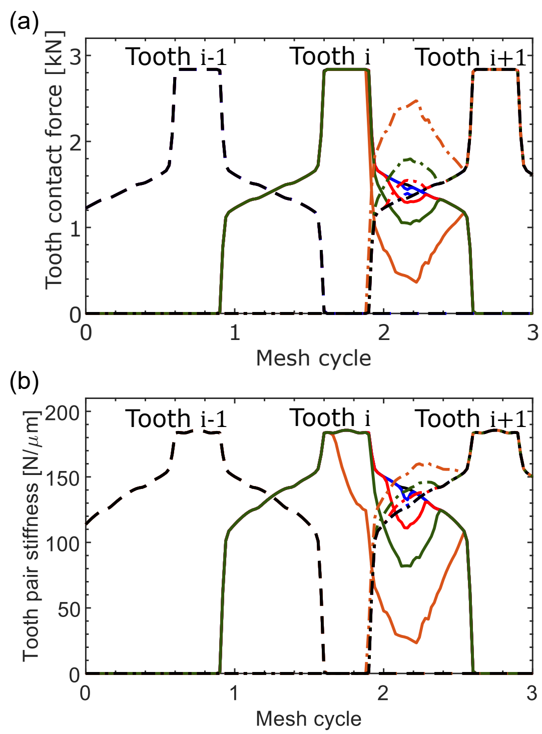

Figure 2.10: FE/CM calculation of (a) tooth contact force and (b) tooth pair stiffnesses of the spur gear pair with varying sizes of pit damage located in the recess. The black line is for healthy teeth without damage. The blue, red, green, and orange lines are for pit damage that covers 1%, 6%, 16%, and 39% of the tooth surface, respectively. The tooth with damage is shown by solid lines. The tooth that engages immediately before (after) is shown by dashed (dash-dotted) lines.

2.4 Damage Case Comparison

Figure 2.11 shows the peak-to-peak static transmission error (PPSTE) for varying percentage of damaged area (i.e., the ratio of the pit area to the total active surface area). The PPSTE increases monotonically for increasing damage area when the pit is centered at the pitch (solid (black) line). For pits centered in the approach (dashed (blue) line), the PPSTE does not change with damage area for percentages less than 9.2%. For these small pits, the damage causes differences only in the region where two pairs of teeth are in contact (see the 1% and 6% damage areas in Figure 2.7(b)). The PPSTE, therefore, is unaffected by the damage. For areas larger than 9.2%, the PPSTE increases with increasing damage. The PPSTE for the pit centered in the recess (dotted (red) line) is insensitive to damage areas below 16%. Beyond 16% damage area, the PPSTE increases with increasing damage.

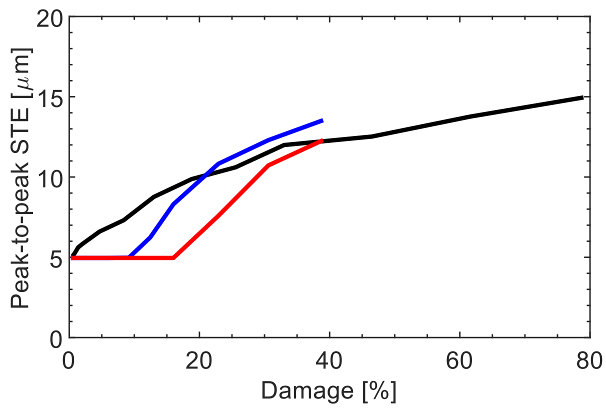

Figure 2.11: Peak-to-peak static transmission error for varying percent of pit damaged area. The results for pits centered at the pitch, approach, and recess are shown by solid (black), dashed (blue), and dotted (red) lines, respectively.

2.5 Conclusions

A finite element/contact mechanics (FE/CM) approach is used to characterize the gear tooth mesh interface for spur gear pairs with pitting damage. Pits with elliptical geometry were considered. A wide range of pit sizes analyzed for cases when the damage originates at the pitch, in the approach, and the recess of the meshing gear teeth.

Tooth surface pits lead to increases in static transmission error. A local maximum generally occurs near the pit. When the pitting damage is large and originates in the approach or recess, the maximum static transmission error occurs for single tooth contact near the location where the number of tooth pairs in contact changes from one to two. Pitting damage causes the tooth pair stiffnesses to decrease. Larger pits result in larger decreases in stiffness and wider ranges of mesh cycle where differences occur. The tooth pair stiffnesses for healthy teeth without damage increase because these teeth carry more load to compensate for the damage. The amount that tooth stiffness decreases is largest near damage for all pit sizes and locations where the pit originates.

CHAPTER THREE

TOOTH MESH CHARACTERIZATION OF SPUR GEAR PAIRS WITH LOCALIZED DEFECTS: TOOTH ROOT CRACK AND SURFACE PITTING

3.1 Introduction

There are two primary excitation sources in gears: static transmission error excitation and tooth mesh stiffness fluctuations. Accurate calculations of these quantities are important for reliable dynamic response predictions from gear analytical models. The importance of these calculations may be even greater when damage (e.g., tooth root cracks or tooth surface pitting) occurs on the teeth. This is because damage to gear teeth alters the load distribution among the teeth in mesh and causes changes to the pressure distribution on the surfaces in contact. These, in turn, affect the overall deformations of the gears that manifest in localized changes to the static transmission errors and tooth mesh stiffnesses. This work is primarily motivated by methods intended to monitor for damage to gears from the transmission errors produced. However, predicting the transmission errors in geared systems due to damage is important for design, noise emissions, and understanding root causes of failure.

Rotorcraft are an example application where vibrations are measured from the transmission for the purpose of monitoring for damage to the gears, as well as other components, it contains. A review of vibration-based techniques for rotorcraft transmission diagnostics is given in Ref. [5]. Additional diagnostic techniques used in rotorcraft were discussed by Dempsey et al. [6]. Detecting damage in geared systems is not limited to rotorcraft; it is of broad interest in power transmission. Lei et al. [135] summarized condition monitoring methods for both fixed-axis and planetary gears. Among many techniques used for planetary gear damage-detection is the vibration separation method [4,120]. This method strategically isolates the vibrations generated by each individual mesh in the planetary gear.

In this way, the detection of damage from a planetary gear, which contains several meshes, can be evaluated using techniques intended for a single pair of gears. Even with advances in sensor technology, expanded ability to acquire and store measured data, and more sophisticated algorithms, diagnostic methods continue to produce false negatives (where damage has occurred but was not detected) and false positives (where damage is predicted but has not occurred).

Gears vibrate as a result of changing contact conditions on the teeth causing dynamic forces at the mesh [8–14, 41]. Accurate representations of the tooth mesh (e.g., the static transmission errors and mesh stiffness fluctuations) are important parameters for gear dynamic models. This has motivated a number of methods for calculating the static transmission errors and tooth mesh stiffnesses of individual gear pairs. These methods primarily center on analytical models [18–29], conventional finite element formulations [30–32, 53], experiments [33–40], and combined finite element/contact mechanics formulations [14, 17, 41]. Several other models for mesh stiffness calculations can be found in the bibliography of Ref. [130]. Damage to the gear teeth alter the usual fluctuations in static transmission error and tooth mesh stiffness, which can lead to increased vibrations and dynamic response.

The impact of tooth surface pit damage, a common failure mode, on the gear tooth mesh interface of mating gears has been studied by a number of investigators. The mesh stiffness of gear pairs with surface pitting wear and partial tooth fracture was analyzed by Choy et al. [42]. The mesh stiffness of gear pairs with pitting damage that is assumed to have regular geometry was analyzed in Refs. [43, 46–48, 136]. The dynamic response of gear pairs with surface pits was numerically investigated in Ref. [45]. External spur gears with different pitting damage severity levels was discussed by Liang et al. [49]. Pitting damage distributed over multiple teeth was investigated by Liang et al. [50]. Lei et al. [51]

studied the mesh stiffness of spur gears with micro-sized pitting damage distributed across the tooth surface. The effect of pitting damage on tooth mesh stiffness including accurate pit depths was evaluated by Luo et al. [52]. Luo et al. [54] discussed a shape-independent approach to modeling pits in gear pairs. Accurate geometrical representation of pit geometry was analyzed by Huangfu et al. [1]. Yousfi et al. [55] used a potential energy method combined with a discretized tooth surface for contact to determine the tooth mesh stiffness of gears with pits and spalls. Meng et al. [56] analyzed the impact of pit growth on tooth mesh stiffnesses. Pits with irregular shapes were analyzed using a matrix equation with the potential energy method by Meng et al. [57]. Parametric studies of pitting damage on a unity-ratio gear pair was investigated using a FE/CM model in Ref. [137]. This paper uses a FE/CM model to systematically analyze the effects of tooth surface pitting damage on the characteristics of spur gear tooth mesh interfaces.

Tooth root cracks are another common failure mode of gears. Daniewicz et al. [58] used a strain energy formulation to calculate the mesh stiffnesses of gear pairs with cracks. The effect of gear rim thickness and the initial crack location on the propagation of cracks through the gear tooth was studied by Lewicki et al. [59]. The mesh stiffnesses of gear pairs with root cracks was determined analytically by Chaari et al. [44]. Ma et al. [45] numerically investigated the effect of failures on mesh stiffness and dynamics. The effect of tooth root crack length on loaded transmission error and mesh stiffness was studied by Rincon et al. [46]. The effect of varying torque was investigated. Pandya et al. [60] calculated percentage reductions in mesh stiffness between two successive crack levels for varying gear pair parameters like backup ratio, pressure angle, and fillet radius and found that these percentage reductions are not affected for varying gear parameters. Ma et al. [62] reviewed the dynamics of gear with tooth root cracks. Various methods for calculating mesh stiffness for damaged gear pairs were investigated in Liang et al. [64]. Wang et al. [65]

calculated the time-varying mesh stiffness for gear teeth with root cracks connected to blanks with complicated geometry. Chen et al. [53] investigated tooth root crack damage on the gear mesh stiffness of gear pairs with thin-webbed blanks. Yang et al. [66] included the opening state of the crack under the action of mesh force in the analytical model for the calculation of mesh stiffness and compared the results with finite element analysis. Cooley et al. [67] showed the effect of crack initiation, and crack path on mesh stiffness. Wang et al. [68] studied the effect of tooth root cracks on the dynamics. Kumar et al. [69] determined the gear mesh stiffness of un-carburized and carburized gears using the potential energy approach for different crack depths. Chen et al. [138] developed a method for modeling three-dimensional crack paths and their propagation. Han et al. [70] analyzed the tooth mesh stiffnesses of spur gears with broken tooth faults, and analyzed their impact on dynamic response. Yang et al. [71] proposed the time-varying mesh stiffness calculation method of the gear pair considering different spatial crack shapes which are different shapes of cracks in the direction of the facewidth of the tooth. Liu et al. [83] investigated the effects of gearbox flexibility on the vibration generated by tooth root crack damage. This paper examines the force-deflection behavior of spur gear pairs with tooth root crack damage using a FE/CM model previously shown to accurately predict elastic contact in healthy gears.

This work uses a FE/CM method to characterize the gear tooth mesh interface for spur gear pairs with either tooth surface pitting or tooth root crack damage. We analyze a unity-ratio gear pair from the literature and a nonunity-ratio gear pair from a rotorcraft application. The calculated static transmission errors and tooth mesh stiffnesses of the unity-ratio gear pair are compared to results previously published in the literature to demonstrate the accuracy of the methodology. The impact of damage on the magnitude, location, and duration of the static transmission error and tooth mesh stiffnesses are analyzed. The effects caused by tooth surface pits are compared to those caused by tooth root cracks.

The calculated tooth mesh parameters are used as inputs to a lumped-parameter gear pair model. The dynamic response generated by damaged gear teeth is calculated numerically for varying types and severity of damage.

3.2 Tooth mesh characterization

3.2.1 Calyx Finite Element/Contact Mechanics (FE/CM) Formulation

This work uses the finite element/contact mechanics (FE/CM) formulation developed by Vijayakar and co-workers [131, 139, 140]. In brief, purely finite element approaches are difficult for gear contact analyses because they require extensively fine finite element meshes in the vicinity of contact. This includes high nodal density to accurately describe the involute surfaces of the gear teeth and high element density to capture high strain gradients interior to the tooth surrounding the location of contact. Furthermore, the location of contact is not fixed in gear applications; it continuously moves along the tooth profile as the gears kinematically rotate. The entire tooth surface must then have high element density. This increases computation time and may prevent the model from being used in dynamic analyses.

To overcome difficulties associated with a purely finite element approach, the FE/CM method pairs an analytical method for elastic contact with the finite element method for tooth, blank, and other structural deformations of the gears [131]. Because local deformations due to contact are not calculated directly by the finite elements, the FE/CM method eliminates the need for highly refined finite element meshes interior to the tooth surface. The finite element mesh used for the gears is shown in Figure 3.1(a). High nodal density is only needed to precisely define the involute surfaces where contact occurs. Specialized finite elements developed for this purpose are described in [140]. The displacement at any material point $\mathbf{r}$ within the tooth due to a normal load p_{ij} at position $\mathbf{r}_{ij}$ on the tooth surface is $\mathbf{u}(\mathbf{r}_{ij}, \mathbf{r})$. The inward normal deformation on the tooth surface is $u(\mathbf{r}_{ij}, \mathbf{r}) = -\mathbf{u}(\mathbf{r}_{ij}, \mathbf{r}) \cdot \mathbf{n}$, where $\mathbf{n}$

is the outward normal vector to the tooth surface at the load location. The deformation $u(\mathbf{r}_{ij},\mathbf{r})$ consists of contributions due to local deformations of the tooth surface and global deformations due to tooth bending and blank deformations. The magnitude of the local deformations diminishes as the material point varies from a location on the tooth surface to one interior on the tooth. The points where the local deformations are negligible compared to the total overall deformations define a matching interface $\mathbf{q}$. The deformations of the tooth can be written as $u(\mathbf{r}_{ij},\mathbf{r}) = \left[u(\mathbf{r}_{ij},\mathbf{r}) - u(\mathbf{r}_{ij},\mathbf{q})\right] + u(\mathbf{r}_{ij},\mathbf{q})$. Noting that the first term is the local, relative deformation due to contact, it is approximated using a surface integral form $u^{(si)}$. The second term $u(\mathbf{r}_{ij},\mathbf{q}) \approx u^{(fe)}$ is calculated with sufficient accuracy from the finite element method. With these the contact problem is formulated as follows. At each point $\mathbf{r}_{ij}$, the separation d_{ij} between mating surfaces is either a positive value (when the two teeth are not in contact) or vanishes (when the two teeth are in contact). If the separation d_{ij} is positive, the corresponding contact load p_{ij} vanishes. If the separation d_{ij} vanishes the contact load p_{ij} is positive. For gear applications, where the body has small deformations relative to their prescribed kinematic motion, the separation has contributions from (i) an initial separation from geometry, (ii) elastic deformations from $u(\mathbf{r}_{ij},\mathbf{r})$, and (iii) overall motions associated with unconstrained degrees of freedom on the gears. These conditions along with the dynamic equilibrium equations are solved using a modified Simplex algorithm [131].

The accuracy of the FE/CM method has been thoroughly tested in the literature for gears without damage. The FE/CM method has been shown to accurately predict the frequency response of meshing gear pairs, including strongly nonlinear characteristics due to contact loss [14, 17, 141]. It has been shown to accurately predict the tooth root strains in gear pairs [134] and tooth root and ring hoop strains in planetary gears [133]. The FE/CM method has also been used as a benchmark for lumped-parameter gear models [14, 142, 143].

The features of the FE/CM framework are retained with the incorporation of gear damage to preserve computational efficiency and permit dynamic analyses with high accuracy.

Figure 3.1(a) shows the finite element mesh of the nonunity-ratio gear pair analyzed in this work. This gear pair comes from the sun-planet pair of the planetary stage in a rotorcraft transmission. The parameters of the gear pair are given in Table 3.1. Both gears are steel with 200 GPa elastic modulus, 0.3 Poisson's ratio, and 7800 kg/m^3 density. Nodes that are located on the inner diameter of the pinion are constrained (denoted as "C" in Figure 3.1(a)). The nodes located on the inner diameter of the gear have applied loads that result in a specified, net torque (denoted as "T" in Figure 3.1(a)). Higher element density is used for the pinion teeth because tooth root crack damage is applied there.

Tooth surface pitting is a contact fatigue failure where small amounts of material from the tooth surface are lost. This failure may also be referred to as spalling. To model tooth surface pitting, specified cells within the contact grid are constrained to carry no load (i.e., $p_{ij} \to 0$ for i, j that fall within a specified damage area). This leads to alterations of the contact pressure distributions on the tooth surface. A representative contact pressure distribution with tooth surface pitting damage is shown in Figure 3.1(e). Because the material removed from the surface typically has depths on the order of tens to hundreds of micro-meters, the overall compliance of the tooth is largely unaffected by the damage. The local compliance of the tooth surface near the damage is affected by the loss of material, however. The decrease in deformation due to having retained the material lost to damage is generally negligible compared to the increase in deformation due to the increases in load at the damage boundary (see Figure 3.1(e)). Therefore, pitting is modeled solely by modifying the contact in the FE/CM model without altering the tooth surface geometry to include the removal of material. The accuracy of these assumptions will be analyzed by comparisons to models from the literature that account for the removal of material on the tooth surface.

Tooth root cracks are failures where material in the root fractures due to excessive or cycled stresses. Tooth root cracks have irregular geometry that follow complex paths through the tooth root [59, 144]. Tooth root cracks in the FE/CM method are modeled by altering the connectivity of elements in the root of the tooth's finite element mesh. This modeling approach does not account for the exact geometry of the crack path. It does, however, accurately capture the remaining amount of healthy material within the tooth. This amount of material that remains and carries load, not the geometry of the damage that carries no load, is a main contributor of compliance in the gear tooth and blank. A representative tooth root crack is shown in Figure 3.1(c) on the finite element mesh of a tooth with exaggerated deformations. The crack extends through the enitre facewidth of the tooth. Root crack damage leads to considerably more bending deformation of the tooth (Figure 3.1(c)) as compared to when the tooth is healthy and without a root crack (Figure 3.1(b)). The method for incorporating root crack damage into the FE/CM model will be shown to accurately predict tooth mesh stiffness of damaged gear pairs compared to a model that does accurately model the crack path.

Table 3.1: Geometrical parameters for the nonunity-ratio spur gear pair

	Gear	Pinion
Number of teeth	35	27
Module (mm)	2.87	
Outer diameter (mm)	104.98	84.05
Root diameter (mm)	91.54	70.76
Tooth thickness (mm)	4.18	4.52
Facewidth (mm)	31.75	34.925
Center distance (mm)	88.9	
Pressure angle (deg)	24.6	

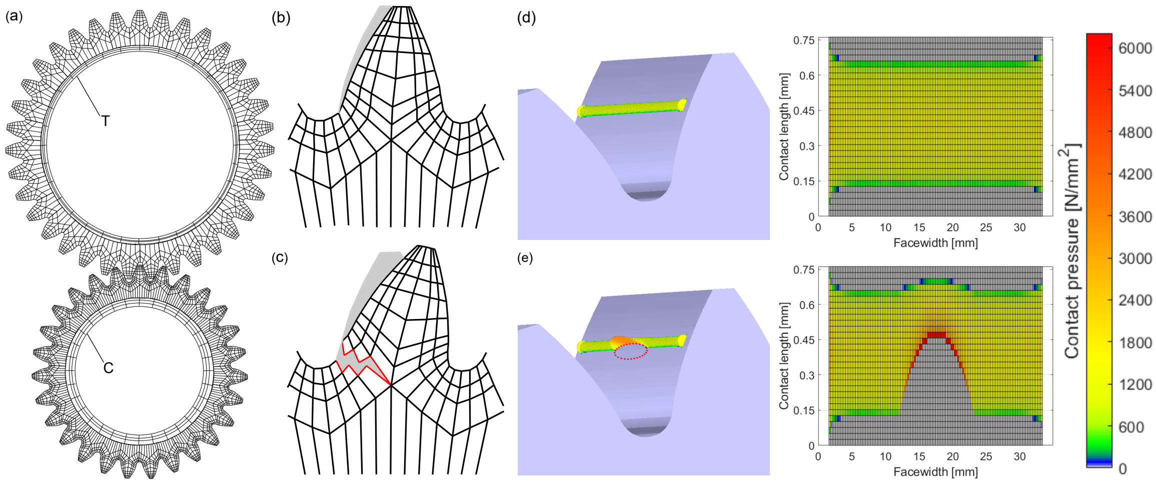

Figure 3.1: (a) Finite element mesh of the nonunity-ratio gear pair analyzed in this work. (b,c) Finite element calculations of deformations for a healthy gear tooth and a gear tooth with root crack damage modeled by releasing the connectivity of elements along a specified path. The undeformed shape of the gear tooth is shown by the grayed regions. Instantaneous contact pressure distribution on (d) a healthy gear tooth and (e) a gear tooth with tooth surface pitting damage.

3.2.2 Force-deflection behavior and mesh stiffness calculations

In this section, the nonunity-ratio gear pair with modified surfaces is analyzed, and its force-deflection (i.e., torque-transmission error) behavior is examined. All pinion and gear teeth have 13.9 μm of linear tip relief that starts at 30 degrees roll angle and ends at the tooth tip. All teeth also have 27.8 μm of symmetric lead crown. To fully capture the overall force-deflection behavior of the gear pair, a number of static simulations are analyzed over a complete mesh cycle for a specified load. We analyzed a total of 100 applied loads ranging from 0.424 $\mathrm{N \cdot m}$ (0.1% of the nominal torque) to a maximum torque of 424 $\mathrm{N \cdot m}$ (nominal torque). The force-deflection behavior for the modified nonunity-ratio gear pair with no damage is shown in Figure 3.2(a). The presence of nonvanishing transmission error at nearly vanishing applied load from nearly 0 to 0.4 mesh cycle is due to the tooth surface modifications. For perfectly involute teeth without modifications, the transmission error vanishes for vanishing load at all points within the mesh cycle [41]. As seen in Figure 3.2(a), the transmission error increases with increasing applied load, as expected, for all instances within the mesh cycle. These increases are notably nonlinear with hardening features, particularly between 0 and 0.4 mesh cycle where the tooth surface modifications are active. Hardening nonlinearity is expected in gears because increases in mesh force increase the contact area between the meshing gear teeth. The region of the mesh cycle where one and two pairs of teeth are in contact changes as the load applied increases. At 424 $N \cdot m$, the gear pair has two pairs of teeth in contact (called double tooth contact) from nearly 0.02 to 0.66 mesh cycle. A single pair of teeth (called single tooth contact) is in contact for the remaining portion of the mesh cycle. Using these results, the involute contact ratio of the gear pair is 1.64, which is larger than the theoretical involute contact ratio of 1.45 because the profile modifications are not large enough to completely remove premature corner tooth contact.

Figure 3.2(b) shows the force-deflection behavior for the modified nonunity-ratio gear pair with a root crack on a single pinion tooth. The root crack extends through one-half of the tooth thickness (Figure 3.1(c)). The transmission error for nearly vanishing load when the tooth has a root crack is nearly identical to that when all teeth are healthy (Figure 3.2(a)), as expected. Increasing the applied load increases the transmission error, with larger transmission errors occurring due to the increase in tooth bending deformation from the root crack damage (as seen by comparing Figs. 3.1(b) and (c)). The transmission error of the gear pair with tooth root crack damage at 424 $N \cdot m$ is 3.74% larger at 0.4 mesh cycle (within the double tooth contact region) and 17.89% larger at 0.78 mesh cycle (within the single tooth contact region) when compared to the gear pair without damage.

Figure 3.2(c) shows the force-deflection behavior for the modified nonunity-ratio gear pair with tooth surface pitting damage on a single pinion tooth. The tooth surface pit, which is shown in Figure 3.1(e), has elliptical geometry with 12.7 mm width and 2.76 mm height. Pitting damage generates high contact pressure gradients near the damaged location. This increases transmission error. The transmission error increases even for nearly vanishing applied load due to the removal of material from the tooth surface from lead modifications and pitting damage. At 424 $\mathrm{N \cdot m}$, the transmission error of the gear pair with pitting damage is maximum at 0.72 mesh cycle (in a region of single tooth contact) with an increase of 43.55% compared to the gear pair without damage.

Figure 3.2(d) compares the force-deflection behavior at 0.72 mesh cycle, which is within a region of single tooth contact for this gear pair. These results are representative of other instances in the mesh cycle, although the differences between tooth root crack and pitting damage are less pronounced from 0 to 0.3 mesh cycle (see Figs. 3.2(b) and (c)). The dashed (blue) line is for the case that a tooth has a root crack. The case that a tooth has a surface pit is shown by the dash-dotted (red) line. The solid (black) line corresponds to the case that all teeth are healthy and none have damage. The additional compliance due to the tooth root crack is evident from the monotonic increases in transmission error for increasing mesh force compared to the case of healthy teeth. The transmission error increases further for the case when the tooth has a surface pit. Notably, the transmission errors increase even near vanishing applied loads due to the modifications impacting the location on the tooth surface where contact occurs. For unmodified teeth, these additional increases in transmission error do not occur and the no-load transmission errors for teeth with pitting damage are nearly identical to those for healthy teeth (not shown).

The mesh stiffnesses of the gear pair are calculated from the force-deflection curves either using the average or local slope calculation approaches [41]. The average slope approach calculates the mesh stiffness by dividing the mesh force by the corresponding mesh deflection at that load as

$$k_a = \frac{F_m}{\delta_m}, \tag{3.1}$$

where F_m is the mesh force and $\delta_m = r_p\theta_p + r_g\theta_g - \varepsilon$ is mesh deflection. The base radius of the pinion and gear are r_p and r_g, respectively. Their rotational deflections are θ_p and θ_g, respectively. These are direct outputs from the FE/CM model. The no-load transmission error is ε. It is calculated from the FE/CM model at a sufficiently small nominal torque that the elastic deflections are negligible compared to the deflections caused by the removal of material from the tooth surface. Specifically, the no-load transmission error is calculated from $\varepsilon = r_p\theta_{p0} + r_g\theta_{g0}$, where the rotational deflections θ_{p0} and θ_{g0} obtained from the FE/CM model analyzed at small applied torque. In this work 0.1% of the nominal torque was used to simulate no-load conditions. The average slope calculation of mesh stiffness is illustrated for the force-deflection curve with pitting damage in Figure 3.2(d). Calculations of average slope stiffness require two analyses: one at low load to calculate the no-load transmission error (ε), and the other at the nominal, operating torque to obtain the static transmission error ($r_p\theta_p + r_g\theta_g$).

The mesh stiffnesses of the modified nonunity-ratio gear pair without damage, with tooth root crack damage, and with tooth surface pitting damage calculated using average slope approach are shown in Figure 3.2(e). The average slope mesh stiffnesses do not have the characteristic high stiffness values corresponding to regions where two pairs of teeth are in contact due to the presence of tooth surface modifications. Instead, the tooth surface modifications result in constantly changing values from 0.02 to 0.66 mesh cycle within the region where two pairs of teeth are in contact. When a tooth has a root crack the mesh stiffnesses decrease, as expected, due to the increased compliance of the tooth. These decreases are not uniform over the mesh cycle, however. The largest decrease in mesh stiffness occurs near unity mesh cycle, where the value decreases from 291.53 N/μm to 232.97 N/μm. The region where the mesh stiffness is affected by the tooth root crack damage extends beyond one mesh cycle. The mesh stiffnesses for the case of pitting damage (dash-dotted (red) line) both increase and decrease from values associated with the undamaged, healthy teeth. The increase in mesh stiffness occurs from 0.3 to 0.64 and from 0.96 to 1.06 mesh cycle. Decreases in mesh stiffness occur from 0.64 to 0.96 mesh cycle. For this damage type, the maximum decrease in mesh stiffness occurs near 0.72 mesh cycle where the stiffness decreases from 291.90 N/μm to 246.53 N/μm. The range of mesh cycle where the mesh stiffness is affected is smaller for tooth surface pitting damage (i.e., between 0.3 and 1.1 mesh cycle) than for tooth root crack damage (i.e., between 0.3 and 1.7 mesh cycle).

The local slope mesh stiffness is calculated from the slope of the force-deflection curve at a nominal mesh deflection according to

$$k_l = \frac{F_m(\delta_m + \Delta\delta_m) - F_m(\delta_m - \Delta\delta_m)}{2\Delta\delta_m}, \tag{3.2}$$

where $F_m(\delta_m + \Delta\delta_m)$ is the mesh force at a deflection above nominal, and $F_m(\delta_m - \Delta\delta_m)$ is the mesh force at a deflection below nominal. $\Delta\delta_m$ is the change in the mesh deflection about the nominal value. Like calculations of mesh stiffness using the average slope approach, calculations that use the local slope approach also require two simulations: one at a deflection above the nominal value and the other at a deflection below nominal value.

Figure 3.2(f) shows the mesh stiffnesses calculated using the local slope approach in Eq. (3.2). For the case of healthy teeth (solid (black) line), the mesh stiffnesses have lower values when a single pair of teeth are in contact, and they have higher values when two pairs of teeth are in contact. Sharp changes in stiffness occur near 0 and 0.68 mesh cycle when the number of teeth in contact changes. These are expected features for spur gear pairs. The mesh stiffness for the case that a tooth has root crack damage is shown in the dashed (blue) line in Figure 3.2(f). The mesh stiffnesses decrease from nearly 0.04 mesh cycle to 1.68 mesh cycle. Outside of this range the mesh stiffnesses are nearly identical to those when the gear teeth are healthy. The mesh stiffnesses for the case of tooth surface pitting damage is shown in the dash-dotted (red) line. The local slope approach, like the average slope approach, shows both increases and decreases in mesh stiffness due to tooth surface pitting damage. The increases are less substantial for the average slope approach (Figure 3.2(e)) than the local slope approach (Figure 3.2(f)), however.

Compared to the stiffness values calculated using the average slope approach in Figure 3.2(e), the stiffness values obtained using the local slope approach in Figure 3.2(f) are meaningfully higher for healthy, undamage teeth and for cases when the teeth have root crack or surface pit damage. This difference is evident from the force-deflection behavior shown in Figure 3.2(d). The differences between the local and average slope approaches for un-modified and modified gear pairs are discussed in detail by Cooley et al. [41].

The average slope approach is used to compare the mesh stiffnesses calculated in this work to those from the literature because they also use the average slope approach. Mesh stiffnesses calculated using the local slope approach are used in parametric studies on important gear damage parameters because of their excellent ability to capture damage-induced dynamics response shown later.

3.2.3 Comparison of healthy gear pair stiffnesses

This section compares mesh stiffnesses calculated using the FE/CM model to those from Refs. [1, 53] for healthy, undamaged gears. The system analyzed in this section is a unity-ratio gear pair. Each gear has 25 teeth, 20 degree pressure angle, 16 mm facewidth, and 6 mm module. Their pitch and outer diameters are 150 mm and 162 mm, respectively. These diameters, along with the 150 mm center distance, gives the (theoretical) contact ratio

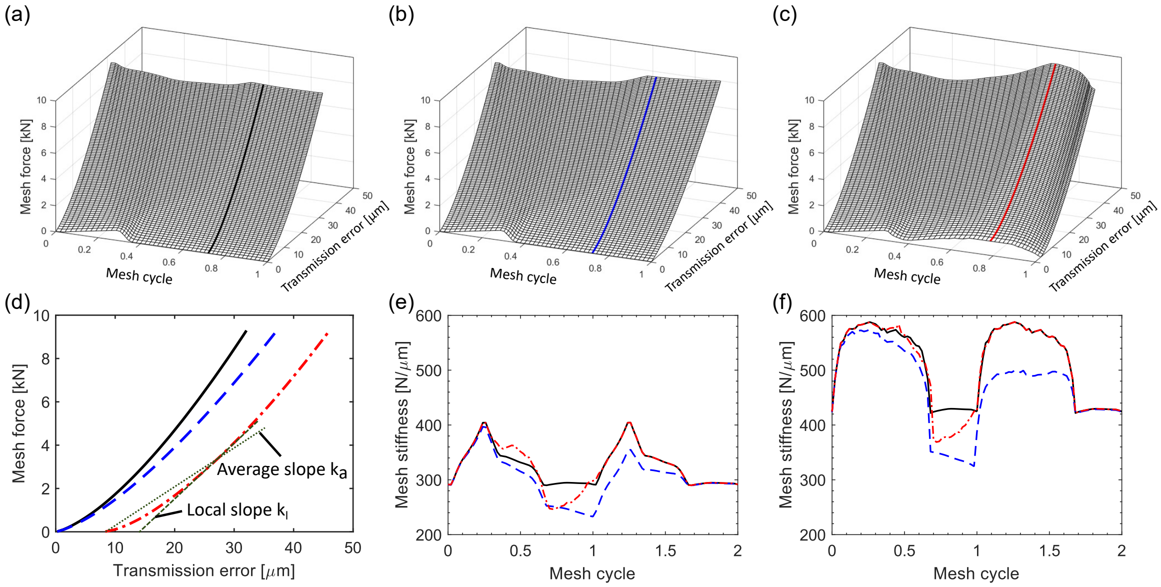

Figure 3.2: FE/CM calculation of force-deflection behavior over one mesh cycle for modified nonunity-ratio gear pair (a) without damage, (b) with tooth root crack damage on a pinion tooth, and (c) with tooth surface pitting damage on a pinion tooth. (d) Mesh force for varying transmission error at 0.72 mesh cycle when the gear pair has a single pair of teeth in contact. (e) Average slope calculation of mesh stiffness over one mesh cycle. (f) Local slope calculation of mesh stiffness over one mesh cycle. In (d)-(f), the solid (black), dashed (blue), and dash-dotted (red) lines are the results for healthy teeth without damage, tooth root crack damage, and tooth surface pitting damage, respectively.

as 1.61. The gears are made of steel with 212 GPa elastic modulus and 7800 kg/m^3 density. All gear teeth have involute geometry without tooth surface modifications. A 200 N$\cdot$m torque is applied to the inner diameter of the output gear, and the inner diameter of the input gear is constrained to have no rotation. Figure 3.3 shows the comparison of the gear pair mesh stiffnesses calculated from the FE/CM model compared to those from Ref. [1]. These stiffnesses are calculated using the average slope approach to be consistent with Ref. [1]. Both stiffnesses show the expected fluctuations for low-contact ratio spur gears. Large stiffnesses occur for more than 80 percent of the mesh cycle in Figure 3.3, even though the gear pair has a (theoretical) contact ratio of 1.61. The increase in duration of high stiffness values is due to premature contact of a second pair of teeth because of elastic deformations (i.e., corner tooth contact). The FE/CM calculation of mesh stiffness compares well to the results in Ref. [1], as expected. The difference between the two calculations is within two percent. Results demonstrating agreement for cases of tooth root crack and surface pitting damage will be shown later.

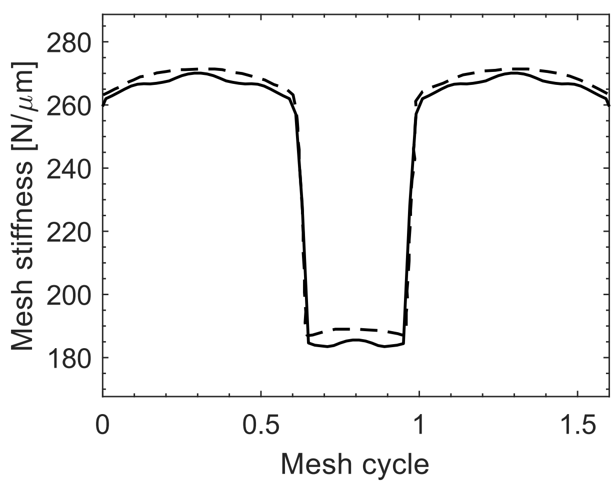

Figure 3.3: FE/CM calculation of tooth mesh stiffness for varying mesh cycle of a unity-ratio gear pair from Ref. [1] at 200 N $\cdot$ m torque. The dashed line are mesh stiffness calculations from Ref. [1].

3.2.4 Tooth surface pitting damage

3.2.4.1 Unity-ratio gear pair The mesh stiffness of the unity-ratio gear pair from Section 3.2.3 with irregular tooth surface pitting damage is analyzed in this section. The pitting damage is applied to the tooth surface of the input gear. Figure 3.4(a) shows the irregular geometry of the pitting damage using the solid (black) line, which is a particular damage case analyzed in Ref. [1]. In addition to having irregular geometry, this damage occurs asymmetrically about the midface of the tooth surface. The pit is located in the recess portion of the mesh cycle. The irregular pit geometry is approximated in the FE/CM model using multiple ellipses with varying geometry. The ellipses are shown in the dashed (red) lines of Figure 3.4(a). A total of five ellipses were used. Further refinement with more ellipses was also analyzed, however, the results changed only modestly from those using the five ellipses shown.

Figure 3.4(b) shows the comparison of mesh stiffnesses between Ref. [1] and the FE/CM model. To be consistent with the stiffnesses from Ref. [1], the average slope method was used. The FE/CM model accurately predicts the initial location in the mesh cycle where the stiffness is affected, the range of mesh cycle where the pit is active, and the overall reductions in mesh stiffness due to damage. The percentage difference between the FE/CM model and Ref. [1] in the region where pitting damage is active (i.e., between 1 and 1.3 mesh cycle) is within two percent. The results from Ref. [1] include the removal of material from the tooth surface, which is not included in the present FE/CM approach. The impact of this small amount of material appears to be minor for this particular case. The finite element model used in Ref. [1] had a dense finite element mesh near the damage. We note that by not modeling the removal of material due to pitting, fewer finite elements are needed on and near the tooth surface in the current FE/CM model. This reduces computational effort without significantly impacting the solution accuracy.

3.2.4.2 Damage parametric studies This section presents parametric studies that vary the pit length (along the tooth profile direction) at specified locations along the tooth profile. The system analyzed is the nonunity-ratio gear pair with parameters in Table 3.1. Unless otherwise indicated these gears are loaded with a 424 $\mathrm{N \cdot m}$ torque on the gear.

Figure 3.5 shows the active tooth surface of the pinion. Indicated on the surface are the start of the active profile (SAP), lowest point of single tooth contact (LPSTC), pitch, highest point of single tooth contact (HPSTC), and end of the active profile (EAP). These were determined using theoretical formulas for perfectly rigid gears. Two pairs of teeth

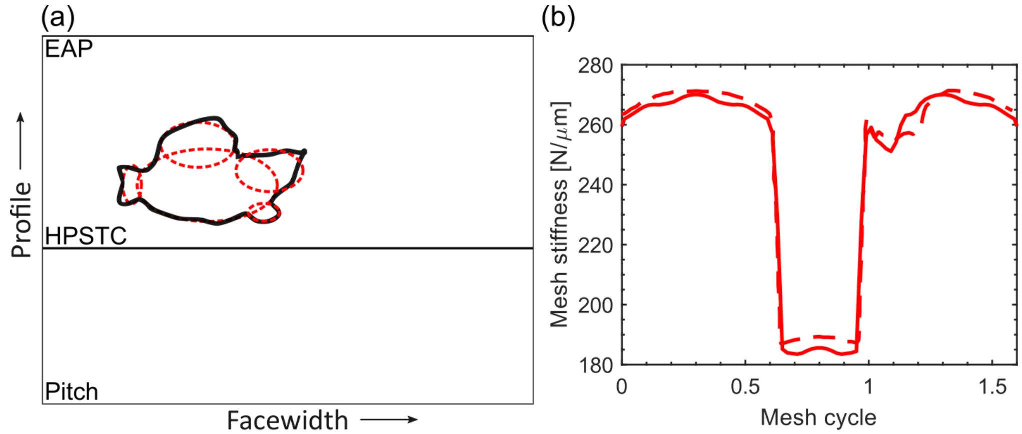

Figure 3.4: (a) Irregular pit geometry from Ref. [1] (solid (black) line) shown on a tooth surface from the unity-ratio gear pair. The FE/CM model appromximation of the pit geometry using multiple ellipses is shown in the dashed (red) lines. (b) Calculations of mesh stiffness for varying mesh cycle. The dashed (red) line is from Ref. [1]. The FE/CM model calculation is shown by the solid (red) line. The applied torque is 200 N · m. HPSTC and EAP are the highest point of single tooth contact and the end of the active profile, respectively.

are in contact between the SAP and LPSTC and between the HPSTC and EAP. Between the LPSTC and HPSTC only one pair of teeth are in contact. Pitting damage can occur at any location on the tooth surface, although it is most likely to occur near the pitch of the input gear (i.e., the pinion). We investigate the effects of pitting damage on the gear mesh for cases when there are one and two pairs of teeth in contact. For the case that two pairs of teeth are in contact, damage in the approach and recess areas are analyzed separately. All cases are shown schematically in Figure 3.5, where the dashed and solid lines denote the smallest and largest pit analyzed. The amount of damage is varied by changing the semi-major and semi-minor distances of the ellipse.

3.2.4.2.1 Damage in the single tooth contact region Pitting damage is applied to the center of the single tooth contact region (grayed region) at the mid-face of the tooth, as shown in Figure 3.5. The pit has fixed widths of 9.525 mm and depths of 0.254 mm. The

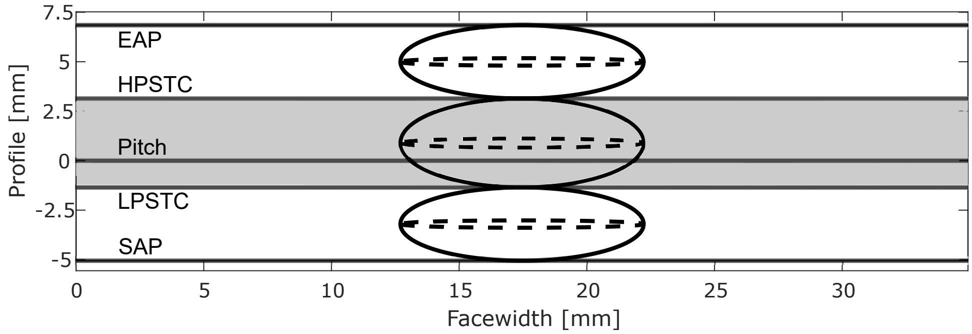

Figure 3.5: Tooth surface of the pinion from the nonunity-ratio gear pair with parameters in Table 3.1. The horizontal lines denote the start of the active profile (SAP), lowest point of single tooth in contact (LPSTC), pitch, highest point of single tooth in contact (HPSTC), and end of the active profile (EAP). The solid (dashed) ellipse is the maximum (minimum) pit size analyzed in each region.

total length of the single tooth contact region between the LPSTC and HPSTC is 4.488 mm. To fully capture the effects of pitting damage, a number of pit lengths (along the tooth profile direction) are analyzed. The smallest pit (dashed line in Figure 3.5) has length 0.4488 mm, which is 10 percent of the total single tooth contact length. The largest pit (solid line in Figure 3.5) completely covers the region of single tooth contact between the LPSTC and HPSTC.

The static transmission error and the local slope approach calculation of mesh stiffness for varying pit lengths in the single tooth contact region are shown in Figure 3.6. Increasing the pit length increases the maximum static transmission error for lengths up to 70 percent (see the yellow-orange line in Figure 3.6(b)). Pit lengths larger than 70 percent result in nearly identical maximum static transmission error. For these larger pit lengths, increasing the damage mostly increases the duration of the mesh cycle where the static transmission error of the damaged gear pair differs from that of the healthy pair. The minimum mesh stiffness in Figure 3.6(c) decreases monotonically with increasing pit length for lengths below 70 percent. Beyond 70 percent pit length, the minimum mesh stiffness is nearly unchanged for increasing length, although the duration of the mesh cycle where the mesh stiffness differs from healthy continues to increase. The percentage difference between the gear pair without damage and the gear pair with 70 percent pit length (yellow-orange line) in Figure 3.6(a,b) for static transmission error is 15.92%. This difference is similar for the mesh stiffness in Figure 3.6(c,d); for the 70 percent pit length the difference between the damaged and healthy mesh stiffness is 15.35%.

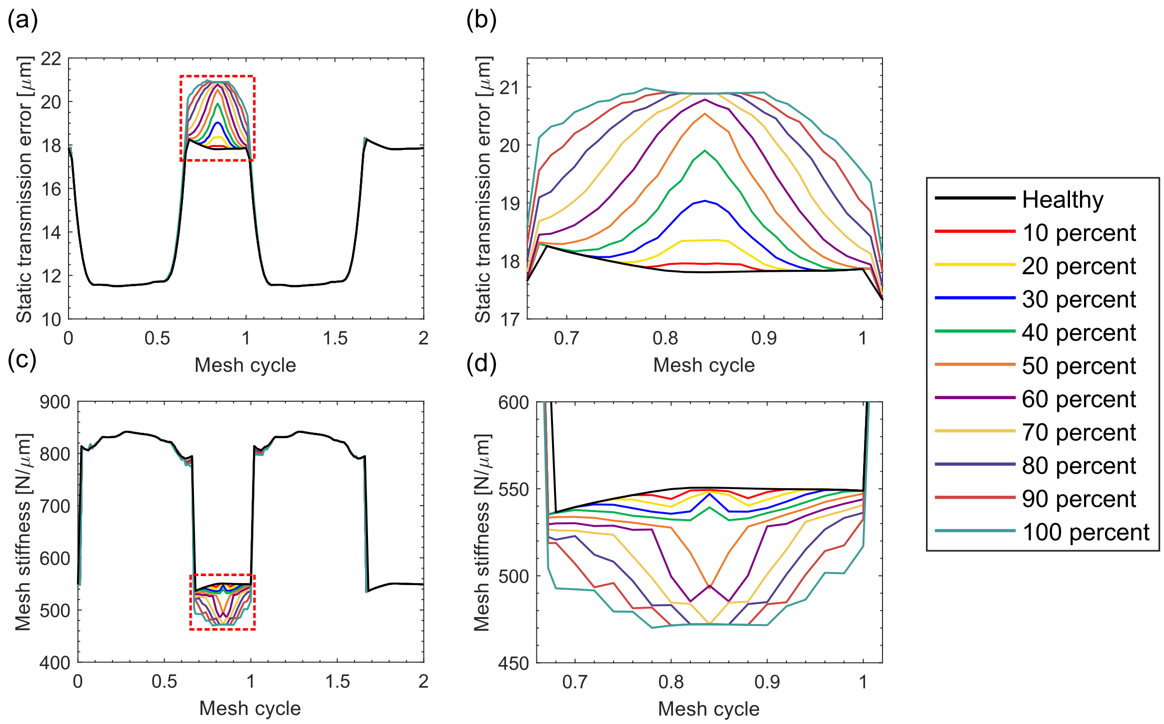

Figure 3.6: FE/CM calculation of (a,b) static transmission error and (c,d) mesh stiffness for varying mesh cycle when a tooth has a surface pit with varying length (along the profile direction). The black lines are for the case that all teeth are healthy and without damage. The remaining lines are for varying pit lengths from 10 to 100 percent of the length of single tooth contact (Figure 3.5). (b) and (d) are the regions shown in the dotted, red box in (a) and (c), respectively. The gear pair has nonunity ratio with parameters in Table 3.1.

3.2.4.2.2 Damage in the regions of double tooth contact There are two regions of double tooth contact, and the effect of pitting damage is considered separately for each region in this section. The first case considered is in the approach when contact occurs between the SAP and LPSTC (see Figure 3.5). The second case considered, which is also shown in Figure 3.5, is within the recess when contact occurs between the HPSTC and EAP. The pitting damage is placed at the center of these regions and at the mid-face of the tooth. Both regions have 3.702 mm length. The pit length (along the tooth profile direction) is varied from ten to 100 percent of the total length (i.e., between 0.3702 mm and 3.702 mm) in increments of ten percent for both cases. The remaining pit parameters are held fixed so that the facewidth is 9.525 mm and depth is 0.254 mm.

Figure 3.7 shows the static transmission error and the tooth mesh stiffness (local slope calculation) for varying pit lengths in the double tooth contact region of the approach (i.e., between the SAP and LPSTC in Figure 3.5). The effect of pitting damage is localized to approximately 0.1 to 0.6 mesh cycle. Damage causes a local maximum (minimum) in static transmission error (tooth mesh stiffness) near 0.35 mesh cycle. The local maximum (minimum) of static transmission error (tooth mesh stiffness) increases (decreases) monotonically with increasing damage for pit lengths up to 60 percent (the purple line). The duration of the mesh cycle where the results are impacted also increases monotonically with damage in this range. For pit lengths greater than 60 percent, however, the static transmission errors and mesh stiffnesses near 0.35 mesh cycle do not change meaningfully with further increases in the length. For these pit lengths, only the duration of the mesh cycle increases with increasing pit length.

Figure 3.8 shows the impact of increasing pit length on the static transmission error and tooth mesh stiffness (local slope calculation) when the damage is located in the double tooth contact region of the recess (i.e., between the HPSTC and EAP in Figure 3.5). Because the pit is within the recess, the range of mesh cycle where the static transmission error and tooth mesh stiffness are affected is between approximately 1.1 and 1.6 mesh cycle. Many of the features for pits in the region of double tooth contact in the recess (Figure 3.8) are

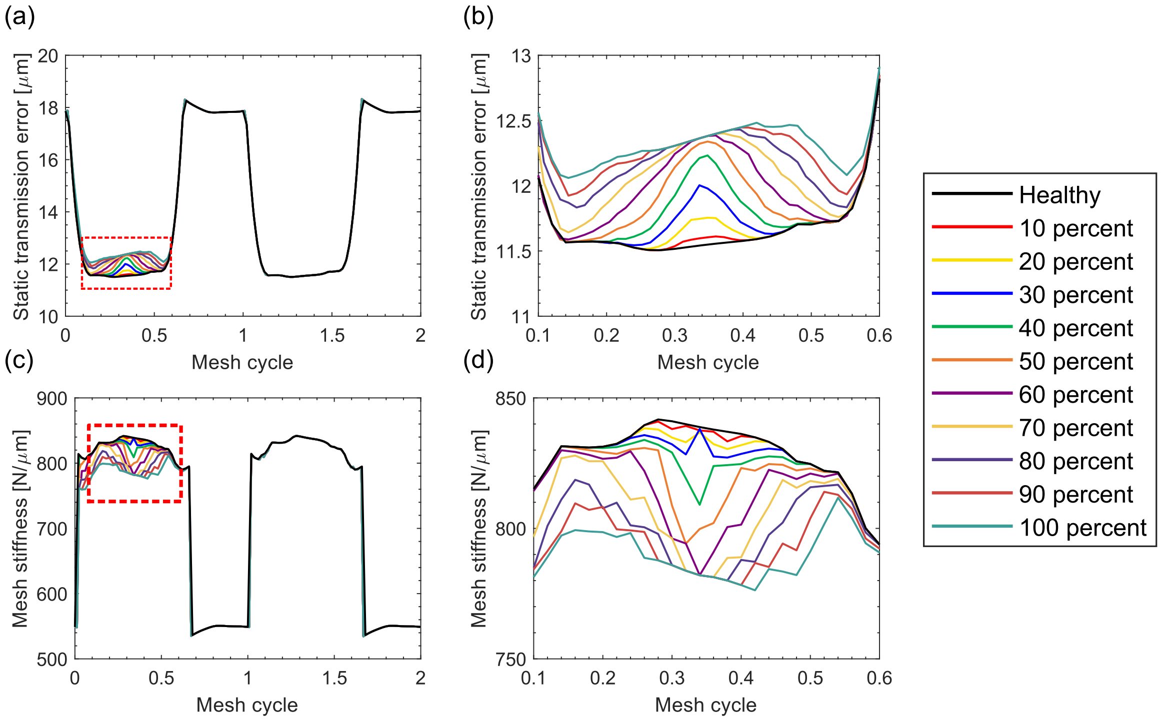

Figure 3.7: FE/CM calculation of (a,b) static transmission error and (c,d) mesh stiffness for varying mesh cycle when a tooth has a surface pit with varying length (along the profile direction). The black lines are for the case that all teeth are healthy and without damage. The remaining lines are for varying pit lengths from 10 to 100 percent of the double tooth contact region in the approach (between SAP and LPSTC in Figure 3.5). (b) and (d) are the regions shown in the dotted (red) box in (a) and (c), respectively. The gear pair has nonunity ratio with parameters in Table 3.1.

similar to those observed in the approach (Figure 3.7). Monotonic changes occur in the local extremums of static transmission error and tooth mesh stiffness near 1.34 mesh cycle with increasing pit length for pit lengths below 60%. The extrema are nearly identical for pits with lengths 60% and larger. Monotonic increases in the duration of mesh cycle affected occur with increasing pit length for all pit lengths shown. The differences between the damaged and healthy results at a given mesh cycle are nearly identical for both double tooth contact regions.

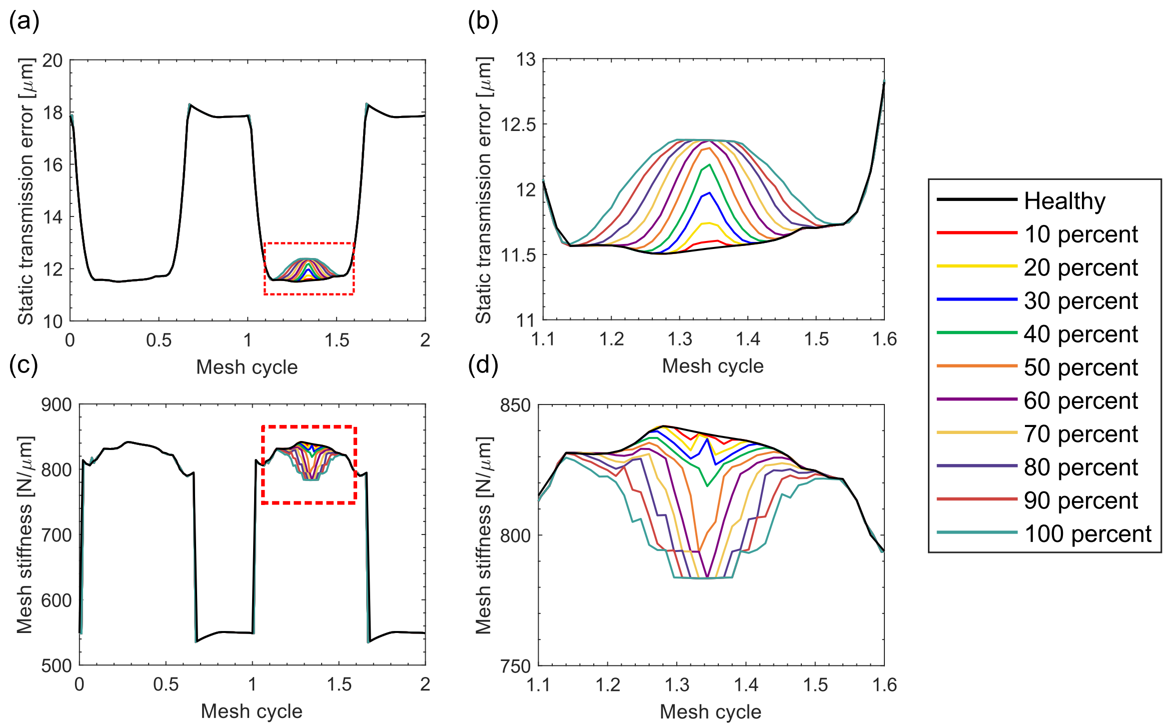

Figure 3.8: FE/CM calculation of (a,b) static transmission error and (c,d) mesh stiffness for varying mesh cycle when a tooth has a surface pit with varying length (along the profile direction). The black lines are for the case that all teeth are healthy and without damage. The remaining lines are for varying pit lengths from 10 to 100 percent of the double tooth contact region in the recess (between the HPSTC and EAP in Figure 3.5). (b) and (d) are the regions shown in the dotted (red) box in (a) and (c), respectively. The gear pair has nonunity ratio with parameters in Table 3.1.

3.2.4.2.3 Damage at pitch line This section analyzes the impact of pitting damage centered at the pitch line and at the mid-face of the gear. We consider pits that simultaneously vary in width (along the face) and length (along the tooth profile). The pit geometries are shown in Figure 3.9(a). The widths (lengths) of the damage in terms of increasing pit area are 6.35 mm (1.38 mm), 12.7 mm (2.76 mm), 16.51 mm (3.35 mm), 20.32 mm (3.94 mm), 22.86 mm (4.29 mm), and 25.4 mm (4.63 mm), respectively. The depth of all pits is kept fixed at 0.254 mm. The static transmission errors and tooth mesh stiffnesses for the pit geometries in Figure 3.9(a) are shown in Figs. 3.9(b) and (c), respectively. For the smallest pit (red line) the static transmission errors and tooth mesh stiffnesses have changes primarily in the region of single tooth contact. For this pit size the changes are modest. The maximum static transmission error is 18.2583 μm when healthy and 19.6505 μm when damaged. Similar differences occur for the mesh stiffness. As the pit area increases, wider regions of the mesh cycle are affected by damage and the differences between the healthy and damaged results increase. For larger pit sizes (e.g., those shown in the blue, green, orange, and purple lines) the pitting damage affects the results in the lower region double tooth contact, the region of single tooth contact, and the upper region of double tooth contact. At each point in the mesh cycle where the pit is active, the static transmission error increases (Figure 3.9(b)) and the mesh stiffness decreases. The maximum (minimum) static transmission error (tooth mesh stiffness) occurs immediately above the LPSTC for all pit sizes shown. This is likely due to the damage being larger when the contact is near the LPSTC than when it is near the HPSTC (see Figure 3.9(a)).

Pitting damage that occurs on the driven gear of the nonunity-ratio gear pair is identical to that shown when the damage is applied to the pinion. This is because pitting damage alters the contact pressure distribution on both teeth in mesh identically. We have confirmed this numerically by applying the pitting damage shown in Figure 3.9(a) to the driven gear of the FE/CM model. The static transmission errors and tooth mesh stiffnesses obtained were identical to those shown in Figs. 3.9(b) and (c) and are not shown.

3.2.4.2.4 Damage at pitch line on one edge of the tooth A case of practical interest is when pitting damage occurs at one edge of the tooth but still centered at the pitch [4, 121]. This pitting damage is schematically shown on the pinion tooth surface in Figure 3.10(a). In increasing area the pits shown in Figure 3.10(a) have widths (along the face) of 3.5 mm, 7.0 mm, 10.5 mm, 14.0 mm, 17.5 mm, 21.0 mm, and 24.5 mm, respectively. Their lengths

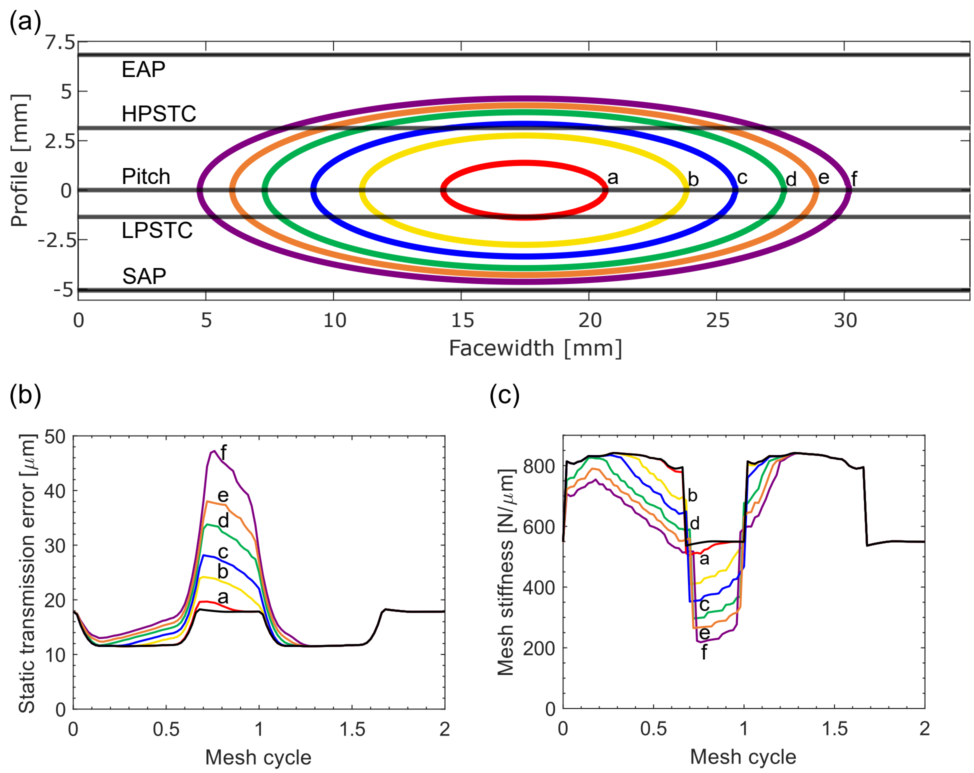

Figure 3.9: (a) Pinion tooth surface showing the pits centered at the pitch line with simultaneously-varying width (along the face) and length (along the profile). FE/CM calculation of (a) static transmission error and (b) mesh stiffness for varying mesh cycle with pitting damage centered at the pitch. The healthy results are shown in black lines. The remaining lines are for varying pit sizes.The gear pair has nonunity ratio with parameters in Table 3.1.

(along the profile) are 0.6 mm, 1.2 mm, 1.8 mm, 2.4 mm, 3.0 mm, 3.3 mm, and 3.5 mm, respectively. All pits have 0.254 mm depth. The static transmission error and tooth mesh stiffnesses (local slope calculation) for the pitting damage in Figure 3.10(a) are shown in Figs. 3.10(b) and (c), respectively. Like for pits centered at the gear midface (Figure 3.9), the results for pits centered at one edge (Figure 3.10) have largest differences between the damaged and healthy cases near the LPSTC. As seen in Figs. 3.10(b) and (c) for pits centered at the edge, the damage most significantly impacts the static transmission error and tooth mesh stiffness in the regions of single tooth contact and double tooth contact in the approach. Only small differences occur within the region of double tooth contact in the recess.

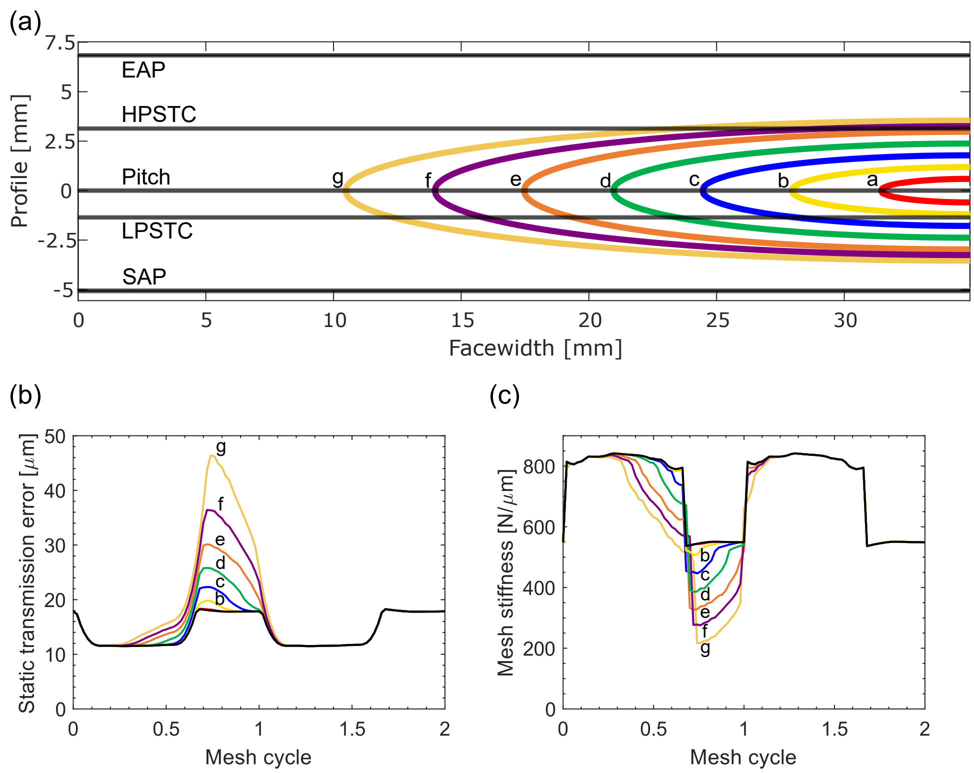

Figure 3.10: (a) Pinion tooth surface showing pitting damage at one edge of the tooth that is centered at the pitch line with simultaneously-varying width (along the face) and length (along the profile). FE/CM calculation of (a) static transmission error and (b) mesh stiffness for varying mesh cycle for the pits shown in (a). The results for healthy teeth are shown in black lines. The remaining lines are for varying pit sizes. The nonunity-ratio gear pair has parameters in Table 3.1.

3.2.5 Tooth root crack damage

3.2.5.1 Unity-ratio gear pair Before analyzing the effect of tooth root crack damage on the nonunity-ratio gear pair, we first demonstrate the accuracy of the FE/CM approach by comparing its results to those from Ref. [53]. We compare the mesh stiffness of the unity-ratio gear pair from Section 3.2.3 for the case that a single tooth on the input gear has a root crack of varying length that extends through the entire facewidth. In Ref. [53], accurate geometrical representations of the tooth root crack are included. In order to preserve computational efficiency, the current FE/CM model does not precisely model this geometry. As will be shown, accurate crack geometry is not necessary for accurate static transmission error and tooth mesh stiffness calculations.

The tooth root cracks analyzed are shown in the inset figure of Figure 3.11. The actual crack path, which was determined computationally in Ref. [53], is shown by the curve a-b-c-d. To accurately capture the complex geometry of this path, a dense finite element mesh interior to the tooth surfaces was used in Ref. [53]. In the FE/CM model used in this work, high nodal density is used only to represent the involute tooth surfaces with high precision. Within the tooth, the finite element mesh is purposely less dense to improve computational efficiency. We retain this specialized finite element mesh for teeth with root crack damage. To model the crack, additional nodes are added so that the connectivity between select finite elements along a specified path are broken. This allows portions of the tooth root to separate during deformation. We only consider cases when the root crack is on the drive side of the gears so that the crack always opens during deformation. We do not consider cases when the crack closes during deformation, which would occur when the damage occurs on the coast side of the gears.

Figure 3.11 shows the tooth mesh stiffness for the unity-ratio gear pair with a tooth root crack on the input gear. The applied torque is 100 $N \cdot m$. The case that all teeth are healthy and without damage is included for comparison. The results from the FE/CM method are shown using solid lines; the dashed lines are results from Ref. [53]. The mesh stiffnesses for healthy teeth without damage calculated using the FE/CM method (solid (black) line) are noticeably lower than those from Ref. [53] (dashed (black) line) for the entire range of mesh cycle shown. The reason for the observed difference is not known. It is particularly surprising considering the close agreement shown in Figure 3.3 was calculated from the same gear pair but at larger applied torque.

As seen in Figure 3.11, tooth root crack damage decreases mesh stiffness, as expected. The decrease in mesh stiffness increases with increasing crack length. For all crack lengths, the FE/CM model calculations (solid lines) qualitatively agree with those from Ref. [53] (dashed lines). In all cases the FE/CM method predictions are lower than those from Ref. [53]. The percent difference in stiffness for crack a-b (red lines) is nearly 8.3 percent at 0.5 mesh cycle. For crack a-c (green lines) the percent differences increase slightly to nearly 18 percent at 0.8 mesh cycle. These percentage differences with damage are comparable to that for the case of healthy teeth without damage. The percent differences between the FE/CM model and Ref. [53] are more substantial for the largest crack a-b-c-d. The maximum percent difference for this case is approximately 45 percent.

Tooth root crack damage alters the load sharing between teeth, which affects the width (in the profile direction) of the contact zone on all teeth. The FE/CM calculation of contact width for the gear pair without damage is 0.22 mm at 1.2 mesh cycle. The contact width decreases to 0.15 mm on the damaged tooth for crack a-b-c. The contact width further decreases to 0.09 mm for crack a-b-c-d. As the contact width decreases on the damaged tooth, the contact width increases on the next adjacent, healthy tooth in contact as the load shifts from the damaged to healthy tooth. These changes in the contact width may be partially responsible for the increased differences in mesh stiffness observed between the FE/CM model and Ref. [53].

3.2.5.2 Nonunity-ratio gear pair In this section, the effect of tooth root crack damage on the static transmission errors and tooth mesh stiffnesses are investigated for the nonunity-ratio gear pair with parameters in Table 3.1. Figures 3.12(a,b) show the results for the case that

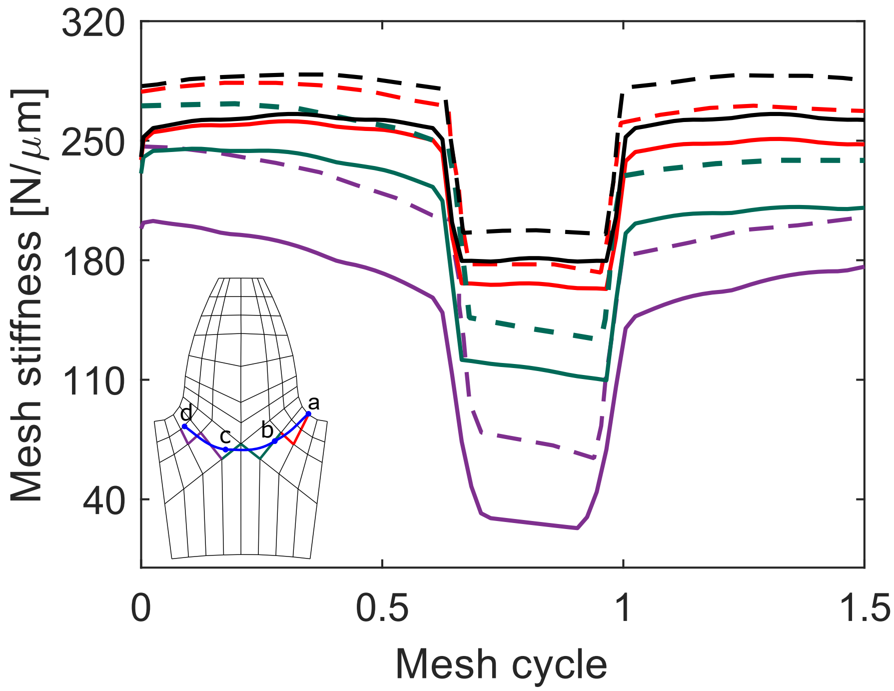

Figure 3.11: FE/CM calculation of tooth mesh stiffness for varying mesh cycle for a unity-ratio gear pair at 100 N·m torque. The inset figure shows the tooth root crack path from Ref. [53] and the approximate crack geometry used in the FE/CM model. The solid lines are from the FE/CM model. The dashed lines are from Ref. [53]. The healthy, crack a-b, crack a-b-c, and crack a-b-c-d are shown by black, red, green, and purple lines, respectively.

the tooth root crack damage is applied to the input pinion. Three crack lengths are shown, which correspond to nearly 20% (blue lines), 50% (red lines), and 80% (green lines) through the tooth thickness (see the inset figure of Figure 3.12(a)). All cracks extend completely through the tooth's facewidth. The static transmission error (tooth mesh stiffness) in Figure 3.12(a) (Figure 3.12(b)) increases (decreases) with increasing crack length. The portion of the mesh cycle where the results deviate from that of healthy teeth begins near 0.05 and ends near 1.7 mesh cycle, regardless of the length of the crack. When the tooth has root crack damage, the largest static transmission error (smallest tooth mesh stiffness) occurs slightly below unity mesh cycle. This point in the mesh cycle is near the HPSTC, where the the load on the cracked tooth is located further along the profile and generates a larger bending moment.

Figures 3.12(c) and (d) show the static transmission error and tooth mesh stiffness for the case that tooth root crack damage occurs on the driven gear of the nonunity-ratio pair. The usual increases (decreases) in static transmission error (tooth mesh stiffness) occur. In this case, however, the largest static transmission errors (smallest tooth mesh stiffnesses) occur earlier in the mesh cycle because the damage is on the output gear. This corresponds to locations where the load is further along the profile of the output gear. Indeed, the maximum static transmission error (minimum tooth mesh stiffness) occurs near the LPSTC at 0.7 mesh cycle, which is different from the case when the crack is on the input pinion (see Figs. 3.12(a) and (b)). The maximum static transmission error (minimum tooth mesh stiffness) are larger (smaller) when the damage occurs on the output gear of this unity-ratio pair. The results for the nearly 80% tooth root crack (dash-dotted (green) lines) have noticeably larger region of double tooth contact due to the added tooth compliance from damage causing a second pair of teeth to come into mesh.

3.3 Differentiating Damage Type and Evaluating its Severity

It is of practical interest in condition monitoring and damage detection systems to use measured transmission errors, or tooth mesh stiffnesses calculated from the transmission errors, to identify the presence, severity, and type of damage on the gear teeth. In this section, we discuss features of the static transmission errors that may permit damage detection. Similar findings apply if the mesh stiffnesses are used instead.

The amplitudes of the static transmission error are useful metrics for identifying the presence of damage. Clear increases in static transmission error occur when the teeth are damaged compared to when they are healthy, which can be seen in Figure 3.9 for tooth

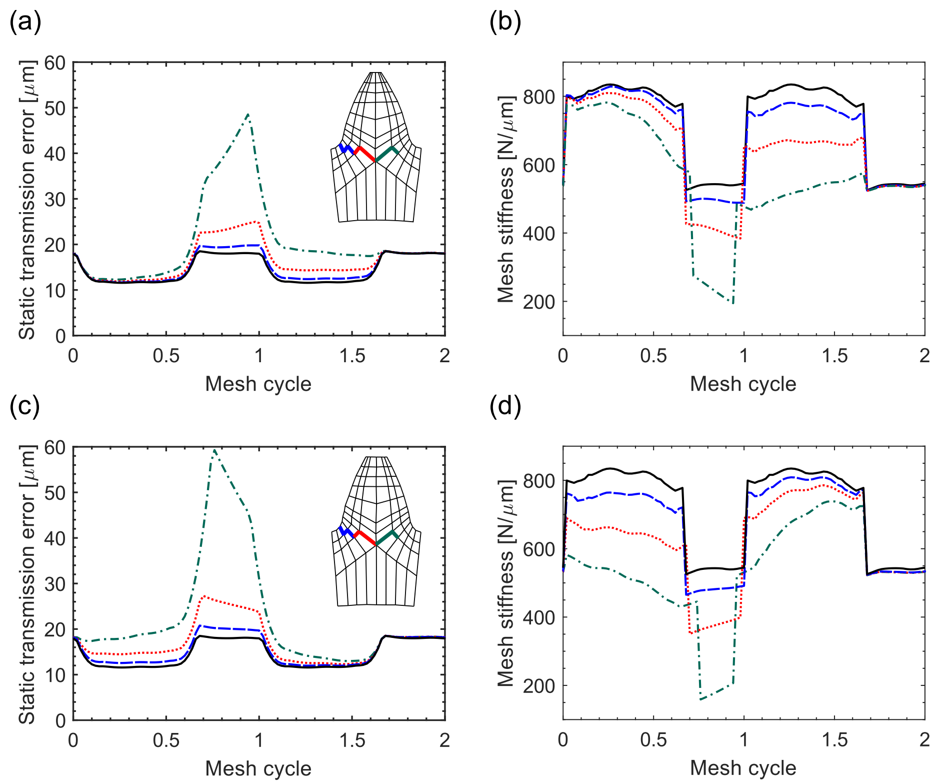

Figure 3.12: FE/CM calculation of (a,c) static transmission error and (b,d) tooth mesh stiffness for varying mesh cycle when a tooth has root crack damage. In (a,b) the root crack is on the input gear. The root crack is on the output gear in (c,d). The inset figures in (a,c) show the tooth root crack path on the finite element mesh of the tooth. The healthy teeth without damage results are shown in the solid (black) lines. The dashed (blue), dotted (red), and dash-dotted (green) lines are for cracks with nearly 20%, 50%, and 80% length through the thickness, respectively. The nonunity-ratio gear pair has parameters in Table 3.1.

surface pitting and Figure 3.12 for tooth root cracks, for example. The differences in the static transmission errors between damaged and healthy teeth increase with increasing severity of tooth surface pitting (Figure 3.9) and tooth root crack (Figure 3.12) damage. Figure 3.13(a) shows the maximum static transmission error for varying amount of damage. For pitting damage, the percentage damage is calculated as the ratio of the area of the elliptical pit to the total active area of the tooth surface. The percentage for tooth root crack damage is calculated as the ratio of the crack length to the total length of the path in the root. As seen in the figure, the maximum static transmission error for the case of pitting is generally larger than that of tooth root cracks for the same percentage of damage. For example, the maximum static transmission error for a pit with 20.9288% damage is 28.1620 μm. The maximum static transmission error is just 19.7924 μm for a slightly larger tooth root crack with 24.2942% damage.

The maximum static transmission errors alone are not effective indicators of the type of damage, however. As seen in Figure 3.13(a), and by comparing the waveforms in Figure 3.9 for tooth surface pits and Figure 3.12 for tooth root cracks, the overall increases in static transmission error are comparable for both types of damage. Indeed, the maximum static transmission error for the largest-sized tooth surface pit in Figure 3.13(a) is 47.2424 μm (see the purple line in Figure 3.9). For the case of tooth root cracks, the maximum static transmission error is 48.522 μm (see the dash-dotted (green) line in Figure 3.12(a)). Hence, a maximum static transmission error measurement of 48 μm would not clearly differentiate a pit with nearly 45% damage from a root crack with nearly 81% damage.

It may be possible to detect damage type from the duration of the mesh cycle where the static transmission error from the damaged gear pair deviates from that of the healthy gear pair. Figure 3.13(b) shows the duration of the mesh cycle where damage affects the static transmission error for varying amounts of damage. Each marker is determined from the range of mesh cycle where the static transmission error exceeds the values for the case of undamaged, healthy teeth by more than 1%. The range of mesh cycle affected by tooth root crack damage remains near the gear pair involute contact ratio (1.45) for all amounts of damage shown. This small variation can also be seen from the static transmission error waveforms in Figs. 3.12(a). Pitting damage generally affects the static transmission error for smaller portions of the mesh cycle than tooth root crack damage. Smaller-sized pits increase the static transmission error in a relatively narrow range of mesh cycle. As pitting damage increases, the portion of the mesh cycle where the static transmission error is affected increases. Larger pits affect a smaller region of the mesh cycle than root cracks. For example, the pit corresponding to the purple curve in Figure 3.9, which corresponds to nearly 44.49% damage, affects the mesh cycle for a range of nearly 1.2. For comparison the tooth root crack damage shows differences between damaged and healthy for nearly 1.62 mesh cycle. Only when pitting damage covers the entire profile of the tooth will the static transmission error deviate for such large regions of the mesh cycle.

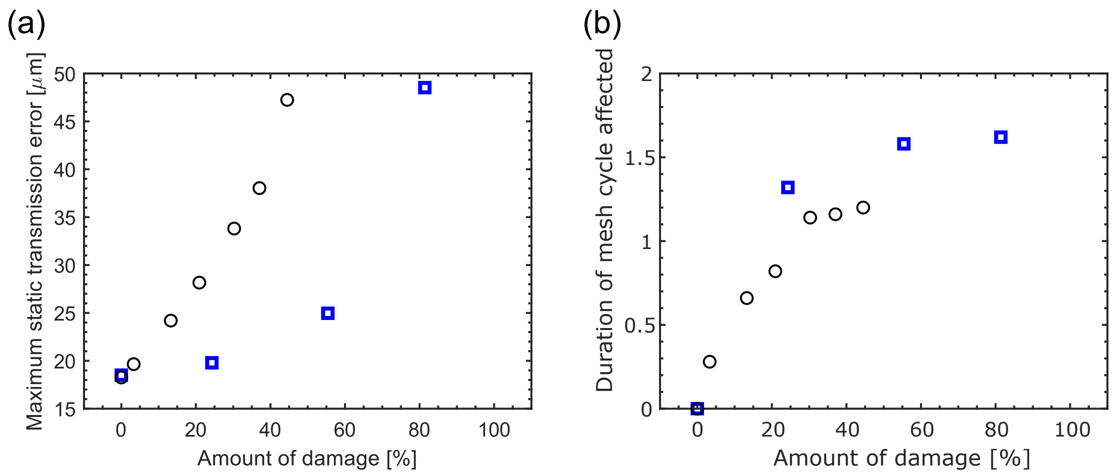

Figure 3.13: FE/CM calculation of (a) maximum static transmission error and (b) region of the mesh cycle affected for varying amounts of damage. The circle (square) markers are for tooth surface pitting (tooth root crack) damage.

3.4 Dynamic response

This section demonstrates the use of the calculated static transmission errors and tooth mesh stiffnesses for damaged gear teeth in a typical lumped-parameter gear pair model from the literature. Comparisons are made to the FE/CM model to demonstrate the accuracy of the lumped-parameter model when accurate gear mesh parameters are obtained from characterization. We analyze the nonunity-ratio gear pair as an example, which has geometrical parameters in Table 3.1.

3.4.1 FE/CM formulation

The same FE/CM model of the gear pair used for mesh characterization can be dynamically analyzed to find the response at operating speed. For dynamic analyses, the FE/CM method is discretized in time using the Newmark method [14, 145]. Importantly, the elastic contact at the tooth mesh interface is calculated at every time step accounting for the elastic deformations of the tooth and blank and the vibration of the gears. Because the contact is calculated at each time instant, the FE/CM formulation can predict tooth contact loss at higher amplitude vibrations, if it occurs.

The FE/CM model of the gear pair is analyzed at a specified operating speed. A sufficient number of time steps are analyzed so that all transient response diminishes before the steady-state dynamic response is obtained. All analyses used 50 time steps over a mesh cycle. This permits accurate dynamic response calculations without overly high computational burden.

3.4.2 Lumped-parameter model

Lumped-parameter dynamic models can provide accurate response calculations with significantly reduced computation time. A lumped-parameter model of a gear pair is shown in Figure 3.14. Each gear is modeled as a rigid disk with radius r_h, mass m_h, and mass moment of inertia J_h ($h = p, g$). The gears are supported by a combination of discrete stiffness (k_h) and damping (c_h) elements that represent the elastic and dissipative behavior of the shafts, bearings, and housing. The gears are loaded with applied torques T_h. Each gear has two degrees-of-freedom representing the translation along the line-of-action y_h

and the rotational vibration θ_h. Neglecting friction between meshing gear teeth and other off-line-of-action effects, the translation perpendicular to the line-of-action is omitted. We use the local slope approach for calculation of the mesh force, which has been shown to accurately predict the dynamic response in gear pairs without damage [41, 143]. Using this model the mesh force is $f_m = k_l(t)\,[\delta - \delta_0(t)]$, where $k_l(t)$ is the local slope calculation of mesh stiffness, $\delta = y_p - y_g + r_p\theta_p + r_g\theta_g$ is the mesh deflection, and $\delta_0(t)$ is the static transmission error. In the lumped-parameter model, the gear mesh interface is represented as a discrete mesh stiffness k_l in series with a prescribed displacement excitation $\delta_0(t)$. Dissipative behavior of the gear mesh is captured using the discrete damping element c_m. The parameters used in the lumped-parameter model are given in Table 3.2. The static transmission errors and tooth mesh stiffnesses are taken from the FE/CM results presented in Section 2.

Table 3.2: Lumped-parameter gear pair model parameters for the nonunity-ratio gear pair. The gear geometrical parameters are given in Table 3.1.

	Gear	Pinion
Base radius, $r_{g,p}$ (mm)	45.63	35.20
Mass, $m_{p,g}$ (kg)	0.8537	0.7294
Torque, $T_{p,g}$ ($\mathrm{N \cdot m}$)	424	327
Moment of inertia, $J_{p,g}$ ($\mathrm{kg \cdot m^2}$)	0.0050	0.0008
Support stiffness, $k_{p,g}$ (N/m)	1×10^{12}	1×10^{12}
Support damping, $c_{g,p}$ ($\mathrm{N \cdot s/m}$)	800	800
Mesh damping, c_m ($\mathrm{N \cdot s/m}$)	3660	

The equations of motion when the gear teeth remain in contact are

$$m_p\ddot{y}_p + (c_p + c_m)\dot{y}_p - c_m\dot{y}_g + c_m\dot{x} + (k_p + k_l)y_p - k_l y_g + k_l x = k_l\delta_0 - f_0, \tag{3.3a}$$

$$m_g\ddot{y}_g - c_m\dot{y}_p + (c_g + c_m)\dot{y}_g - c_m\dot{x} - k_l y_p + (k_g + k_l)y_g - k_l x = f_0 - k_l\delta_0, \tag{3.3b}$$

$$m_e\ddot{x} + c_m\dot{y}_p - c_m\dot{y}_g + c_m\dot{x} + k_l y_p - k_l y_g + k_l x = k_l\delta_0, \tag{3.3c}$$

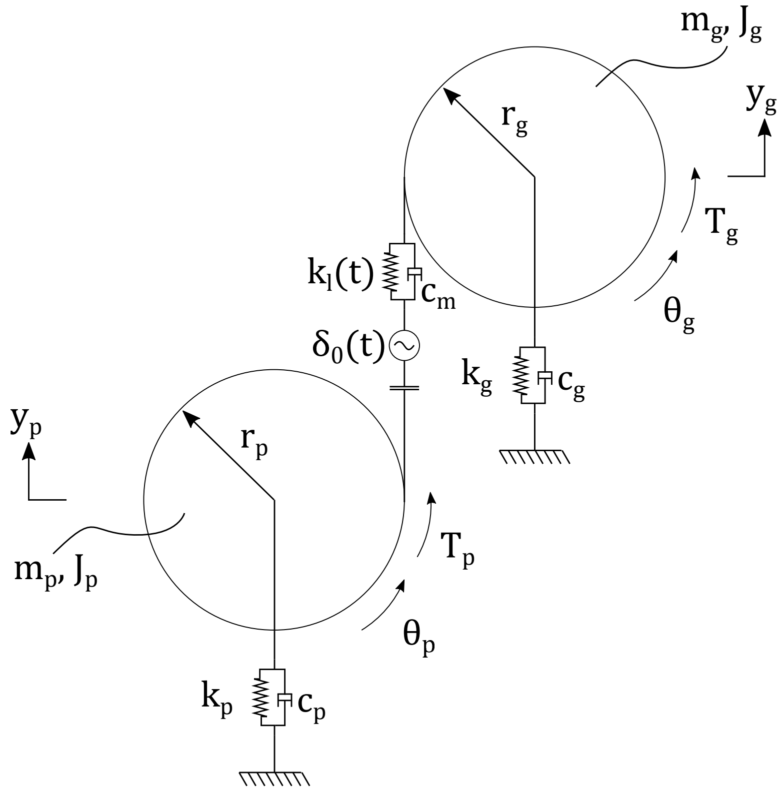

Figure 3.14: Schematic of the lumped-parameter model of the gear pair.

$$m_e = \frac{J_p J_g}{{r_p}^2 J_g + {r_g}^2 J_p}, \quad f_0 = \frac{r_p J_g T_p + r_g J_p T_g}{{r_p}^2 J_g + {r_g}^2 J_p}, \tag{3.3d}$$

where $x = r_p\theta_p + r_g\theta_g$ is the dynamic transmission error of the gear pair. There are two excitation sources in Eq. (3.3): parametric excitation from mesh stiffness fluctuations and direct forcing excitation from the product of static transmission error and local slope mesh stiffness. When the mesh deflection δ vanishes or becomes negative the gear teeth separate and the mesh force f_m vanishes. The equations that govern the gears when contact between mating gear teeth is lost are obtained from Eq. (3.3) with $k_l \to 0$ and $\delta_0 \to 0$. The equations of motion in Eq. (3.3) are converted to first-order form and numerically integrated using standard subroutines. Because the equations differ when there is contact compared to when there is not contact, the instant that contact is lost or regained must be detected and equations that are solved changed.

3.4.3 Accuracy of the lumped-parameter model

Before analyzing the dynamic response initiated by damage, we first demonstrate the accuracy of the lumped-parameter model for the case that all teeth are healthy and none have damage. The gear pair parameters are given in Table 3.2. The static transmission error and mesh stiffness for healthy gear teeth are given in the solid (black) lines in Figure 3.6. Like for the FE/CM model, a region of transient response must first be calculated from the lumped-parameter model before steady-state response can be obtained. Figure 3.15(a) shows the steady-state dynamic transmission error calculated from the lumped-parameter model (solid (black) line) compared to that obtained from dynamic analysis of the the FE/CM model (circle (blue) markers). As seen in the figure, the lumped-parameter model accurately predicts the dynamic transmission error compared to the FE/CM model over the entire range of mesh cycle. This includes accurate prediction of the maximum dynamic transmission error over the mesh cycle and the response due to higher harmonics of excitation.

Figure 3.15(b) compares the dynamic transmission error calculated by the lumped-parameter and FE/CM models for the case that a pinion tooth has a tooth surface pit. The pit has elliptical geometry with 12.7 mm width (along the face) and 2.76 mm height (along the profile). It is shown in the yellow curve in Figure 3.9(a). The lumped-parameter model accurately predicts the dynamic response compared to the FE/CM model for the entire range of mesh cycles shown. This includes the substantial increases in dynamic transmission error that occur due to the tooth surface pitting damage.

The accuracy of the lumped-parameter model remains for the case that the pinion has a tooth root crack, as seen in Figure 3.15(c). For this case with a tooth root crack, the maximum dynamic transmission error is below that observed for the tooth surface pit.

The computational time needed to analyze the lumped-parameter model was approximately one minute, which includes the calculation of the transient response prior to predictions of steady-state response. The simulation of the FE/CM model took approximately three to four hours to complete. The close agreement combined with the significantly reduced computational cost makes the lumped-parameter model attractive for analyzing the dynamic response induced by damage.

3.4.4 Damaged gear pair response

This section analyzes the dynamic response of the nonunity-ratio gear pair with tooth surface pitting and tooth root crack damage using the lumped-parameter model. The gear pair is analyzed at 2000 rpm input speed at the pinion. This corresponds to 900 Hz mesh frequency. The static transmission errors and tooth mesh stiffnesses are determined over a complete rotation of the pinion, which corresponds to 27 mesh cycles. Damage is applied to a tooth midway along the gear so that the damaged tooth engages in mesh at 14 mesh cycle. This allows the normal vibrations due to meshing of healthy teeth to be clearly visible before the damaged tooth engages, and allows for a sufficient number of mesh cycles after the damaged tooth engages so the effects that damage have on the dynamic response can be fully captured.

Figure 3.16 shows the dynamic response of the nonunity-ratio gear pair with varying amounts of tooth surface pitting damage on a single pinion tooth. The tooth surface pit geometries are shown by the yellow, green, and purple lines in Figure 3.9(a). The dynamic transmission error calculated over a full rotation of the pinion is shown in Figure 3.16(a).

As seen in the figure, the response is at steady-state prior to the tooth with pitting damage engaging at 14 mesh cycle. After the damaged tooth engages a region of transient response occurs, where the dynamic transmission error generally increases from that for healthy teeth. The transient response due to damage decays with increasing mesh cycle and the response reaches steady-state again after approximately 20 mesh cycles. Figure 3.16(b) shows the region of damage-induced dynamic response denoted by the dashed (red) box in Figure 3.16(a). After the damage tooth engages, the maximum dynamic transmission error increases monotonically with the increasing pit size, as expected. For small-to-moderate pit sizes, the dynamic transmission error largely follows that of the healthy case except with variations in amplitude. For the largest sized pit (dash-dotted (green) line), the dynamic transmission error has substantial differences with that of healthy gears. The maximum dynamic transmission error for the large pit is 75.1 μm at 14.88 mesh cycle. For instances where the dynamic transmission error falls below zero, tooth contact loss occurs. As seen in the figure, there are several regions of contact loss where the dynamic transmission error remains below the dotted (purple) line. The minimum dynamic transmission error is -25.2 μm, which occurs at 15.16 mesh cycle.

Figure 3.17 shows the calculated dynamic response from the lumped-parameter model for cases when a single pinion tooth has root crack damage. The static transmission errors and tooth mesh stiffnesses used as inputs are shown in Figs. 3.12(a,b). When the tooth with root crack damage engages, the dynamic transmission error locally increases in amplitude for several mesh cycles following damaged tooth engagement. The maximum dynamic transmission error increases with increasing tooth root crack length. For root cracks that extend 20% (dashed (blue) line) and 50% (dotted (red) line) through the tooth thickness only modest changes to the dynamic transmission error are observed. The 80% tooth root crack length generates sufficiently-large enough transient response that tooth contact loss occurs between 15.13 to 15.22 mesh cycle. The minimum dynamic transmission error is -4.99 μm at 15.18 mesh cycle.

3.5 Conclusions

A finite element/contact mechanics (FE/CM) method is used to analyze the impact of tooth surface pit and tooth root crack damage on the force-deflection behavior of the tooth mesh interface in spur gear pairs. Tooth surface pitting is modeled by eliminating select cells within the contact grid that fall within a prescribed area defining the damage on the tooth surface. Tooth root cracks are modeled by removing the connectivity of select finite elements within the gear tooth finite element mesh. Modeling damage in this way preserves the established contact model between gear teeth and provides the computational efficiency needed for dynamic analyses. The mesh stiffnesses determined from the FE/CM are compared to results from the literature to demonstrate the effectiveness of the damage models.

The damage from tooth surface pits and root cracks impact the gear mesh differently. Tooth surface pits cause changes to the contact pressure distribution on the gear teeth, which locally alter the static transmission errors and tooth mesh stiffnesses of the gear pair. When the pitting damage is contained entirely within a region of single or double tooth contact, the static transmission error increases (tooth mesh stiffness decreases) locally with increasing pit size up to a certain threshold. Beyond this threshold, further increases in the pit size do not further change their extremum values. Instead, the duration of mesh cycle where the static transmission errors and tooth mesh stiffnesses are altered because of damage increases. For cases where the pit extends into regions of both single and double tooth contact, both the maximum static transmission error (minimum mesh stiffness) and the region of mesh cycle where it is effected increase with increasing pit area. The largest increases in static transmission error (decreases in tooth mesh stiffness) occur near the lowest point of single tooth contact. Tooth root cracks increase the overall compliance of the gear. This damage type leads to increases in static transmission error (decreases in tooth mesh stiffness) for a range of mesh cycles that is largely independent of the crack length but related to the involute contact ratio of the gear pair.

The distinct features of the static transmission errors, or alternatively the tooth mesh stiffnesses, of damaged gear teeth could be used to identify the presence, type, and severity of damage. Increases in static transmission error or decreases in tooth mesh stiffnesses indicate damage is present. The type of damage could be determined from the range of mesh cycle that is affected. Tooth root cracks impact the static transmission errors and tooth mesh stiffnesses for a range of mesh cycle that is related to the involute contact ratio. The range of mesh cycle where pitting damage affects the static transmission error and tooth mesh stiffness is meaningfully smaller than the involute contact ratio. Once the damage type is determined, the severity could be estimated from the difference in the results compared to that for healthy gears.

The calculated static transmission errors and tooth mesh stiffnesses were used as inputs to a lumped-parameter gear pair dynamic model. The lumped-parameter model accurately predicts dynamic transmission error compared to full dynamic solutions of the FE/CM model for tooth surface pit and tooth root crack damage with substantially reduced computational time. The computational efficiency of the lumped-parameter model permits parametric studies on the damage severity. Increasing the amount of damage increases the maximum dynamic transmission error of the gear pair. Contact loss nonlinearity was observed for large amounts of damage.

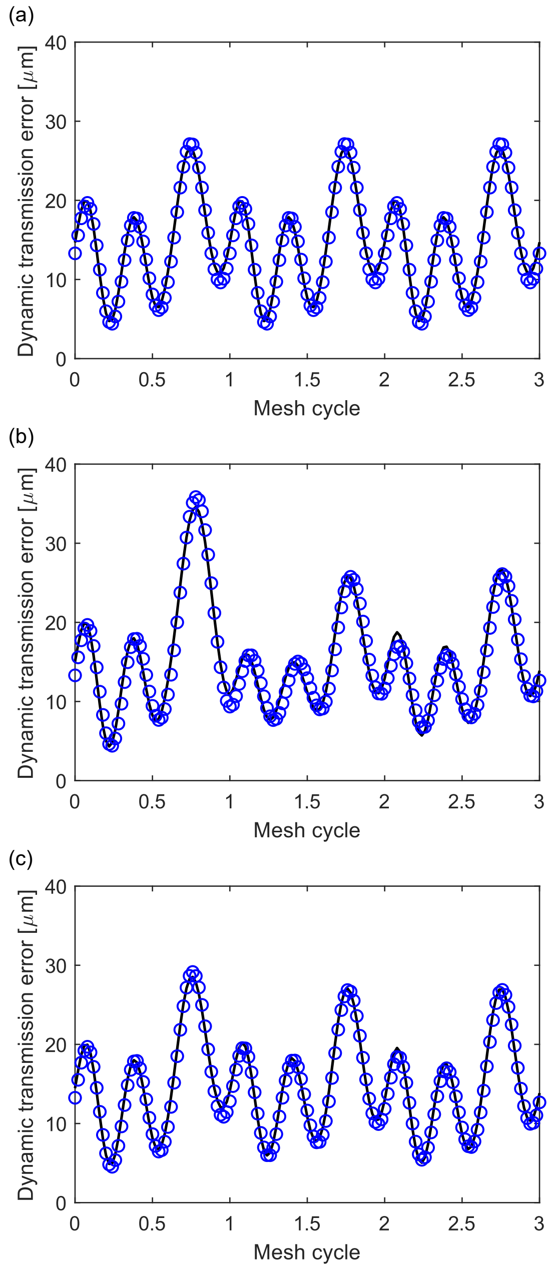

Figure 3.15: Steady-state dynamic transmission error of the nonunity-ratio gear pair at 900 Hz mesh frequency when (a) all teeth are healthy and without damage, (b) a single pinion tooth has a tooth surface pit, and (c) a single pinion tooth has a root crack on a single pinion tooth. The lumped-parameter results are shown by solid (black) lines. The circle (blue) markers are calculated from the FE/CM model. In (b) the tooth surface pit is shown by the yellow line in Figure 3.9(a). In (c) the tooth root crack is shown by the blue line in the inset figure of Figure 3.12(a).

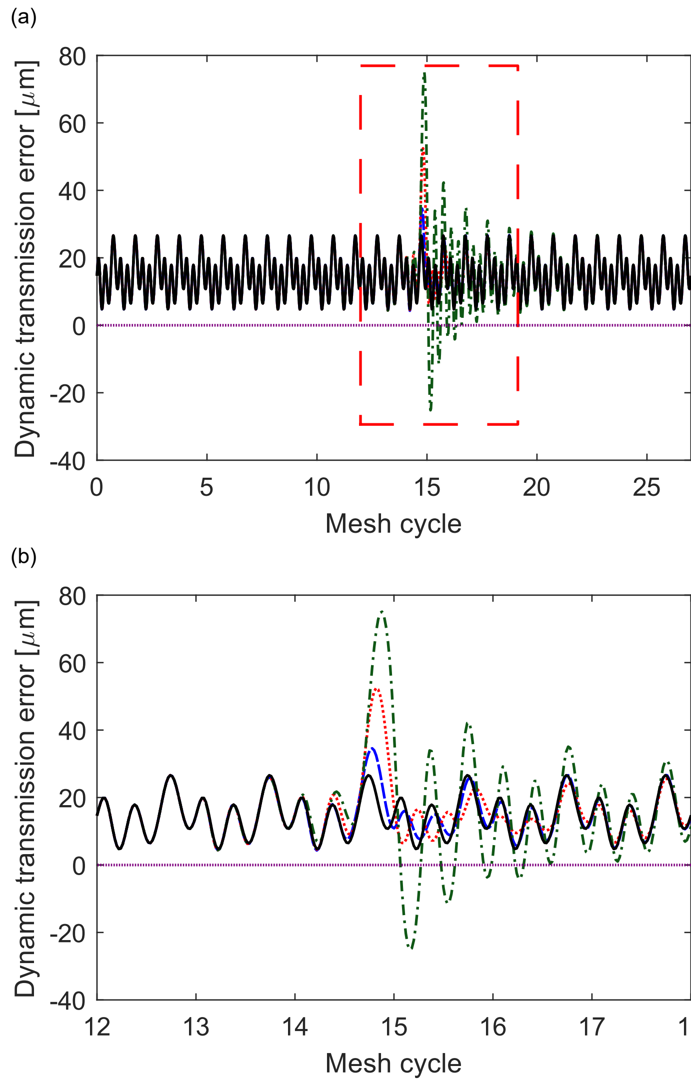

Figure 3.16: Dynamic transmission error of the nonunity-ratio gear pair with tooth surface pitting damage on pinion of the gear pair. The tooth surface pitting damage is shown in Figure 3.9(a) in yellow, green, and purple lines. The healthy gear pair results are shown in black (solid) and the dynamics of the gear pair with tooth surface pitting damage on the pinion are shown in other colors.

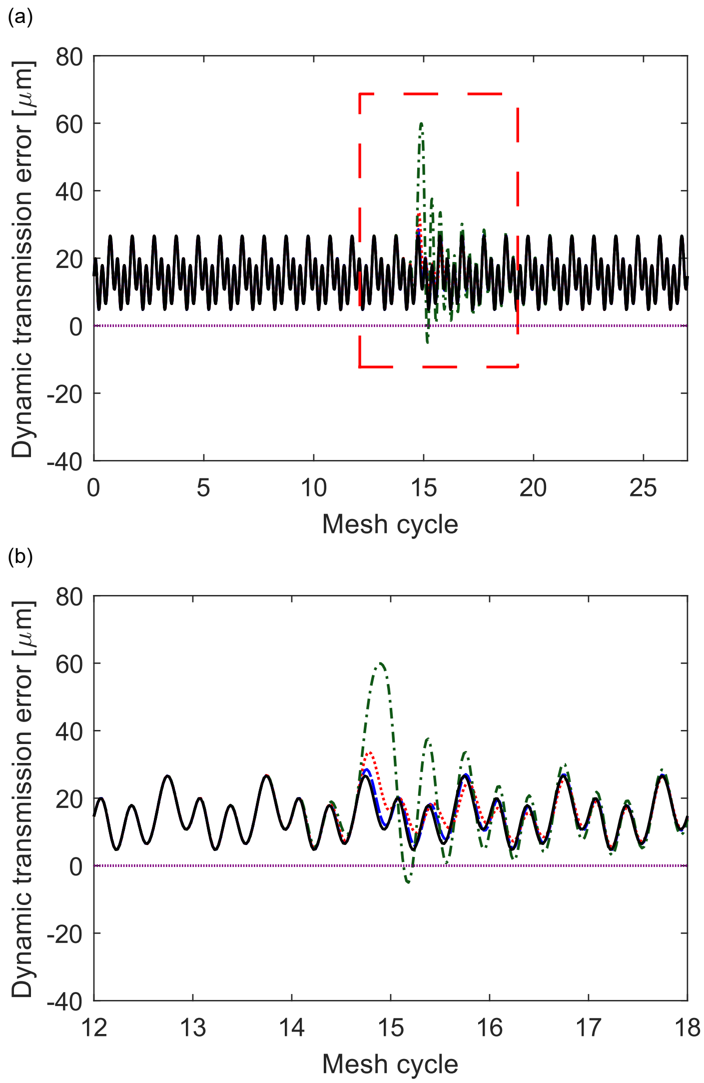

Figure 3.17: Dynamic transmission error of the nonunity-ratio gear pair with tooth root crack damage on pinion of the gear pair. The tooth root crack damage is shown in the inset of Figure 3.12(a). The healthy gear pair results are shown in black (solid) and the dynamics of the gear pair with tooth root crack damage on the pinion are shown in other colors.

CHAPTER FOUR

DAMAGE-INDUCED DYNAMIC RESPONSE IN SPUR GEAR PAIRS WITH LOCALIZED DEFECTS

4.1 Introduction

Localized defects, such as root crack damage and surface pitting damage, can significantly affect the vibration patterns generated by geared transmissions. Changes in these vibration patterns often make damage detection difficult, as the vibrations caused by such defects can be quite small compared to the normal vibrations of healthy gears. As a result, distinguishing between the vibrations of healthy gears and damaged gears requires several signal processing techniques and evaluation of condition indicators.

Condition indicators that provide a statistical measure of the geared transmission vibrations are used to evaluate the vibrations and have shown ability to detect damage in the gear tooth [5, 6, 59, 86–96]. The ability of these condition indicators to detect damage from vibration signatures is a significant area of research. This study aims to explore the performance of various condition indicators and enhance our ability to detect localized defects through measured vibrations, contributing to more effective maintenance practices and increased reliability of geared systems.

The accuracy of the calculation of condition indicators depends on the accurate evaluation of damaged dynamic response. The dynamic response of gear systems has been extensively studied to understand how different types of damage affect the overall vibration characteristics. For tooth root cracks several dynamic models have been proposed. Howard et al. [72] derived the dynamic response of the gear pair with tooth crack including the friction in the modeling. The dynamical characteristics of the gear pair with crack and spall damage were compared by evaluating dynamic response with a 26-DOF model in

Ref. [73]. Chen et al. [74] determined the dynamic response of spur gear pair with tooth root crack propagating along both tooth width and crack depth utilizing a 6-DOF model and assessed statistical indicators for varying damage severity. The failure characteristics of the dynamic response of gear pair with root crack damage and surface pitting damage were established in Ref. [45] and showed the dynamic response to have good agreement with experiments. Ma et al. [62] has reviewed the dynamic models of gear systems with tooth root crack and its bibliography contains dynamic response evaluation models for spur gear pairs utilizing analytical, finite element or hybrid modeling methods. The dynamic response of gear with crack using different DOF models were compared in Ref. [75] and calculated the vibration-based condition indicators to determine the presence of damage. Mohammed et al. [76] determined the dynamic response using 6-DOF model and proposed a short-time Fourier Transform method for crack detection and size estimation. Gear pair with symmetric and asymmetric tooth profiles and with tooth root crack damage dynamic response was determined in Ref. [79] utilizing 6-DOF model. The dynamic response of the gear pairs with the crack considering the open state of the crack in meshing was investigated and calculated the condition indicators for fault diagnosis in Ref. [66]. Wang et al. [68] determined the dynamic response of gear pair for varying crack lengths utilizing the finite element/contact mechanics model. The dynamic response of carburized spur gear pair with tooth root crack was determined utilizing a 8-DOF model in Ref. [69]. Yang et al. [71] determined nonlinear dynamic response of the spur gear for two different crack types: root crack and crack in the middle of the tooth surface. Kalay et al. [81] developed a one-dimensional convolutional neural network to detect the presence of tooth root crack damage using the dynamic response of the gear pair with symmetric and asymmetric profiles. The dynamic characteristics of the gear pair with tooth crack that has the flexibility of the gearbox included was determined in Ref. [83]. Zhou et al. [84] proposed an improved dynamic model to derive the response that considers the delay in the meshing due to tooth root crack. The dynamic response of the gear pair with coupled faults: crack and wear was derived in Ref. [85]. We investigated the dynamic response of nonunity-ratio spur gear pair with varying lengths of tooth root crack damage using a finite element/contact mechanics model and calculated the condition indicators showing the dependence of gear pair dynamic properties and damage severity on condition indicator values.

Several models exist for deriving the dynamic response of a gear pair with consideration for surface pitting damage. Choy et al. [42] numerically simulated the dynamic response of gear pair with surface pitting damage by changing different parameters like phase and amplitude of gear mesh stiffness, and number of damaged teeth. The spectrum of the dynamic response of the gear pair with spall and broken tooth was analyzed along with the appearance of sidebands due to gear tooth faults in Ref. [43]. Jiang et al. [47] studied the dynamic characteristics of gear pairs with pitting damage considering the varying sliding friction. The dynamic response of the gear pair with tooth surface pitting damage utilizing 8-DOF model for varying damage amounts was analyzed in Ref. [50] and ranked the statistical condition indicators based on the Pearson correlation coefficient for different amounts of pitting damage. Yu et al. [77] determined the dynamic response of gear pairs with small depth spalls and deep depth spalls by considering the nonlinear elliptical contact pattern. Different dynamic response derivation models of gear pairs with several gear faults are reviewed in Ref. [64]. Luo et al. [78] proposed a dynamic model considering the changes due to tooth surface roughness and geometric deviations from spalling and pitting and validated with experimental results. The pitting damage is accurately captured from the fatigue experiment and the simulated dynamic response of the gear pair is compared with experimental results in Ref. [1]. Cheng et al. [80] determined dynamic response of the gear pair with localized spalling and validated with experiments. The gear pair with localized spalling showed chaotic characteristics and rich bifurcation. The dynamic response of spur gear pair with weight reduction structure and spalling damage was determined in Ref. [82] and validated the results with the finite element method. We analyzed the dynamic response of the non-unity-ratio spur gear pair with varying amounts of tooth surface pitting damage. The damage was considered to be centered at the pitch and midface of the gear tooth, and condition indicators were calculated.

A focus of most analyses has been the impact of damage on the condition indicators. The gear pair dynamic properties are not considered in the majority of the analyses. This work reveals the importance of the gear's dynamics on typical condition indicators used for damage detection in rotorcraft.

In this work, a finite element/contact mechanics (FE/CM) approach is used to calculate the dynamic response of gear pairs with localized tooth root crack and surface pit damage. The dynamic responses are characterized in terms of damage type, severity, and the dynamic behavior of the gear pair. A simplified phenomenon-based model is proposed that captures the essential features of the dynamic behavior caused by damage. Several condition indicators are calculated, and closed-form expressions are derived for these indicators using the proposed phenomenon-based model. The dependence of the condition indicators to damage severity and gear dynamic behavior is examined.

4.2 Gear dynamic model - Finite element/contact Mechanics

We determine the gear dynamic response using a combined finite element/contact mechanics (FE/CM) approach developed by Vijayakar and co-workers [131, 139, 140]. In this approach, the finite element method for calculating the overall deformation due to gear blank and tooth bending deformations is combined with an analytical solution for the local deformations near the tooth surface due to elastic contact. The geometry of involute gear tooth profiles is captured by specialized finite elements that have high resolution along the profile. These finite elements use shape functions with continuous slopes so that the local curvatures of the deformed surfaces are accurately captured. The contact pressure distribution on the individual gear teeth is calculated at each time instant. Because of the finite element method, the deformations of gear teeth are accurately captured without the need for making modeling assumptions between gear teeth, root, and blank. Accurate modeling of small micro-sized modifications of the gear teeth is possible with this FE/CM approach. The method is computationally efficient, permitting the calculation of dynamic responses. It has been used to accurately calculate the dynamic response of gear pairs Refs. [14, 17, 141]. The load distribution and deformations of the gear pair are used in the equations of motion of the gear pair to calculate the dynamics of the gear pair.

Tooth root crack and tooth surface pitting damage are incorporated into the established FE/CM model so that accuracy and computational efficiency are maintained. Tooth root cracks are modeled by releasing the connectivity of the select elements along a specified crack path. This method accurately represents the remaining healthy portion of the gear tooth, which is an important parameter affecting the tooth mesh and gear pair dynamic response. The FE/CM models the surface pitting damage by approximating them as ellipses. The FE/CM model requires the width of the pit along the facewidth, the height of the pit along the profile direction, and the center of the ellipse on the tooth surface geometry for modeling pitting damage. The FE/CM removes the contact between the mating surfaces in the specified region of the tooth surface. The cells on the edge of the pitting damage have high gradients in the contact pressure distribution of the gear pair.

4.3 Gear dynamic response

The gear pair considered in this work is the sun-planet pair from the output planetary stage of a rotorcraft transmission [112]. It is a nonunity-ratio spur gear pair with geometrical parameters in Table 4.1. The finite element model of the gear pair is shown in Figure 4.1. The speed of the pinion is 4000 rpm, which corresponds to 1800 Hz mesh frequency. The torque applied to the gear is 424 $\mathrm{N} \cdot \mathrm{m}$.

Table 4.1: Geometrical parameters for the nonunity-ratio spur gear pair

	Gear	Pinion
Number of teeth	35	27
Module (mm)	2.87	
Outer diameter (mm)	104.98	84.05
Root diameter (mm)	91.54	70.76
Tooth thickness (mm)	4.18	4.52
Facewidth (mm)	31.75	34.925
Center distance (mm)	88.9	
Pressure angle (deg)	24.6	

The gear pair in Figure 4.1 is dynamically analyzed to determine its baseline vibration in the case without damage. The steady-state dynamic response of the gear pair is calculated for one complete rotation of the pinion, which consists of 27 total mesh cycles, to fully capture the effects of damage. Prior to reaching steady-state, a region of transient response is calculated and discarded. To fully capture all important features of the spectra, we calculate the dynamic response for 50 steps per mesh cycle. The total solution time for one analysis is approximately three to four hours on a conventional computer. The rotational deformations of the gear (θ_g) and pinion (θ_p) calculated from the FE/CM model are used to determine the dynamic transmission error $x(t) = r_{bp}\theta_p + r_{bg}\theta_g$, where the base radii of the gear and pinion are r_{bg} and r_{bg}, respectively.

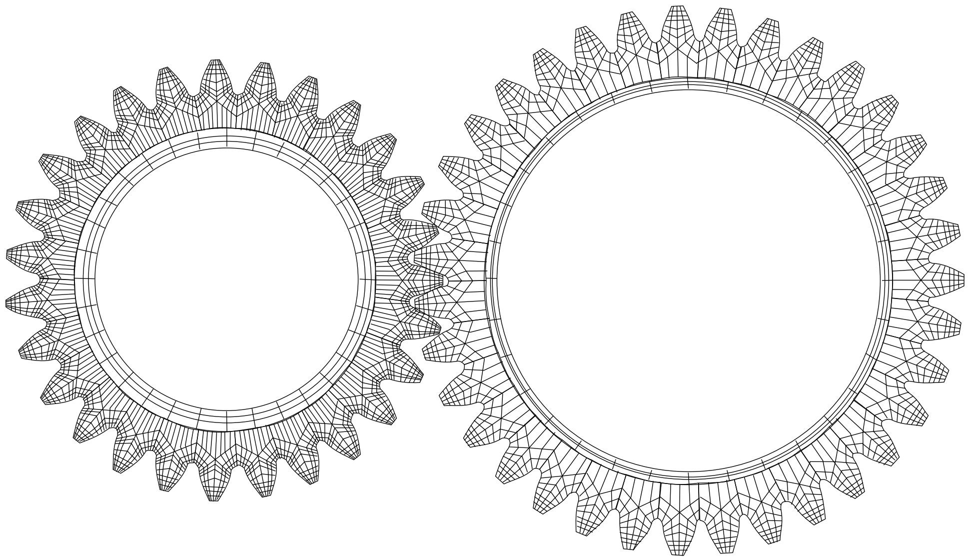

Figure 4.1: Finite element model of the nonunity-ratio gear pair with parameters in Table 4.1.

The natural frequency and damping ratio of the gear pair in Figure 4.1 are determined using numerical impulse tests [14,16,33,34,41], where the transient response in the gear pair without damage is initiated by an impulsive torque about the nominal torque of 424 $\mathrm{N\cdot m}$. These impulse tests are analyzed for the case that the gears are rotating so slowly that they are approximately stationary. The effective stiffness from elastic contact varies as the gears roll and the contact conditions on the gear teeth change. The most dramatic changes in spur gears occur when the number of tooth pairs in contact changes from one to two (for low-contact ratio gears). To estimate the overall vibration of the gear pair, we select two configurations for numerical impulse tests. One configuration is when only one pair of teeth is in contact. The other is when two pairs of teeth are in contact. Numerical impulse tests at each configuration gives transient response that is then used to determine the configuration-dependent natural frequency f_{ni} and damping ratio ζ_{ni} for $i = 1,2$. We determine the natural frequency and damping ratio from the vibration spectra with the half-power formula, but they can also be determined directly from the time history with the formula for the logarithmic decrement. The overall natural frequency $f_n = (\mathrm{ICR}-1)f_{n2} + (2-\mathrm{ICR})f_{n1}$ and damping ratio $\zeta = (\mathrm{ICR}-1)\zeta_2 + (2-\mathrm{ICR})\zeta_1$ are calculated as an average over the mesh cycle using the involute contact ratio ICR. For the case that one pair of teeth are in contact the natural frequency $f_{n1} = 2370.73$ Hz and damping ratio $\zeta_1 = 0.048$. When two pairs of teeth are in contact, $f_{n2} = 2916.63$ Hz and $\zeta_2 = 0.039$. Because the gear teeth are unmodified and corner tooth contact occurs, the range of mesh cycle when the gear pair has two teeth in contact is meaningfully extended. This results in the actual contact ratio 1.64 being larger than the theoretical contact ratio 1.45 determined solely from the gear geometry. Averaging over the mesh cycle using the actual involute contact ratio ICR = 1.64, gives the resulting gear pair natural frequency $f_n = 2720.11$ Hz and damping ratio $\zeta = 0.042$.

The steady-state response of the gear pair without damage is shown in Figure 4.2(a). The response is periodic because all gear teeth without damage are identical. Indeed, the dynamic transmission error is identical for the remaining 24 mesh cycles that correspond to a pinion rotation (not shown). The spectrum of the dynamic response is shown in Figure 4.2(b). The spectrum only contains amplitudes at the mesh frequency and its harmonics (i.e., at 1800 Hz, 3600 Hz, and 5400 Hz). This is the expected behavior when all gear teeth are undamaged [8–14, 18].

We consider tooth root crack damage that occurs on a single pinion tooth. Three different crack lengths are considered, which are shown on the tooth's finite element mesh in Figure 4.3(d). All root cracks start at the same location in the root; they all extend through the entire facewidth of the tooth. The steady-state dynamic transmission error for one complete rotation of the pinon with tooth root crack damage is shown in Figure 4.3(a). Deviations from the response of the gear pair without damage occur when the damaged tooth comes into contact at 14.02 mesh cycle. These differences are largest shortly after the damaged tooth engages but diminish with each subsequent oscillation cycle. The differences

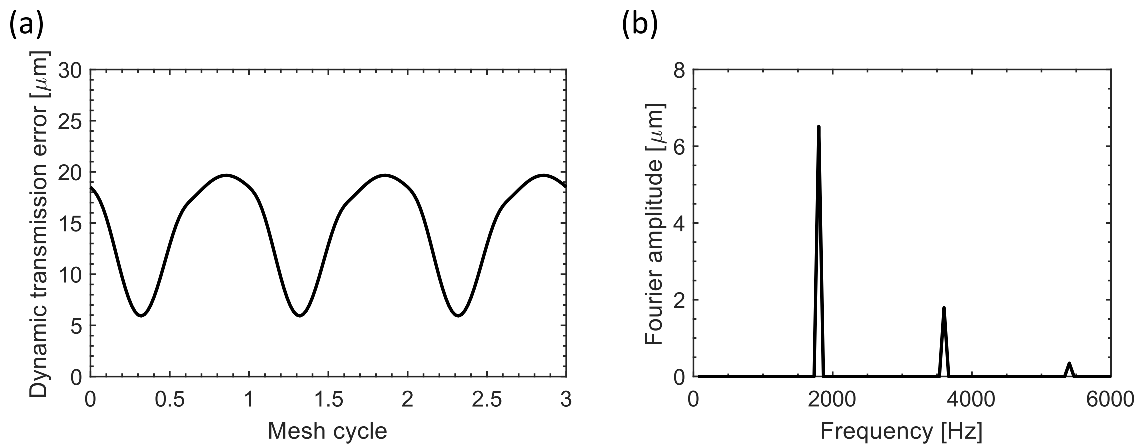

Figure 4.2: FE/CM calculation of (a) dynamic response and (b) frequency spectrum for the nonunity-ratio spur gear pair without damage.

from healthy increase with increasing amount of damage. The spectrum of the response in Figure 4.3(a) is shown in Figure 4.3(b). The amplitudes at the mesh frequency and its harmonics have modest changes with damage. For example, the component at the mesh frequency increases from 6.52 μm when healthy to 6.68 μm when a pinion tooth has a crack 50% through the thickness of the tooth. This corresponds to an increase of just 2.45%. When the crack is 80% through the thickness, the amplitude increases to 7.63 μm, which corresponds to an 17.02% increase from healthy. Modest sensitivity in the normal meshing components due to damage, like that seen in Figure 4.3(b), makes them unsuitable for damage detection. The changes in the spectrum from 0 to 1700 Hz caused by tooth crack damage result from slight variations in the dynamic response of the gear pair before the engagement of a damaged tooth. More prominent differences in the spectrum occur near 2733.33 Hz, which is near the natural frequency of the gear pair. These components are noticeably smaller than the regular meshing harmonics. They are much more sensitive to damage severity, however. There is no contact loss nonlinearity for 50% and 20% root crack lengths. For the tooth root crack with 80% length (dash-dotted (green) line), the spectrum has broadband amplitudes from zero to near the gear pair's natural frequency. The spectrum near resonance is unlike that seen for the smaller crack lengths, likely due to the presence of nonlinear tooth contact loss between 15.32 and 15.62, 16.14 and 16.46, and 18.29 and 18.38 mesh cycle in Figure 4.3(a), where the dynamic transmission error is negative.

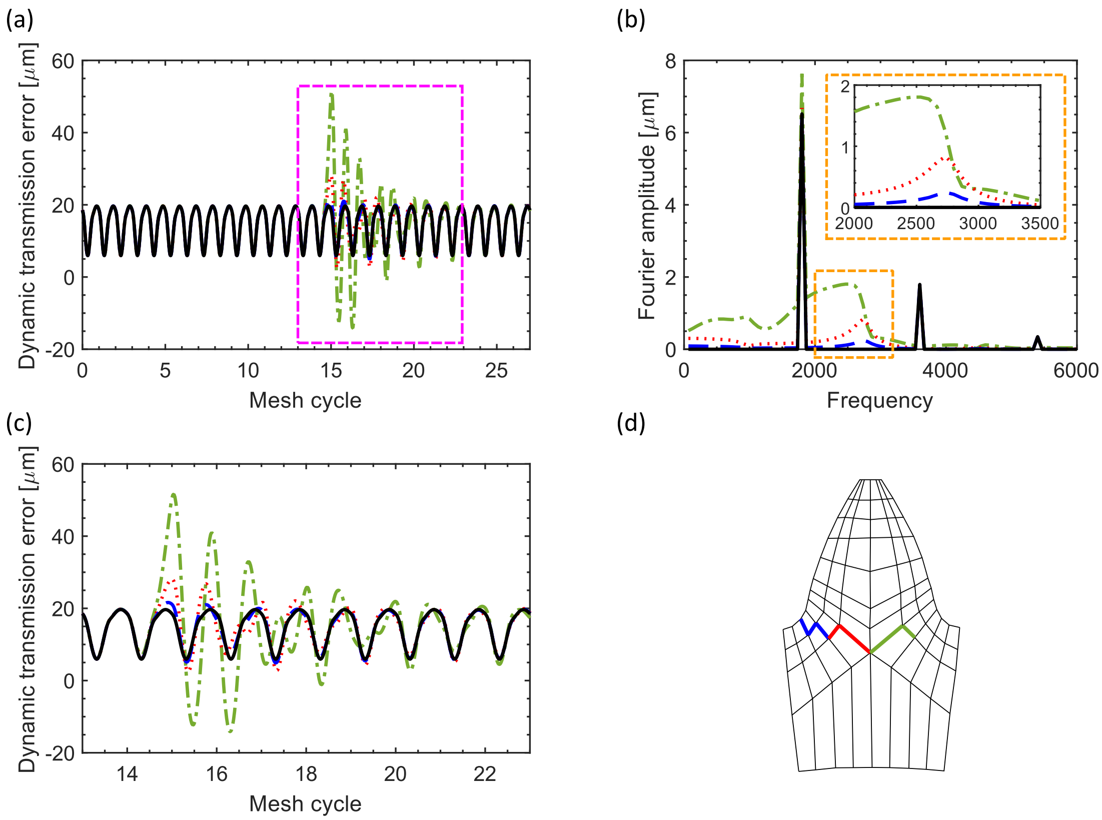

Figure 4.3: FE/CM calculation of (a) dynamic response and (b) frequency spectrum for the nonunity-ratio spur gear pair with tooth root crack damage on a single tooth of the pinion. The plot of dynamic response in (c) is a zoomed-in view of the region highlighted by the dashed (magenta) box on the left plot in (a). The inset figure in (b) shows a zoomed-in view of the frequency range from 2000 to 3500 Hz. (d) A finite element mesh of pinion tooth showing three different tooth root crack lengths. The solid (black) line is the dynamic response of the gear pair without damage. Dashed (blue), dotted (red), and dash-dotted (green) lines represent the dynamic response of gear pair with 20%, 50%, and 80% tooth root crack lengths respectively.

The tooth surface pitting damage on a single tooth of pinion is investigated. All pits have elliptical geometry that is centered at the middle of the facewidth and at the pitch along the profile. The pit geometries are shown on the active area of the tooth surface in Figure 4.4(d). The pit shown in the dashed (blue) line has a width of 6.35 mm (dimension along the facewidth) and a height of 1.38 mm (dimension along the tooth profile). The pit shown in the dotted (red) line has a 12.7 mm width and 2.76 mm height. The largest pit shown in the dash-dotted (green) line has a 20.32 mm width and 3.94 mm height. The pitting damage areas are 3.32%, 13.28%, and 30.28% of the total active surface of the pinion tooth. The dynamic response of the gear pair with tooth surface pitting damage is shown in Figure 4.4(a). The dynamic response of the gear pair with tooth surface pitting damage is the same as that for the gear pair without damage prior to the damaged tooth coming into contact. When the damaged tooth engages at 14.02 mesh cycle, the dynamic response locally increases, like it did for the case of tooth root cracks in Figure 4.3(a) because the pitting damage is applied to the same tooth as the root crack damage. The maximum dynamic transmission error seen in Figure 4.4(a) increases with increasing size of the pit. The dynamic response in Figure 4.4(a) with tooth surface pitting damage is larger than that for tooth root crack damage in Figure 4.3(a). The spectrum of the response for tooth surface pitting damage is shown in Figure 4.4(b). It shows similar behavior as the spectrum of the tooth root crack damage in Figure 4.3(b). The regular meshing components at mesh frequency harmonics change modestly with damage, even for large pit areas. Local maxima occur in the spectrum near 2733.33 Hz. The spectrum for the largest pit (dash-dotted (green) line) has more broadband frequency content in the spectrum. The time history in Figure 4.4(a) shows two regions of tooth contact loss. Despite the presence of tooth contact loss within two distinct regions of the mesh cycle being consistent for root crack and surface pit damages, meaningful differences occur in the resulting vibration spectra.

The additional vibrations caused by tooth root cracks in Figure 4.3 and tooth surface pits in Figure 4.4 have similarities that will be leveraged for damage detection. Notably, both damage types generate transient dynamic response that more closely relates to the gear pair dynamic properties than the specific type of damage. In Section 4.4, we characterize the additional vibrations caused by damage in the absence of the normal meshing components observed when the gears are healthy.

4.4 Damage-induced dynamic response

Motivated by the small changes observed in the normal meshing vibrations in the presence of damage, most condition indicators seek to first remove the normal meshing components from the vibration signal prior to its analysis. The vibration due to damage alone is called the difference signal. The difference signal is commonly constructed solely from the measured vibration from the gear pair. Because the normal meshing components are generally insensitive to damage, these components are removed from the signal, then the corresponding time-domain signal is reconstructed using an inverse Fourier transform. In practical applications, upper and lower sidebands may also be removed if they are thought to be associated with manufacturing errors of the individual gears or assembly errors from the pair. Also associated with practical construction of the difference signal is time-domain averaging for the removal of noise. Time-domain averaging is not needed for the FE/CM model because the gears and teeth have perfect geometry without variations that occur from manufacturing or assembly errors. To isolate the vibrations created by damage from the normal meshing vibrations of the gear pair we calculate the difference signal exactly from $y(t) = x_d(t) - x_h(t)$, where $x_d(t)$ is the dynamic transmission error of the gear pair with damage and $x_h(t)$ is the dynamic transmission error of gear pair without damage. The characteristics of this difference signal, including the similarities in it with damage type and its relation to the gear pair dynamic properties, will be analyzed subsequently. Then, the difference signal will be used as an input to example condition indicators to examine the ability to detect damage from it.

The damage-induced dynamic response, or exact difference signal, is defined similarly to the difference signal. The difference signal is the disparity between the measured vibration signal and the signal containing only meshing components. However, with the exact difference signal, the vibration signal containing only meshing components is derived from the gear pair without damage (Figure 4.2(a)), while the measured signal is from the damaged gear pair (Figure 4.3(a) or 4.4(a)). The expected differences between the difference signal and the exact difference signal are that the frequency spectrum of the difference signal has amplitudes equal to 0 at mesh frequencies and its harmonics. However, in the exact difference signal, these amplitudes are not equal to 0. The damage-induced dynamic response of the gear pair without damage provides a signal with zero vibrations (not shown).

Figures 4.5(a,b) show the difference signal and spectrum for the case that a tooth has root crack damage. Each difference signal is calculated by the subtraction of the normal meshing vibrations in Figure 4.2 from the damaged vibrations in Figure 4.3. The difference signal nearly vanishes until the damaged tooth comes into contact near 14.02 mesh cycle. Noticeable increases in the difference signal from zero occur for a few mesh cycles before damaged tooth engagement. The difference signal has oscillatory response that decays in amplitude with every oscillation cycle. Immediately after the engagement of the damaged tooth at 14.02 mesh cycle, the difference signal has meaningful local increases. For all crack lengths, the maximum in the difference signal occurs near 15 mesh cycle, which is nearly one mesh cycle after the damaged tooth engages in mesh. The period of the oscillation for each crack length is nearly 0.66 mesh cycle. After accounting for the 1800 Hz mesh frequency, this corresponds to a frequency of 1800/0.66= 2727.3 Hz. This is closely related to the gear pair natural frequency. We have determined that the instant the difference signal is maximum corresponds to a configuration of the gears where contact is solely carried by the damaged tooth and is furtherest up the tooth's profile. This corresponds to a instant when the largest bending occurs on the tooth (not shown). The spectrum shows the difference signal largely contains response at 2733 Hz.

Figures 4.5(c,d) shows the difference signal and spectrum for the case that the tooth has surface pitting damage. The characteristics of the difference signal and spectrum with surface pitting damage are similar to the difference signal of the gear pair with tooth root crack damage. Regardless of the type and extent of damage, the difference signal oscillates at a frequency close to the natural frequency of the gear pair. In the case of pitting damage, the maximum is observed at around 14.9 mesh cycle, where the mating teeth are at the pitch which is the maximum dimension of the pitting damage located.

The presence of damage in the gear pair is determined by evaluating select condition indicators calculated from the damaged-induced dynamic response from the gear pair. We consider the condition indicators RMS, FM4, and M8A in this work because of their use in rotorcraft systems. Each of these indicators provide a statistical measure of the vibration response. The deviation of condition indicator values from the threshold values indicates the presence of damage.

The RMS is the root mean square of the vibration response calculated from [146]

$$\mathrm{RMS} = \sqrt{\frac{1}{N}\sum_{i=1}^{N} {y_i}^2} \tag{4.1}$$

where N is the number of data points, and $y_i = y(t_i)$ is the difference signal at time t_i. The RMS provides an overall measure of energy in the vibration [88]. The RMS of the exact difference signals obtained from the FE/CM model with tooth root cracks (Figure 4.5(a)) and tooth surface pits (Figure 4.5(c)) are given in Table 4.2. The RMS values for tooth root crack damage are comparable to those for tooth surface pits. The RMS increases with increasing amount of damage, which is an ideal behavior for a condition indicator. The presence of damage is determined from the values of the RMS. Typically values that exceed a certain threshold are classified as damaged. We use noise with a Gaussian distribution of mean μ_n and variance σ_n as the threshold for the current discussion. The RMS of Gaussian noise is $\sqrt{\mu_n^2 + \sigma_n^2}$. Because of the RMS dependence on the parameters of the noise, the ability to detect damage depends on the specific features of the noise.

The FM4 indicator is calculated by dividing the fourth moment of the vibration signal by the square of its variance [97]

$$\mathrm{FM4} = \frac{N \sum_{i=1}^{N} (y_i - \bar{y})^4}{[\sum_{i=1}^{N} (y_i - \bar{y})^2]^2} \tag{4.2}$$

where $\bar{y}$ is the average of the difference signal. FM4, because it uses the fourth moment of the vibration signal, generally responds to damage isolated to a limited number of teeth. The values of FM4 obtained from the FE/CM calculations of the difference signal in Figure 4.5 are given in Table 4.2. The FM4 values are substantially larger than those for the RMS, illustrating a generally higher sensitivity to damage. The increases in FM4 wtih increasing damage amount are not as large for FM4 as they were for RMS, however. Indeed, the FM4 increases by just 15.43% as the root crack length increases from 20% to 80%. For the tooth surface pit, an increase of just 5.73% occurs when the pitting area increases from 3.32% to 30.28%. For Gaussian noise the FM4 has a value of three, regardless of the specific mean and variance of the noise. Because the values shown in Table 4.2 are substantially larger than this threshold, it is expected that all amounts of damage are detectable.

The M8A indicator is calculated by dividing the eight moment of the vibration response by the fourth power of the variance [147]

$$\mathrm{M8A} = \frac{N^3 \sum_{i=1}^{N} (y_i - \bar{y})^8}{[\sum_{i=1}^{N} (y_i - \bar{y})^2]^4} \tag{4.3}$$

The M8A calculations of the exact difference signals obtained from FE/CM models in Figure 4.5 are given in Table 4.2. The large values of M8A compared to those for FM4 and RMS demonstrate this indicator's expected increased responsiveness to damage [147]. For Gaussian noise, the M8A has a value of 105. Because all values in Table 4.2 are substantially larger than 105, it is expected that all amounts of damage would be identified by the M8A indicator. The severity of pitting damage would be difficult to detect from the M8A indicator. The M8A values interestingly decrease with increasing pitting damage area.

A number of additional condition indicators have been proposed for detecting damage from vibration signals. We concentrate on the RMS, FM4, and M8A because of their use in rotorcraft diagnostics systems [5]. Additionally, these indicators in many instances are the foundation of more advanced metrics. For example, the Crest Factor indicator uses RMS in its calculation [148]. FM4 has its foundation from the kurtosis, which is also used for NA4* [86, 149, 150]. M8A is calculated from a higher moment of the signal than FM4. Other moments of the vibration include S_r [151], S_α [152], and M6A [147].

Table 4.2: Calculation of condition indicators using the exact difference signals obtained from the FE/CM model.

Crack length	**RMS**	**FM4**	**M8A**
20%	0.45	15.04	8911
50%	1.58	16.11	11702
80%	5.38	17.36	13992

Pitting area	**RMS**	**FM4**	**M8A**
3.32%	0.31	14.83	8899
13.28%	1.48	15.05	8890
30.28%	4.57	15.68	8097

4.5 Phenomenon-based model for damage-induced dynamic response

4.5.1 Underdamped oscillator model

The difference signal for the gear pair with tooth root crack or surface pit damage in Figure 4.5 resembles the free underdamped response of a linear oscillator. The results from the FE/CM model show that the frequency of vibrations and the rates that they decay are nearly uniform for varying amounts of damage. Based on these observations, we propose to approximate the difference signal as

$$y(t) = Ae^{-\zeta\omega_n(t-t_d)}\sin[\omega_d(t-t_d)]u(t-t_d), \tag{4.4}$$

where ω_n and ζ are the natural frequency and damping ratio of the nonunity-ratio gear pair. $u(t)$ is the unit step function, which vanishes when the argument is negative and is equal to unity when the argument is positive or zero. The damped natural frequency depends on the natural frequency and damping ratio through $\omega_d = \omega_n\sqrt{1-\zeta^2}$. The natural frequency (ω_n), damping ratio (ζ), and damped natural frequency (ω_d) are the properties of the gear pair and do not depend on the damage or its severity. A is an amplitude that depends on the damage type and severity. t_d is a delay time; it also depends on the damage. The inclusion of the delay time ensures the maximum of the proposed model occurs near the same time instant as that in the FE/CM model. The time at which maximum occurs is $t_{\max} = t_d + \frac{1}{\omega_d}\tan^{-1}(\omega_d/\zeta\omega_n)$. The maximum amplitude of the proposed model is $y_{max} = y(t_{\max}) = A\sqrt{1-\zeta^2}\exp\left[-\frac{\zeta}{\sqrt{1-\zeta^2}}\tan^{-1}\left(\frac{\sqrt{1-\zeta^2}}{\zeta}\right)\right]$. The decay of the proposed model follows the logarithmic decrement $\delta = 2\pi\zeta/\sqrt{1-\zeta^2}$. We label the local maxima $A_1, A_3, A_5, \ldots$. The minima are labeled $A_2, A_4, A_6, \ldots$. The first maximum $A_1 = y_{\max}$. The ratio of successive maxima or minima amplitudes is given by $A_{i+2}/A_i = e^{-\delta}$. The ratio between successive extrema is $A_{i+1}/A_i = -e^{(\delta/2)}$. Therefore, the minimum amplitude, which occurs at $t_{\max} + T_d/2$, is $A_2 = -\exp(-\delta/2)$. We will refer to the model in Eq. (4.4) as the phenomenon-based model.

The phenomenon-based model has just four parameters. The natural frequency ω_n and damping ratio ζ, along with the damped natural frequency ω_d calculated from them, are parameters specific to the gear pair being analyzed. These can be determined from analytical models, computational models, or experiments. For the nonunity-ratio gear pair analyzed in this work, the natural frequency and damping ratio were determined from the FE/CM model to be $\omega_n/2\pi = 2733.33$ and $\zeta = 0.03992$. The amplitude A and delay time t_d were determined by using a least square fit to the difference signal calculated from the FE/CM model shown in Figure 4.5(a,c). The amplitude and delay time for the 20% tooth root crack damage were determined to be $A = 2.798$ μm and $t_d = 0.000475303$ sec. A comparison of the results from the phenomenon-based model in Eq. (4.4) using these parameters with those from the FE/CM model are shown in Figs. 4.6(a,b). As seen in the time history in Figure 4.6(a), the phenomenon-based model accurately captures the maximum amplitude, the frequency of oscillations, and the overall decay of the vibration. The corresponding spectrum in Figure 4.6(b) is also accurately captured across a wide range of frequencies. The maximum amplitude of the phenomenon-based model is 9.15% larger than that of the FE/CM model. Notable differences occur at low frequencies, where the phenomenon-based model does not capture the increases in amplitudes below 1,000 Hz. These components may be due to the non-vanishing amplitudes prior to 0.5 mesh cycle in Figure 4.6(a) when the damaged tooth comes into contact. Figures 4.6(b,c) show comparisons of the phenomenon-based model with the FE/CM model for the 50% tooth root crack. The least-square fit determined amplitude $A = 10$ μm and delay time $t_d = 0.0004985$ sec. The overall agreement shown for the 20% tooth root crack length persists for this meaningfully larger crack length where substantial increases in the difference signal occur.

Agreement between the phenomenon-based model and the FE/CM model deteriorates for large amounts of damage like that shown in Figure 4.6(e,f) for 80% tooth root crack length. For this large tooth root crack, the substantially-large amplitudes are less accurately captured over the entire range of mesh cycles. The FE/CM model also shows noticeable changes in the oscillation cycle that are not captured by the phenomenon-based model. These differences result in meaningfully different predictions of the spectrum in Figure 4.6(f). These differences are an expected result for the simplified phenomenon-based model in Eq. (4.4). This model does not capture nonlinear effects that become meaningful for larger amounts of damage when the difference signal has large amplitudes.

The values for amplitude A and delay time t_d in Eq. (4.4) for the 20% crack are close to the values that would be obtained by tuning the delay time t_d so that the peak amplitude of the difference signal occurs at the same time instant as that for the FE/CM model, then tuning A to match the maximum that for the FE/CM model. This method to determine A and t_d becomes difficult for larger amounts of damage when increased prominence of nonlinear effects occur in the resulting vibration. For larger tooth root crack lengths, determining A and t_d using a least square curve fit provides the best overall agreement between the phenomenon-based model and FE/CM model. The use of a least-squares approach to determine the peak amplitude in the frequency spectrum of the exact difference signal provided meaningfully worse agreement between the phenomenon-based model and FE/CM model in the time domain. Because the condition indicators considered are evaluated from the time-domain signals, we decided to select the amplitude A and delay time t_d using the least-square method in the time domain.

The amplitude and delay time of the phenomenon-based model for varying amounts of tooth root crack lengths are shown in Figs. 4.7(a) and (b), respectively. The amplitude A increases monotonically with increasing crack length (Figure 4.7(a)). The increases are larger for higher crack lengths than for lower crack lengths. The delay time increases monotonically with increasing crack length for crack lengths less than 70%. A substantial decrease occurs for 80% crack length. This is due to nonlinear effects when the difference signal amplitudes become large.

4.5.2 Confirmation of condition indicator accuracy

The accuracy of the phenomenon-based model is demonstrated by comparing the condition indicators calculated from it compared to those calculated from the FE/CM model. Figure 4.8 shows calculations of RMS, FM4, and M8A for varying crack length using the FE/CM model (circle (blue) markers) and the phenomenon-based model (square (red) markers). The RMS calculated from the phenomenon-based model agrees with that from the FE/CM model for the entire range of crack lengths shown in Figure 4.8(a). For the 20% tooth root crack length, the RMS calculated from the phenomenon-based model is 0.435736 μm, which is only 2.2% different when compared to the RMS calculated from the FE/CM model. When the crack length increases to 80%, the percentage difference is 0.0024%, even though noticeable differences occur in the difference signals shown in Figure 4.6(e). Excellent agreement between the FM4 calculated from the phenomenon-based and FE/CM models occurs for crack lengths of 30% and below. For example, the percentage difference in the two calculations is just 1.84% for the 20% crack length. For crack lengths above 30% meaningful differences in the FM4 calculations occur. The deviation in FM4 calculations increases with increasing crack length from 30% to 70% crack length. The difference decreases from 70% to 80% crack length, although noticeable deviation occurs between the two models (Figure 4.6(e,f)). The calculations of M8A have similar behavior as those for the FM4. The phenomenon-based model calculation of M8A is just 2.56% different from the FE/CM model for 20% crack length. Similar agreement occurs for other crack lengths of 30% and below. The deviations between the two models for crack lengths above 30% are more substantial, however.

The RMS increases monotonically with the increasing amount of damage, a feature captured in both the phenomenon-based and FE/CM models. Calculations of FM4 and M8A using the response from the FE/CM model are insensitive to damage for crack lengths up to 30%. Further increases in crack length from 30% result in increases in the indicators. This is not captured by the phenomenon-based model. The FM4 and M8A calculations from the phenomenon-based model are largely insensitive to the amount of damage.

4.6 Condition indicator derivations

4.6.1 Closed-form expressions

The simplicity of the phenomenon-based model permits the calculation of closed-form expressions for the condition indicators. The closed-form expressions can provide considerable insight into the sensitivity of the indicator to damage, but also provide fundamental understanding of the dependence of gear pair dynamic properties on the condition indicators. Substitution of the phenomenon-based model in Eq. (4.4) into the time-domain formulas for the condition indicators in any of Eqs. (4.1), (4.2), or (4.3), which are commonly used to evaluate the dynamic responses, do not yield sufficiently simple expressions for our purpose. Therefore, the use of amplitude-domain formulas for the calculation of condition indicators are explored.

4.6.1.1 Analysis in the amplitude domain An alternate method of calculation is needed to determine closed-form solutions for condition indicators of interest using the simplified form of the difference signal in Eq. (4.4). We found this alternate method from elementary statistics. A key element of this analysis is the probability density function $f(y)$. This function provides the probability that a given amplitude of the difference signal y will be found. Once the probability density function $f(y)$ is known, calculation of the statistical features of the difference signal in Eq. (4.4) can be readily determined through basic integration. For example, the mean and variance of the difference signal are determined from [153]

$$\text{Mean} = \mu = \int y f(y) dy \tag{4.5}$$

$$\text{Variance} = \sigma^2 = \int (y-\mu)^2 f(y) dy \tag{4.6}$$

The integrations are understood to cover the entire range of amplitudes possible in the difference signal $y(t)$. The probability density function corresponding to Eq. (4.4), and shown in Figure 4.6, has been previously determined in the literature. We will present an approximate form of the probability density function, sufficiently accurate for the damage-induced dynamic response of gears, in Section 4.6.1.2.

The indicators of focus in this work have corresponding amplitude-domain integral forms that were determined from their corresponding definitions. The RMS is calculated from

$$\text{RMS} = \sqrt{\int y^2 f(y) dy} \tag{4.7}$$

Because FM4 is the fourth moment divided by the square of the variance, its amplitude-domain form is

$$\text{FM4} = \frac{\int (y-\mu)^4 f(y) dy}{\sigma^4} \tag{4.8}$$

M8A, which is the eighth moment divided by the fourth power of variance, is given as

$$\text{M8A} = \frac{\int (y-\mu)^8 f(y) dy}{\sigma^8} \tag{4.9}$$

We have not found the amplitude-domain expressions given in Eqs. (4.7), (4.8), and (4.9) in the literature. To build confidence in their accuracy, we evaluated them for the case that the input is a Gaussian distribution with mean μ and standard deviation σ. Exact values are known for this case. The expected values RMS = $\sqrt{\mu_n^2 + \sigma_n^2}$, FM4 = 3, and M8A = 105 were found.

4.6.1.2 Probability density function This section determines a probability density function corresponding to the phenomenon-based model in Eq. (4.4) suitable for use in the amplitude-domain integral forms of the condition indicators. The phenomenon-based model described by Eq. (4.4) is a decaying sinusoid. Its probability density function is not available in the literature. Therefore, we seek an accurate approximate form. Without loss of generality, we assume the delay time in Eq. (4.4) vanishes (i.e., $t_d \to 0$) so that the signal considered simplifies to $y(t) = Ae^{-\zeta \omega t} \sin \omega_d t$. This physically corresponds to the case that the damage tooth engages at time $t = 0$.

Figure 4.9(a) shows an approximate numerical calculation of the probability density function corresponding to the difference signal shown in Figure 4.6(a) for the case that a tooth has a root crack 20% through its thickness without delay time. This function is determined from a histogram of the amplitudes of $y(t)$. Specifically, we specify 10000 regions between the maximum amplitude 2.63 μm and minimum amplitude -2.32 μm. Then, the number of data points of y that fall within each region are counted. To provide an approximate probability density function, the resulting data are normalized so that the total area of all regions is unity. Accurate representation of the probability density function depend on the number of data points contained in $y(t)$ and the number of regions specified over the amplitudes. The approximate calculation of the numerical histogram in Figure 4.9(a) uses one million time steps per mesh cycle and 10000 regions between the extrema. However, we found that using at least 500 time steps over a mesh cycle for $y(t)$ and using at least 500 regions in the amplitudes resulted in sufficient accuracy.

The approximate probability density function in Figure 4.9(a) has several local maxima for positive and negative amplitudes. The probability density function decreases sharply with increasing (decreasing) amplitude from the maxima at negative (positive) amplitudes. The probability density function has large values near vanishing amplitude. This makes sense intuitively because the vibrations decay to small values above 10 mesh cycle.

To better understand the features observed in the probability density function in Figure 4.9(a), and how to approximate it, we consider the truncated difference signal shown in Figure 4.9(b). This signal contains only the first three halves of the oscillation cycle. Two local maxima occur for positive displacements. The first is $A_1 = 2.63$ μm at time $t = 0.161$ mesh cycle. The other is $A_3 = 2.05$ μm a damped period later at $t = 0.820$ mesh cycle. The lone local minimum occurs at amplitude $A_2 = -2.32$ μm at $t = 0.490$ mesh cycle. The corresponding approximate probability density function is shown in Figure 4.9(c). For positive amplitudes, two maxima occur near $A_1 = 2.63$ μm and $A_3 = 2.05$ μm identified in Figure 4.9(b). Similarly, a maximum occurs near $A_2 = -2.32$ μm.

The results in Figure 4.9(c) suggest that overall behavior of the probability density function is captured by a sequence of amplitudes obtained over one-half of an oscillation cycle. Noting again that no formula is available in the literature for decaying sinusoids, we turn our efforts to non-decaying sinusoids, where results are available. Indeed, the signal $b(t) = A\sin(\omega t - \phi)$ has the probability density function $g(b) = 1/\pi\sqrt{A^2 - b^2}$ for $-\mathrm{A} < b < \mathrm{A}$ and vanishes otherwise [154]. The probability function $g(b)$ has large values as the amplitude approaches A. It decreases sharply with amplitudes locally from A. Less sharp, monotonic decreases occur with further decreases in amplitude until the probability density function reaches the value $1/\pi A$ at vanishing amplitude. The probability density function is symmetric about the amplitude axis so the features for negative amplitudes as the same as those described for positive amplitudes.

The overall features described mirror those seen in Figure 4.9(c) for negative amplitudes. Specifically, the probability density function is large near the amplitude $A_2 = -2.32\ \mu$m, which corresponds to the minimum in Figure 4.9(b). For near vanishing amplitudes from the negative side, the probability density function is 0.091. The value calculated from $2/3\pi A_2 = 0.092$, which is only 1.1% different from that in Figure 4.9(c). We approximate the probability density function using $2/3\pi\sqrt{A_2^2 - y^2}$ for $-A_2 < y < 0$. Approximating the probability density function for the decaying sinusoid like one for a non-decaying sinusoidal is accurate provided the damping remains low. This is the case for gear systems, where damping ratios generally vary from three to five percent. For larger damping values that exceed 10%, the accuracy of the approximate probability density function diminishes. Numerical experiments have shown that the deviations in the approximate probability density function are primarily concentrated in the region of lower amplitudes, however.

The extension of the probability density function to cases where more than one oscillation cycle occurs is illustrated using the positive amplitudes in Figure 4.9(b). For amplitudes from $A_3 = 2.05\ \mu$m to $A_1 = 2.63\ \mu$m, the probability density function can be accurately approximated using $2/3\pi\sqrt{A_1^2 - y^2}$ obtained from a non-decaying sinusoid of amplitude A_1. The accuracy is confirmed in Figure 4.9(c) between $A_3 = 2.05\ \mu$m to $A_1 = 2.63\ \mu$m. For amplitudes $0 < y < A_3$, the probability density function must be modified to include amplitudes corresponding to the second region of positive amplitudes between $t = 0.66$ mesh cycle and 0.99 mesh cycle in Figure 4.9(b). These amplitudes can be accurately captured in the probability density function by the addition of a second sinusoid term with appropriate amplitude. For the response in Figure 4.9(b) this function is

$$f(y) = \frac{2}{3\pi\sqrt{A_1^2 - y^2}} + \frac{2}{3\pi\sqrt{A_3^2 - y^2}}, \quad 0 < y < A_3 \tag{4.10}$$

The first term in Eq. (4.10) captures positive amplitudes below $A_3 = 2.05\ \mu$m from $t = 0$ to $t = 0.33$ mesh cycle. The second term captures the additional amplitudes in that range from $t = 0.66$ and 0.99 mesh cycle. Figure 4.9(c) shows Eq. (4.10) accurately captures the probability density function for amplitudes from 0 to A_3.

The expressions for the probability density function can be further extended to difference signals in Eq. (4.4) with an arbitrary number of oscillation cycles. The corresponding number of half-cycles is determined from $n = 2t_{\text{end}}/T_d$, where t_{end} is the total time of the difference signal $y(t)$ and $T_d = 2\pi/\omega_d$ is the damped period of vibration. Because the difference signal is practically constructed over a complete rotation of the damaged gear, $t_{\text{end}} = ZT_m$, where Z is the number of teeth on the damaged gear and the mesh period $T_m = 2\pi/\omega_m$. Use of this result gives $n = 2Z\omega_d/\omega_m$. In general, the ratio of the damped frequency to the mesh frequency ω_d/ω_m is not an integer and the number of half-cycles n, too, is not an integer. Restricting our analysis to cases when the difference signal fully diminishes within a rotation of the damaged gear, we take the floor of $2Z\omega_d/\omega_m$ so that n becomes an integer.

The closed-form expressions of the probability density function for one and two oscillation cycles are used to extrapolate the probability density function for n half-sine oscillations. The probability density function is defined separately for odd and even numbers of half-sine oscillations. In an even number of half-sine oscillations, there are $n/2$ positive amplitudes and $n/2$ negative amplitudes which results in the generalized probability density function of the phenomenon-based model having $(n/2+1)$ terms for positive amplitudes and $(n/2+1)$ for negative amplitudes. The probability density function of the phenomenon-based model with an even number of half-sine oscillations is given by

$$f(y) = \begin{cases} 0, & y < A_2 \\ . & \\ . & \\ \sum_{k=1}^{(i-1)} \frac{2}{n\pi\sqrt{A_{2k}^2 - y^2}}, & A_{2i-2} < y < A_{2i}\ (for\ term\ i = 2,3,...,\frac{n}{2}) \\ \sum_{k=1}^{n/2} \frac{2}{n\pi\sqrt{A_{2k}^2 - y^2}}, & A_n < y < 0\ (for\ term\ \frac{n}{2}+1) \\ 0, & y > A_1 \\ . & \\ . & \\ \sum_{p=1}^{(j-1)} \frac{2}{n\pi\sqrt{A_{2p-1}^2 - y^2}}, & A_{2j-1} < y < A_{2j-3}\ (for\ term\ j = 2,3,...,\frac{n}{2}) \\ \sum_{p=1}^{n/2} \frac{2}{n\pi\sqrt{A_{2p-1}^2 - y^2}}, & 0 < y < A_{n-1}\ (for\ term\ \frac{n}{2}+1) \end{cases} \tag{4.11}$$

There are $(n+1)/2$ positive amplitudes and $(n-1)/2$ negative amplitudes when the number of half-sine oscillations is an odd number. The probability density function of the phenomenon-based model with an odd number of half-sine oscillations is given by

$$f(y) = \begin{cases} 0, & y < A_2 \\ . & \\ . & \\ \sum_{k=1}^{(i-1)} \frac{2}{n\pi\sqrt{A_{2k}^2 - y^2}}, & A_{2i-2} < y < A_{2i} \ (for\ term\ i = 2,3,...,\frac{n-1}{2}) \\ \sum_{k=1}^{(n-1)/2} \frac{2}{n\pi\sqrt{A_{2k}^2 - y^2}}, & A_{n-1} < y < 0 \ (for\ term\ \frac{n-1}{2}+1) \\ 0, & y > A_1 \\ . & \\ . & \\ \sum_{p=1}^{(j-1)} \frac{2}{n\pi\sqrt{A_{2p-1}^2 - y^2}}, & A_{2j-1} < y < A_{2j-3} \ (for\ term\ j = 2,3,...,\frac{n+1}{2}) \\ \sum_{p=1}^{(n+1)/2} \frac{2}{n\pi\sqrt{A_{2p-1}^2 - y^2}}, & 0 < y < A_n \ (for\ term\ \frac{n+1}{2}+1) \end{cases} \tag{4.12}$$

The probability density function of the phenomenon-based model in Eq. (4.11) and Eq. (4.12) adheres to all requirements of probability density functions, $f(y) > 0$ and $\int f(y)dy = 1$ The phenomenon-based model response of the gear pair with 20% crack damage for one complete rotation of the pinion is shown in Figure 4.9(e) which corresponds to 82 half-sine oscillation cycles and its numerically calculated probability density function is shown in Figure 4.9(f). The probability density function for one complete rotation of pinion behaves similarly to one and two oscillation cycle probability density function, i.e., larger probabilities are observed at the extremum of the oscillation cycles. The probability density function is large at low amplitudes due to the signal's large number of low-amplitude oscillations.

4.6.1.3 Condition indicators Analytical expressions for the probability density function permit the calculation of the closed-form expressions for the condition indicators of the phenomenon-based model response with n half-sine oscillations. Substitution of the probability density function into the amplitude-domain formula of the condition indicators in Eq. (4.5) - (4.9) gives,

$$\mu = \frac{2A_1}{n\pi}\sum_{i=1}^{n}(-1)^{i+1}e^{-\delta\left(\frac{i-1}{2}\right)} \tag{4.13a}$$

$$\sigma^2 = \frac{A_1^2}{2n}\sum_{i=1}^{n}e^{-\delta(i-1)} - \mu^2 \tag{4.13b}$$

$$\text{RMS} = \sqrt{\frac{A_1^2}{2n}\sum_{i=1}^{n}e^{-\delta(i-1)}} \tag{4.13c}$$

$$\begin{aligned}\text{FM4} = \frac{1}{\sigma^4}\Bigg[&\frac{3A_1^4}{8n}\left(\sum_{i=1}^{n}e^{-2\delta(i-1)}\right) + \frac{3\mu^2A_1^2}{n}\left(\sum_{i=1}^{n}e^{-\delta(i-1)}\right)\\ &-3\mu^4 - \frac{16\mu A_1^3}{3n\pi}\left(\sum_{i=1}^{n}(-1)^{i+1}e^{-3\delta\left(\frac{i-1}{2}\right)}\right)\Bigg]\end{aligned} \tag{4.13d}$$

$$\begin{aligned}\text{M8A} = \frac{1}{\sigma^8}\Bigg[&\frac{35A_1^8}{128n}\left(\sum_{i=1}^{n}e^{-4\delta(i-1)}\right) + \frac{35\mu^2A_1^6}{4n}\left(\sum_{i=1}^{n}e^{-3\delta(i-1)}\right)\\ &+\frac{105\mu^4A_1^4}{4n}\left(\sum_{i=1}^{n}e^{-2\delta(i-1)}\right) + \frac{17\mu^6A_1^2}{n}\left(\sum_{i=1}^{n}e^{-\delta(i-1)}\right)\\ &-7\mu^8 - \frac{224\mu^5A_1^3}{3n\pi}\left(\sum_{i=1}^{n}(-1)^{i+1}e^{-3\delta\left(\frac{i-1}{2}\right)}\right)\\ &-\frac{896\mu^3A_1^5}{15n\pi}\left(\sum_{i=1}^{n}(-1)^{i+1}e^{-5\delta\left(\frac{i-1}{2}\right)}\right) - \frac{256\mu A_1^7}{35n\pi}\left(\sum_{i=1}^{n}(-1)^{i+1}e^{-7\delta\left(\frac{i-1}{2}\right)}\right)\Bigg]\end{aligned} \tag{4.13e}$$

The closed-form expressions of the condition indicators for the phenomenon-based model are derived in Eq. (4.13). The parameters utilized in the derivation of the phenomenon-based model response are used in Eq. (4.13) to evaluate the condition indicators. The RMS, FM4, and M8A condition indicators for 20% crack phenomenon-based model response evaluated using the closed-from expressions given in Eq. (4.13) are only 0.03%, 0.04%, and 0.14% different from the condition indicators evaluated using time-domain formula in Eq. (4.1) - (4.3). The same excellent agreement can be observed for the other damage cases.

The obtained closed-form expressions in Eq. (4.13) of the condition indicators contain several terms with multiple summations. These expressions make it difficult to evaluate the direct dependencies of important system parameters on the condition indicators. The range of mean (μ) for varying amounts of damage is observed to be between 0.004 to 0.134 μm which is very small compared to their respective amplitudes in the phenomenon-based model response. For the simplification purposes of the closed-form expressions, the mean (μ) is removed from the expressions in Eq. (4.13). Also, the summations in the expressions are approximated using their representative Taylor series expression, for example, $\sum_{i=1}^{n} e^{-\delta(i-1)} = 1 + e^{-\delta} + e^{-2\delta} + e^{-3\delta} + \ldots = \frac{1}{1-e^{-\delta}}$. This assumption of expressing the summation terms with their Taylor series expression might be less effective for responses with a limited number of half-sine oscillation (n) cycles because the Taylor series expressions are generally for summation with infinite terms. The closed-from expressions of the condition indicators with these assumptions included are given by,

$$\sigma^2 = \frac{A_1^2}{2n}\left[\frac{1}{1-e^{-\delta}}\right] \tag{4.14a}$$

$$\text{RMS} = \frac{A_1}{\sqrt{2n}}\sqrt{\frac{1}{1-e^{-\delta}}} = A_1\sqrt{\frac{\pi f_m}{2Z_p\omega_d(1-e^{-\delta})}} \tag{4.14b}$$

$$\text{FM4} = \frac{3n}{2}\left[\frac{(1-e^{-\delta})^2}{1-e^{-2\delta}}\right] = \frac{3Z_p\omega_d}{2\pi f_m}\left[\frac{(1-e^{-\delta})^2}{1-e^{-2\delta}}\right] \tag{4.14c}$$

$$\mathrm{M8A} = \frac{35n^3}{8}\left[\frac{(1-e^{-\delta})^4}{1-e^{-4\delta}}\right] = \frac{35Z_p^3\omega_d^3}{8\pi^3 f_m^3}\left[\frac{(1-e^{-\delta})^4}{1-e^{-4\delta}}\right] \tag{4.14d}$$

The closed-form expressions of the condition indicators in Eq. (4.14) directly link gear pair dynamic and damage parameters to the condition indicators. The RMS increases with increase in the damage amount and it is clearly captured in its closed form expression. Interestingly, the condition indicators FM4 and M8A showed no dependence on the amount of damage which is similar to the condition indicators for phenomenon-based model response as shown in Figure 4.8 which are evaluated using the time-domain formula in Eq. (4.1) - (4.3).

The condition indicators of the phenomenon-based model response evaluated using the closed-form expressions (dash-dotted (green) line with cross markers) in Eq. (4.14) are compared to the condition indicators of exact difference signal (solid (blue) line with circle markers) and the phenomenon-based model response evaluated with time-domain formula (dashed (red) line with square markers) are shown in Figure 4.8. Good agreement is observed between the numerically calculated condition indicators and analytically calculated from closed-form expressions condition indicators for varying amounts of damage. It is clear that the RMS condition indicator is dependent on the amplitude of the phenomenon-based signal whereas the FM4 and M8A are not. The simplified closed form expressions of condition indicators showed direct relation between the gear pair dynamic properties and damage parameters.

4.6.2 CI's sensitivity due to gear pair properties

The closed-form expressions of condition indicators for phenomenon-based model allows to understand how the condition indicators react for different varying gear pair parameters like damping ratio, natural frequency, number of oscillations. RMS, FM4, and

M8A condition indicators are calculated for varying gear pair properties for a fixed amount of damage, i.e., 20% crack and shown in Figure 4.10. The dashed (red) vertical line in Figure 4.10 represents the nonunity-ratio gear pair dynamic parameters. The sensitivity of the damping ratio is studied by varying it between 0.01 and 0.2, keeping the other parameters same as the nonunity-ratio gear pair parameters. The RMS condition indicator showed decrease with increase in the damping ratio whereas the FM4 and M8A increases as shown in Figure 4.10(a). The sensitivity of natural frequency of the gear pair and the number of oscillations cycles are also studied and shown in Figure 4.10(b) and (c). The results are observed to be similar to varying damping ratio, i.e., RMS decreases and FM4, M8A increases with increasing parameter value. The natural frequency is varied between 1000 and 5000 Hz and the number of half-sine oscillations are varied between 20 and 160 cycles. From the closed-form expressions it is clearly evident that the condition indicators have dependence on the number of half-sine oscillation cycles n and damping ratio ζ. The dependence of natural frequency comes in calculating the number of half-sine oscillation cycles.

4.7 Conclusions

The dynamic response of the nonunity-ratio spur gear pair which is the sun-planet pair in the planetary stage of two-stage rotorcraft transmission is derived the finite element/contact mechanics (FE/CM) model. The dynamic response is a periodic response with amplitudes present only at the mesh frequency and its harmonics in the spectrum. The localized defects analyzed are tooth root crack and tooth surface pitting damage. The damage is considered on single tooth of the pinion of the gear pair. The dynamic response of the nonunity-ratio spur gear pair with localized defects exhibits increased and transients in nature vibrations. These transients and amplitudes of the dynamic response are increased as the damage amount increases. The spectrum of the dynamic response with localized defects, not only has amplitudes at regular meshing frequencies but also displays resonance amplitudes at the natural frequency of the gear pair. The larger damage amounts showed prominent nonlinearity behavior both in the dynamic response and its spectrum.

The damage-induced dynamic response or the exact difference signal response is derived from the FE/CM model results of gear pair without damage and gear pair with localized defects. The RMS, FM4, and M8A condition indicators are evaluated using the damage-induced dynamic response. Higher values than typical thresholds were obtained, which clearly indicated the presence of damage in the gear pair. The damage-induced dynamic response has oscillating behavior with decaying amplitudes. A phenomenon-based model based on the underdamped, free vibration of a linear oscillator was proposed. This model was shown to accurately capture the damage-induced dynamic response compared to the FE/CM model. Good agreement was observed for the RMS values determined from the damage-induced dynamic response obtained from the FE/CM model and the phenomenon-based model. FM4 values tend to deviate for higher crack lengths due to the increase in the nonlinear nature of the damage-induced dynamic response.

The simplicity of the phenomenon-based model permitted to derive the closed-form expressions for condition indicators by exploring the amplitude-domain formula. The expression for probability density function of the phenomenon-based model response is determined and used to evaluate the closed-form expressions of the condition indicators. The condition indicators evaluated for varying amounts of damage using closed-form expression showed very good agreement with the numerically calculated condition indicators and also the dependency of damage parameters and gear pair dynamic properties were clearly observed with the closed-form expressions of the condition indicators. The RMS condition indicator is observed to be dependent on the amplitude of the phenomenon-based model and increases with increasing amount of damage. However, FM4 and M8A show constant condition indicator values due to the independence of amplitude in the closed-form expressions. The condition indicator sensitivity for varying gear pair parameters like damping ratio, natural frequency and number of oscillation cycles of the gear pair is studied utilizing these closed-form expressions. The RMS is observed to decrease with the increase in the damping ratio or natural frequency or number of oscillation cycles and the FM4, M8A values show increasing behavior. This research could improve the ability to detect damage from the measured vibrations of geared systems.

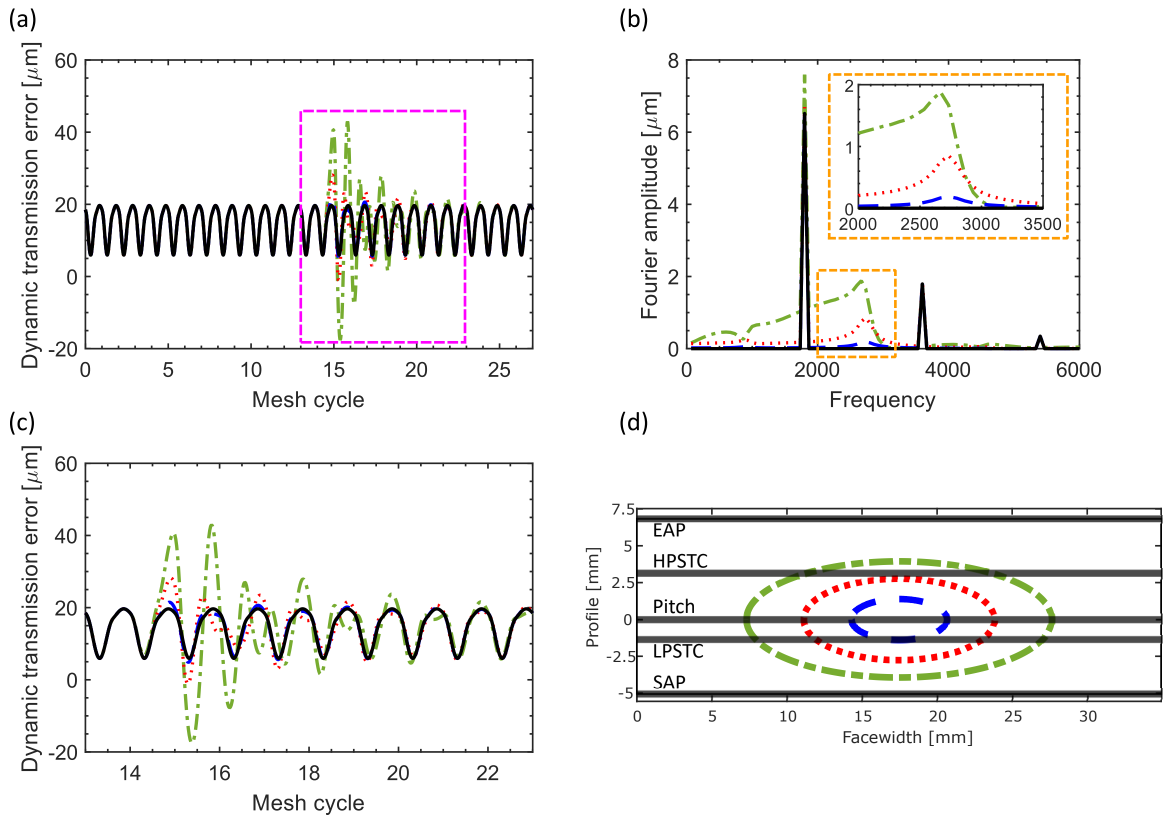

Figure 4.4: FE/CM calculation of (a) dynamic response and (b) frequency spectrum for the nonunity-ratio spur gear pair with tooth surface pitting damage on a single tooth of the pinion. The plot of dynamic response in (c) is a zoomed-in view of the region highlighted by the dashed (magenta) box on the left plot in (a). The inset figure in (b) shows a zoomed-in view of the frequency range from 2000 to 3500 Hz. (d) Active tooth surface profile of the pinion showing the location and amounts of the pitting damage analyzed. Solid (black) line is the dynamic response of the gear pair without damage. The dynamic response of gear pair with tooth surface pitting damage, as shown in (d), is represented by dashed (blue), dotted (red), and dash-dotted (green) lines. In (d) the horizontal lines represent the start of active profile (SAP), the lowest point of single tooth in contact (LPSTC), pitch, the highest point of single tooth in contact (HPSTC), and end of the active profile (EAP) of the pinion tooth profile.

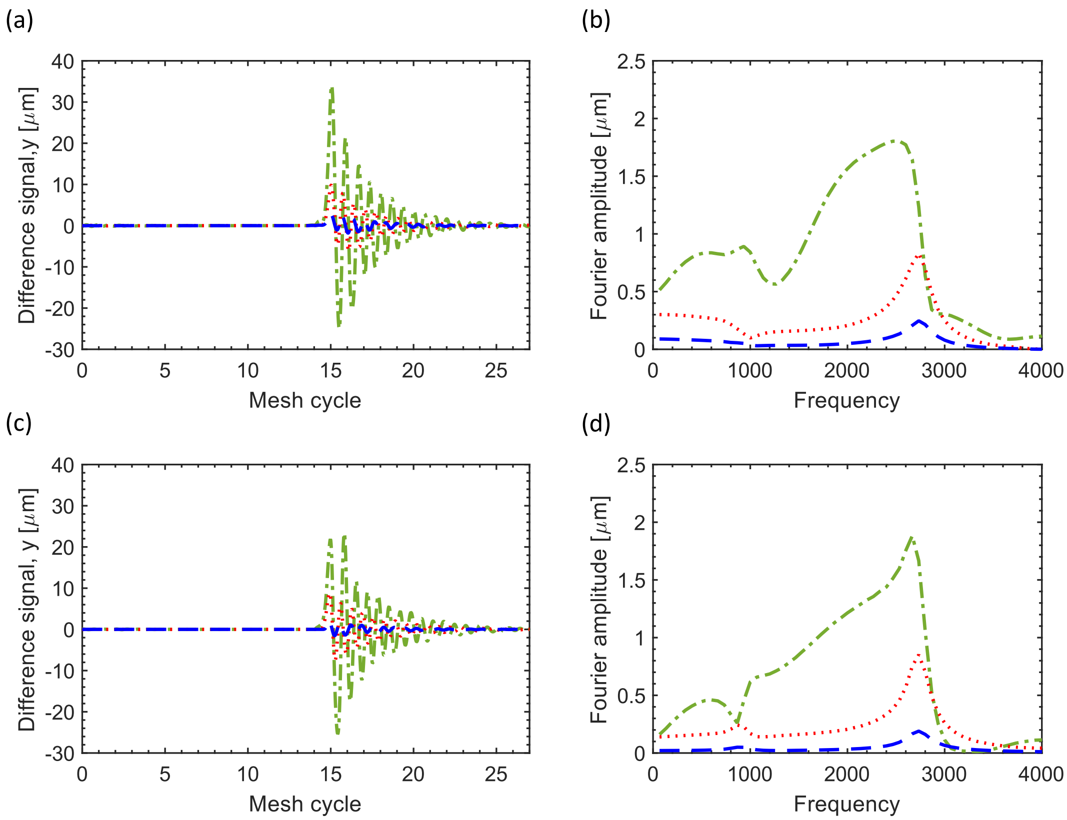

Figure 4.5: (a) Damage-induced dynamic response or exact difference signal and (b) its frequency spectrum of 20%, 50%, and 80% crack in the inset of Figure 4.3(b) shown in dashed (blue), dotted (red), and dash-dotted (green) lines. (c) Damage-induced dynamic response or exact difference signal and (d) frequency spectrum of pitting damage in Figure 4.4(b) shown in dashed (blue), dotted (red), and dash-dotted (green) lines.

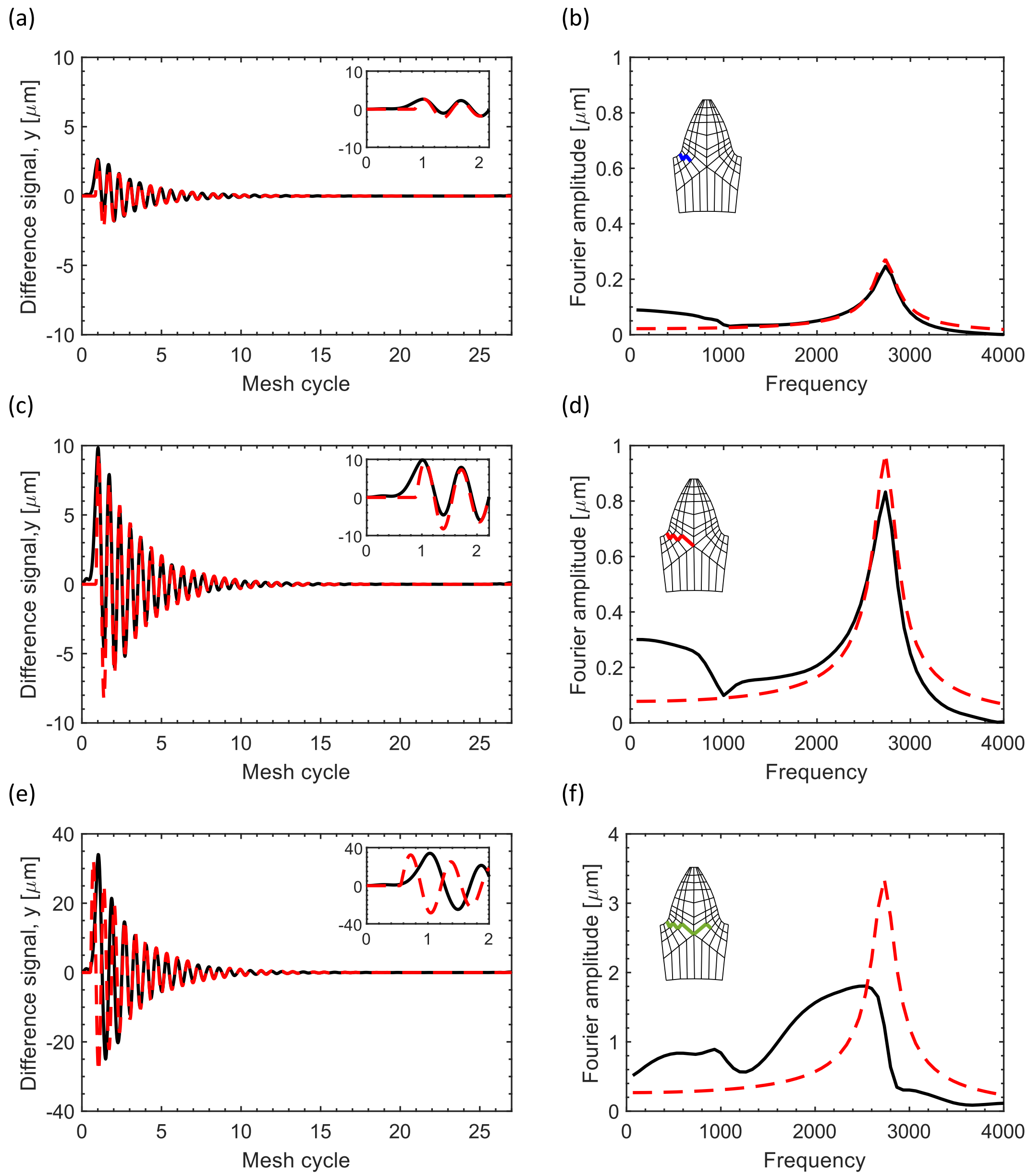

Figure 4.6: Comparison of the exact (solid (black) line) and approximate (dashed (red) line) difference signals over a pinion rotation. The tooth root crack lengths are (a,b) 20%, (c,d) 50%, and (e,f) 80%.

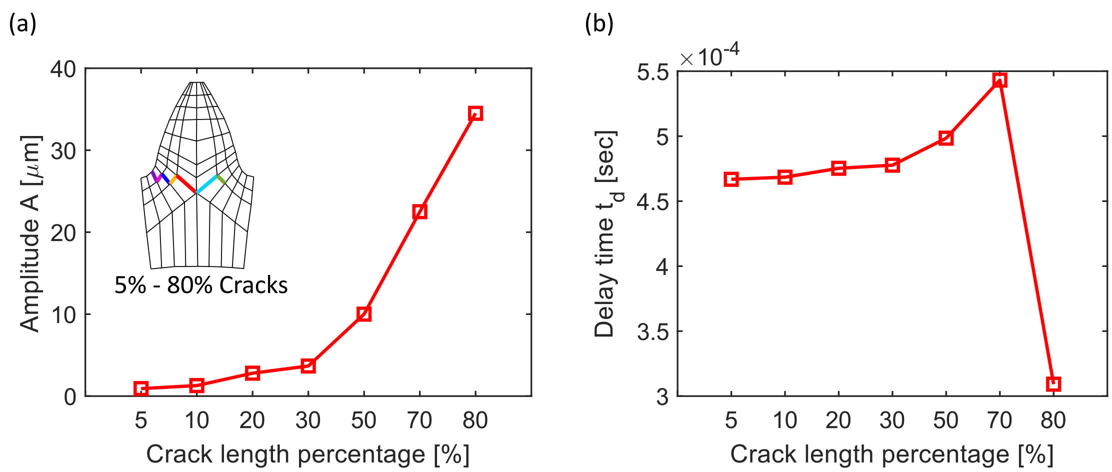

Figure 4.7: (a) Amplitudes and (b) time delay in the phenomenon-based model for the increasing amount of tooth root crack damage. The 5% to 80% tooth root crack lengths are shown in the inset figure of (a).

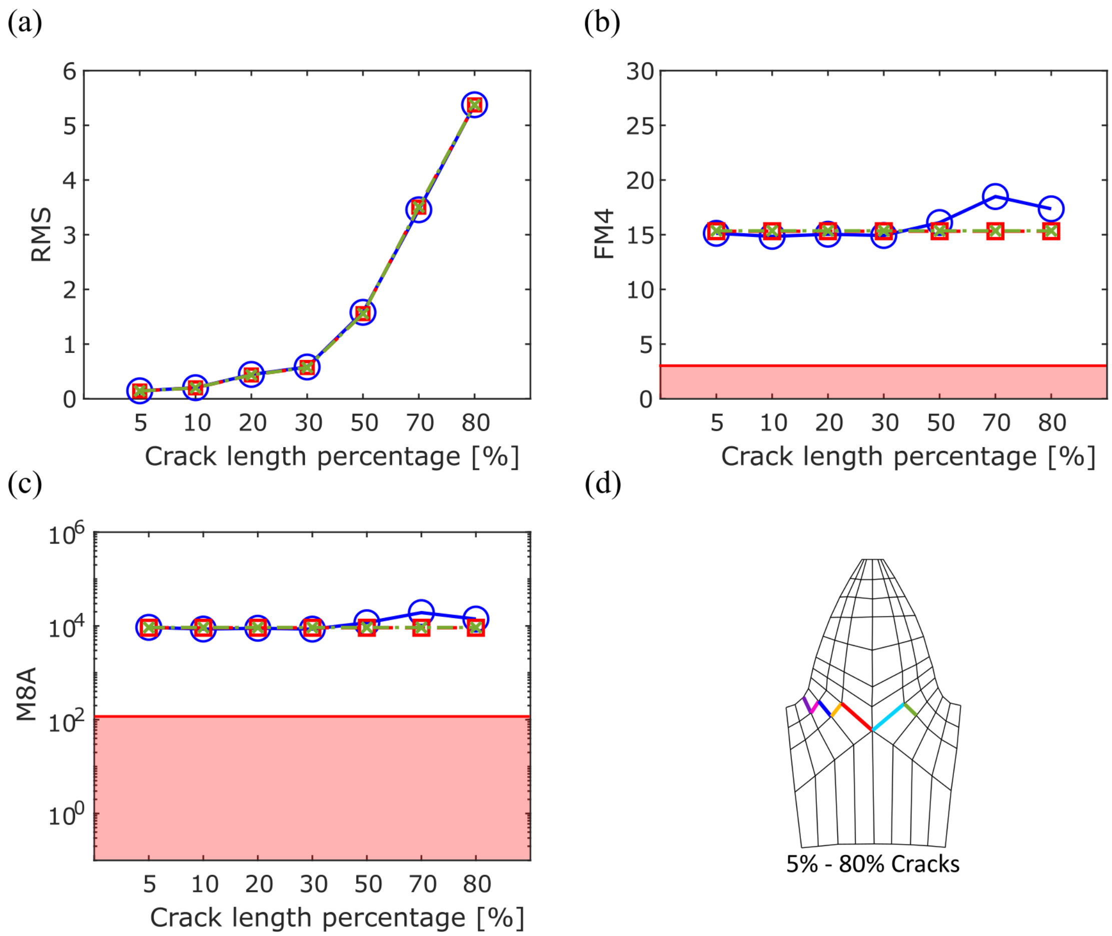

Figure 4.8: Calculation of condition indicators (a) RMS, (b) FM4, and (c) M8A for varying crack lengths shown in (d). The circle (blue) markers are from the FE/CM model. The square (red) markers are from the phenomenon-based model. The dot (green) markers are closed-form expressions for tooth crack lengths 5% to 80%.

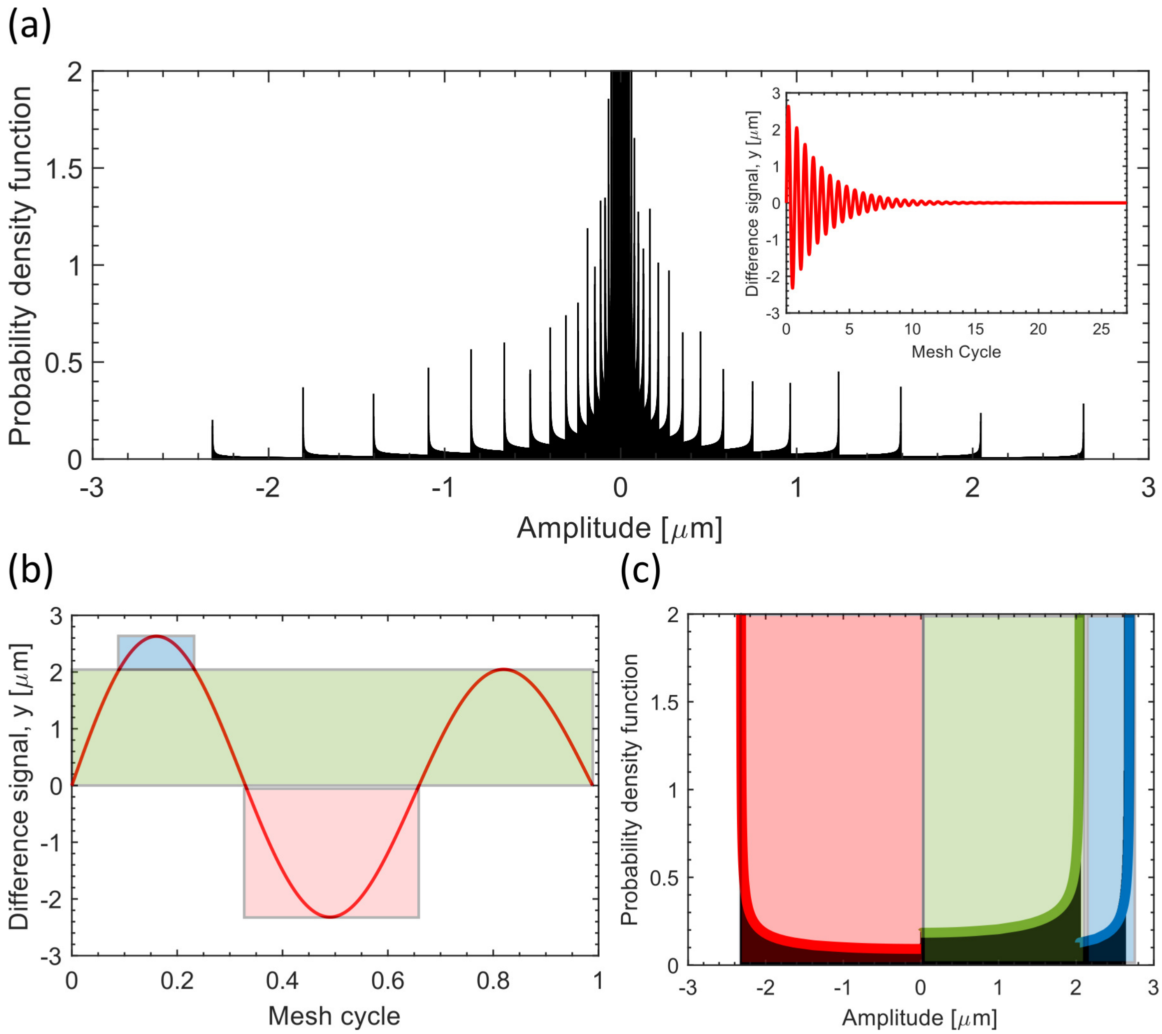

Figure 4.9: Damped sinusoidal signal with (a,b) two and (c,d) four half-sine oscillations and comparison of numerically determined probability density function (black bins) and analytically determined probability density functions (others). (e,f) Phenomenon-based model response of 20% crack and their probability density function.

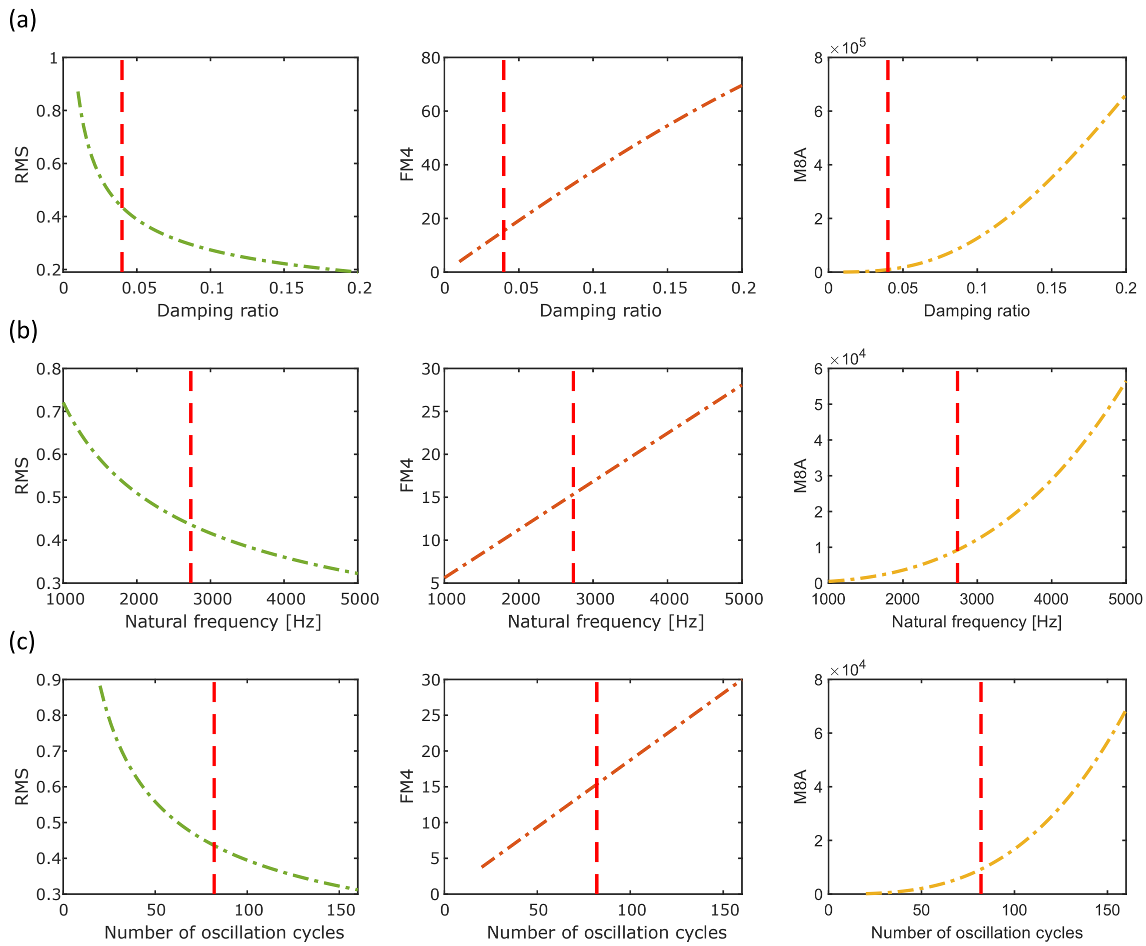

Figure 4.10: Condition indicators RMS, FM4, and M8A calculated for 20% crack length phenomenon-based model using the closed-form expressions in Eq. (4.14) for varying (a) damping ratio, (b) natural frequency and (c) number of half-sine oscillation cycles of the gear pair.

CHAPTER FIVE

DAMAGE-INDUCED DYNAMIC RESPONSE IN GEARED TRANSMISSIONS WITH APPLICATION TO SPACE-FIXED (RING) GEAR TOOTH DAMAGE DETECTION

5.1 Introduction

Geared transmissions are an important system in rotorcraft because they convert and direct all the engine's power to the rotors for lift, stability, and maneuver. Loss of power during flight poses mobility issues for rotorcraft vehicles and safety concerns for their occupants. Health and Usage Monitoring Systems (HUMS) are used in rotorcraft vehicles to monitor the performance of their transmissions and other critical components [5, 6]. Vibration measurements are one input used by these systems to detect damage. Further analyzing the characteristics of the vibration signatures generated by damage and quantifying their impact on detection could improve the performance of HUMS and improve rotorcraft vehicle readiness, reliability, and safety.

The detection of damage from the measured vibrations of transmissions has been a long-standing challenge for condition monitoring systems. Early work in gearbox diagnostic techniques is summarized by Stewart [97]. Randall [98] showed that changes in the vibration signatures of gearboxes could be used to detect faults. An early detection method for localized defects like gear tooth root cracks used amplitude and phase demodulation [99,100]. Since that work, a number of damage detection methods have appeared, including those that separate the vibrations in harmonic and residual errors [101], analyze features of the vibration in the frequency domain [102, 103] and incorporate time-frequency methods [104–109]. A number of other methods for detecting damage to gearboxes have been proposed, which can be found in the bibliographies of the review articles in Refs. [91, 92, 155–157].

Planetary gears are common elements in rotorcraft transmissions because they have high power capacity with small overall packaging. Because the planets kinematically rotate during operation, the location where the gear teeth come into contact, thus the path followed by the power transferred, varies in location. This gives rise to modulation-like vibrations measured by space-fixed sensors with unique spectral properties [110–116]. Seeking to eliminate path-dependent effects that cause modulation, McFadden [117, 118] constructed tooth meshing vibrations of the individual planets using a time domain averaging technique. Samuel and Pines [119] extended the synchronous averaging technique to use multiple sensors. This technique was further developed into the Vibration Separation Method for use in rotorcraft transmission diagnostics [4, 120, 121].

Like for transmissions with fixed-axis gears, a number of different damage detection techniques have been developed for planetary gear transmissions. Samuel and Pines [122] developed a diagnostic method based on the Constrained Adaptive Lifting (CAL) algorithm. Bartelmus and Zimroz [123, 124] developed a new diagnostic feature by calculating the linear dependence between spectral conditions and the operating condition for monitoring the gearbox health under varying external loads. Feng and Zuo [125] tracked spectral peaks at the faulty gear characteristic frequency in the Fourier spectrum enabling detection and locating damage in the planetary gearbox using a vibration signal considering both amplitude and frequency modulation. In addition to these, other fault detection techniques used for planetary gearboxes include wavelet neural network [126], those that use piezoelectric strain sensors [158], and torsional vibrational signal analysis [127]. A review of the fault detection techniques specific to rotorcraft transmissions can be found in Ref [5].

Several condition indicators have been developed to predict the occurrence of damage from the vibrations of gears. The performance of several condition indicators used in rotorcraft applications can be found in Refs. [59, 86, 87, 149], for example. Other relevant references for the analysis of condition indicators include [88–96]. The majority of these works evaluate the condition indicators using measured vibrations from experiments, where faults have been purposely placed on select components. We analyze the vibrations of a transmission using a finite element/contact mechanics (FE/CM) model that accurately captures the gear tooth mesh excitations accounting for the kinematic motion of the planets, changing contact conditions at the gear teeth, tooth bending and rim deformation, vibration, and damage.

In this research work, a FE/CM model of a rotorcraft transmission that contains an input spiral bevel stage, and output planetary stage, and their mechanical coupling (i.e., shafts, lumped-stiffness bearings, the carrier, and housing) is used to quantify the effects of damage on the vibrations generated on the housing. The experimental results of housing vibrations, when all gear teeth are healthy in the transmission, are used to validate the results of the FE/CM model used in this study. The characteristics of the resulting vibrations are identified for healthy transmissions without damage and the case of a localized tooth root crack on the ring. Different calculations of difference signals are explored to isolate the damaged vibrations from normal meshing vibrations of the planetary stage. The effect of tooth root crack size on condition indicator performance is examined for the FM4 condition indicator which is typically used in rotorcraft applications to detect the presence of damage.

5.2 Finite Element/Contact Mechanics (FE/CM) Model of Geared Transmission

This work uses the finite element/contact mechanics formulation developed by Vijayakar and co-workers [131, 139, 140]. This formulation takes advantage of the relatively small size of the contact region between mating gear teeth relative to the overall tooth's dimensions. Because of this, the displacement at any point within the gear tooth can be approximated as the superposition of a relative displacement near the gear tooth surface and an absolute displacement away from it. The relative displacements, which are due to the local deformations of the tooth surface due to contact, can be accurately approximated using classical solutions from elasticity theory for concentrated loads acting on an elastic half-space. The absolute displacements, which are due to tooth bending and structural deformations, are calculated using the finite element solution. These two solutions are paired at a matching interface that is sufficiently far from the tooth surface that the local contact deformations are negligible. By combining these two solutions, accurate displacements due to loading are obtained throughout the tooth, including near the tooth surface. The FE/CM method avoids the need for excessively refined finite element meshes immediately interior to the tooth surface. This saves computational effort and permits full finite element modeling of all gear teeth, blanks, shafts, and other elastic components. Importantly, this formulation allows time-domain dynamic response calculations, where the elastic contact between teeth is determined at each time step, without *a priori* assumptions of the nature of that contact, accounting for kinematic motion of the gears, tooth bending, structural deformations, and vibration. Further details of the methodology applied to gear dynamics studies can be found in Refs. [14, 132, 145]. The FE/CM method has been shown to accurately predict the experimentally-measured nonlinear dynamic response of unmodified [14] and modified [17] gear pairs using two-dimensional finite element models. The accuracy was shown to persist for three-dimensional models [132]. The FE/CM formulation was shown to accurately predict dynamic tooth root strains compared to experiments, even when large amplitude vibrations caused tooth contact loss [134]. The FE/CM method has also been shown to accurately predict ring tooth root stresses compared to experiments [133].

The FE/CM model of the rotorcraft transmission is shown in Figure 5.1(a). The transmission has two stages, which consist of an input spiral bevel stage that is connected to an output planetary stage. This two-stage reduction configuration is used to convert the high-speed and low-torque engine power to low-speed and high-torque power for driving the vehicle's main rotor. The transmission is analyzed at 219 kW, which corresponds to the typical power level that occurs at cruise conditions. The spiral bevel stage consists of a single mesh. The input pinion has 19 teeth and operates at 6060 rpm. The output gear has 71 teeth. The gears have 30 degree spiral angle. The shaft angle is 95 degrees. The transverse chordal tooth thickness of the pinion and gear are 6.24 mm and 3.36 mm, respectively. The pinon has a 30.48 mm facewidth with a 15.27 degree pitch angle. The gear has the same facewidth as the pinion and has a pitch angle of 79.73 degrees. The power from the spiral bevel gear is transferred to the sun of the planetary stage, which is shown in Figure 5.1(b). The ring, because it is attached to the housing, is stationary and does not rotate. The carrier is the output. The sun, planets, and ring are spur gears with 27, 35, and 99 teeth, respectively. Additional parameters for the planetary gear are shown in Table 5.1.

Table 5.1: Geometric parameters for the planetary gear stage of the rotorcraft transmission system.

Gear parameters	Sun	Planet	Ring
Number of teeth	27	35	99
Module (mm)		2.87	
Outer diameter (mm)	84.05	104.98	296.55
Inner diameter (mm)	62.23	77.9	271.75
Center distance (mm)		88.9	
Pressure angle (deg)	24.6	24.6	20.19
Facewidth (mm)	34.93	31.75	25.4

The FE/CM model includes accurate geometry of the housing, carrier, carrier shaft, spiral bevel gear shaft, and spiral bevel pinion shaft whose finite element meshes were developed from solid models of these components. The gear teeth of all the input and output stage gears of the rotorcraft transmission system were generated using standard finite element mesh templates using the actual gear geometry. The contact grid parameters

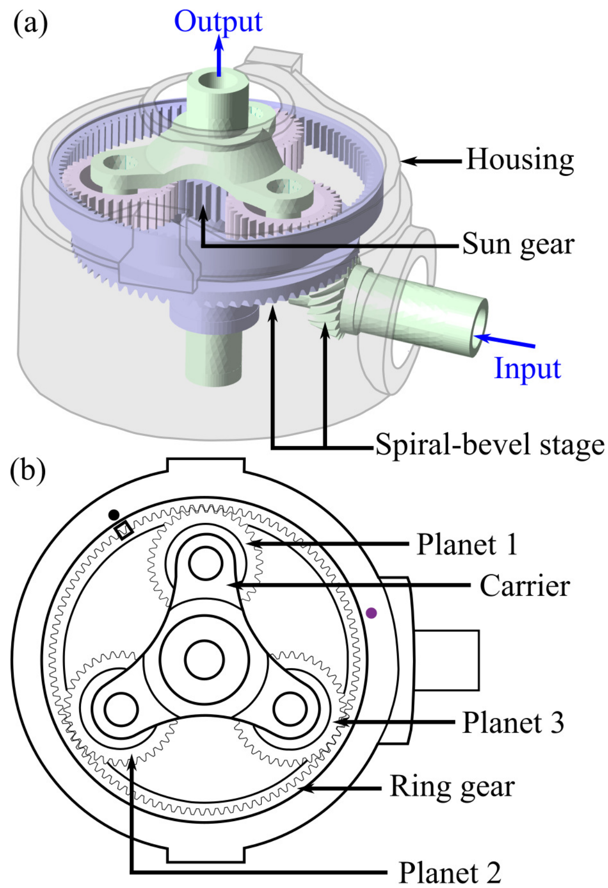

Figure 5.1: (a) Finite element/contact mechanics model of the rotorcraft transmission system with two stages: an input spiral-bevel stage and an output planetary stage and the housing of rotorcraft transmission shown in transparent to show the inner components of the transmission system. (b) The top view of the system shows the ring gear tooth (square marker) where the damage has been considered and the accelerometers (black and purple circle markers) locations measuring vibrations in the radial direction.

were selected at the sun-planet, planet-ring, and spiral bevel pairs so that the contact pressure distribution has the typical Hertzian form with sufficiently high resolution that the dynamic response is accurate but the resulting computational times are manageable. For computational efficiency, the spline between the ring gear and housing is not modeled. All bearing connections (i.e., the bearings between the housing and carrier shaft, spiral bevel pinion shaft and housing, spiral bevel gear/sun gear shaft and housing, and planets) are modeled using stiffness matrices with lumped-parameter elements. The vibrations generated at specific nodal locations on the housing near the planetary gear stage were analyzed. The nodal locations are shown in Figure 5.1(b). The nodal location shown in the purple circle marker is the same location used in experiments in Ref. [3]. This location is observed to be near the input stage of the geared transmission. The FE/CM model housing accelerations are validated against the experimental results at this location. The other nodal location shown in the black circle marker on the housing is considered near the damaged ring gear tooth. These locations represent the locations where accelerometers would be placed in HUMS.

This work focuses on tooth root crack damage on the ring. We assume the damage is localized to a single tooth. Figure 5.1(b) shows the location of the damaged tooth on the ring where the damage is applied. The tooth root crack is modeled by releasing the connectivity of select finite elements along a pre-selected crack path. The effect of crack initiation and crack path on the mesh stiffness of the gear pair is discussed in Ref. [67]. The effect of tooth surface pitting damage on mesh stiffness of gear pair in [137]. Wang et al. [68] and Cooley et al. [159] studied the effect of tooth root cracks on the dynamics of spur gear pair using FE/CM models.

Before analyzing the dynamic response of the transmission, we briefly present a kinematic analysis so that important components in the resulting vibration spectra can be identified. The input speed of the spiral bevel pinion is 6060 rpm. The speed of the spiral bevel gear is $\Omega_g = Z_p\Omega_p/Z_g = 1621.7$ rpm. The corresponding input spiral bevel stage mesh frequency is $f_{sb} = 1919$ Hz. The sun speed is the same as the spiral bevel gear because their corresponding shafts are connected by a spline. The sun frequency is 27 Hz. The ring is fixed and does not rotate so its speed is $\Omega_r = 0$ rpm. From planetary gear kinematics, the carrier rotates at $\Omega_c = Z_r\Omega_s/(Z_r+Z_s) = 347.5$ rpm (5.8 Hz). Using this result, the planet-pass speed is $\Omega_{pp} = N\Omega_c = 1,042.5$ rpm (17.375 Hz). The planetary gear mesh frequency is 573.4 Hz.

The FE/CM model is analyzed dynamically at operating torque and speed. The input spiral bevel pinion speed is specified to be 6060 rpm. The output carrier torque is 6106 N-m. Because our focus is primarily on damage to the ring and the planetary gear response that results, we chose to numerically calculate 50 steps over a planetary gear mesh period. This ensures accurate spectra calculations below 10 kHz. Based solely on kinematics, the system requires 105 rotations of the carrier to return to the configuration where the same tooth pairs are in contact. However, the given sun gear tooth will align with the given ring gear tooth for every three carrier rotations [121]. Because all teeth are identical, it was only necessary to dynamically analyze the system for three carrier rotations to obtain periodic vibrations from the housing. For the dynamic simulation, a region of transient response occurs prior to reaching the system's steady state. We found that running the system for one planet-pass cycle (i.e., one-third of a carrier rotation) was sufficient for all transients to diminish. The FE/CM model was analyzed for a total of ten planet-pass periods, which corresponded to 16,500 numerical time steps. The total simulation time was 129 hours using a conventional workstation computer with 64 GB RAM, 3.50 GHz processor, and SSD hard disk.

5.3 Dynamic Response

5.3.1 Healthy Transmissions without Damage

The FE/CM model of the transmission is dynamically analyzed at steady state to determine the housing accelerations when all gear teeth are healthy. The accelerations that are shown are normalized by gravity. The housing accelerations of the transmissions with all gears healthy and without damage are shown in Figure 5.2(a), which are taken from the purple accelerometer on the outer surface of the housing as shown in Figure 5.1(b).

The accelerations contain vibrations from both stages of the transmission, which results in noticeable non-periodicity over the carrier cycle period. It is not until three carrier cycles have occurred that the accelerations repeat (Figure 5.2(a). We have validated the periodicity of the vibrations shown in Figure 5.2(a) numerically by analyzing four carrier cycles (not shown). A planet passes the location where vibrations are measured at carrier cycle 0.092 and every one-third of a carrier cycle after that. The accelerations in Figure 5.2(a) show the characteristic variations in amplitude as the planets move kinematically relative to the location where vibrations are measured. Hood [3] conducted experiments on the geared transmission shown in Figure 5.1. The healthy transmission housing accelerations determined from the experiments at the accelerometer (purple circle marker in Figure 5.1(b)) in Ref. [3] are shown in Figure 5.2(b). The accelerations predicted by the FE/CM model have features similar to those seen in the experiments. Comparing the experimental results and the FE/CM model results, differences are observed in the amplitudes are observed. The mean square error calculated between the two results is 139.

The spectrum of the baseline accelerations in Figure 5.2(a) are shown in Figure 5.3(a). The spectrum has clusters of frequency content near planetary gear mesh frequency and spiral bevel gear mesh frequency harmonics. Each cluster near planetary gear harmonics contains upper and lower sideband components (solid (purple) line in Figure 5.3(c,d)). The sidebands near planetary gear harmonics occur at multiples of the planet-pass frequency $f_{pp} = 17.375$ Hz. The sideband amplitudes are noticeably asymmetric. The clusters near higher planetary gear mesh frequency harmonics are similar to that shown in Figure 5.3(c,d). The spectrum (not shown) near the harmonic of the spiral bevel gear frequency $f_{sb} = 1919$ Hz have sideband frequencies occurring at the planet-pass frequency, similar to those near the planetary gear mesh frequency. The amplitudes of the clusters of planetary gear mesh frequency and spiral bevel mesh frequency are meaningful even at high frequencies near

(a)

(b)

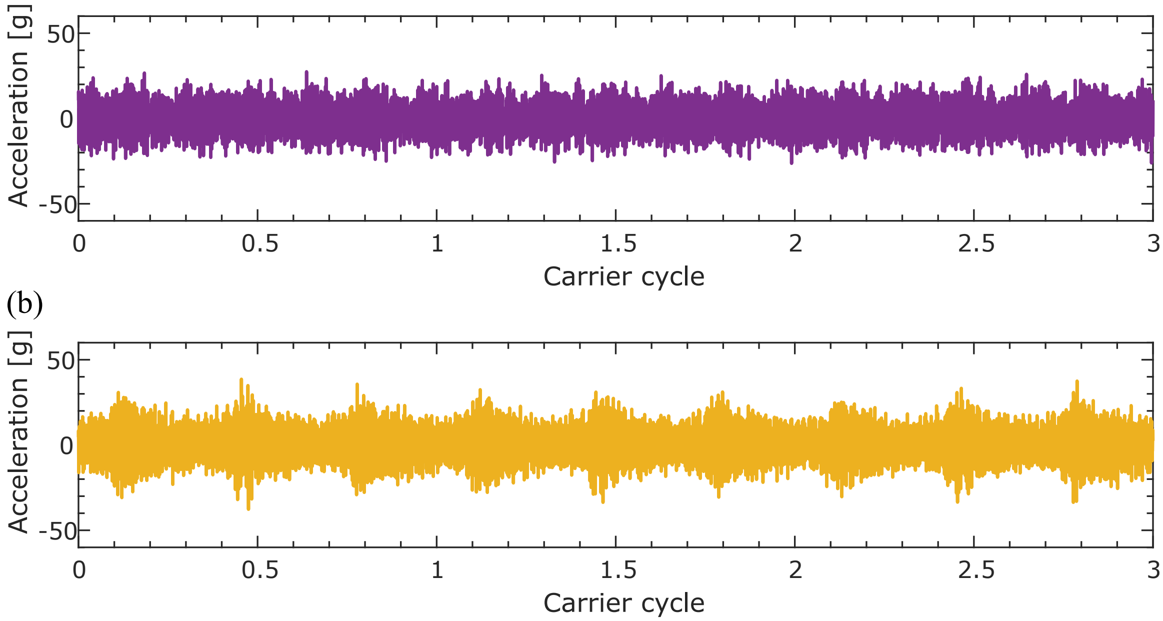

Figure 5.2: Housing accelerations of transmission without damage determined (a) using FE/CM calculation and (b) experimentally at accelerometer (purple circle marker) shown in Figure 5.1(b).

10 kHz. The maximum amplitude seen in the spectrum is 3.56 g, which occurs at 1884 Hz near the first harmonic of spiral bevel mesh frequency. The frequency spectrum of the housing accelerations of healthy transmission determined from experiments in Figure 5.2(b) is shown in Figure 5.3(b). The FE/CM model (solid (purple) line) shows higher amplitudes at the first harmonic of mesh frequency in the first harmonic planetary stage mesh frequency cluster when compared to the experimental results (solid (yellow) line) which can be seen in Figure 5.3(c). The experimental results show sidebands at the carrier frequency, which the FE/CM model does not predict. However, the amplitudes of sidebands occurring at planet-pass are accurately captured by the FE/CM model. Similar characteristics are observed at the planetary stage mesh frequency second harmonic cluster shown in Figure 5.3 (d). The FE/CM model predicted a lower amplitude of the spiral-bevel stage mesh frequency component when compared to the experimental results. The difference between

the FE/CM model and the experiments is expected due to differences in some cast parts with intricate geometry, lubrication, estimation of bearing stiffnesses and damping in the geared transmission. However, the FE/CM model captures the overall characteristics of the acceleration signals when compared to the experimental results. The FE/CM model is used to determine the healthy transmission and damaged transmission housing accelerations at the accelerometer (black circle marker) shown in Figure 5.1(b) and the performance of condition indicators to detect the presence of damage in the geared transmission is analyzed.

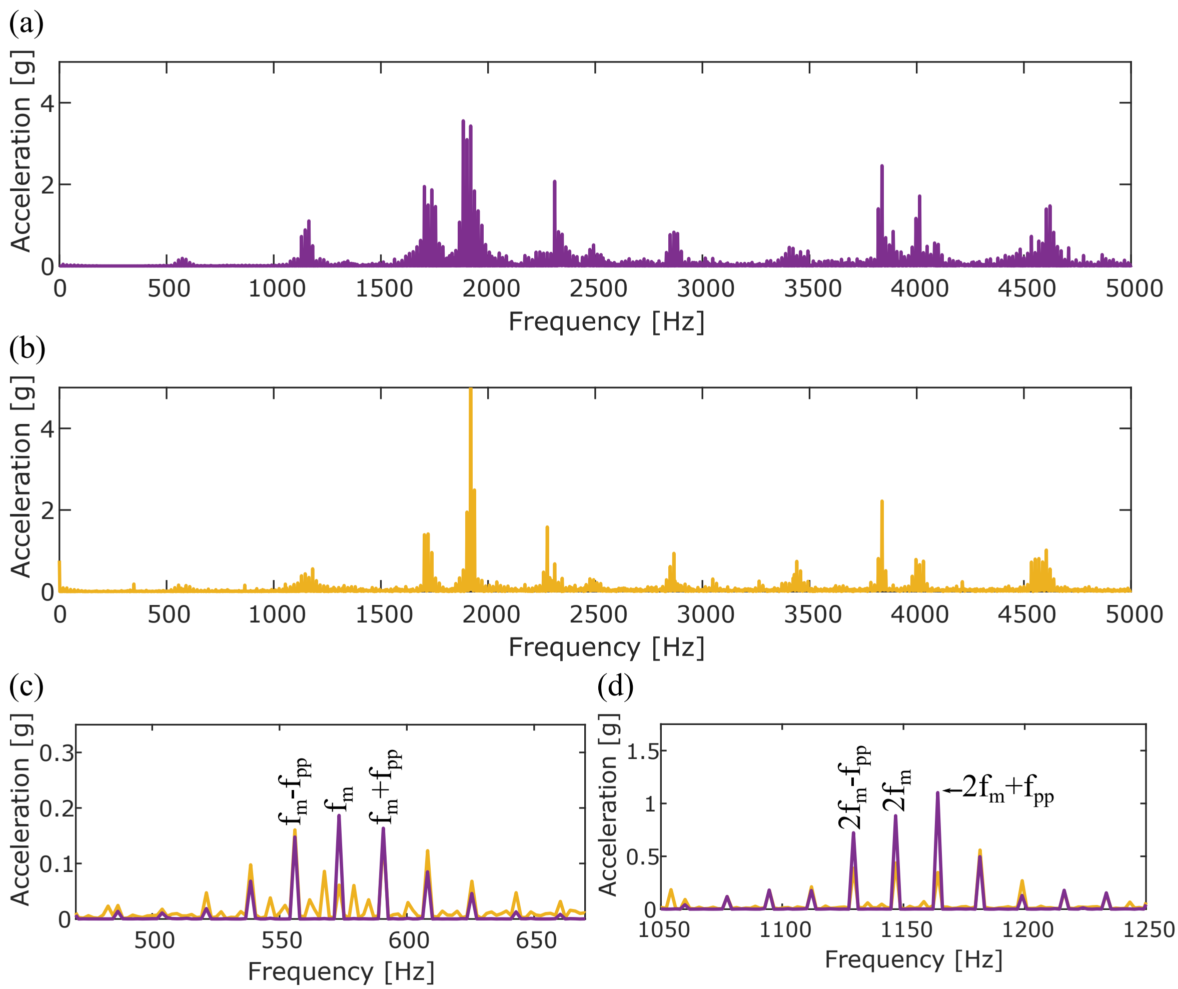

Figure 5.3: (a,b) Frequency spectrum of housing accelerations in Figure 5.2. The comparison of frequency spectrum clusters at (c) first and (d) second harmonics of the planetary gear mesh frequency.

The healthy transmission housing accelerations and their frequency spectrum are shown in Figure 5.4 which are measured from an accelerometer (black circle marker in Figure 5.1(b)) placed near the damaged ring tooth on the outer surface of the housing. The accelerations and frequency spectrum at the measured location near to damaged ring tooth are observed to follow the same characteristics as results at the location near the input port. However, the maximum amplitude in the spectrum is observed to be 4.7 g at 3838 Hz, which is near the second harmonic of the spiral-bevel stage mesh frequency.

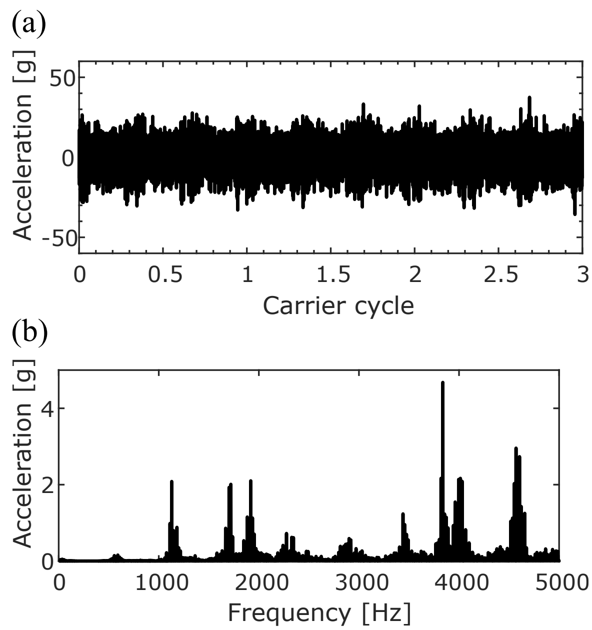

Figure 5.4: (a) FE/CM calculation of housing accelerations for three carrier rotations of geared transmission without damage. (b) The frequency spectrum of healthy transmission housing accelerations.

5.3.2 Damaged Transmissions

The tooth root crack damage on a single tooth of space-fixed or stationary or ring gear is introduced into the FE/CM model of the geared transmissions at the location shown in Figure 5.1(b). Three different tooth root crack lengths are analyzed to quantify the effects of varying severity of damage. Crack lengths are 20 percent, 50 percent, and 80 percent of the ring tooth thickness. The finite element meshes of the ring tooth with different crack lengths are shown in Figure 5.5(e). The housing accelerations of geared transmission with ring crack damage are shown in Figure 5.5(a). The planets engage with the damaged ring tooth once during a planet-pass cycle. This engagement is characterized by a localized increase in the housing accelerations immediately above 0.1 carrier cycle (Figure 5.5(b, c, and d)). Following a planet's engagement with the damaged ring tooth, a region of transient response occurs that diminishes prior to the engagement of the next planet. A total of nine engagements of a planet with the damaged ring tooth are observed in three carrier rotations of the transmission. The transient, damage-induced vibrations for tooth root cracks less than 50 percent of the tooth thickness are not substantially larger than the baseline vibrations of the transmission without damage (Figure 5.5(b,c).

The acceleration spectrum for transmissions with ring tooth root crack damage (not shown) generally has increased amplitudes, although the amount that the components increase may not be substantial. The changes in the spectrum due to tooth root crack damage are not significant. The changes in amplitude of the first five harmonics of planetary gear mesh frequency in the spectrum for varying tooth root crack lengths are observed to be almost constant, even for the larger crack lengths (Ref. [160]). The significance of damage on the amplitudes of the sidebands of the planetary stage mesh frequency clusters is also expected to remain constant. Because of the relatively small changes, it would be difficult to detect damage in the transmission based on changes to the amplitudes of planetary gear mesh frequency alone.

The vibration waveforms from other locations on the housing, but still located near the mid-face of the planetary stage, differ meaningfully in shape and peak amplitude from those shown in Figure 5.4(a) (not shown). This is likely due to the non-axisymmetric features

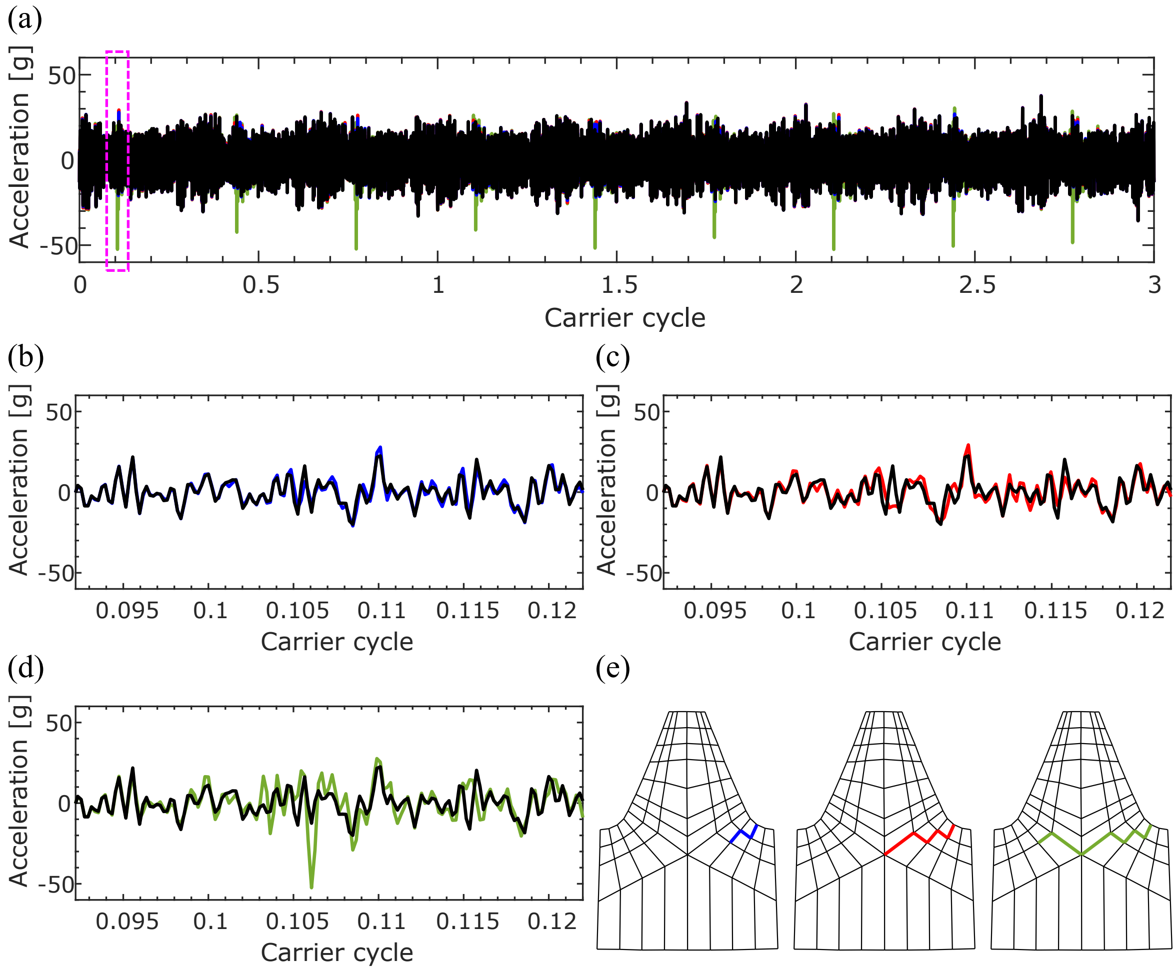

Figure 5.5: (a) FE/CM calculation of housing accelerations for three carrier rotations of damaged transmission compared to the healthy accelerations. The first engagement of the damaged ring tooth in the first planet-pass period is shown using the dashed (magenta) box. The damaged transmission accelerations near the first damaged tooth engagement with (b) 20 percent, (c) 50 percent, and (d) 80 percent root crack lengths on the ring tooth are compared to the healthy accelerations. The healthy vibrations without damage are shown by a black line. The vibrations when the ring tooth has a root crack with 20, 50, and 80 percent of the tooth thickness are shown by blue, red, and green lines, respectively. (d) Finite element meshes of the ring tooth with root crack damage. The tooth root crack lengths are 20 percent (blue), 50 percent (red), and 80 percent (green) of the ring tooth thickness.

of the housing, including the location of the two supports, the input port, and internal rib features used for stiffening (see Figure 5.1). The spectral characteristics of these vibration waveforms are similar to those shown in Figure 5.4(b), however.

5.4 Damage Detection

Health and Usage Monitoring Systems (HUMS) for geared transmissions monitor the condition of gears using values of condition indicators calculated from the vibration signals [5]. Condition indicators are generally based on statistical features of vibration signals, which are assumed to change in the presence of damage. In this work, the vibrations are evaluated using the FM4 condition indicator to detect the presence of damage in the geared transmission. The performance of other condition indicators that are typically used for geared transmissions is discussed in detail in Appendix A. The evaluation of the FM4 condition indicator requires difference signal accelerations as its input. The processing of the difference signal requires a time synchronous averaged (TSA) signal. Time synchronous averaging (TSA) is a technique used to separate a known vibration signal from noise and other nonsynchronous components [161, 162]. TSA is used to isolate the vibrations generated by the planetary from those generated by the input spiral-bevel stage. Analyzing the vibrations of the planetary stage alone, it is expected that damage will be better detected than if additional vibration components from the input stage are included. TSA is possible from any one of the three fundamental periods in the planetary stage: the mesh period, the planet-pass period, and the carrier period. TSA using the planetary gear mesh period inherently removes the majority of effects that damage has on the resulting vibration (not shown). Its use is not recommended. In this work, the TSA over planet-pass period accelerations is analyzed (Appendix A shows the condition indicators calculated using either of the TSA signals results in very similar values). The housing accelerations in Figure 5.5 are partitioned into nine blocks and averaged to derive the TSA over planet-pass cycle accelerations (not shown). The difference signals for evaluating the FM4 condition indicator are calculated using exact and approximate methods.

5.4.1 Difference Signal - Exact Calculation

The exact difference signal also known as the damage-induced dynamic response of the geared transmission is defined as the signal that contains accelerations purely due to damage. The exact difference signal ($d(t) = x_d(t) - x(t)$) is calculated by removing the healthy accelerations ($x(t)$) from damaged accelerations ($x_d(t)$). The exact difference signal for TSA over the planet-pass period is calculated by determining the difference between damaged transmission and healthy transmission TSA over planet-pass accelerations. Figure 5.6(a) shows the exact difference signal or the damage-induced dynamic response accelerations of the damaged transmission with varying amounts of damage. The exact difference signal is dependent on the healthy transmission accelerations. There is no exact difference signal for healthy transmission, as the difference will lead to zero accelerations. The exact difference signal amplitudes tends to increase with the increase in the damage severity. The accelerations in the exact difference signal are observed to be almost zero for the 0 to 0.096 carrier cycle (the time till the planet comes into contact with the damaged tooth on the ring) and 0.158 to 0.333 carrier cycle (the time after the transients due to damaged tooth are reduced). The transient vibrations begin at 0.096 of a carrier cycle. Since one complete carrier cycle corresponds to a 360 degree angle, the angle for 0.096 of a carrier cycle is approximately 34.56 degrees. The angle of the center of the damaged ring tooth shown in Figure 5.1(b) is 35.6 degrees. It is observed that the calculated angle of 34.56 degrees provides an estimate of the damaged tooth location. However, this transmission has a planetary system with three planets and at the same time of 0.096 carrier cycle, the damaged tooth can be in-mesh with either of the three planets. Based on this, the damaged tooth location can be estimated to be 34.56, 154.56, or 274.56 degrees.

The frequency spectrum of the exact difference signal or damaged-induced dynamic response is shown in Figure 5.6(b). The amplitudes in the frequency spectrum are observed to increase with the increase in the crack lengths. It is observed that the spectrum of the exact difference signal of the spur gear pair with localized defects contains amplitudes at the natural frequency of the gear pair. Based on this, the frequency spectrum of the exact difference signal of the damaged geared transmission is expected to contain different natural frequencies of the different components of the geared transmission. According to Lin and Parker [163], the planetary stage of the geared transmission in Figure 5.1 has four rotational modes and four translational modes, with natural frequencies that range below 5000 Hz. Other than the modes of the planetary stage, the housing of the geared transmission is also expected to have natural frequencies in the range of interest. For the 80 percent crack length (solid (green) line), the peaks can be observed to be for the broader range of frequencies which is the result of prominent nonlinearity. It is observed the amplitudes at the natural frequencies are sensitive to the amount of damage in the geared transmission. For the 80 percent crack length (solid (green) line), the peaks can be observed to be for the broader range of frequencies which is the result of prominent nonlinearity. The exact difference signal spectrum shows content at all harmonics of the planetary stage mesh frequency and their sidebands, in contrast to the approximate difference signal spectrum discussed in the next section.

5.4.2 Difference Signal - Approximate Calculation

The mesh frequency components and their sidebands in the housing accelerations are largely insensitive to damage (Ref. [160]), it has been proposed to create a modified acceleration signal with these components removed [97]. The amplitudes of planetary stage mesh frequency and its first-order upper and lower sidebands at all harmonics in the spectrum of the TSA over planet-pass signal are removed to generate the difference signal spectrum. The time-domain signal, which is the approximate difference signal is derived from the

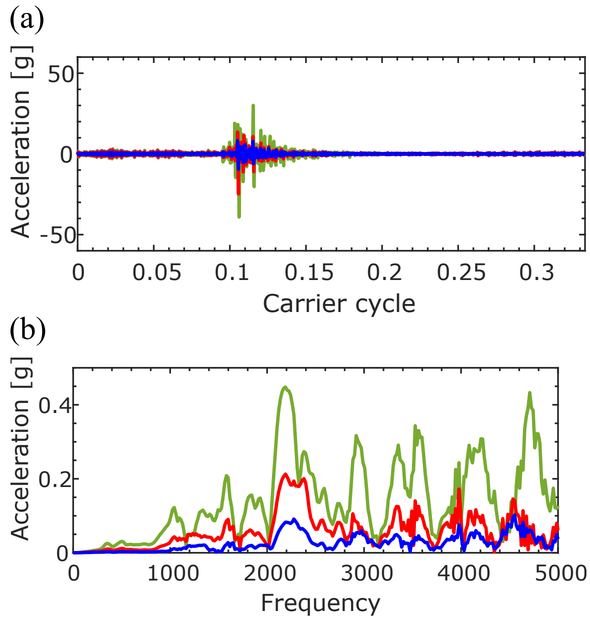

Figure 5.6: (a) Damage-induced dynamic response or the exact difference signal of TSA over planet-pass accelerations for the geared transmission and (b) their frequency spectrum. The vibrations when the ring tooth has a root crack with 20, 50, and 80 percent of the tooth thickness are shown by blue, red, and green lines, respectively.

inverse Fourier transform of the spectrum with the components removed. The approximate difference signal, denoted as $d^{(1)}(t)$, would contain predominantly the vibrations caused by damage without the usual vibrations generated by the normal meshing of the gears. The approximate difference signal of the geared transmission, when all gear teeth are healthy and with varying amounts of ring crack damage at the measured location, is shown in Figure 5.7. The approximate difference signals are derived using one measurement/simulation, without the dependence of other transmission accelerations. The engagement of damaged tooth location in the planet-pass period is shown using the dashed (magenta) box in Figure 5.7(a) and the healthy approximate difference signal is compared to the damaged approximate difference signal with varying amounts are shown in Figure 5.7(b, c, and d) The approximate difference signals for crack lengths less than 50 percent do not show significant differences when compared to healthy transmission (Figure 5.7(b,c)). It has been observed that removing content from the frequency spectrum plot and calculating the approximate difference signal accelerations using the inverse Fourier transform generates new steady-state vibrations. As a result, it is challenging to isolate the vibrations caused by the damage from the normal meshing vibrations in the approximate difference signal, at the engagement of the damaged tooth especially for lower amounts of damage.

5.4.3 Condition Indicators - FM4

The FM4 condition indicator is evaluated to analyze the performance of the different difference signal calculations. The Figure of Merit (FM4) is calculated from [97]

$$\text{FM4} = \frac{N\sum_{i=1}^{N}(d_i - \bar{d})^4}{[\sum_{i=1}^{N}(d_i - \bar{d})^2]^2} \tag{5.1}$$

where $d_i = d(t_i)$, $i = 1, 2, \ldots, N$ is the exact difference signal at time t_i and $\bar{d}$ is the mean of the exact difference signal. The FM4 of the approximate difference signal is evaluated using the same equation Eq. (5.1). The nominal value of FM4 for Gaussian noise is three. We consider cases where the damage causes the FM4 values to exceed three as detectable. Conversely, damage that results in FM4 values below three would not be detectable. FM4 has been shown to work well for identifying localized damage to a small number of teeth [97]. The FM4 condition indicator values for exact difference and approximate difference signals are calculated for healthy and damaged transmissions and tabulated in Table 5.2.

Table 5.2: Calculation of FM4 condition indicator for approximate and exact difference signals.

Cases	Approximate	Exact
Healthy	2.97	
20%	3.00	46.25
50%	2.94	74.06
80%	5.98	60.58

The FM4 values of approximate difference signal change modestly for tooth root crack lengths less than 50 percent of the tooth thickness. Detection of these damages would likely be difficult. A substantial increase in FM4 values of approximate difference signal occurs at 80 percent crack length, where the value of the indicator is nearly six and this damage level is meaningfully above the threshold of three and would likely be detectable. FM4 values calculated using exact difference signal are an order of magnitude higher than the FM4 value of 3 and truly detect the presence of damage in the transmission, even for the smaller crack lengths less than 50 percent of the ring tooth thickness.

The approximate difference signal is constructed by removing only the planetary gear mesh frequency components and their first-order sidebands. Normal vibrations produced by the planetary gear have multiple sideband orders. The higher-order sideband amplitudes are observed to show no significance to their amplitudes due to damage. It is expected that the removal of higher sideband orders will further differentiate the vibrations associated with damage from the normal meshing vibrations present in healthy transmissions without damage. The approximate difference signal with k sideband orders removed is denoted by $d^{(k)}(t)$. The FM4 condition indicator is calculated using the approximate difference signals $d^{(0)}(t)$ to $d^{(5)}(t)$ as its input for healthy transmission and ring crack damaged transmission. Figure 5.8(c) shows the FM4 values for different numbers of sidebands removed from the approximate difference signal. As the number of sidebands that are removed increases toward the fourth order, the FM4 value increases for all crack lengths shown, which suggests an improved ability to detect damage. For three and higher-order sidebands removed from the difference signal, noticeable differences in FM4 occur for the 50 percent crack length. The reason for this is that approximate difference signal, corresponding to 50 percent crack length, can be distinguished from those of a healthy condition. This observation is illustrated in Figure 5.8(a,b), which displays the approximate difference signals $d^{(3)}(t)$ and $d^{(5)}(t)$.

The 80 percent crack length shows substantial increases when higher-order sidebands are removed. We note the increases associated with the 20 percent crack length are modest. This small crack length may still be difficult to detect, even with the changes to the construction of the approximate difference signal.

5.5 Parametric Studies

5.5.1 Sensitivity to Measurement Location

The sensitivity of the FM4 condition indicator for varying the damage severity and using different difference signal calculations are analyzed at an accelerometer placed very next to the damaged tooth location as shown in Figure 5.1(b), which is an ideal case. To evaluate the performance of the FM4 condition indicator for damage detection at various locations on the housing of the geared transmission, an accelerometer has been added on the housing for each tooth of the ring gear, except in the areas near the supports. A total of 85 accelerometers are placed on the housing circumference at the planetary stage level and measure the housing radial vibrations when the geared transmission model is dynamically analyzed for steady-state response in the FE/CM. Radial accelerations in housing are determined for healthy transmission and for transmissions with 20, 50, and 80 percent ring crack damage. TSA over planet-pass accelerations are generated and used to derive both approximate and exact difference signals at all accelerometer locations. The natural logarithmic values of the FM4 condition indicator are evaluated for both approximate and exact difference signals and overlaid onto the housing using a polar plot. The polar plots overlaid on the housing for varying amounts of damage are shown in Figure 5.9.

The FM4 condition indicator calculated using the approximate difference signal can be seen to be very near the threshold value. However, the FM4 values calculated using the exact difference signal exhibit considerable deviation from the threshold value, even for smaller crack lengths. The FM4 values using different difference signals do not show monotonic increase with the increase in the damage amount at most of the accelerometer locations. The minimum FM4 values calculated using the exact difference signal for 20, 50, and 80 percent ring crack damaged transmission are 14.03, 10.89, and 14.85 observed at 344.7, 93.8, and 344.7 degrees of the housing respectively. This indicates that at all accelerometer locations, the FM4 condition indicator values of the exact difference signal are above the threshold value of 3 and the damage can be detected, even for the smaller crack lengths. The calculation of the FM4 condition indicator using the exact difference signal accelerations successfully detected damage, even for smaller crack lengths, across all accelerometer locations. This indicates that placing one accelerometer on the housing of the planetary stage is the optimum option. However, accelerometers are not only used for damage detection of the tooth, they are also used for condition monitoring of the gear tooth, so having more than one accelerometer is recommended.

5.5.2 Sensitivity to Damage Tooth Location

The results for varying damage severity and varying accelerometer locations for constant damage location are analyzed in the previous sections. In this section, the sensitivity of ring crack damaged tooth location is studied. In the FE/CM model of the geared transmission, the angle of the center of the damaged tooth is provided to generate the model with the cracked tooth at the specified location. Figure 5.10(a) and (b) shows the comparison of natural logarithmic values of FM4 polar plots using exact difference signal, calculated at accelerometers placed around the housing for 20 percent and 50 percent crack lengths, considering damage individually at 35.6 degrees, 155.6 degrees, and 275.6 degrees and overlaid on the housing. The analyzed damaged tooth locations are spaced 120 degrees apart, corresponding to the planet separation angle in the geared transmission. In Figure

5.10(a), the FM4 polar plots for a 20 percent crack length show a minimum FM4 value of 10.80, which exceeds the threshold and provides clear indication of damage in the geared transmission. The damage at the 35.6 degree location demonstrates a clear increase in the FM4 values near the affected tooth. Conversely, while the FM4 values for the damaged teeth at 155.6 degrees and 275.6 degrees also increased, they did not rise to the same level as those at 35.6 degrees. The FM4 polar plots comparison for 50 percent crack length showed increases in their FM4 values in the vicinity of the damaged tooth location. The exact difference signal accelerations are not the same for the cracks considered at distinct locations around the housing.

5.6 Conclusions

The vibrations of a geared transmission are analyzed using a finite element/contact mechanics (FE/CM) approach that includes accurate representation of the changing contact forces on the gear teeth, multiple reduction stages with different gear types, mechanical coupling between stages, and damage. Accelerations from the housing are calculated for cases where the transmission is healthy and without damage and when a single ring tooth has a root crack. The effect of increasing damage severity is analyzed using root cracks of varying lengths. Tooth root cracks with 20 percent, 50 percent, and 80 percent length of the ring tooth thickness are considered.

The housing accelerations contain dynamics from both the spiral-bevel stage and the planetary stage. The accelerations exhibit distinct variations in amplitude as the planets move relative to the measurement location. The acceleration spectrum contains frequency content that appears in clusters near the planetary gear mesh frequency and spiral-bevel mesh frequency harmonics. Planetary gear mesh frequency clusters feature upper and lower sidebands that occur at multiples of the planet-pass frequency. The housing accelerations when all gear teeth are healthy and without damage from the FE/CM model of the geared transmission are validated with results from the experiments measured at the same location on the housing. Differences in amplitudes are observed in the accelerations and frequency spectrum, however, the overall characteristics of the housing vibrations for geared transmission are captured. Planet engages the damaged ring tooth once in the planet-pass period and the accelerations exhibit transient behavior with the engagement. Changes to the acceleration do not clearly indicate damage to the transmission. The frequency components near planetary gear mesh frequency harmonics and sidebands are not sensitive to damage, even when the damage is large. Detecting damage from changes in the amplitudes of these components would be difficult.

The condition indicator FM4 is used to assess the presence of damage in the geared transmission. The characteristics of the exact and approximate difference signal accelerations and frequency spectrum are determined. The accelerations and amplitudes in the spectrum are increased with the increase in the damage amount and the exact difference signal spectrum contains several natural frequencies of the geared transmission. The removal of mesh frequency and its first-order sidebands from the frequency content of the approximate difference signal generated steady-state vibrations, making it difficult to isolate damaged vibrations from healthy ones. The FM4 condition indicator calculated using the approximate difference was able to detect 80 percent crack length, a higher crack length. However, the FM4 values for crack lengths less than 50 percent are very similar to the FM4 value of transmission without damage. FM4 calculated using the exact difference signal showed significantly higher values compared to the FM4 values calculated using the approximate difference signal, indicating the presence of damage even for the smaller crack lengths. Removal of the higher number of sidebands in the derivation of the approximate difference signal improved the 50 percent crack FM4 values but not to the extent of the 80 percent crack FM4 values.

The sensitivity of the FM4 calculated with the exact difference signal accelerations detected the smaller crack lengths damage in the geared transmission when the accelerometers are placed around the housing circumference at the planetary stage. The sensitivity of damaged tooth location is analyzed by evaluating FM4 for various damage tooth locations on the ring gear. It was observed that the exact difference signal accelerations are different for different damage tooth locations and results in different FM4 values. The presence of damage is detected for all the damaged tooth locations analyzed in this study. This research work is carried out to further the development of damage detection in Health and Usage Monitoring Systems (HUMS) and be able to detect damage in its early stage.

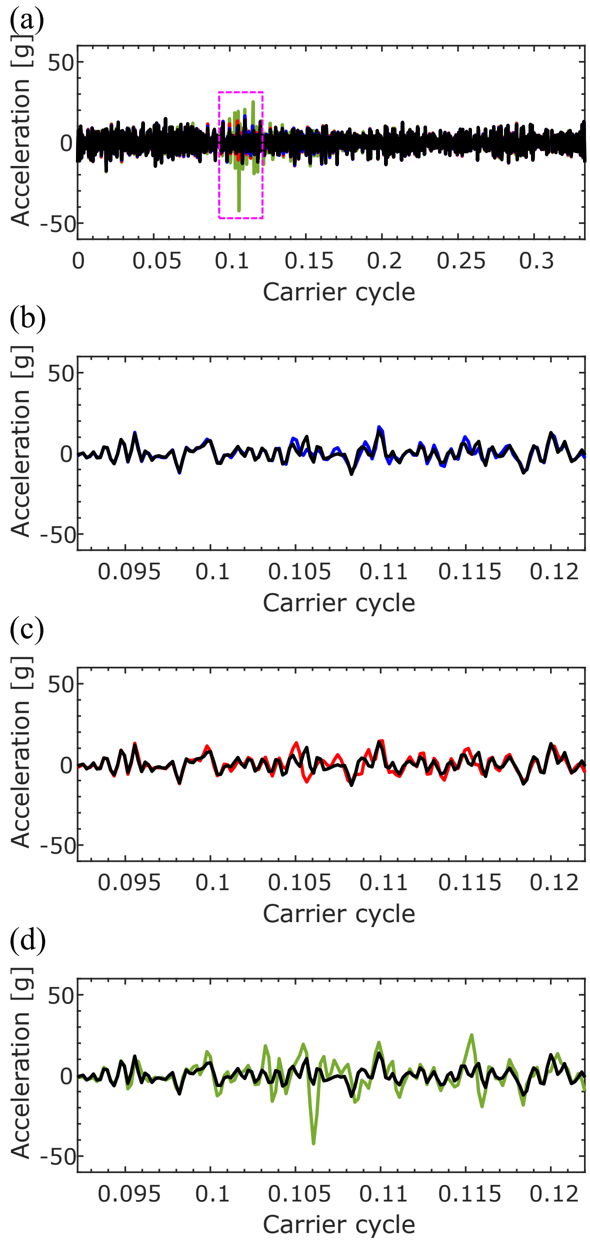

Figure 5.7: (a) The approximate calculation of the difference signal obtained from the elimination of the mesh frequency components and their first upper and lower sidebands of the TSA over the planet-pass spectrum. The approximate difference signal accelerations for (b) 20 percent, (c) 50 percent, and (d) 80 percent tooth root crack lengths of the ring tooth, compared to a healthy transmission, during the engagement of the damaged ring tooth in the planet-pass period. Healthy vibrations without damage are shown by a black line. The vibrations when the ring tooth has a root crack with 20, 50, and 80 percent of the tooth thickness are shown by blue, red, and green lines, respectively.

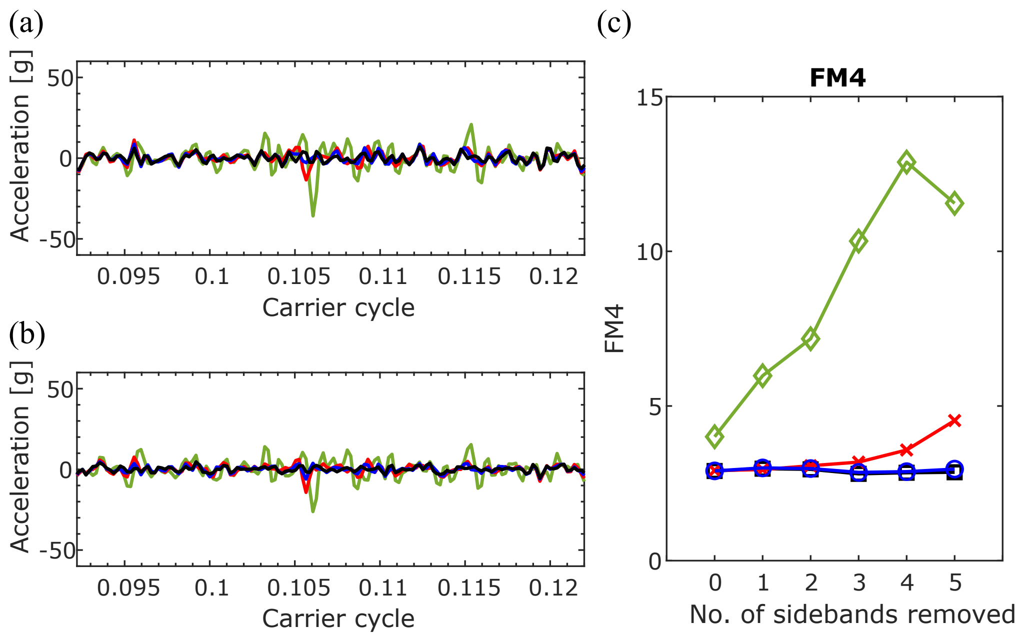

Figure 5.8: The approximate difference signal calculation with (a) three and (b) five upper/lower sideband amplitudes removed along with the mesh frequency components at all harmonics for transmission without damage and transmission with root crack damage on ring tooth. (c)The FM4 condition indicator values of the approximate difference signal with varying number of sidebands removed from the difference signal are calculated. The condition indicators of the system without damage is in the black (square marker) line, and blue (circle marker), red (cross marker), and green (diamond marker) represent the condition indicators of the system with ring gear tooth root crack damage of lengths 20 percent, 50 percent, and 80 percent of tooth thickness respectively.

(a)

(b)

(c)

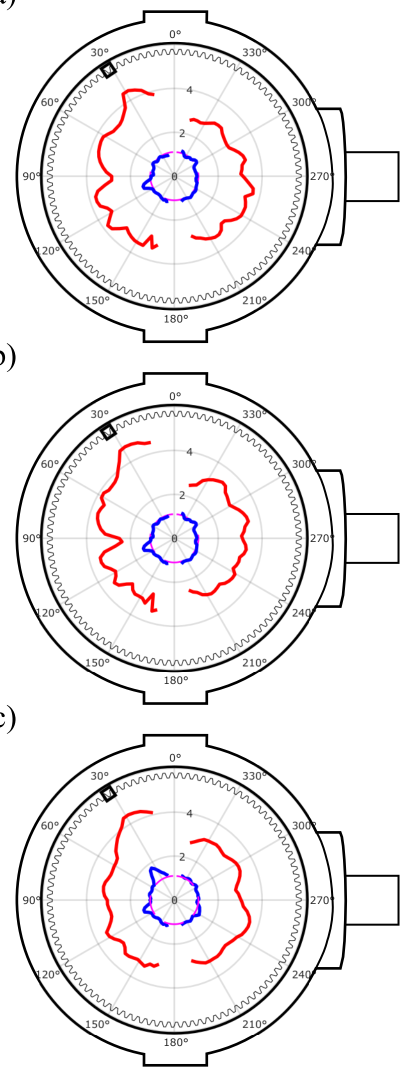

Figure 5.9: The polar plots of the natural logarithmic values of the FM4 for damaged transmission with (a) 20 percent, (b) 50 percent, and (c) 80 percent crack lengths. The values calculated using the exact and approximate difference signals are shown in solid (red) and solid (blue) lines. The polar plots are overlaid onto the top view of the housing. The dashed (magenta) line represents the natural logarithmic value of FM4 threshold value of 3.

(a)

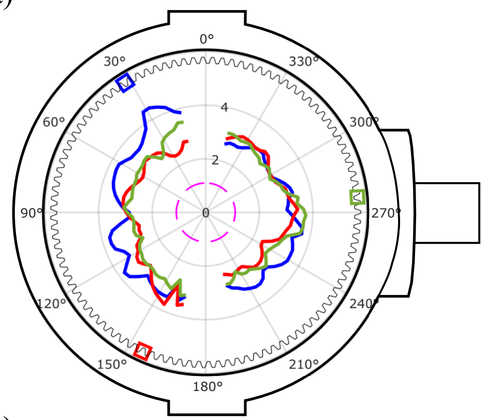

(b)

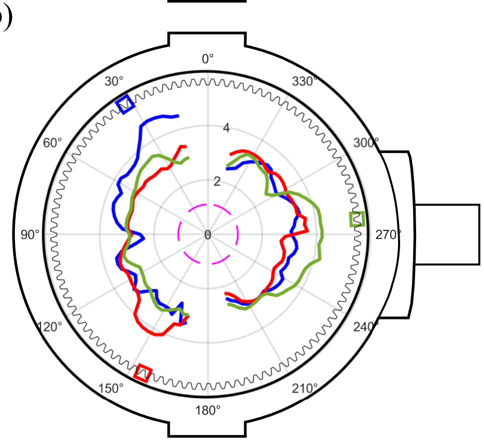

Figure 5.10: The polar plots of the natural logarithmic values of the FM4 calculated using the exact difference signal for damaged transmission with (a) 20 percent and (b) 50 percent crack lengths at accelerometers around housing and with damaged tooth location being at 35.6 (blue), 155.6 (red), and 275.6 (green) degrees of the housing. The polar plots are overlaid onto the top view of the housing. The dashed (magenta) line represents the natural logarithmic value of FM4 threshold value of 3.

CHAPTER SIX

DAMAGE-INDUCED DYNAMIC RESPONSE IN GEARED TRANSMISSIONS WITH APPLICATION TO ROTATING (SUN) GEAR TOOTH DAMAGE DETECTION

6.1 Introduction

Health and Usage Monitoring Systems (HUMS) are employed in the geared transmissions to track the performance of transmissions and other critical components [5, 6]. These systems rely on vibration measurements to detect potential damage and these measurements are one input used by these systems to detect damage. Further analysis of the vibration signatures associated with damage and a better understanding of their impact on detection could enhance the effectiveness of HUMS, ultimately improving the reliability, and safety of the geared transmissions, especially in rotorcraft applications.

The geared transmission considered in this work is a rotorcraft transmission used in the experiments by Lewicki and Coy [112]. The accelerometer signals were analyzed using different techniques for different input speeds and torques. The condition indicator values are the qualitative and quantitative representation of the vibration signal. The condition indicator value of the system without damage is compared to the condition indicator value of the system with damage for gear fault detection in the system [59, 86, 87, 100, 149]. The review of condition indicators used for fault detection in the gears was provided by many researchers in Refs. [5, 88–92, 135, 164]. Dempsey et al. [6, 93–95] performed various studies on the rotorcraft transmission on test rigs and in-flight to come up with threshold values for various condition indicators. Rotorcraft transmissions experience false alarms more commonly and this can be avoided by studying the effect of damage on the vibration signals [96].

Identification of damage on sun gear teeth of the planetary stage is still a challenge for researchers because the kinematic motion of the gear masks its dynamics in the modulation-like behavior with respect to the stationary measurement location on the housing of the rotorcraft transmission system. The vibrations from the measurement location due to the damaged sun gear teeth were observed to be not consistent throughout the carrier rotation. The vibrations were larger when the engagement of the damaged tooth with the neighboring planet tooth happened near the measurement location and vibrations were smaller when the engagement happened elsewhere. This resulted in asynchronous vibration and as a result the loss of content affected by damage in the Time Synchronous Averaging (TSA) signal was observed. McFadden proposed a vibration separation method of planet and sun gears by time-domain averaging [117, 118]. Samuel and Pines [119] extended the synchronous averaging technique to use multiple sensors. Lewicki et al. [4] used vibration separation techniques for the identification of damage in the planet and sun gears by performing seeded fault tests on all the components. The planet gear tooth root crack, surface pitting damage, and sun gear tooth surface pitting damage were all detectable. Hood et al. [120, 121] also conducted the sun gear fault-seeded experiments and proposed a vibration separation technique to isolate the dynamics of sun gear from other components of the planetary gearbox but only the pitting damage was detectable. The fault detection techniques like understanding the spectral structure of planetary gear system [125], synchro-squeezing transform [128], wavelet neural network [126] use techniques other than condition indicators. Zhang et al. [129] proposed a systematic scheme to explore the motion period of the sun gear fault meshing positions and evaluated the statistical condition indicators to detect the damage. The effect of TSA on the FM4 condition indicator performance for tooth root crack damage on the sun gear of geared transmission is the focus of this study.

In this work, the housing accelerations are determined by dynamically analyzing the finite element/contact mechanics (FE/CM) model and validated using the results from experiments. The accelerations of the transmission with varying tooth root crack lengths on single tooth of rotating (sun) gear are determined using the FE/CM model. The condition indicator FM4 is calculated using approximate and exact difference signals to understand its performance for damage detection. The sensitivity of measurement location around the housing circumference of the geared transmission is studied using the evaluation of the FM4 condition indicator.

6.2 Finite Element/Contact Mechanics (FE/CM) Model of Geared Transmission

This work uses the same finite element/contact mechanics (FE/CM) formulation and geared transmission model discussed in the Chapter. 4.7 to determine the housing accelerations. Completed details of the methodology applied to gear dynamics studies can be found in Refs. [14, 132, 145]. The FE/CM method has been shown to accurately predict the experimentally-measured nonlinear dynamic response of unmodified [14] and modified [17] gear pairs using two-dimensional finite element models. The accuracy was shown to persist for three-dimensional models [132]. The FE/CM formulation was shown to accurately predict dynamic tooth root strains compared to experiments, even when large amplitude vibrations caused tooth contact loss [134]. The FE/CM method has also been shown to accurately predict ring tooth root stresses compared to experiments [133]. A brief overview of the formulation and the geared transmission model are provided here. This formulation utilizes the small contact area between mating gear teeth to approximate tooth deformation as a combination of relative displacement near the surface (resulting from local contact deformations) and absolute displacement further away from the surface (caused by tooth bending and gear blank deformations). Relative displacements are modeled using elasticity theory for concentrated loads on an elastic half-space, while absolute displacements are calculated using finite element analysis. These two solutions are paired at a matching interface that is sufficiently far from the tooth surface that the local deformations are negligible. This approach reduces the need for highly refined meshing near the tooth surface, thereby conserving computational resources and enabling comprehensive finite element modeling of all gear components. It also allows for time-domain dynamic response calculations that account for kinematic motions, tooth bending, structural deformations, and vibrations without making assumptions about the contact between the gears.

The geared transmission in Figure 6.1(a) consists of two stages: input spiral-bevel stage and output planetary stage. The torque on the input spiral-bevel pinion shaft is transferred to the gear of the transmission. The shaft of the spiral-bevel gear is splined together with the sun gear shaft of the planetary stage. This torque is transferred to the carrier and to the output using three equally spaced planets around the sun gear and stationary ring gear in the planetary stage. The top view of the geared transmission with input spiral-bevel shaft, carrier, stationary ring gear, three equally placed planets, and housing is shown in Figure 6.1(a). The accelerometer measuring the radial vibrations of the housing is considered near the input port of the geared transmission. The accelerometer is placed to be at the midline of the planetary stage of the transmission. This accelerometer location is the same as in the experiments (A2 accelerometer of OH-58A transmission) in Ref. [3]. The FE/CM model includes accurate geometry of the housing, carrier, carrier shaft, spiral bevel gear shaft, and spiral bevel pinion shaft whose finite element meshes were developed from solid models of these components. In this work, the presence of damage on the rotating (sun) gear tooth is analyzed and Figure 6.1(b) shows the finite element mesh of the gear and the initial location of the damage before the geared transmission begins to kinematically rotate. The input speed of the spiral bevel pinion is 6060 rpm. The planetary gear mesh frequency (f_m)

is 573.4 Hz and the spiral-bevel gear mesh frequency (f_{sb}) is 1919 Hz. The FE/CM model is analyzed dynamically at operating torque and speed. The input spiral bevel pinion speed is specified to be 6060 rpm. The output carrier torque is 6106 N-m. 50 steps over a planetary gear mesh period is used and this provides accurate spectra calculations below 10 kHz. Steady-state accelerations of the geared transmission are determined for three complete carrier rotations after a region transient response is removed. For the dynamic simulation, a region of transient response occurs prior to reaching the system's steady state.

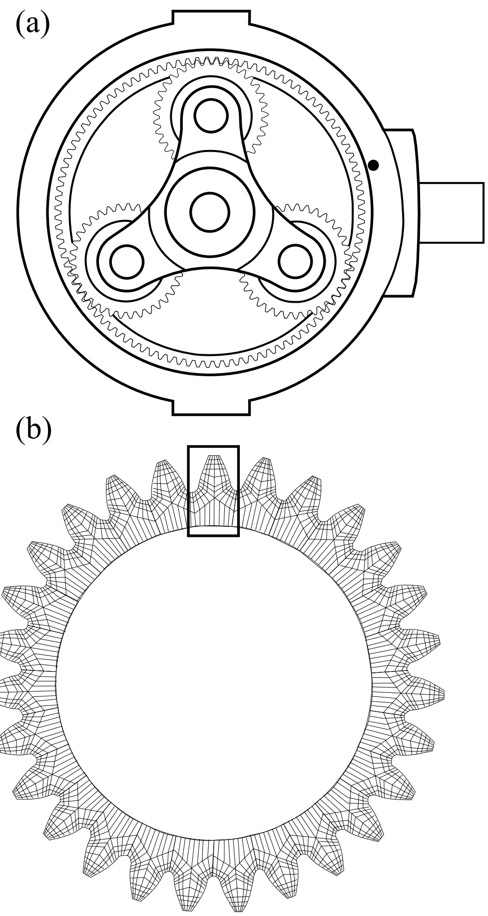

Figure 6.1: (a) The top view of the geared transmission shows the input shaft, housing, carrier, ring gear, and planet gears. The accelerometer (black circle marker) on the housing measures vibrations in the radial direction. (b) The finite element mesh of the rotating (sun) gear in the geared transmissions shows the initial location of the damaged tooth.

6.3 Dynamic Response

6.3.1 Healthy Transmissions without Damage

The FE/CM model of the transmission is dynamically analyzed at steady state to determine the housing accelerations in baseline conditions when all gear teeth are healthy. The accelerations that are shown are normalized by gravity. The housing accelerations of the geared transmission with all gears healthy and without damage are shown in Figure 6.2(a) in blue line. The accelerations contain vibrations from both stages of the transmission. Variation in the housing accelerations is noticed for planet-pass and carrier cycle periodicity as the planets kinematically rotate relative to the accelerometer location. Figure 6.2(b) and (c) show the baseline vibrations in the first planet-pass period (0 to 0.333 carrier cycle) and in the first carrier cycle period.

The spectrum of the baseline accelerations determined from the FE/CM model in the Figure 6.2(a) are shown in Figure 6.3 with a blue line. The spectrum has clusters of frequency content near planetary gear mesh frequency and spiral bevel gear mesh frequency harmonics. Each cluster near planetary gear harmonics contains prominent upper and lower sideband components. Figure 6.3, lower left, lower center shows the clusters of frequency content at the first and second harmonics of planetary gear mesh frequency. The sidebands near planetary gear harmonics occur at multiples of the planet-pass frequency $f_{pp} = 17.375$ Hz. The sideband amplitudes are asymmetric for the second harmonics planetary stage mesh frequency cluster. The spectrum near the first harmonic of the spiral bevel gear frequency $f_{sb} = 1919$ Hz is shown in the lower right plot in Figure 6.3. The sideband frequencies near the spiral bevel mesh frequency occur at the planet-pass frequency, similar to those near the planetary gear mesh frequency. The amplitudes of the clusters of planetary gear mesh frequency and spiral bevel mesh frequency are meaningful even at high frequencies near

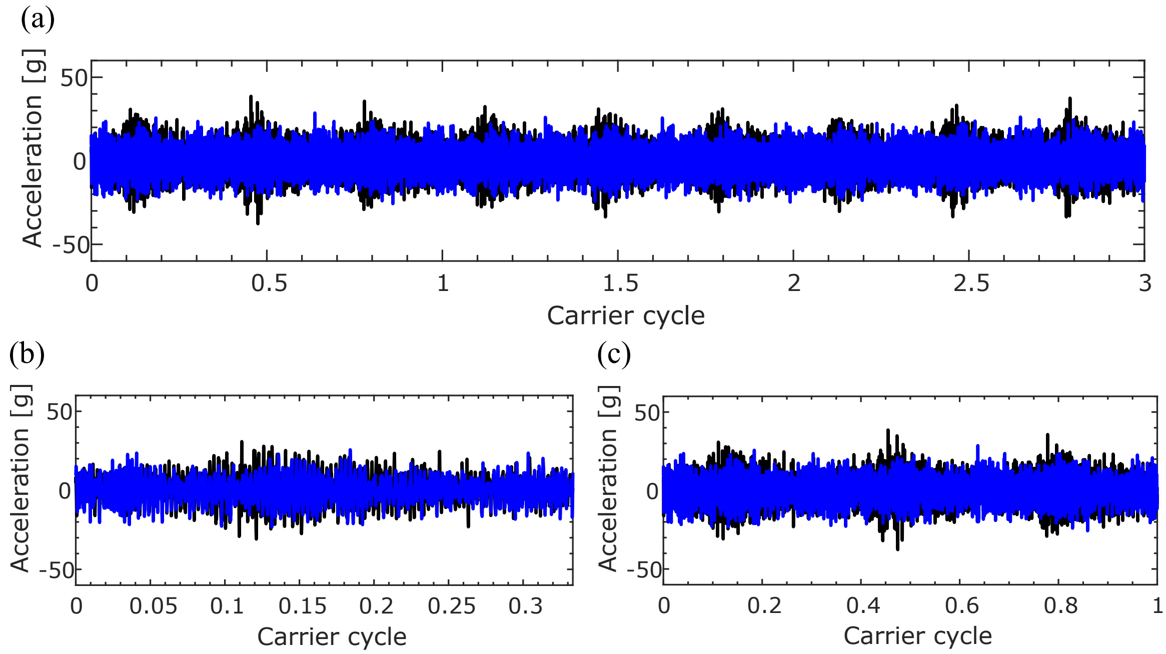

Figure 6.2: (a) Comparison of the FE/CM calculation and experimental results of housing accelerations for three carrier rotations of geared transmission without damage. The comparison zoomed to (b) the first planet-pass period and (c) the first carrier cycle of the accelerations. The experimental and FE/CM calculation results are shown in solid (black) and solid (blue) lines.

10 kHz. The maximum amplitude seen in the spectrum is 3.6 g, which occurs near the first harmonic of spiral bevel mesh frequency.

6.3.1.1 Validation with Experiments Hood [3] conducted experiments on the geared transmission shown in Figure 6.1(a). The housing accelerations of the geared transmission when all gear teeth are healthy at the measurement location shown in Figure 6.1(a) determined from the experiments are shown in Figure 6.2 with a black line. The accelerations predicted by the FE/CM model have similar features as those seen in the experiments. Comparing the experimental results and the FE/CM model results, differences are observed in the amplitudes. The mean square error calculated between the two results is 139. The frequency spectrum is shown in Figure 6.3. The amplitude differences between the experimental and

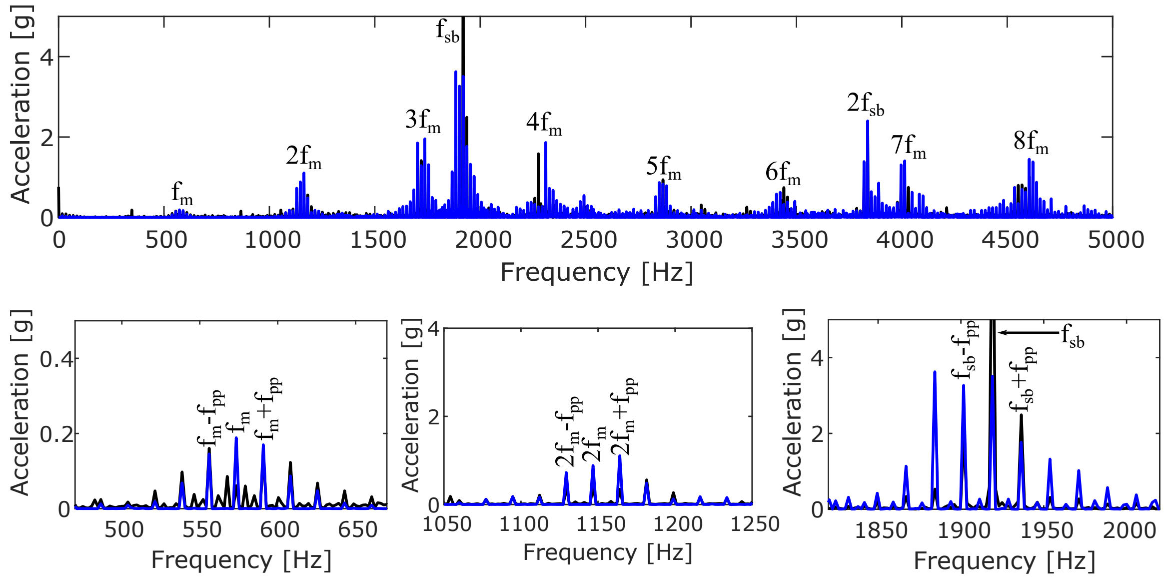

Figure 6.3: The frequency spectrum comparison of the healthy transmission housing accelerations calculated from the FE/CM model and experiments (upper). The frequency spectrum is zoomed (lower) to the first and second planetary stage mesh frequencies and the first spiral-bevel stage mesh frequency. The experimental and FE/CM calculation results are shown in solid (black) and solid (blue) lines.

FE/CM model results are seen in the first planet-pass and first carrier cycle plots shown in Figure 6.2(b) and (c). The FE/CM model shows higher amplitudes at the first harmonic of mesh frequency in the first harmonic planetary stage mesh frequency cluster which can be seen in Figure 6.3, lower left plot. The experimental results show sidebands at the carrier frequency, which the FE/CM model does not predict. However, the amplitudes of sidebands occurring at planet-pass are accurately captured by the FE/CM model. Similar characteristics are observed at the second harmonics of mesh frequency cluster shown in Figure 6.3, lower center plot. The FE/CM model predicted a lower amplitude of the spiral-bevel stage mesh frequency component shown in Figure 6.3, lower right plot, however, the sideband amplitudes are comparable to the experimental results. The difference between the FE/CM model and the experiments is expected due to differences in some cast parts with intricate geometry, lubrication, estimation of bearing stiffnesses, and damping in the geared transmission. However, the FE/CM model captures the overall characteristics of the acceleration signals and is used for determining the damaged transmission accelerations and the performance of condition indicators to detect the presence of damage in the geared transmission.

6.3.2 Damaged Transmissions

This work focuses on tooth root crack damage on the rotating (sun) gear. We assume the damage is localized to a single tooth. The tooth root crack is modeled by releasing the connectivity of select finite elements along a pre-selected crack path. Three different sun root crack lengths are analyzed to quantify the effects of varying severity of damage. The crack lengths are 20 percent, 50 percent, and 80 percent of the sun tooth thickness. The finite element meshes of the sun teeth with the different tooth root cracks are shown in Figure 6.4(c). The damaged sun tooth with its initial location before geared transmission kinematically rotates shown in Figure 6.1(b) comes into contact with the planets at 0.023, 0.114, etc., carrier cycles. The total number of engagements of the damaged sun tooth with the planet tooth is observed to be 11 in one carrier cycle rotation. In three carrier cycles, the damaged sun tooth engages into healthy teeth of the planets 33 times. The damaged transmission accelerations compared to healthy housing accelerations are shown in Figure 6.4(a). The crack lengths less than 50 percent (red and green lines) of the tooth thickness of the sun are not significantly different compared to the healthy accelerations (blue line). Figure 6.4(b) shows one of the engagements in the first planet-pass period of the carrier cycle. This engagement is characterized by a localized increase in the housing accelerations immediately above the 0.21 carrier cycle. Following a planet's engagement with the damaged sun tooth, a region of transient response occurs that diminishes prior to the engagement of the next planet. The ring tooth damage is space-fixed or stationary in the planetary stage and produces nearly constant amplitudes and transients for different engagements in the measured acceleration. On the other hand the kinematic motion of the sun gear and the relative differences between the engagement location and the measured location result in varying amplitudes of damaged transmission accelerations at different engagements. At 80 percent crack length, damaged accelerations show significant differences in the amplitudes compared to healthy for all the engagements. The frequency spectrum of the sun root crack damaged transmission accelerations were observed to have constant amplitudes for planetary stage mesh frequency and its sidebands at all harmonics, even for larger crack lengths (not shown). The changes in accelerations and frequency spectrum caused by sun tooth root crack damage complicate damage detection.

6.4 Difference Signal Calculations

In this study, vibrations are analyzed using the FM4 condition indicator to detect damage in the geared transmission. Calculations of additional condition indicators for geared transmission can be found in Appendix B. The FM4 indicator requires difference signal accelerations as input, which are processed from the time synchronous averaged (TSA) signal. TSA is a method that isolates vibration signals from noise and other nonsynchronous components [161, 162], allowing separation of vibrations from the planetary stage and the input spiral-bevel stage. Analyzing the vibrations of the planetary stage alone as the damaged tooth is located in the planetary stage, it is expected that damage will be better detected than if additional vibration components from the input stage are included. The transfer path of the sun gear vibrations to the accelerometer on the housing is through the sun-planet, planet-ring, and ring-housing engagements. Isolating the damaged accelerations from the normal meshing vibration is more challenging in cases of sun tooth damage compared to the ring tooth damage. TSA can be performed using any of the three fundamental periods in the

(a)

(b)

(c)

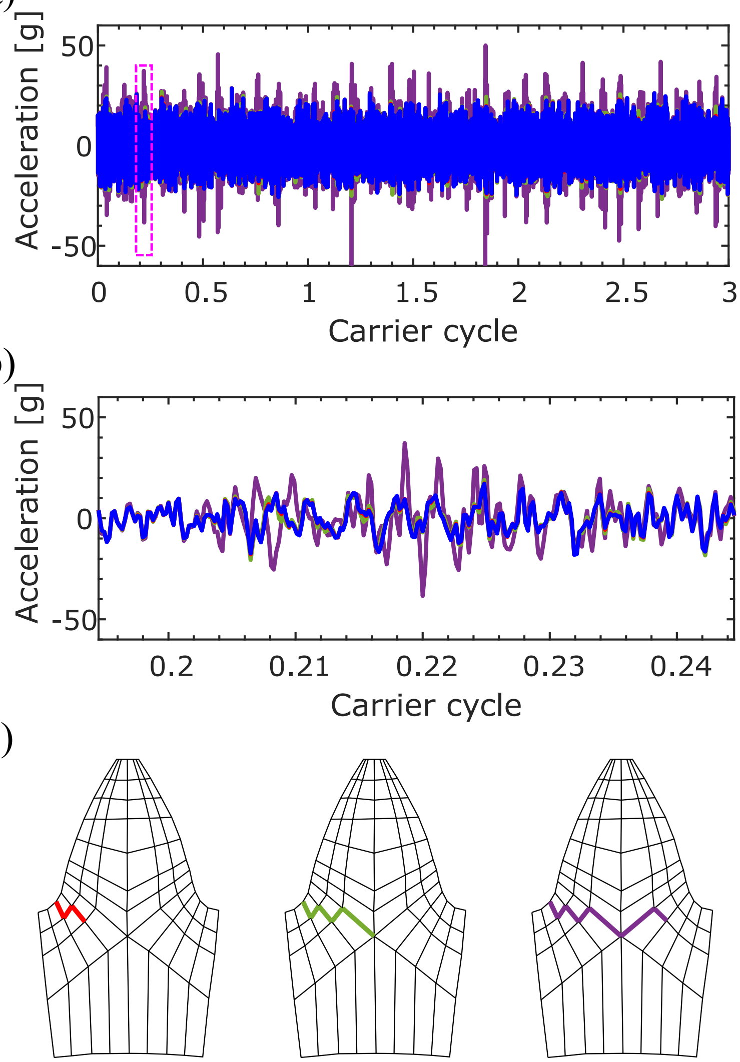

Figure 6.4: (a) FE/CM calculation of housing accelerations for three carrier rotations of damaged transmission and (b) one of the engagements of damaged sun tooth in the first planet-pass period. The FE/CM calculation of healthy vibrations without damage is shown by a blue line. The vibrations when the sun tooth has a root crack with 20, 50, and 80 percent of the tooth thickness are shown by red, green, and purple lines, respectively. (c) Finite element meshes of the sun tooth with root crack damage. The tooth root crack lengths are 20 percent (red), 50 percent (green), and 80 percent (purple) of the ring tooth thickness.

planetary stage: the mesh period, the planet-pass period, and the carrier period. However, using the mesh period for TSA removes most of the damage-related vibration effects and is therefore not recommended. The housing accelerations in Figure 6.4, are divided into nine blocks for the planet-pass period and three blocks for the carrier period and averaged to calculate the TSA over the planet-pass and TSA over the carrier period (not shown). Due to differences between the sun damaged tooth engagements and the location of the accelerometer, the TSA over the planet-pass period is observed to lose the dynamics of the damaged tooth engagement. Difference signals for the FM4 condition indicator are then computed using both exact and approximate methods.

6.4.1 Approximate Difference Signal

The mesh frequency components and their sidebands in the housing accelerations are observed to be largely insensitive to damage as a result it has been proposed to create a modified acceleration signal with these components removed [97]. To generate the approximate difference signal spectrum, the amplitudes of the planetary stage mesh frequency and its first-order upper and lower sidebands at all harmonics in the TSA signal spectrum are eliminated. The approximate difference signal, denoted as $d^{(1)}(t)$, is obtained by performing an inverse Fourier transform on the modified spectrum. The difference signal primarily captures vibrations caused by damage, excluding the typical vibrations from normal gear meshing. The approximate difference signal of the geared transmission, when all gear teeth are healthy and with varying amounts of sun crack damage at the measured location for TSA over the planet-pass and the carrier period, is shown in Figure 6.5(a) and (b). The 80 percent crack length is significantly different compared to the healthy approximate difference signal and the engagements of sun damaged tooth can be clearly observed in the approximate difference signal of the TSA over the carrier period. The approximate difference signal accelerations of the crack lengths less than 50 percent (red and green lines) cannot be distinguished from the healthy accelerations.

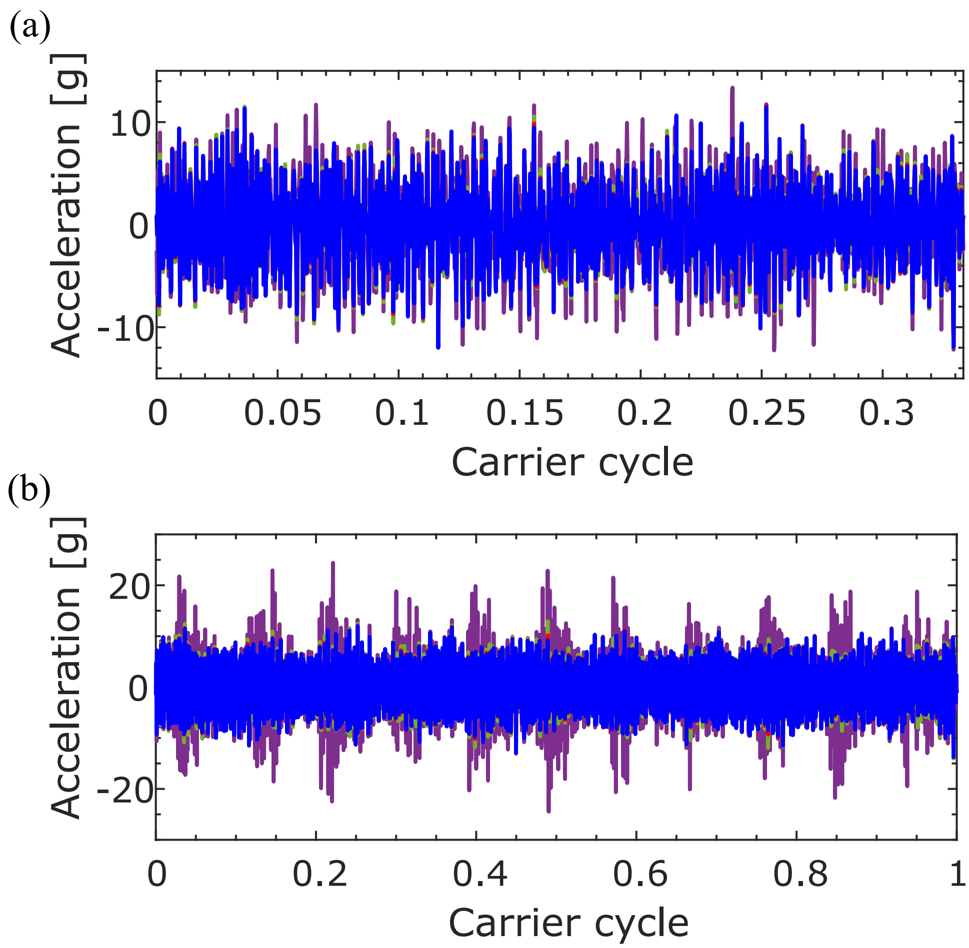

Figure 6.5: The approximate difference signal of (a) TSA over the planet-pass period and (b) TSA over the carrier period accelerations for the geared transmission. The vibrations when the sun tooth has a root crack with 20, 50, and 80 percent of the tooth thickness are shown by red, green, and purple lines, respectively.

6.4.2 Exact Difference Signal

The exact difference signal also referred to as the damage-induced dynamic response of the geared transmission, is defined as the signal that reflects accelerations solely caused by damage. It is calculated by subtracting the healthy accelerations ($x(t)$) from the damaged accelerations ($x_d(t)$), resulting in the exact difference signal ($d(t) = x_d(t) - x(t)$). The exact difference signal accelerations for TSA over the planet-pass period and TSA over the carrier period for 20, 50, and 80 percent crack lengths of sun gear is shown in Figure 6.6(a) and (b). The exact difference signal of the TSA over the carrier period shows engagement and disengagement of the damaged sun gear tooth. However, the exact difference signal, derived from the unaltered accelerations (or without TSA processed) shown in Figure 6.6(c), has amplitudes ranging from -41 g to 38 g. In contrast, the amplitudes in the TSA over the carrier period range from -22 g to 24 g which suggests that the damage content is being averaged out in the TSA processing. The engagement and disengagement of the damaged sun gear tooth can be observed for all different crack lengths.

6.5 Condition Indicator - FM4

Health and Usage Monitoring Systems (HUMS) for geared transmissions assess gear condition by calculating condition indicators from vibration signals [5]. These indicators are typically based on statistical features of the vibration signals, which are expected to change in the presence of damage. The FM4 condition indicator is used to evaluate the performance of different difference signal calculations. The Figure of Merit (FM4) is calculated from [97]

$$\mathrm{FM4} = \frac{N\sum_{i=1}^{N}(d_i - \bar{d})^4}{[\sum_{i=1}^{N}(d_i - \bar{d})^2]^2} \tag{6.1}$$

where $d_i = d(t_i)$, $i = 1, 2, \ldots, N$ is the exact difference signal at time t_i and $\bar{d}$ is the mean of the exact difference signal. The FM4 value for the approximate difference signal is calculated using the same Eq. (6.1). The nominal FM4 value for Gaussian noise is three, and values exceeding three are considered to detect the presence of damage. FM4 has been shown to effectively identify localized damage in a small number of teeth [97]. Figure 6.7(a) and (b) shows the FM4 condition indicator values evaluated using the approximate and exact difference signal accelerations. The FM4 values of TSA over planet-pass (magenta star markers) and TSA over carrier period (yellow diamond markers) approximate difference signals are observed to be very near to the threshold value of three and this complicates the damage detection of sun tooth root crack at the measured location. The same is observed with the exact difference signal of TSA over the planet-pass period (green square markers). The FM4 values are observed to be greater than six for the unaltered (blue circle markers) and TSA over the carrier period (red cross markers) exact difference signals, more than 100 percent of the threshold value. The damage detection of the sun tooth root crack at the measured location is possible even for the smaller crack lengths when the FM4 condition indicator is evaluated using the unaltered or TSA over the carrier period exact difference signals.

6.5.1 Sensitivity to Measurement Location

The sensitivity of the FM4 condition indicator for the unaltered and TSA over the carrier period exact difference signals is studied for accelerometers considered around the housing circumference. One accelerometer on the housing for every ring gear tooth, except near the housing supports are added to the simulation. The housing accelerations are determined and processed to derive the unaltered and TSA over the carrier period exact difference signals at all accelerometer locations. The FM4 polar plots for varying crack lengths of the sun tooth root crack using different signals are shown in Figure 6.8. The polar plots are overlaid on the top view of the housing. The FM4 threshold value of three is added to the polar plots (dashed magenta line). The FM4 values are observed to be above five, more than 66.7 percent from the threshold value, for different crack lengths and different exact difference signal accelerations. The accelerations from different accelerometer locations are not the same and result in different FM4 values around the housing. The FM4 values do not increase with the increase in the damage severity.

6.6 Conclusions

The finite element/contact mechanics (FE/CM) approach is used to dynamically analyze the geared transmission to determine housing accelerations. The FE/CM approach includes the accurate representation of the changing contact forces on the gear teeth, multiple reduction stages with different gear types, mechanical coupling between stages, and damage. The housing accelerations contain dynamics from both the spiral-bevel stage and the planetary stage. The accelerations exhibit distinct variations in amplitude as the planets move relative to the measurement location. The frequency spectrum of the healthy transmission has content in the form of clusters at the spiral-bevel and planetary stage mesh frequencies and their harmonics. Sidebands are observed at planet-pass frequencies at both stages. The housing accelerations when all gear teeth are healthy and without damage from the FE/CM model of the geared transmission are validated with results from the experiments measured at the same location on the housing. Differences in amplitudes are observed in the accelerations and frequency spectrum, however, the overall characteristics of the housing vibrations for geared transmission are captured.

The housing accelerations of the tooth root crack damage on the rotating (sun) gear tooth for geared transmission are determined using the FE/CM model. The damaged tooth on the sun gear engages into healthy planet teeth 11 times in a carrier cycle. The engagement exhibits increased amplitudes with transient behavior in the housing accelerations. The dynamics of the sun gear are masked by several other component vibrations and isolating the damage from normal meshing vibrations is challenging. The housing accelerations of tooth root crack lengths less than 50 percent are not significantly different than the healthy transmission accelerations. The frequency spectrum of the damaged transmission did not affect the amplitudes of the harmonics of the planetary stage mesh frequency and its sidebands. Damage detection from damaged transmission acceleration and frequency spectrum has proven to be difficult.

The condition indicator FM4 is used to assess the presence of damage in the geared transmission. The difference signals are calculated using the approximate and exact methods for TSA over the planet-pass, TSA over the carrier period, and unaltered (without TSA) accelerations. The signature of the damage engagement and disengagement is completely lost in the calculation of TSA over the planet-pass period. The damage content is averaged out in the processing of TSA over the carrier period. The FM4 values calculated for unaltered and TSA over carrier period exact difference signals show a prominent indication of damage at the measured location, even for the smaller crack lengths in the geared transmission compared to the other input signals. The sensitivity of the measurement location on the FM4 condition indicator performance is studied for the unaltered and TSA over the carrier period exact difference signals. The FM4 condition indicator is able to detect damage at all measurement locations around the housing circumference. This work suggests unaltered (no TSA) or TSA over the carrier period accelerations and the calculation of their exact difference signals for detecting damage on the rotating (sun) gear tooth of the geared transmission.

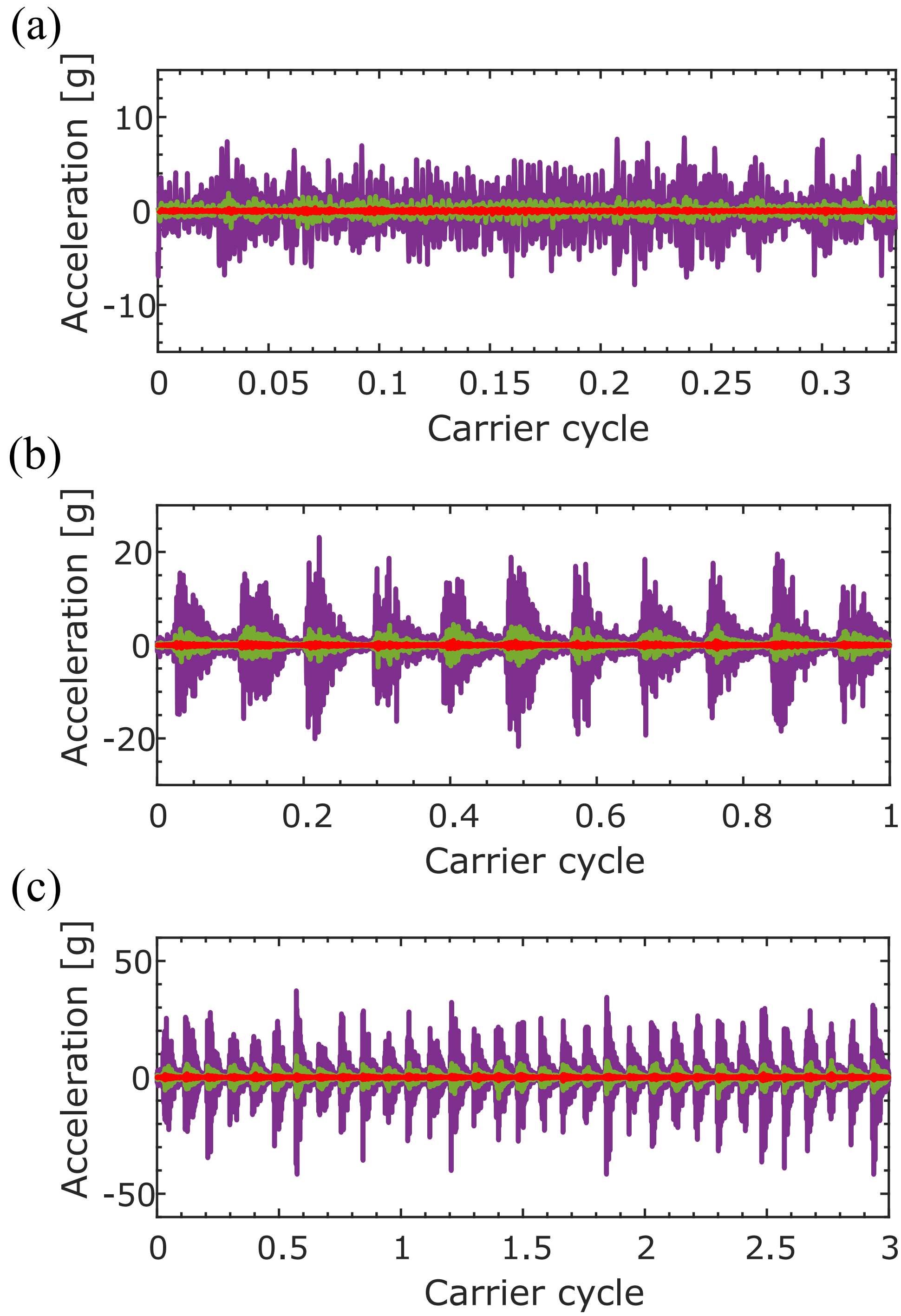

Figure 6.6: Damage-induced dynamic response or the exact difference signal of (a) TSA over the planet-pass period, (b) TSA over the carrier period, and (c) unaltered accelerations for the geared transmission. The vibrations when the sun tooth has a root crack with 20, 50, and 80 percent of the tooth thickness are shown by red, green, and purple lines, respectively.

(a)

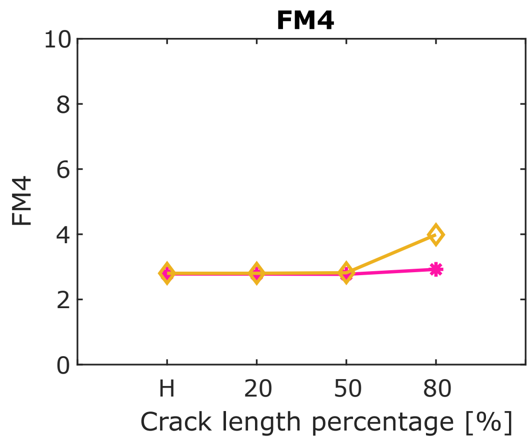

(b)

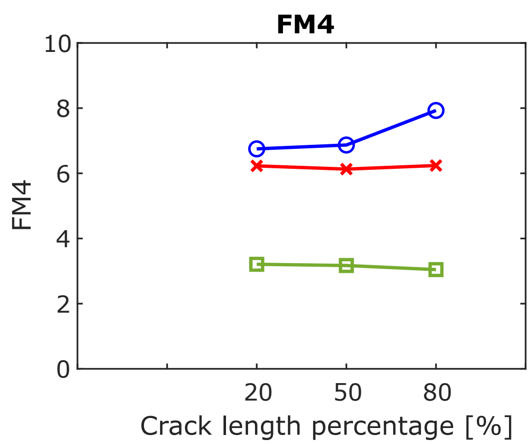

Figure 6.7: The FM4 condition indicator evaluated using (a) approximate difference signals and (b) exact difference signals for healthy transmission (H) and sun root crack damaged transmission. In (a) the FM4 calculated using TSA over planet-pass and TSA over carrier period approximate difference signals are shown by magenta line with star markers and yellow line with diamond markers. In (b) the FM4 calculated using unaltered, TSA over planet-pass and TSA over carrier period exact difference signals are shown by blue line with circle markers, green line with square markers, and red line with cross markers.

(a)

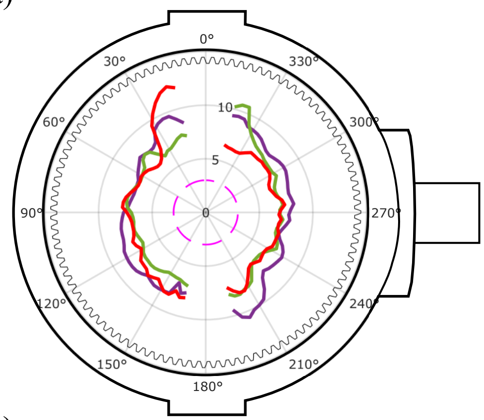

(b)

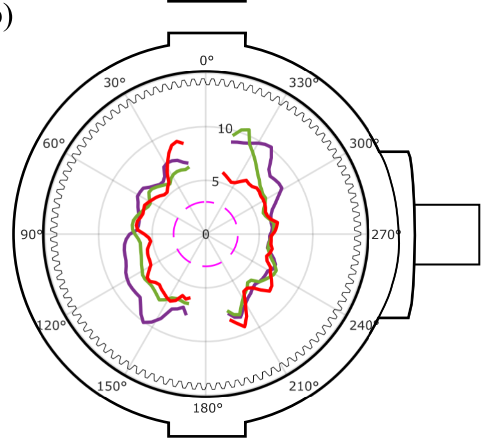

Figure 6.8: The polar plots of the FM4 evaluated using (a) unaltered exact difference signal vibrations and (b) TSA over the carrier period exact difference signal vibrations for damaged transmission with 20, 50, and 80 percent crack lengths. The polar plots are overlaid onto the top view of the housing. The FM4 values when the sun tooth has a root crack with 20, 50, and 80 percent of the tooth thickness are shown by red, green, and purple lines, respectively. The dashed (magenta) line represents the FM4 threshold value of 3.

CHAPTER SEVEN

NONLINEAR DYNAMIC RESPONSE AND DAMAGE-INDUCED DYNAMIC RESPONSE FOR VARYING SPEED IN SPUR GEAR PAIRS WITH LOCALIZED DEFECTS

7.1 Introduction

Gears vibration is transmitted to the surrounding structure through shafts, bearings, and other connected components, often resulting in unwanted noise and vibrations that can affect the overall system performance. At specific rotational speeds, particularly near resonant frequencies, dynamic tooth loads can lead to excessive stresses on both the gear teeth and bearings. Gears operating under complex loading conditions, lead to increased dynamic responses and result in nonlinearity such as tooth contact loss. The effect of tooth root crack or tooth surface pitting damage on the dynamic response can influence the nonlinearity of the gear pair. Understanding the nonlinear behavior is crucial for damage detection, as it affects the dynamic responses used to evaluate the condition indicators. This work studies the effect of localized defects on the nonlinear response of the gear pair.

The accuracy of the dynamic response of the spur gear pair depends on the accuracy of the tooth mesh interface parameters. The analytical lumped-parameter model uses the static transmission error and tooth mesh stiffness of the gear pair as their excitation sources. Many researchers have proposed methods to determine the time-varying mesh stiffness and static transmission error of the gear pair. These methods primarily center on analytical models [18–29], conventional finite element formulations [30–32, 53], experiments [33–40], and combined finite element/contact mechanics formulations [14, 17, 41]. Several other models for mesh stiffness calculations can be found in the bibliography of Ref. [130]. Damage to the gear teeth alter the usual fluctuations in static transmission error and tooth mesh stiffness, which can lead to increased vibrations and dynamic response. Ma et al. [62] reviewed the tooth root crack damaged gear pair mesh stiffness evaluated to determine the damaged dynamic response. Different dynamic response derivation models of gear pairs with several gear faults are reviewed in Ref. [64]. Wang et al. [65] calculated the time-varying mesh stiffness for gear teeth with root cracks connected to blanks with complicated geometry. Chen et al. [53] investigated tooth root crack damage on the gear mesh stiffness of gear pairs with thin-webbed blanks. Yang et al. [66] included the opening state of the crack under the action of mesh force in the analytical model for the calculation of mesh stiffness and compared the results with finite element analysis. Cooley et al. [67] showed the effect of crack initiation, and crack path on mesh stiffness. Wang et al. [68] studied the effect of tooth root cracks on the dynamics. Kumar et al. [69] determined the gear mesh stiffness of un-carburized and carburized gears using the potential energy approach for different crack depths. Han et al. [70] analyzed the tooth mesh stiffnesses of spur gears with broken tooth faults, and analyzed their impact on dynamic response. Yang et al. [71] proposed the time-varying mesh stiffness calculation method of the gear pair considering different spatial crack shapes which are different shapes of cracks in the direction of the facewidth of the tooth. We analyzed the static transmission error and mesh stiffness of the nonunity-ratio spur gear pair using a finite element/contact mechanics model for tooth root cracks starting in the root and extending into the tooth thickness.

Kahraman and Blankenship [12, 13, 16] have experimentally measured the RMS of the oscillating component dynamic response of the gear pair for various operating torques, speeds, and contact ratio. Parker et al. [14] showed excellent agreement with experimental results when calculated using the FE/CM formulation. Cooley et al. [132] extended the FE/CM formulation for three-dimensional gears, as part of an efficient frequency-domain approach for dynamics calculations and showed good agreement with experimental results.

The work carried out is for the unity-ratio spur gear pair and when all gear teeth are healthy. We investigated the nonlinear dynamic response of the nonunity-ratio spur gear pair when all gear teeth are healthy and when a single tooth of pinon has tooth root crack damage.

Lumped-parameter model is used to derive the dynamic response of the nonunity-ratio gear pair without damage and with tooth root crack damage on a single pinion tooth. The peak-to-peak dynamic transmission error is determined for varying speeds of the gear pair to characterize the nonlinear dynamic response with tooth root crack damage. The dynamic responses and frequency spectrum at speed with multiple steady-state responses are compared for healthy and tooth root crack damaged nonunity-ratio spur gear pair. The range of speed for the quasi-static and impulse-like damage-induced dynamic responses of the gear pair for varying tooth root crack lengths is identified.

7.2 Dynamic Response - Analytical Lumped Parameter Model

The gear pair analyzed in this study is the sun-planet pair from the output planetary stage of a rotorcraft transmission [112]. It is a nonunity-ratio spur gear pair with geometric parameters listed in Table 7.1. The dynamic response of the gear pair is derived using an analytical lumped-parameter model, shown in Figure 7.1(b). Each gear is modeled as a rigid disk with radius r_h, mass m_h, and mass moment of inertia J_h $(h = p, g)$. The gears are supported by discrete stiffness (k_h) and damping (c_h) elements, representing the elastic and dissipative properties of the shafts, bearings, and housing. Applied torque T_h to each gear, and each gear has two degrees of freedom: translation along the line-of-action y_h and the rotational vibration θ_h. The translation perpendicular to the line of action is neglected, as is friction between meshing gear teeth and other off-line-of-action effects. The mesh force is calculated using the local slope approach, which accurately predicts dynamic responses in undamaged gear pairs [41, 143]. The mesh force is given by $f_m = k_l(t)\,[\delta - \delta_0(t)]$, where

$k_l(t)$ is the local slope calculation of mesh stiffness, $\delta = y_p - y_g + r_p\theta_p + r_g\theta_g$ is the mesh deflection, and $\delta_0(t)$ is the static transmission error. In the lumped-parameter model, the gear mesh interface is represented as a discrete mesh stiffness k_l in series with a prescribed displacement excitation $\delta_0(t)$. The dissipative behavior of the gear mesh is modeled with a discrete damping element c_m. The parameters used in the lumped-parameter model are given in Table 7.2 and the static transmission error and mesh stiffness at the gear pair mesh interface are determined using the finite element/contact mechanics (FE/CM) model.

The FE/CM model of the gear pair is built and analyzed in Calyx Transmission3D to determine static transmission error and mesh stiffnesses. Elastic deformations and tooth load distributions of gear pairs which change due to gear rotation kinematics are precisely calculated using the FE/CM approach. The geometry of involute gear tooth profiles is captured by specialized finite elements that have high resolution along the profile. These finite elements use shape functions with continuous slopes so that the local curvatures of the deformed surfaces are accurately captured. The contact pressure distribution on the individual gear teeth at each time instant is calculated. Because of the finite element method, the deformations of gear teeth are accurately captured without the need to make modeling assumptions between gear teeth, root, and blank. Accurate modeling of small micro-sized modifications of the gear teeth is possible with this FE/CM approach. This method of modeling appears to accurately capture the deformations and have comparable results when the crack is modeled with a high density of elements. The FE/CM model of the nonunity-ratio gear pair is statically analyzed at nominal torque (424 $\mathrm{N \cdot m}$), at torque slightly (one percent) higher than nominal torque, at torque slightly (one percent) lower than nominal torque. The mesh force and rotational deformations at nominal torque, at torque one percent above nominal and at torque one percent below nominal, give static transmission error and mesh stiffness. The more detailed calculation of the static transmission error and mesh stiffness of the gear pair is studied in Chapter 2.5.

The equations of motion when the gear teeth remain in contact are

$$m_p\ddot{y}_p + (c_p + c_m)\dot{y}_p - c_m\dot{y}_g + c_m\dot{x} + (k_p + k_l)y_p - k_l y_g + k_l x = k_l\delta_0 - f_0, \tag{7.1a}$$

$$m_g\ddot{y}_g - c_m\dot{y}_p + (c_g + c_m)\dot{y}_g - c_m\dot{x} - k_l y_p + (k_g + k_l)y_g - k_l x = f_0 - k_l\delta_0, \tag{7.1b}$$

$$m_e\ddot{x} + c_m\dot{y}_p - c_m\dot{y}_g + c_m\dot{x} + k_l y_p - k_l y_g + k_l x = k_l\delta_0, \tag{7.1c}$$

$$m_e = \frac{J_p J_g}{{r_p}^2 J_g + {r_g}^2 J_p}, \quad f_0 = \frac{r_p J_g T_p + r_g J_p T_g}{{r_p}^2 J_g + {r_g}^2 J_p}, \tag{7.1d}$$

The equations of motion when the gear teeth lose contact and the terms k_l, δ_0 will be equal to 0. These equations of motion are converted to first-order form and numerically integrated to determine the dynamic response of the gear pair.

Table 7.1: Nonunity-ratio spur gear pair geometrical parameters

	Gear	Pinion
Number of teeth	35	27
Module (mm)	2.87	
Outer diameter (mm)	104.98	84.05
Root diameter (mm)	91.54	70.76
Tooth thickness (mm)	4.18	4.52
Facewidth (mm)	31.75	34.925
Center distance (mm)	88.9	
Pressure angle (deg)	24.6	

7.2.1 Healthy Spur Gear Pair Dynamic Response

The static transmission error and mesh stiffness of the nonunity-ratio gear pair without damage are derived from static analysis using the FE/CM model for one mesh cycle.

Table 7.2: Parameters for the analytical lumped-parameter model to determine the dynamic response of the nonunity-ratio spur gear pair in Figure 7.1(a).

	Gear	Pinion
Base radius, $r_{g,p}$ (mm)	45.63	35.20
Mass, $m_{p,g}$ (kg)	0.8537	0.7294
Torque, $T_{p,g}$ (N $\cdot$ m)	424	327
Moment of inertia, $J_{p,g}$ (kg $\cdot$ m^2)	0.0050	0.0008
Support stiffness, $k_{p,g}$ (N/m)	1×10^{12}	1×10^{12}
Support damping, $c_{g,p}$ (N $\cdot$ s/m)	800	800
Mesh damping, c_m (N $\cdot$ s/m)	3660	

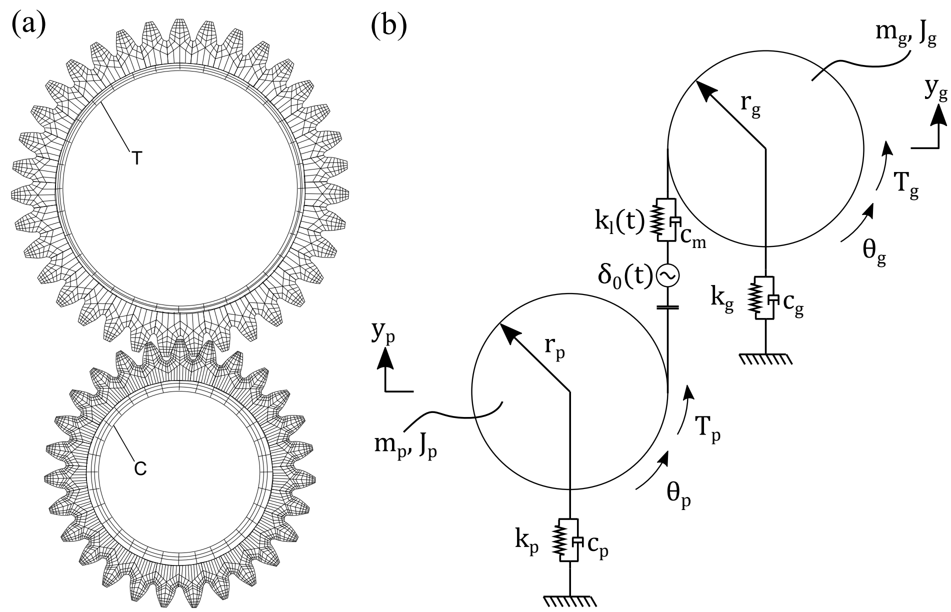

Figure 7.1: (a) The finite element mesh of the nonunity ratio spur gear pair analyzed in this work to determine the static transmission error and mesh stiffnesses. Torque 'T' is applied to the inner diameter of the gear and the inner diameter of the pinon is constrained 'C'. (b) Schematic of the lumped-parameter model of the gear pair.

As all gear tooth are without damage, the tooth mesh interface parameters are repeated for one rotation of pinion (27 mesh cycles). Utilizing these tooth mesh interface parameters and the parameters in Table 7.2, the dynamic response of the gear pair is derived for one complete rotation of the pinion (27 mesh cycles) at mesh frequency 1800 Hz or speed 4000 rpm. Figure 7.2 shows the dynamic response and the frequency spectrum of the gear pair without damage. The dynamic response shows periodic behavior meaning, the response for the first mesh cycle is the same as response for all other mesh cycles which was expected behavior. The spectrum of the dynamic response only shows amplitudes at mesh frequency and its harmonics.

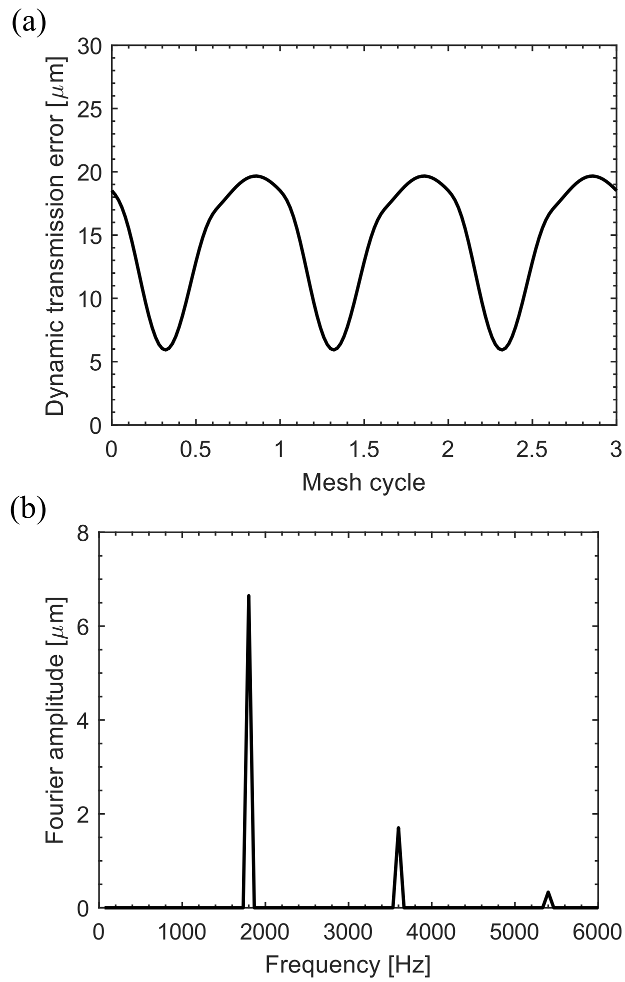

Figure 7.2: (a) The dynamic transmission error of the gear pair without damage determined using the analytical lumped-parameter model. (b) The frequency spectrum of the healthy gear pair dynamic response.

7.2.2 Damaged Spur Gear Pair Dynamic Response

Two different tooth root crack lengths, 20 and 50 percent of the tooth thickness of the gear tooth which starts at root and goes into the tooth thickness are analyzed. The static transmission error and mesh stiffness of the nonunity-ratio gear pair with root crack damage on single tooth of pinion are analyzed statically using FE/CM model. The tooth root crack damage in the FE/CM is modeled by removing the element connectivity in the crack path. The tooth mesh interface parameters for gear pair without damage and gear pair with tooth root crack damage are utilized to create the inputs for the analytical lumped-parameter model. Figure 7.3 shows the dynamic response and frequency spectrum of the gear pair with tooth root crack damaged, compared to the healthy gear pair results. The dynamic response resembles that of the undamaged gear pair prior to contact. However, when contact occurs, the dynamic response exhibits transients and increased amplitudes. This transient behavior is seen for mesh cycles after the damaged tooth contact leaves the mesh. The dynamic response amplitudes and transient behavior increase with the increase in the damage amount. The spectrum of the dynamic response of the gear pair with tooth root crack damage contains amplitudes at mesh frequency and its harmonics and change in amplitude with respect to spectrum of gear pair without damage was minimal making the damage detection difficult from tracking the amplitudes. Apart from the regular meshing components seen in the spectrum of the dynamic response of the gear pair without damage, the spectrum of the dynamic response of root crack damage has resonance like amplitude at natural frequency of the gear pair. This amplitude increases with increase in the damage amount.

7.3 Dynamic Response for Varying Speeds

In the earlier sections, the dynamic response of the gear pair is evaluated at one mesh frequency of 1800 Hz or speed of 4000 rpm. The analytical lumped-parameter model is used

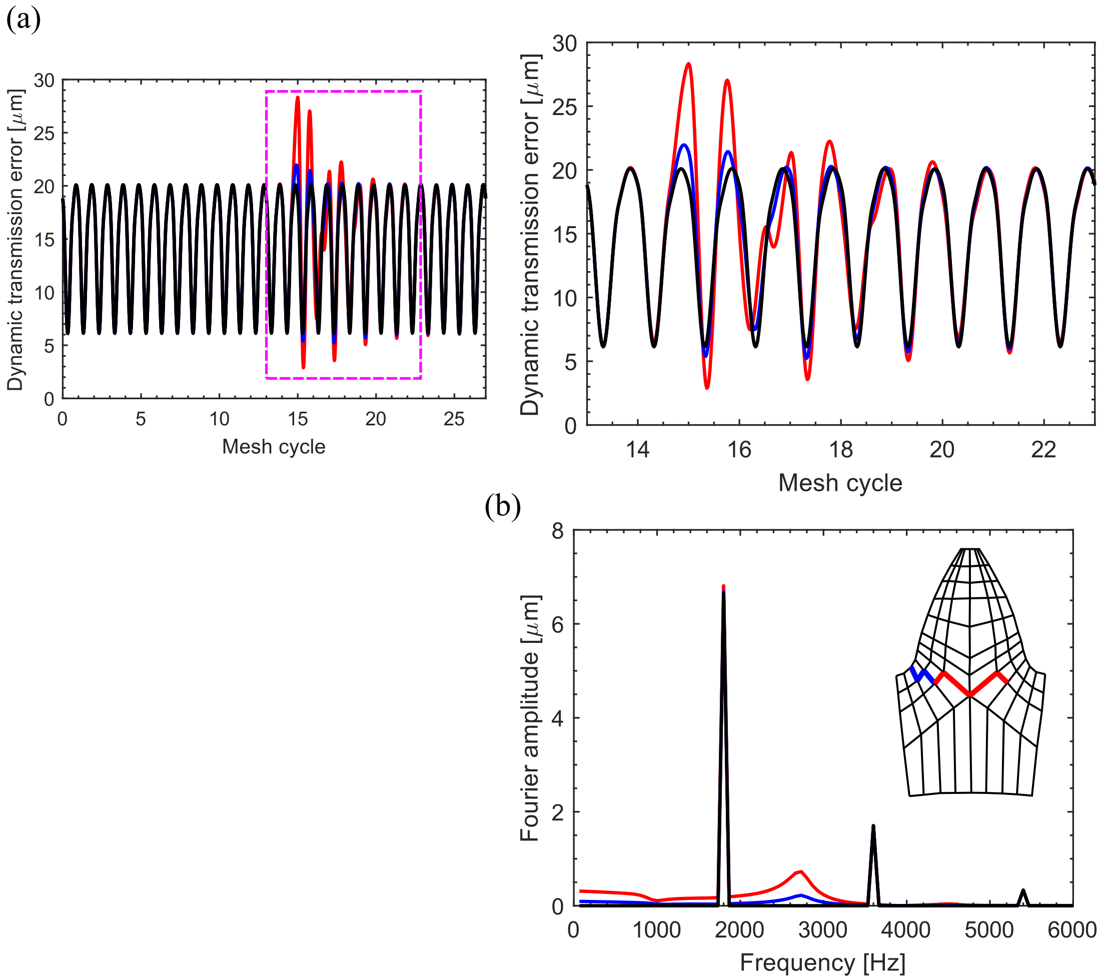

Figure 7.3: (a) The dynamic transmission error and (b) frequency spectrum of the gear pair with tooth root crack damage on single tooth of the pinion of the gear pair for one complete rotation of the pinon. The healthy gear pair results are shown in the black line. The tooth root crack damaged results of 20 and 50 percent of tooth thickness of pinon are shown in blue and red lines respectively. The finite element mesh of the pinon tooth with varying crack lengths is shown in the inset figure in (b).

to evaluate the dynamic responses of the gear pair without damage and the gear pair with tooth root crack damage for speeds ranging between 200-4000 Hz, the typical operating speeds. The model is analyzed with increasing speed from 200 to 4000 Hz with 50 Hz increments and also analyzed with decreasing speed from 4000 to 200 Hz to determine the nonlinear dynamic response of the gear pair. The nonlinear dynamic response of the gear pair without damage is shown in Figure 7.5(a). Softening nonlinearity is observed for the nonlinear dynamic response of the healthy gear pair. The natural frequency of the spur gear pair in Figure 7.1(a) is 2733.33 Hz, calculated using the impulse tests in the FE/CM model. It is observed that the nonlinear dynamic response exhibits a jump phenomenon from the lower branch to the upper branch at 2300 Hz mesh frequency, near the natural frequency of the gear pair. This is referred to as the primary resonance of the gear pair. For speeds from 1700 to 2300 Hz, multiple steady-state responses are possible. The secondary resonances, superharmonic resonances, are also captured in the nonlinear response of the healthy gear pair. The nonlinear dynamic response of the gear pair with tooth root crack damage is shown in Figure 7.4(b). The increase in the amount of damage severity increased the peak-to-peak transmission error for varying speeds. The nonlinear dynamic response of the gear pair with tooth root crack damage exhibits similar characteristics as the healthy gear pair.

The dynamic transmission error and frequency spectrum of a healthy gear pair and a tooth root crack-damaged gear pair are compared at a speed of 1750 Hz, where multiple steady-state responses are present and are shown in Figure 7.5. Dynamic responses are shown between 13 and 23 mesh cycles where the damaged tooth engages and transients end. The dynamic response of the gear pair in the lower branch exhibits the same characteristics as the dynamic response discussed in the Section 7.2. For the upper branch results, the amplitudes of both the dynamic transmission error and the frequency spectrum are higher. The meshing teeth in the gear pair lose contact for large portions of the mesh cycle. The transients due to the engagement of damaged gear tooth are lower with the upper branch dynamic response results. The frequency spectrum of the upper branch response does not have amplitudes at the natural frequency of the gear pair, however, sideband amplitudes are observed at 129 Hz apart from the mesh frequency harmonics for the tooth root crack damaged gear pair.

(a)

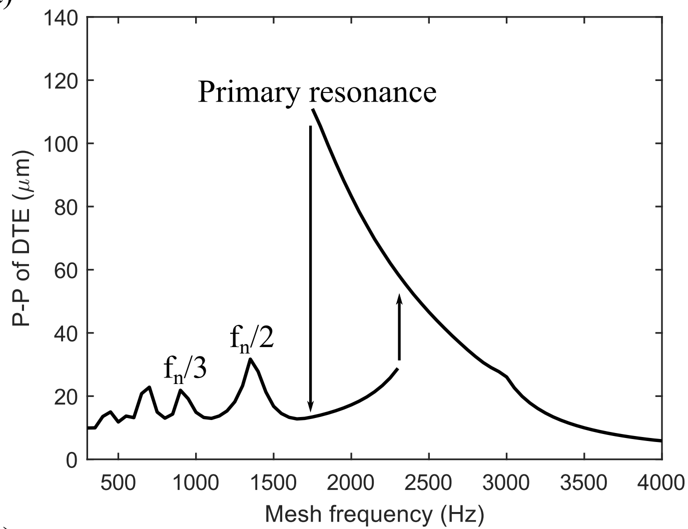

(b)

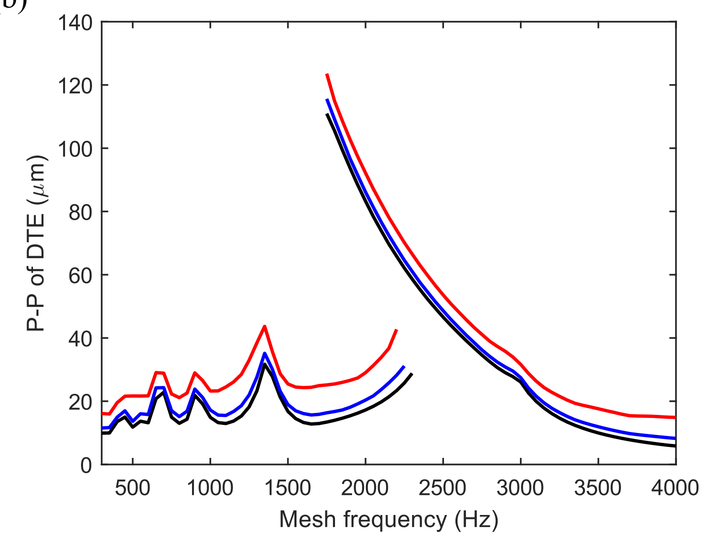

Figure 7.4: (a) The peak-to-peak dynamic transmission error of healthy gear pair for varying speeds of the gear pair. (b) The peak-to-peak dynamic transmission error of 20 percent (blue) and 50 percent (red) crack damaged pinion tooth compared with healthy gear pair results.

7.4 Damage-Induced Dynamic Response for Varying Speeds

The damage-induced dynamic response provides the actual vibrations that are purely due to damage. This can also be referred to as true difference or exact difference signal. The damage-induced dynamic response is constructed by removing the dynamic response of the

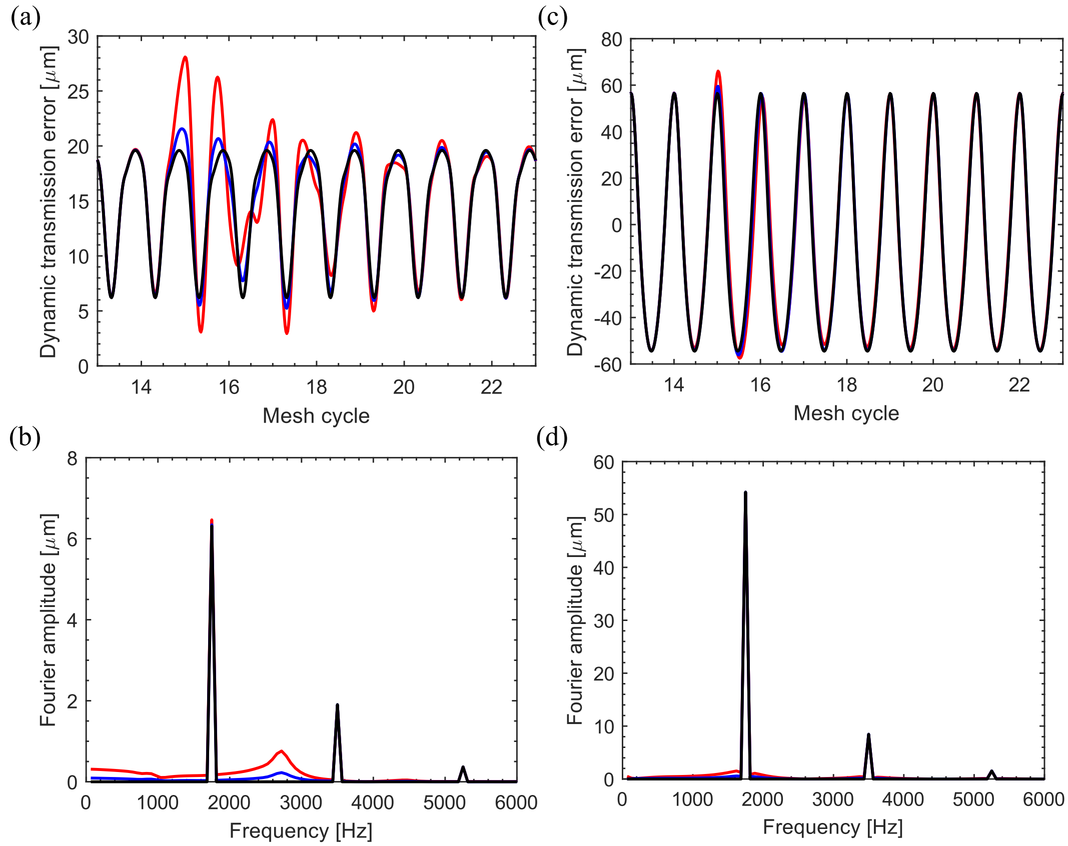

Figure 7.5: The dynamic transmission error and frequency spectrum of healthy and crack damaged gear pairs in the (a,b) lower branch and (c,d) upper branch of the dynamic response of the gear pair. The healthy gear pair results are shown in the black line. The tooth root crack damaged results of 20 and 50 percent of tooth thickness of pinon are shown in blue and red lines respectively.

gear pair without damage from the dynamic response of the gear pair with damage, i.e., the difference between dynamic response of the gear pair with damage and the dynamic response of gear pair without damage. Figure 7.6 shows the damage-induced dynamic response and the frequency spectrum for the gear pair with 20 percent crack length. The damage-induced dynamic response resembles the response of an underdamped linear oscillator. The frequency spectrum of the damage-induced dynamic response contains amplitudes at the natural frequency of the gear pair (2733.33 Hz).

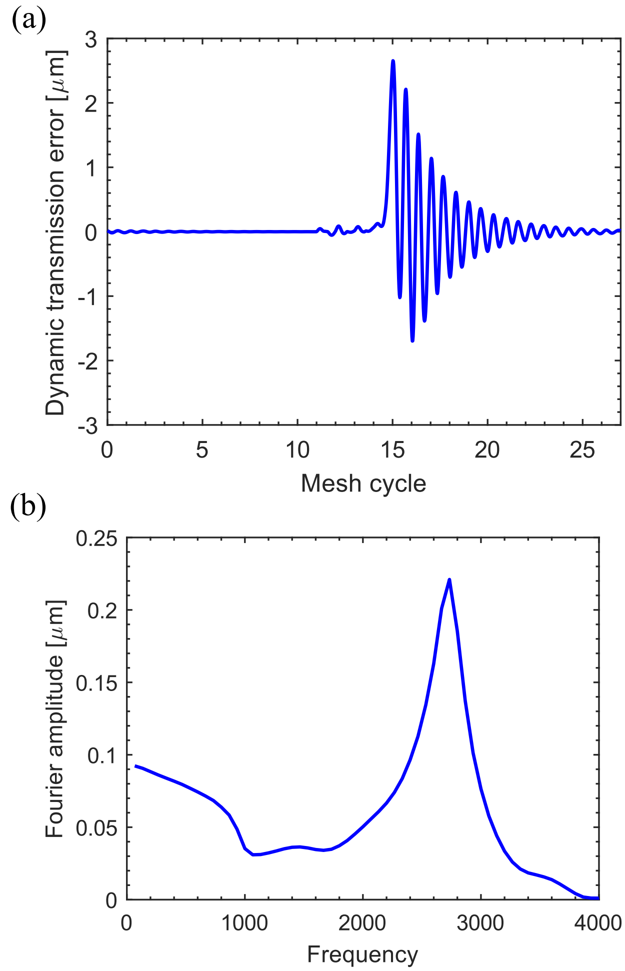

Figure 7.6: (a) The damage-induced dynamic response and (b) frequency spectrum of the gear pair with 20 percent crack on the pinon tooth.

The damage-induced dynamic response shown in Figure 7.6(a) is calculated at one mesh frequency of 1800 Hz or speed of 4000 rpm. At this speed, the damage-induced dynamic response exhibits impulse-like dynamic behavior. The damage-induced dynamic response can also display quasi-static behavior. To determine the speed range at which the damage-induced dynamic response transitions between quasi-static and impulse-like behavior, the exact difference signal is computed for the static case of the gear pair and the maximum amplitude in the frequency spectrum is observed to be 0.085 μm and 0.298 μm for

20 percent and 50 percent crack lengths. The damage-induced dynamic response of the gear pair for varying speeds from 200-4000 Hz is determined and the maximum amplitude in their frequency spectrum is plotted against the varying speed. Figure 7.7 shows the maximum amplitude in the frequency spectrum of the damage-induced dynamic response for varying speeds and varying damage lengths. The maximum amplitudes determined in the static case are used as threshold values (blue dashed line) above which the damage-induced dynamic response will exhibit an impulse-like response. It is observed that the gear pair with tooth root crack damage on a single tooth of the pinion will have an impulse-like damage-induced dynamic response for speeds greater than a third of the natural frequency ($f_n/3$). Below the third of natural frequency, except at the harmonics of the natural frequency, the maximum amplitudes of the spectrum are less than the threshold value.

7.5 Conclusions

The analytical lumped-parameter model is used to determine the dynamic response of the gear pair without damage and with tooth root crack damage. The static transmission error and mesh stiffness, the tooth mesh interface parameters in the lumped-parameter model are used from the static analysis of the finite element/contact mechanics model of the gear pair. The dynamic response of the gear pair without damage is observed to be periodic for every mesh cycle and the frequency spectrum contains only the amplitudes at the mesh frequency harmonics. The tooth root crack damage on a single tooth of the pinion of the gear pair has transients due to the engagement of the damaged tooth. The amplitudes of the dynamic transmission error increased with an increase in the damage severity. The frequency spectrum of the damaged gear pair has amplitudes at the natural frequency of the gear pair other than the amplitudes at mesh frequency harmonics. The lumped-parameter model is used to evaluate for varying speeds to determine the nonlinear

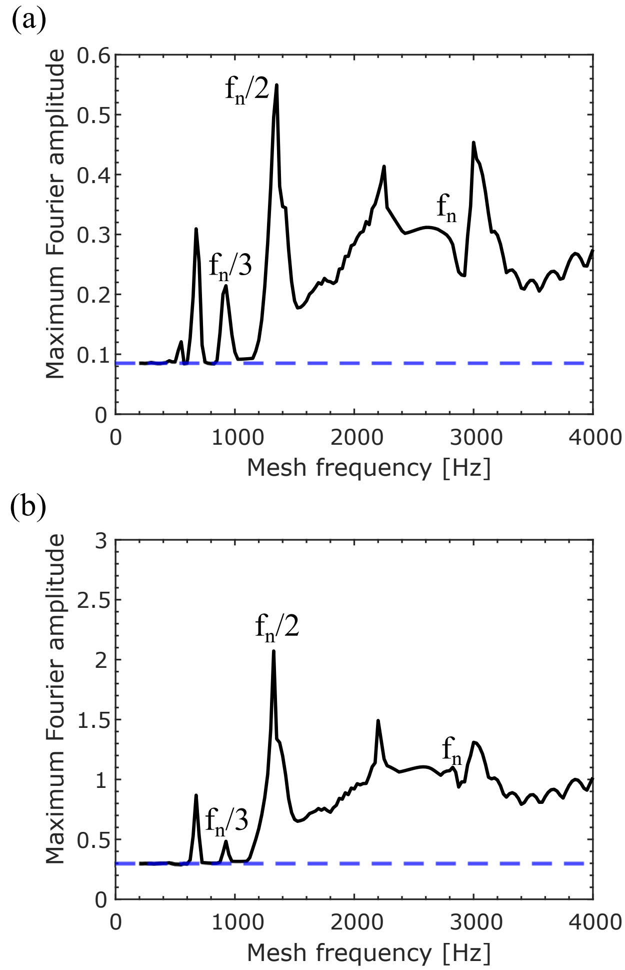

Figure 7.7: The maximum Fourier amplitude in the spectrum of the damage-induced dynamic response for varying speeds of the gear pair with (a) 20 percent and (b) 50 percent tooth root crack damage on the pinion. The blue dashed line represents the maximum Fourier amplitude analyzed at static speed of 1 Hz.

dynamic response of the gear pair without damage and with tooth root crack damage. The response has softening nonlinearity with primary and secondary resonances. The damaged gear pair increased the amplitudes of the nonlinear dynamic response at all speeds. Multiple steady-state responses are possible for the gear pair at speeds of 1700 to 2300 Hz. The results from the upper branch of the nonlinear response have higher amplitudes compared to the lower branch results and more contact loss is observed for the upper branch responses. The damage-induced dynamic response or the exact difference signal for the gear pair exhibits impulse-like dynamic responses for speeds greater than a third of the natural frequency.

CHAPTER EIGHT

CONCLUSIONS AND FUTURE WORK

8.1 Conclusions

Health and Usage Monitoring Systems (HUMS) are used in the geared transmission to monitor the condition of the gear teeth, ensuring the reliability and safety of the system. One of the functions of HUMS is to acquire vibration damage data from sensors on the geared transmission and evaluate the system's condition using statistical indications derived from the vibration signals. The statistical indicator values are used to detect the presence of damage in the geared transmission. The challenge lies in isolating the vibrations caused by damage from the normal meshing vibrations, which requires characterizing the accelerations of the geared transmission both when all gear teeth are healthy without damage and when damage is present. A thorough understanding of the dynamic response of the gear pair and the integration of damage is essential for accurately isolating the damage related vibrations in the geared transmissions.

Accurate dynamic response of the gear pair requires precise tooth mesh interface parameters, which are determined using a finite element/contact mechanics (FE/CM) approach. Tooth mesh interface parameters involve evaluating the static transmission error and mesh stiffness for teeth with damage, such as root cracks or surface pitting. The characterization of the tooth mesh is assessed for damage occurring on a single tooth. The FE/CM method effectively predicts the tooth mesh stiffnesses for a healthy unity-ratio gear pair, as well as for those with root cracks or surface pitting by comparing the results to the published literature. The root crack damage is observed to affect the global deformations of the gear while the pitting damage affected the local deformations near the tooth surface. The contact conditions and load distributions are altered in the presence of damage. Many parametric studies of gear pairs with root cracks or surface pitting damage are carried out for the unity-ratio and nonunity-ratio spur gear pairs to understand the effect of damage on the tooth mesh interface parameters. As the size of the pitting damage or the length of the cracks increases, the static transmission error tends to increase, while the tooth mesh stiffness decreases. The tooth mesh interface parameter with root cracks deviates from the healthy for the duration equal to the contact ratio of the gear pair regardless of the crack length, whereas, the pitting damage effects are very local in the mesh cycle. The length of pitting damage in the profile direction is the factor for the amount of duration that deviates from healthy. The differences in the duration of these effects, observed between surface pitting and root crack, could potentially allow for their detection through static transmission error or mesh stiffness measurements.

The dynamic transmission error of the gear pair is calculated using a lumped-parameter model, which correlated very well with the dynamic response results from the FE/CM gear pair model. The lumped-parameter model predicts well for the gear pair with tooth root cracks and surface pitting damage. The increase in the damage severity increased the amplitudes of the dynamic response of the gear pair. The frequency spectrum of the damaged gear pair has amplitudes at the natural frequency of the gear pair other than the amplitudes at mesh frequency harmonics. The larger damage amounts showed prominent nonlinearity behavior both in the dynamic response and its spectrum. The dynamic response evaluated for varying speeds shows softening nonlinearity for the gear pair without damage and the gear pair with damage. The dynamic transmission error evaluated in the upper branch has higher amplitudes, and more tooth contact loss compared to the lower branch nonlinear dynamic response. The damage-induced dynamic response or the exact difference signal of the gear pair isolates the vibrations that are purely due to damage from the normal meshing vibrations in the damaged gear pair. The damage-induced dynamic response or the exact difference signal for the gear pair exhibits impulse-like dynamic responses for speeds greater than a third of the natural frequency. The condition indicators RMS, FM4, and M8A are evaluated using the damage-induced dynamic response and observed higher values than typical thresholds, which clearly indicate the presence of damage in the gear pair. The damage-induced dynamic response has oscillating behavior with decaying amplitudes for high speeds. A phenomenon-based model based on the underdamped, free vibration of a linear oscillator was proposed. The phenomenon-based model was shown to accurately capture the damage-induced dynamic response. Good agreement was observed for the RMS values determined from the damage-induced dynamic response obtained from the FE/CM model and the phenomenon-based model. FM4 and M8A values tend to deviate for higher amounts of damage due to the increase in the nonlinear nature of the damage-induced dynamic response. The simplicity of the phenomenon-based model permitted to derive the closed-form expressions for condition indicators by exploring the amplitude-domain formula. The expression for the probability density function of the phenomenon-based model response is determined and used to evaluate the closed-form expressions of the condition indicators. The condition indicators evaluated for varying amounts of damage using closed-form expression showed very good agreement with the numerically calculated condition indicators and also the dependency of damage parameters and gear pair dynamic properties were clearly observed with the closed-form expressions of the condition indicators. The RMS condition indicator was observed to be dependent on the amplitude of the phenomenon-based model and increases with increasing amount of damage. However, FM4 and M8A show constant condition indicator values due to the independence of amplitude in the closed-form expressions. The RMS is observed to decrease with the increase in the damping ratio or natural frequency or number of oscillation cycles and the FM4, M8A values show increasing behavior. The complete characterization of the dynamic response of the gear pair with localized defects provides a better understanding of the accelerations in the geared transmission with two stages.

Geared transmission housing vibrations are analyzed using the FE/CM approach that includes an accurate representation of the changing contact forces on the gear teeth, multiple reduction stages with different gear types, the mechanical coupling between stages, and damage. The housing accelerations contain dynamics from both the planetary and spiral-bevel stages of the geared transmission. The FE/CM model results were observed to capture the overall characteristics of the geared transmission when validated against the experimental results at the same measurement location. The frequency spectrum of the housing accelerations has frequency content that appears in the form of clusters at the planetary and spiral-bevel stage mesh frequency harmonics. The tooth root crack damage is analyzed for varying lengths to quantify the effects of damage severity. The ring damaged housing accelerations were observed to have similar increases in the transients and amplitudes at all engagements because of the stationary nature of the measurement location and the ring gear. However, in the sun damaged housing accelerations this is changed completely due to damage on the rotating gear relative to the measurement location on the housing. In both cases, the crack lengths less than 50 percent through its tooth thickness do not show significant differences when compared to the healthy accelerations. Modest changes to the amplitudes of the planetary stage mesh frequency and sidebands are observed for both ring damaged and sun damaged accelerations. The time synchronous averaging (TSA) techniques worked quite well for the ring damaged accelerations, however, for the sun damaged, the damage content in the acceleration is observed to be averaged out in the process. The approximate difference signal and exact difference signal or damage-induced dynamic response calculation methods are used to isolate the damaged accelerations from the normal meshing vibrations. Their performance is evaluated using the FM4 condition indicator values against the threshold value of 3. The ring damaged transmissions have FM4 values very near to the threshold value for crack lengths less than 50 percent when evaluated using the approximate difference signal while the exact difference signal has FM4 values an order of magnitude higher than the threshold value. Unlike similar values for TSA over the planet-pass period and TSA over the carrier period in the ring-damaged transmission, the sun damaged transmission has different FM4 values for both TSA processes. The presence of damage on the sun tooth in the geared transmission is determined using the FM4 values evaluated with TSA over the carrier period exact difference signal and unaltered (no TSA) exact difference signals. The damage detection of root cracks on the ring or sun gear tooth in the geared transmission is possible with the FM4 condition indicator using the exact difference signal at all measurement locations placed at the planetary stage level on the housing circumference. The exact difference signal contains accelerations purely due to damage and the other normal meshing vibrations are removed. This research work provides development to the HUMS to detect the presence of damage in the geared transmission at an early stage of failure.

8.2 Future Work

- This work focused on the nonlinear dynamic response of the spur gear pairs calculated for gear pairs with healthy teeth and gear pairs with tooth root crack damage. The effect of tooth root crack damage on tooth contact forces and tooth contact loss are to be studied. The analysis of the nonlinear dynamic response of the gear pair with tooth surface pitting damage is also recommended. The validation of the finite element/contact mechanics (FE/CM) results of tooth mesh interface parameters, dynamic responses for nonunity-ratio gear pair with tooth root crack and tooth surface pitting damage can be validated against the experimental results.

- The damage-induced dynamic response of the gear pair consists of one natural frequency of the gear pair. Based on the resemblance of the damage-induced dynamic response to the underdamped linear oscillator response, a phenomenon-based model is used and the closed-form expressions for the condition indicators are derived. This work can be extended to the planetary system which will have multiple frequencies and will help understand the dependence of planetary system dynamic properties on the condition indicators and later to complete geared transmission system.

- Geared transmission housing accelerations are determined using the FE/CM model for transmission with all gear teeth healthy and transmission with tooth root crack damage on ring or sun gear. It is recommended to characterize the transmission for tooth surface pitting damage, damage on the planet gear tooth which meshes with both sun gear and ring gear, and damage in spiral-bevel gears tooth. The characterization of the transmission accelerations is to be explored for measurement locations not only on the housing but on other components of the geared transmission.

- In this dissertation, the condition indicator FM4 detects the presence of tooth root crack damage for sun and ring gear tooth when calculated using the damage-induced dynamic response or the exact difference signal accelerations. Vibration separation methods can be used to further the development of damage detection in the geared transmission.

- Artificial Intelligence and Machine Learning techniques need to be implemented on the geared transmission for the condition monitoring of the gear tooth in the transmission. The ability to pinpoint the damaged tooth location needs to be achieved for more reliable and safe geared transmissions.

APPENDIX A

ADDITIONAL CONDITION INDICATOR RESULTS FOR RING DAMAGE IN GEARED TRANSMISSION

The performance of additional condition indicators for the housing accelerations of transmission without damage and transmission with varying amounts of damage on space-fixed or ring gear tooth at location shown in Figure 5.1(b) is evaluated.

A.1 RMS

The root mean squared (RMS) of the vibration signal is calculated from [146]

$$\text{RMS} = \sqrt{\frac{1}{N}\sum_{i=1}^{N}(a_i)^2} \tag{A.1}$$

where $a_i = a(t_i)$ is the acceleration at time t_i and the index $i = 2, 3, \ldots, N$, where N is the total number of time steps in the vibration signal. The units of the RMS are the same as those of the input signal. The RMS provides an overall measure of the energy in the signal [88]. Damage to the gear teeth will result in more vibrations than when all gears are healthy. These increases in vibration will lead to increases in energy that will be seen in RMS calculations.

Figure A.1 shows the RMS calculation of the transmission vibrations for the case that the transmission is healthy and without damage and when one tooth on the ring has a root crack of varying length. The RMS of the original accelerations are shown by square markers. The vibrations used in this calculation contain components from the spiral bevel gear stage, in addition to the planetary gear stage. The accelerations using TSA over the planet-pass period (circle marker) and the carrier cycle (cross marker) are also shown. The RMS values for the unaltered accelerations without TSA are larger than those processed with TSA for all amounts of damage, as expected, because of the added vibration components from the spiral bevel gear stage. For this transmission, the spiral bevel stage dynamics result in an increase of approximately 1.5 g in the RMS values. We note the RMS values for TSA using the planet-pass cycle (circle markers) are nearly identical to those for the carrier cycle (cross markers). Either method of using TSA would be acceptable to remove the spiral bevel gear stage vibrations.

The percentage change in the RMS (with respect to the RMS of the healthy transmission without damage) is shown in Figure A.1(b). The change in the percentage of RMS calculated from unaltered accelerations without TSA are similar to those for accelerations processed using TSA. For the crack lengths below 50 percent of the tooth thickness of the ring, the RMS percentage change decreases with increasing damage, although the decrease is within one percent of the healthy RMS value. For an 80 percent crack length meaningful increases in the vibration occur, however, these vibrations only result in a few percent increases in the RMS calculation. The ability to detect damage from changes in the RMS values is uncertain.

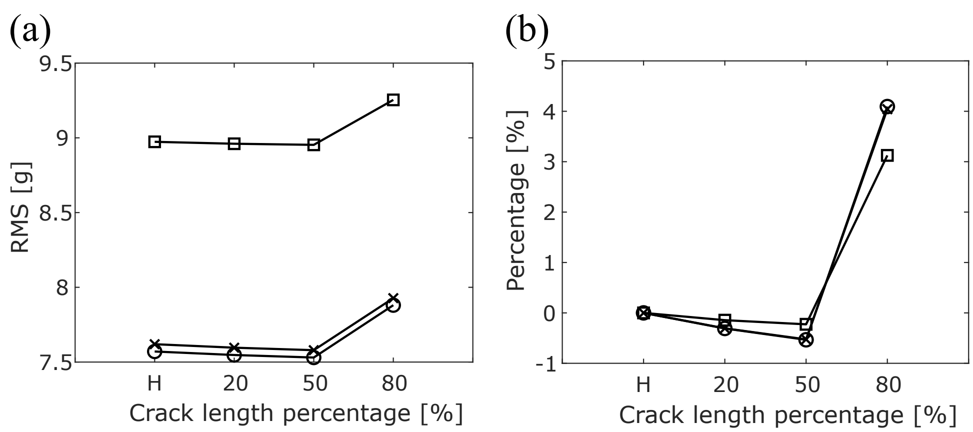

Figure A.1: (a) The RMS condition indicator value of the healthy transmission without damage (H) compared to the cases with tooth root crack damage on a single ring tooth with varying crack lengths. (b) The percentage change of RMS with respect to the healthy transmission without damage. The square markers are for unaltered accelerations without TSA. The circle and cross markers are for the accelerations processed using TSA over the planet-pass and carrier cycle, respectively.

A.2 Crest Factor

The Crest Factor (CF) is determined from the ratio of the maximum absolute value of acceleration to the RMS of the signal [148]

$$\mathrm{CF} = \frac{\max(|a|)}{\mathrm{RMS}} \tag{A.2}$$

The Crest Factor is generally more sensitive to damage than the RMS because it varies with changes in the amplitudes of the vibration [5]. Alternate definitions of Crest Factor have been used. One alternate definition is the ratio of the peak-to-peak of the acceleration to the RMS. Another is the ratio of maximum acceleration to the RMS of the signal. We have observed meaningfully different Crest Factor calculations using these three different formulae. We use Eq. (2) for calculating the Crest Factor in this work.

Figure A.2(a) compares the values of Crest Factor calculated from the accelerations without TSA (square markers) to those with TSA over the planet-pass period (circle markers) and the carrier period (cross markers). The Crest Factors for the accelerations without TSA are larger than those with TSA for the healthy, undamaged transmission and the damaged transmission with tooth root cracks of length 50 percent and below. Interestingly, the Crest Factor for the 80 percent tooth root crack length is larger for accelerations processed using TSA than for those without TSA. The percentage change of Crest Factor values with tooth root crack damage are shown in Figure A.2(b). The Crest Factor value for 80 percent crack length increased by almost 100 percent when TSA was used. The percentage change of Crest Factor values for crack lengths less than 50 percent is less than five percent. This Crest Factor condition indicator showed a clear indication of damage when the ring tooth crack length was 80 percent through the thickness of the tooth.

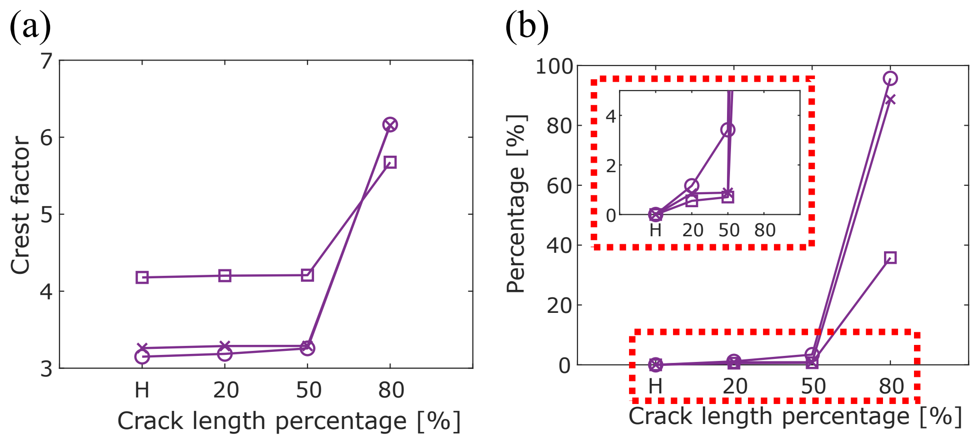

Figure A.2: (a) The Crest Factor condition indicator value of the healthy transmission without damage (H) compared to cases with tooth root crack damage on a ring tooth with varying crack lengths. (b) The percentage change of the Crest Factor with respect to the system without damage. The square markers are for unaltered accelerations without TSA. The circle and cross markers are for the accelerations processed with TSA over the planet-pass and carrier cycle, respectively.

A.3 Kurtosis

The kurtosis of the acceleration provides a measure of the distribution of its amplitudes. The kurtosis is the fourth moment of the acceleration normalized by the square of its variance, which is calculated from

$$\text{Kurtosis} = \frac{N\sum_{i=1}^{N}(a_i - \bar{a})^4}{[\sum_{i=1}^{N}(a_i - \bar{a})^2]^2} \tag{A.3}$$

where $\bar{a}$ is the mean of the acceleration. The value of kurtosis for an acceleration with amplitudes that differ according to a normal distribution is equal to three. The kurtosis values of the accelerations for the healthy transmission without damage and those with a ring tooth root crack of varying length are shown in Figure A.3(a). The percentage changes are shown in Figure A.3(b). The kurtosis values of the accelerations without TSA (square markers) are not offset from those calculated from accelerations with TSA (circle and cross markers). This differs with that for RMS (Figure A.1) and Crest Factor (Figure A.2), where the vibrations generated by the input spiral bevel stage led to meaningful increases in the indicator.

The kurtosis values in Figure A.3 are nearly identical for root cracks that have lengths of 50 percent or smaller. More substantial increases in the kurtosis occur when the crack length increases from 50 percent to 80 percent of the tooth thickness. The corresponding percentage change for an 80 percent crack length is nearly 35 percent for the accelerations with TSA. The increase is only 15 percent for accelerations without TSA.

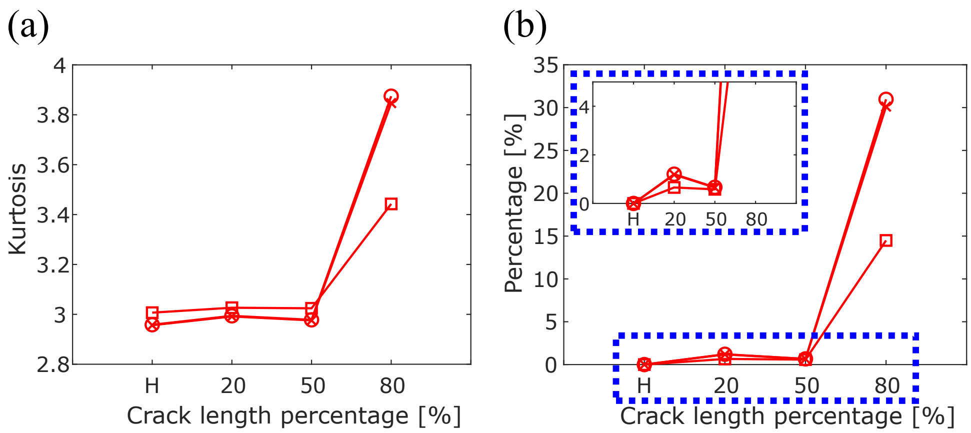

Figure A.3: (a) The kurtosis condition indicator value of the healthy transmission without damage (H) compared to cases with tooth root crack damage on ring gear tooth with varying crack lengths. (b) The percentage change of kurtosis with respect to the system without damage kurtosis value is calculated. The square markers are for unaltered accelerations without TSA. The circle and cross markers are for the accelerations processed with TSA over the planet-pass and carrier cycle, respectively.

A.4 Energy Operator

The energy operator is calculated using Eq. (A.3) with a modified input signal $\hat{a}(t)$. The value of the signal $\hat{a}(t)$ at time t_i is calculated from $\hat{a}_i = a_i^2 - (a_{i+1} \cdot a_{i-1})$ for $i = 2, 3, \ldots, N-1$. The first (last) element is calculated from $\hat{a}_1 = a_1^2 - a_2 \cdot a_N$ ($\hat{a}_N = a_N^2 - a_1 \cdot a_{N-1}$). The energy operator values and their percentage change are shown in

Figure A.4. The changes in the values of the energy operator are similar to those of the kurtosis (Figure A.3). We note the values, and their percentages, are larger than those for kurtosis, which may be beneficial for damage detection.

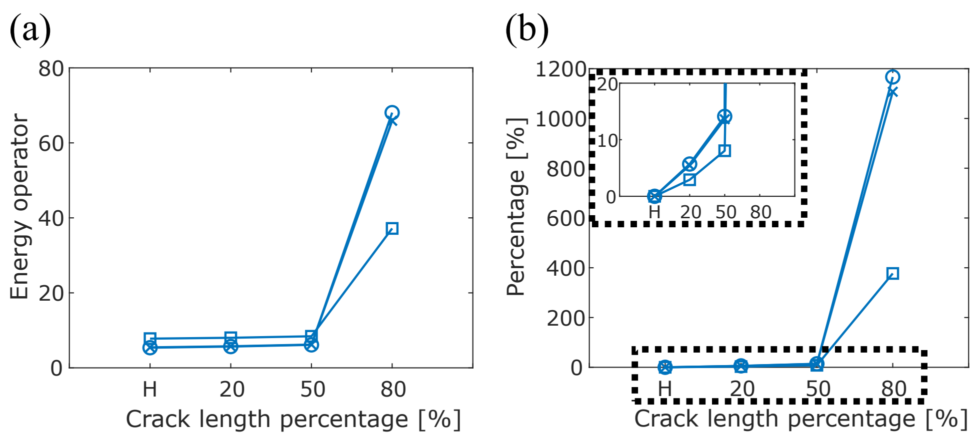

Figure A.4: (a) The energy operator condition indicator value of the healthy transmission without damage (H) compared to cases with tooth root crack damage on a ring tooth with varying crack lengths. (b) The percentage change of energy operator with respect to the system without damage energy operator value is calculated. The square marker line contains energy operator values of the original signal accelerations, and the circle marker and cross marker lines contain the energy operator of the TSA signal accelerations over the planet-pass and carrier cycle mesh period.

The RMS, Crest Factor, Kurtosis, and Energy Operator calculated using the planet-pass cycle during TSA differ by less than five percent from those calculated using the carrier cycle in TSA. These results suggest that either the planet-pass period or the carrier period may be used for TSA calculations. Figure A.5 shows the values of RMS and Kurtosis calculated from accelerations processed using TSA of varying number of cycles. We note that these results are not calculated from actual FE/CM results obtained through extremely long simulations. Instead, because we have confirmed the periodicity of these waveforms to be three-carrier cycles, we create artificial waveforms by appending multiple blocks of three-carrier cycle vibrations to the original signal. The RMS values decrease monotonically with increasing number of planet-pass cycles for nine and fewer cycles (Figure A.3(a)). The RMS values deviate slightly as the number of planet-pass cycles increases to 12 and 15. At 18 planet-pass cycles, the RMS value is nearly identical to that at nine planet-pass cycles. This pattern then repeats for each additional nine planet-pass cycles. The housing accelerations are exactly periodic every nine planet-pass cycles. This result is not specific to the RMS; the Kurtosis values show similar behavior. The results in Figure A.5 suggest that condition indicators are most accurately calculated from accelerations processed using TSA when multiples of three carrier cycles or, alternatively, nine planet-pass cycles are used. The crest factor and energy operator (not shown) have similar behavior for varying number of cycles used in the TSA calculation as the kurtosis. Because the results for the condition indicator do not differ with the choice of planet-pass or carrier cycle used in the TSA calculations, we will only present results using TSA with the planet-pass cycle in the remainder of this work.

A.5 RMS Difference

The RMS difference condition indicator is calculated from Eq. (A.1) using the difference signal $d(t)$ in place of the acceleration $a(t)$. The calculated values of RMS difference are shown in Figure A.6(a). The percentage changes from the signal without damage are shown in Figure A.6(b). The values of the RMS calculated from the difference signal (Figure A.6) are lower than those of the RMS calculated from the acceleration (Figure A.1). The values for the RMS of the difference signal in Figure A.6 increase noticeably for the cases of 20 percent and 50 percent tooth root crack lengths when compared to the baseline, healthy case. Increases in RMS below 80 percent root crack length were not observed when the RMS was calculated from the accelerations directly (see Figure A.1). The large tooth root crack with 80 percent length through the thickness results in a more

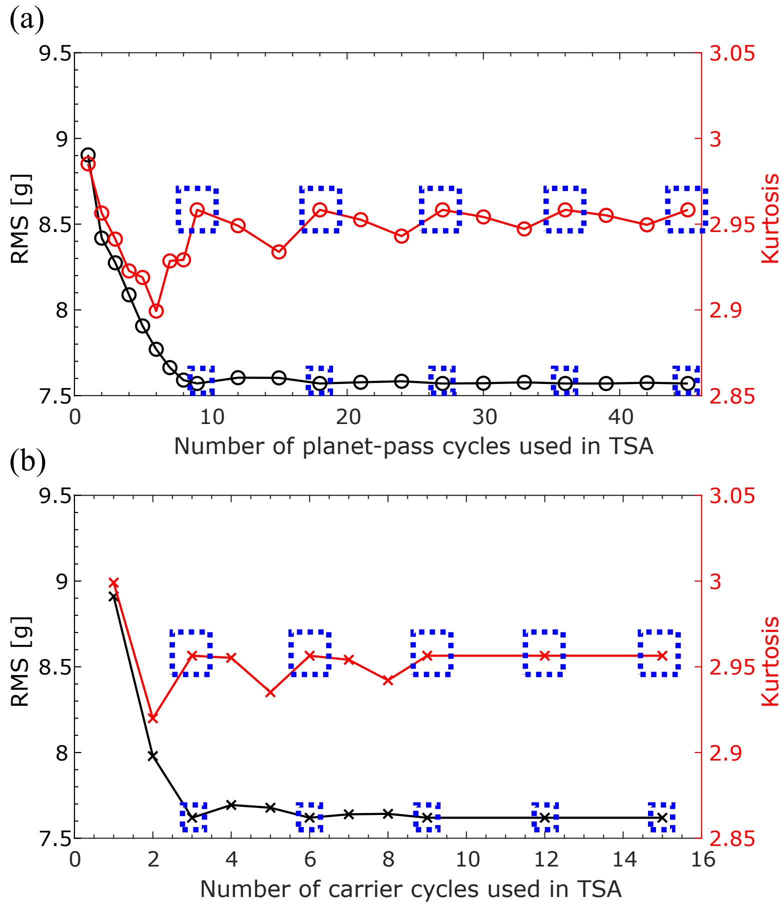

Figure A.5: The condition indicators values for RMS and kurtosis of the transmission without damage for varying numbers of (a) planet-pass cycles and (b) carrier cycles used in the calculation of the TSA signal accelerations. The black line corresponds to the RMS condition indicator values and the red line for kurtosis values. The condition indicator values of TSA signal accelerations with multiples of three (nine) for carrier (planet-pass) rotations are denoted by the blue dotted box.

substantial increase in the RMS of the difference signal. The percent change in this case was 12.5 percent.

Overall, the RMS of the difference signal is more sensitive to the damage than the RMS calculated from accelerations. Even with the improvements using the difference signal, the percentage changes in the RMS due to damage remain below those for the Crest Factor, Kurtosis, and Energy Operator.

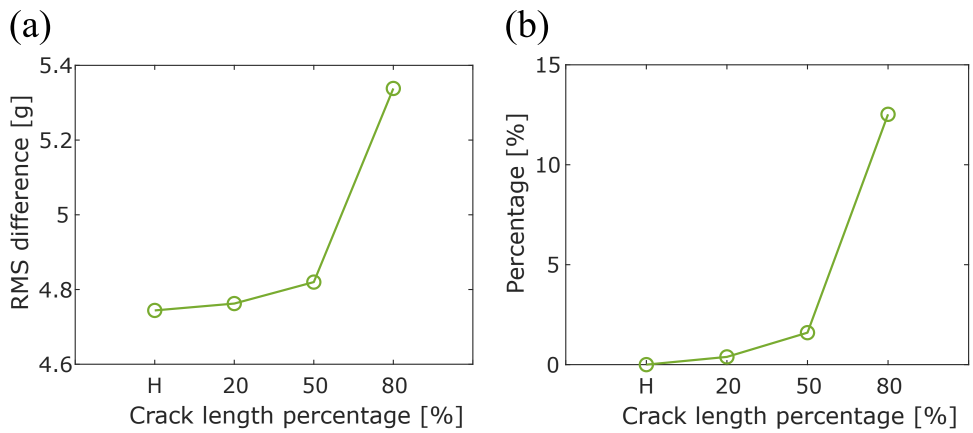

Figure A.6: (a) The RMS (calculated from the difference signal) condition indicator value of the healthy transmission without damage (H) compared to cases with tooth root crack damage on ring tooth with varying crack lengths. (b) The percentage change of RMS (calculated from the difference signal) with respect to the healthy transmission without damage for varying crack size.

A.6 M8A

The M8A condition indicator is given by [147]

$$\mathrm{M8A} = \frac{N^3 \sum_{i=1}^{N} (d_i - \bar{d})^8}{[\sum_{i=1}^{N} (d_i - \bar{d})^2]^4} \tag{A.4}$$

M8A is thought to be more sensitive to peaks in the difference signal because it is calculated from the eight-moment of the difference signal divided by the fourth power of variance. Figure A.7 shows the M8A values. Like for many of the previously presented indicators, the M8A values have modest changes for crack lengths 50 percent through the tooth thickness and less, but substantial changes when the tooth root crack length reaches 80 percent through the tooth thickness. The M8A value obtained for Gaussian noise is 105. Using this as a threshold, ring root crack damage of 50 percent length and less would be difficult to detect using M8A. The substantial increase beyond 105 for 80 percent crack length would likely make it detectable.

(a) (b)

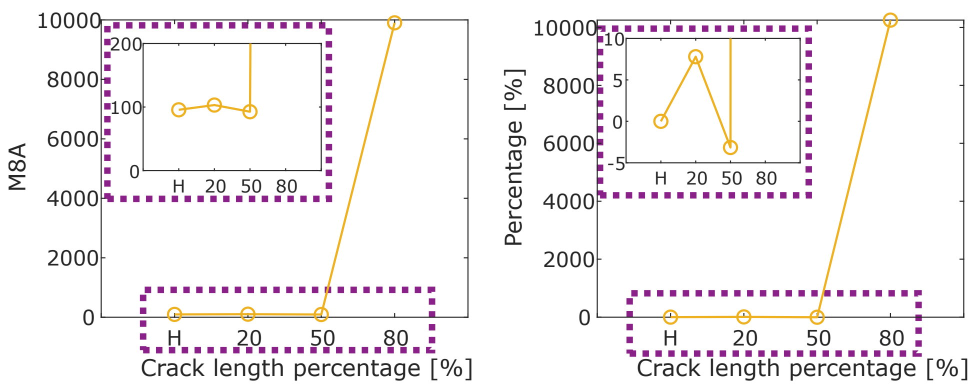

Figure A.7: (a) The M8A condition indicator value of the healthy transmission without damage (H) compared to cases with tooth root crack damage on ring tooth with varying crack lengths. (b) The percentage change of M8A with respect to the healthy transmission without damage.

APPENDIX B

ADDITIONAL CONDITION INDICATOR RESULTS FOR SUN DAMAGE IN GEARED TRANSMISSION

The performance of additional condition indicators for the housing accelerations of transmission without damage and transmission with varying amounts of damage on rotating or sun gear tooth is evaluated.

B.1 RMS, Crest Factor, Kurtosis, and Energy Operator

The raw signal condition indicators are evaluated for the vibration signals without modifications to their frequency spectrum. The input signals used to evaluate the RMS, crest factor, kurtosis, and energy operator condition indicators are the housing accelerations (unaltered), TSA over planet-pass, and TSA over carrier period vibration signals. Figure B.1 shows the raw signal condition indicators evaluated for healthy transmission and transmission with sun crack damage at varying amounts. The RMS of unaltered accelerations are higher because it contains dynamics from both stages of the transmission. The RMS values for TSA processed signals are similar for healthy transmission and transmission with less than 50 percent crack lengths of the sun gear tooth. The crest factor, kurtosis, and energy operator condition indicator values remain similar to the healthy transmission values for crack lengths less than 50 percent. Minimal changes are observed in these condition indicators for varying their input signal. The raw signal condition indicators deviate from the healthy transmission values for 80 percent tooth root crack damage with all different input signals.

B.2 RMS Difference, Energy Ratio, M8A, and NA4

RMS difference, energy ratio, and M8A condition indicators use approximate difference signal as its input. The input for the NA4 condition indicator is the residual signal accelerations. The approximate difference signal and residual signal are derived from the TSA over planet-pass and TSA over carrier period signals. In this work, the housing accelerations are analyzed with only one simulation, at constant torque. This results in $M = 1$ in the NA4 condition indicator evaluation. The NA4 condition indicator calculated

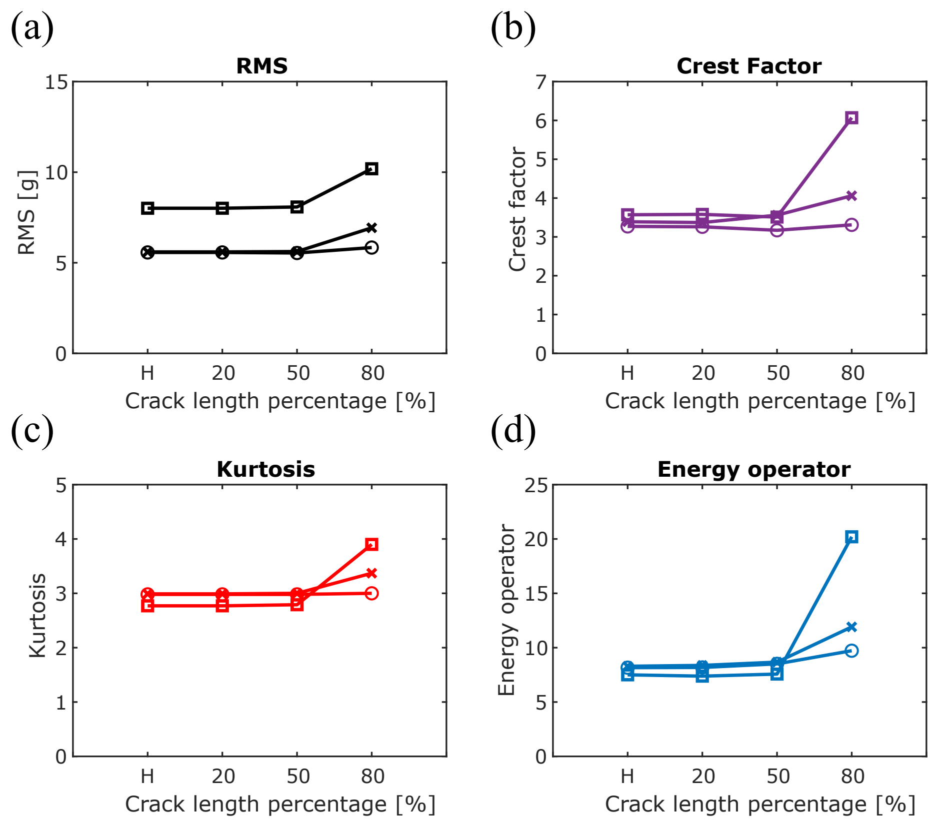

Figure B.1: The (a) RMS, (b) crest factor, (c) kurtosis, and (d) energy operator condition indicators value of the healthy transmission without damage (H) compared to the cases with tooth root crack damage on a single sun tooth with varying crack lengths. The square markers are for unaltered accelerations without TSA. The circle and cross markers are for the accelerations processed using TSA over the planet-pass and carrier cycle, respectively.

provides the residual kurtosis value of the vibration signal in this work. Figure B.2 shows the condition indicators evaluated for healthy transmission and transmission with sun crack damage at varying amounts. These condition indicators provide the same result as raw signal condition indicators that only the 80 percent crack length showed deviation from the healthy transmission values. The condition indicators evaluated using TSA over the carrier and planet-pass period only differ for 80 percent crack length.

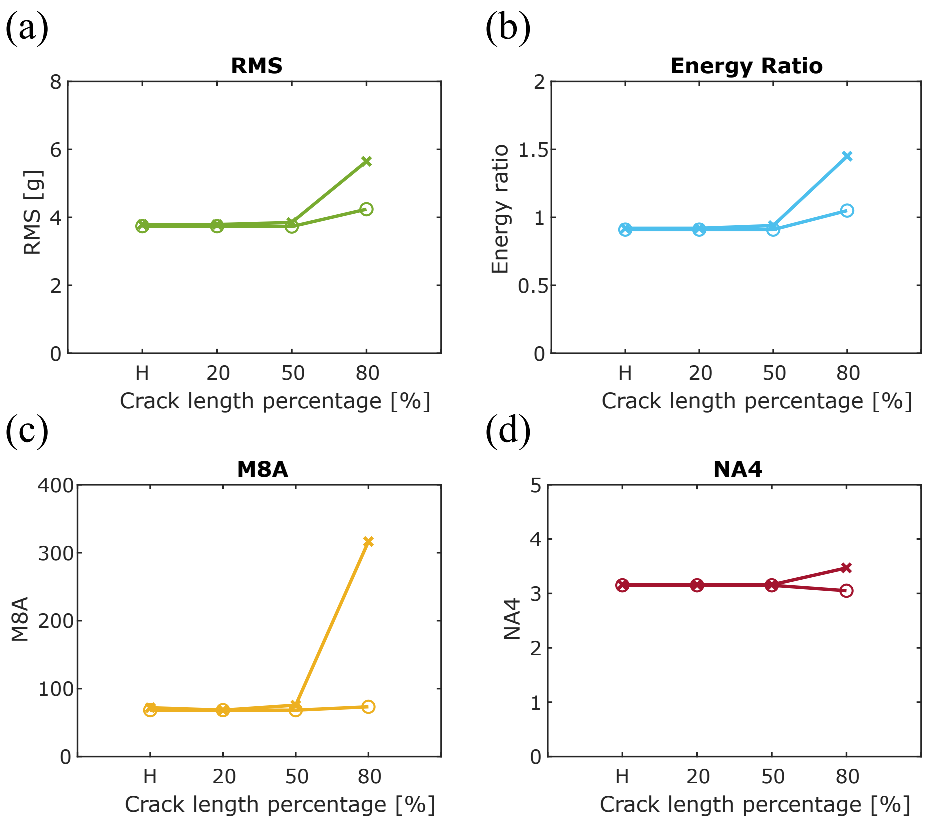

Figure B.2: The (a) RMS difference, (b) energy ratio, (c) M8A, and (d) NA4 condition indicators value of the healthy transmission without damage (H) compared to the cases with tooth root crack damage on a single sun tooth with varying crack lengths. The circle and cross markers are for the accelerations processed using TSA over the planet-pass and carrier cycle, respectively.

B.2.1 Exact Difference Signal Condition Indicators

The RMS difference and M8A condition indicators are evaluated for the exact difference signal or the damage-induced dynamic response vibrations for the TSA processed and unaltered housing vibrations. Figure B.3 shows the condition indicators evaluated transmission with sun crack damage at varying amounts. The M8A condition indicator values evaluated using TSA over planet-pass period (circle markers) exact difference signal shows poor performance compared to the unaltered (square markers) and TSA over carrier period (cross markers) accelerations. It is observed that the M8A values for TSA over the planet-pass period do not show monotonic increase with the increase in the damage severity. Comparing the M8A values of unaltered and TSA over carrier period exact difference signal accelerations to the threshold value of 105, the presence of the sun tooth root crack damage in the geared transmission is detected, even for the smaller crack lengths.

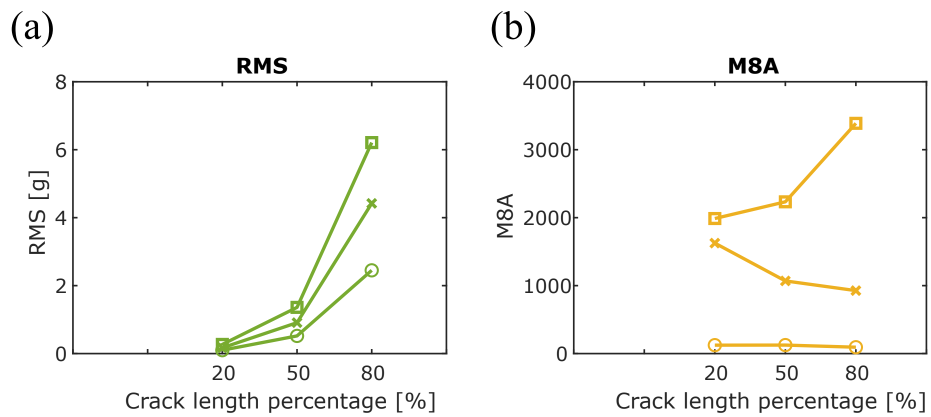

Figure B.3: The (a) RMS difference and (b) M8A condition indicators values for the exact difference signal of tooth root crack damage on a single sun tooth with varying crack lengths. The square markers are for unaltered accelerations without TSA. The circle and cross markers are for the accelerations processed using TSA over the planet-pass and carrier cycle, respectively.

REFERENCES

[1] Y. Huangfu, K. Chen, H. Ma, X. Li, H. Han, and Z. Zhao, “Meshing and dynamic characteristics analysis of spalled gear systems: A theoretical and experimental study,” *Mechanical Systems and Signal Processing*, vol. 139, p. 106640, May 2020.

[2] D. Huebler, “OH-58 helicopter transmission, NASA Technology Images - https://nara.getarchive.net/media/oh-58-helicopter-transmission-950b56,” Oct. 1976.

[3] A. Hood, *Fault detection on a full-scale OH-58 A/C helicopter transmission*. Doctoral dissertation, University of Maryland, College Park, 2010.

[4] D. G. Lewicki, K. E. LaBerge, R. T. Ehinger, and J. Fetty, “Planetary gearbox fault detection using vibration separation techniques,” *AHS 67 Annual Forum-Virginia Beach, VA*, p. 14, 2011.

[5] P. D. Samuel and D. J. Pines, “A review of vibration-based techniques for helicopter transmission diagnostics,” *Journal of Sound and Vibration*, vol. 282, pp. 475–508, Apr. 2005.

[6] P. J. Dempsey, D. G. Lewicki, and D. D. Le, “Investigation of current methods to identify helicopter gear health,” in *2007 IEEE Aerospace Conference*, (Big Sky, MT, USA), pp. 1–13, IEEE, 2007.

[7] F. 52, “An orthographical image of the Bell 206A - https://commons.wikimedia.org/wiki/File:Bell_206a_orthographical_image.svg,” Oct. 2014.

[8] W. D. Mark, “Analysis of the vibratory excitation of gear systems: Basic theory,” *The Journal of the Acoustical Society of America*, vol. 63, pp. 1409–1430, May 1978.

[9] H. N. Özgüven and D. R. Houser, “Dynamic analysis of high speed gears by using loaded static transmission error,” *Journal of Sound and Vibration*, vol. 125, pp. 71–83, Aug. 1988.

[10] P. Velex and M. Ajmi, “On the modelling of excitations in geared systems by transmission errors,” *Journal of Sound and Vibration*, vol. 290, pp. 882–909, Mar. 2006.

[11] R. W. Gregory, S. L. Harris, and R. G. Munro, “Dynamic behaviour of spur gears,” *Proceedings of the Institution of Mechanical Engineers*, vol. 178, pp. 207–218, June 1963.

[12] A. Kahraman and R. Singh, "Non-linear dynamics of a spur gear pair," *Journal of Sound and Vibration*, vol. 142, pp. 49–75, Oct. 1990.

[13] A. Kahraman and G. W. Blankenship, "Experiments on nonlinear dynamic behavior of an oscillator with clearance and periodically time-varying parameters," *Journal of Applied Mechanics*, vol. 64, pp. 217–226, Mar. 1997.

[14] R. Parker, S. Vijayakar, and T. Imajo, "Non-linear dynamic response of a spur gear pair: Modelling and experimental comparisons," *Journal of Sound and Vibration*, vol. 237, pp. 435–455, Oct. 2000.

[15] S. Li and A. Kahraman, "Influence of dynamic behaviour on elastohydrodynamic lubrication of spur gears," *Proceedings of the Institution of Mechanical Engineers Part J-Journal of Engineering Tribology*, vol. 225, pp. 740–753, Aug. 2011.

[16] A. Kahraman and G. W. Blankenship, "Effect of involute contact ratio on spur gear dynamics," *Journal of Mechanical Design*, vol. 121, pp. 112–118, Mar. 1999.

[17] V. K. Tamminana, A. Kahraman, and S. Vijayakar, "A study of the relationship between the dynamic factors and the dynamic transmission error of spur gear pairs," *Journal of Mechanical Design*, vol. 129, pp. 75–84, Jan. 2007.

[18] R. Kasuba and J. W. Evans, "An extended model for determining dynamic loads in spur gearing," *Journal of Mechanical Design*, vol. 103, pp. 398–409, Apr. 1981.

[19] H. Ma, J. Zeng, R. Feng, X. Pang, and B. Wen, "An improved analytical method for mesh stiffness calculation of spur gears with tip relief," *Mechanism and Machine Theory*, vol. 98, pp. 64–80, Apr. 2016.

[20] Y. Luo, N. Baddour, and M. Liang, "Effects of gear center distance variation on time varying mesh stiffness of a spur gear pair," *Engineering Failure Analysis*, vol. 75, pp. 37–53, May 2017.

[21] C. Xie, L. Hua, X. Han, J. Lan, X. Wan, and X. Xiong, "Analytical formulas for gear body-induced tooth deflections of spur gears considering structure coupling effect," *International Journal of Mechanical Sciences*, vol. 148, pp. 174–190, Nov. 2018.

[22] Y. Sun, H. Ma, Y. Huangfu, K. Chen, L. Che, and B. Wen, "A revised time-varying mesh stiffness model of spur gear pairs with tooth modifications," *Mechanism and Machine Theory*, vol. 129, pp. 261–278, Nov. 2018.

[23] X. Liang, H. Zhang, M. J. Zuo, and Y. Qin, "Three new models for evaluation of standard involute spur gear mesh stiffness," *Mechanical Systems and Signal Processing*, vol. 101, pp. 424–434, Feb. 2018.

[24] Y. Yang, L. Cao, H. Li, and Y. Dai, "Nonlinear dynamic response of a spur gear pair based on the modeling of periodic mesh stiffness and static transmission error," *Applied Mathematical Modelling*, vol. 72, pp. 444–469, Aug. 2019.

[25] Y. Xiong, K. Huang, F. Xu, Y. Yi, M. Sang, and H. Zhai, "Research on the influence of backlash on mesh stiffness and the nonlinear dynamics of spur gears," *Applied Sciences*, vol. 9, p. 1029, Mar. 2019.

[26] M. Pleguezuelos, M. B. Sánchez, and J. I. Pedrero, "Analytical model for meshing stiffness, load sharing, and transmission error for spur gears with profile modification under non-nominal load conditions," *Applied Mathematical Modelling*, vol. 97, pp. 344–365, Sept. 2021.

[27] H. Dai, X. Long, F. Chen, and C. Xun, "An improved analytical model for gear mesh stiffness calculation," *Mechanism and Machine Theory*, vol. 159, p. 104262, May 2021.

[28] C. Xie and X. Shu, "A new mesh stiffness model for modified spur gears with coupling tooth and body flexibility effects," *Applied Mathematical Modelling*, vol. 91, pp. 1194–1210, Mar. 2021.

[29] Q. Wang, K. Xu, T. Huai, H. Ma, and K. Wang, "A mesh stiffness method using slice coupling for spur gear pairs with misalignment and lead crown relief," *Applied Mathematical Modelling*, vol. 90, pp. 845–861, Feb. 2021.

[30] M. H. Arafa and M. M. Megahed, "Evaluation of spur gear mesh compliance using the finite element method," *Proceedings of the Institution of Mechanical Engineers, Part C: Journal of Mechanical Engineering Science*, vol. 213, pp. 569–579, June 1999. Publisher: IMECHE.

[31] L. Chang, G. Liu, and L. Wu, "A robust model for determining the mesh stiffness of cylindrical gears," *Mechanism and Machine Theory*, vol. 87, pp. 93–114, May 2015.

[32] C. Natali, M. Battarra, G. Dalpiaz, and E. Mucchi, "A critical review on FE-based methods for mesh stiffness estimation in spur gears," *Mechanism and Machine Theory*, vol. 161, p. 104319, July 2021.

[33] D. R. Houser and G. W. Blankenship, "Methods for measuring gear transmission error under load and at operating speeds," *SAE Transactions*, vol. 98, pp. 1367–1374, 1989. Publisher: SAE International.

[34] R. G. Munro, D. Palmer, and L. Morrish, "An experimental method to measure gear tooth stiffness throughout and beyond the path of contact," *Proceedings of the Institution of Mechanical Engineers, Part C: Journal of Mechanical Engineering Science*, vol. 215, pp. 793–803, July 2001. Publisher: IMECHE.

[35] M. A. Hotait and A. Kahraman, “Experiments on the relationship between the dynamic transmission error and the dynamic stress factor of spur gear pairs,” *Mechanism and Machine Theory*, vol. 70, pp. 116–128, Dec. 2013.

[36] N. K. Raghuwanshi and A. Parey, “Experimental measurement of spur gear mesh stiffness using digital image correlation technique,” *Measurement*, vol. 111, pp. 93–104, Dec. 2017.

[37] N. K. Raghuwanshi and A. Parey, “Experimental measurement of mesh stiffness by laser displacement sensor technique,” *Measurement*, vol. 128, pp. 63–70, Nov. 2018.

[38] A. Palermo, L. Britte, K. Janssens, D. Mundo, and W. Desmet, “The measurement of gear transmission error as an NVH indicator: Theoretical discussion and industrial application via low-cost digital encoders to an all-electric vehicle gearbox,” *Mechanical Systems and Signal Processing*, vol. 110, pp. 368–389, Sept. 2018.

[39] H. Li, S. Chen, J. Tang, W. Chen, and H. Ouyang, “A novel approach for calculating no-load static transmission error based on measured discrete tooth surfaces,” *Mechanism and Machine Theory*, vol. 138, pp. 112–123, Aug. 2019.

[40] X. Chun and C. Siyu, “Experimental study of the effect of assembly error on the lightly loaded transmission error of spur gear with crown modification,” *Journal of Low Frequency Noise, Vibration and Active Control*, vol. 39, pp. 1039–1051, Dec. 2020. Publisher: SAGE Publications Ltd STM.

[41] C. G. Cooley, C. Liu, X. Dai, and R. G. Parker, “Gear tooth mesh stiffness: A comparison of calculation approaches,” *Mechanism and Machine Theory*, vol. 105, pp. 540–553, Nov. 2016.

[42] F. Choy, V. Polyshchuk, J. Zakrajsek, R. Handschuh, and D. Townsend, “Analysis of the effects of surface pitting and wear on the vibration of a gear transmission system,” *Tribology International*, vol. 29, pp. 77–83, Feb. 1996.

[43] F. Chaari, W. Baccar, M. S. Abbes, and M. Haddar, “Effect of spalling or tooth breakage on gearmesh stiffness and dynamic response of a one-stage spur gear transmission,” *European Journal of Mechanics - A/Solids*, vol. 27, pp. 691–705, July 2008.

[44] F. Chaari, T. Fakhfakh, and M. Haddar, “Analytical modelling of spur gear tooth crack and influence on gearmesh stiffness,” *European Journal of Mechanics - A/Solids*, vol. 28, pp. 461–468, May 2009.

[45] R. Ma and Y. Chen, “Research on the dynamic mechanism of the gear system with local crack and spalling failure,” *Engineering Failure Analysis*, vol. 26, pp. 12–20, Dec. 2012.

[46] A. F. D. Rincon, F. Viadero, M. Iglesias, A. de Juan, P. Garcia, and R. Sancibrian, "Effect of cracks and pitting defects on gear meshing," *Proceedings of the Institution of Mechanical Engineers, Part C: Journal of Mechanical Engineering Science*, vol. 226, pp. 2805–2815, Nov. 2012.

[47] H. Jiang, Y. Shao, and C. K. Mechefske, "Dynamic characteristics of helical gears under sliding friction with spalling defect," *Engineering Failure Analysis*, vol. 39, pp. 92–107, Apr. 2014.

[48] A. Saxena, A. Parey, and M. Chouksey, "Time varying mesh stiffness calculation of spur gear pair considering sliding friction and spalling defects," *Engineering Failure Analysis*, vol. 70, pp. 200–211, Dec. 2016.

[49] X. Liang, H. Zhang, L. Liu, and M. J. Zuo, "The influence of tooth pitting on the mesh stiffness of a pair of external spur gears," *Mechanism and Machine Theory*, vol. 106, pp. 1–15, Dec. 2016.

[50] X.-H. Liang, Z.-L. Liu, J. Pan, and M. J. Zuo, "Spur gear tooth pitting propagation assessment using model-based analysis," *Chinese Journal of Mechanical Engineering*, vol. 30, pp. 1369–1382, Nov. 2017.

[51] Y. Lei, Z. Liu, D. Wang, X. Yang, H. Liu, and J. Lin, "A probability distribution model of tooth pits for evaluating time-varying mesh stiffness of pitting gears," *Mechanical Systems and Signal Processing*, vol. 106, pp. 355–366, June 2018.

[52] Y. Luo, N. Baddour, G. Han, F. Jiang, and M. Liang, "Evaluation of the time-varying mesh stiffness for gears with tooth spalls with curved-bottom features," *Engineering Failure Analysis*, vol. 92, pp. 430–442, Oct. 2018.

[53] K. Chen, Y. Huangfu, H. Ma, Z. Xu, X. Li, and B. Wen, "Calculation of mesh stiffness of spur gears considering complex foundation types and crack propagation paths," *Mechanical Systems and Signal Processing*, vol. 130, pp. 273–292, Sept. 2019.

[54] Y. Luo, N. Baddour, and M. Liang, "A shape-independent approach to modelling gear tooth spalls for time varying mesh stiffness evaluation of a spur gear pair," *Mechanical Systems and Signal Processing*, vol. 120, pp. 836–852, Apr. 2019.

[55] B. El Yousfi, A. Soualhi, K. Medjaher, and F. Guillet, "New approach for gear mesh stiffness evaluation of spur gears with surface defects," *Engineering Failure Analysis*, vol. 116, p. 104740, Oct. 2020.

[56] Z. Meng, F. Wang, and G. Shi, "A novel evolution model of pitting failure and effect on time -varying meshing stiffness of spur gears," *Engineering Failure Analysis*, vol. 120, p. 105068, Feb. 2021.

[57] F. Meng, H. Xia, X. Zhang, and J. Wang, "A new tooth pitting modeling method based on matrix equation for evaluating time-varying mesh stiffness," *Engineering Failure Analysis*, vol. 142, p. 106799, Dec. 2022.

[58] S. R. Daniewicz, J. A. Collins, and D. R. Houser, "The stress intensity factor and stiffness for a cracked spur gear tooth," *Journal of Mechanical Design*, vol. 116, pp. 697–700, Sept. 1994.

[59] D. G. Lewicki, R. F. Handschuh, L. E. Spievak, P. A. Wawrzynek, and A. R. Ingraffea, "Consideration of moving tooth load in gear crack propagation predictions," *Journal of Mechanical Design*, vol. 123, pp. 118–124, Mar. 2001.

[60] Y. Pandya and A. Parey, "Simulation of crack propagation in spur gear tooth for different gear parameter and its influence on mesh stiffness," *Engineering Failure Analysis*, vol. 30, pp. 124–137, June 2013.

[61] Z. Chen and Y. Shao, "Mesh stiffness calculation of a spur gear pair with tooth profile modification and tooth root crack," *Mechanism and Machine Theory*, vol. 62, pp. 63–74, Apr. 2013.

[62] H. Ma, J. Zeng, R. Feng, X. Pang, Q. Wang, and B. Wen, "Review on dynamics of cracked gear systems," *Engineering Failure Analysis*, vol. 55, pp. 224–245, Sept. 2015.

[63] H. Ma, X. Pang, R. Feng, J. Zeng, and B. Wen, "Improved time-varying mesh stiffness model of cracked spur gears," *Engineering Failure Analysis*, vol. 55, pp. 271–287, Sept. 2015.

[64] X. Liang, M. J. Zuo, and Z. Feng, "Dynamic modeling of gearbox faults: A review," *Mechanical Systems and Signal Processing*, vol. 98, pp. 852–876, Jan. 2018.

[65] Q. Wang, K. Chen, B. Zhao, H. Ma, and X. Kong, "An analytical-finite-element method for calculating mesh stiffness of spur gear pairs with complicated foundation and crack," *Engineering Failure Analysis*, vol. 94, pp. 339–353, Dec. 2018.

[66] L. Yang, L. Wang, W. Yu, and Y. Shao, "Investigation of tooth crack opening state on time varying meshing stiffness and dynamic response of spur gear pair," *Engineering Failure Analysis*, vol. 121, p. 105181, Mar. 2021.

[67] C. Cooley, A. Hood, and Y. Wang, "Tooth mesh modeling of spur gears with tooth root crack damage using a finite element/contact mechanics approach," SAE Technical Paper 2021-01-0699, SAE International, Warrendale, PA, Apr. 2021. ISSN: 0148-7191, 2688-3627.

[68] Y. Wang, A. A. Hood, and C. G. Cooley, “Finite element/contact mechanics analysis of spur gear pairs with tooth root cracks,” in *Proceedings of the ASME 2021 International Design Engineering Technical Conferences & Computers and Information in Engineering Conference IDETC-CIE 2021*, pp. DETC2021–71896, Nov. 2021.

[69] V. Kumar, A. Kumar, S. Kumar, and S. Sarangi, “TVMS calculation and dynamic analysis of carburized spur gear pair,” *Mechanical Systems and Signal Processing*, vol. 166, p. 108436, Mar. 2022.

[70] H. Han, K. Yuan, H. Ma, Z. Peng, Z. Li, S. Zhao, and B. Wen, “Mesh characteristic analysis and dynamic simulation of spur gear pair considering corner contact and tooth broken fault,” *Engineering Failure Analysis*, vol. 143, p. 106883, Jan. 2023.

[71] Y. Yang, J. Tang, N. Hu, G. Shen, Y. Li, and L. Zhang, “Research on the time-varying mesh stiffness method and dynamic analysis of cracked spur gear system considering the crack position,” *Journal of Sound and Vibration*, vol. 548, p. 117505, Mar. 2023.

[72] I. Howard, S. Jia, and J. Wang, “The dynamic modelling of a spur gear in mesh including friction and a crack,” *Mechanical Systems and Signal Processing*, vol. 15, pp. 831–853, Sept. 2001.

[73] S. Jia and I. Howard, “Comparison of localised spalling and crack damage from dynamic modelling of spur gear vibrations,” *Mechanical Systems and Signal Processing*, vol. 20, pp. 332–349, Feb. 2006.

[74] Z. Chen and Y. Shao, “Dynamic simulation of spur gear with tooth root crack propagating along tooth width and crack depth,” *Engineering Failure Analysis*, vol. 18, pp. 2149–2164, Dec. 2011.

[75] O. D. Mohammed, M. Rantatalo, and J.-O. Aidanpää, “Dynamic modelling of a one-stage spur gear system and vibration-based tooth crack detection analysis,” *Mechanical Systems and Signal Processing*, vol. 54-55, pp. 293–305, Mar. 2015.

[76] O. D. Mohammed and M. Rantatalo, “Dynamic response and time-frequency analysis for gear tooth crack detection,” *Mechanical Systems and Signal Processing*, vol. 66-67, pp. 612–624, Jan. 2016.

[77] W. Yu, C. K. Mechefske, and M. Timusk, “A new dynamic model of a cylindrical gear pair with localized spalling defects,” *Nonlinear Dynamics*, vol. 91, pp. 2077–2095, Mar. 2018.

[78] Y. Luo, N. Baddour, and M. Liang, “Dynamical modeling and experimental validation for tooth pitting and spalling in spur gears,” *Mechanical Systems and Signal Processing*, vol. 119, pp. 155–181, Mar. 2019.

[79] O. Doğan and F. Karpat, "Crack detection for spur gears with asymmetric teeth based on the dynamic transmission error," *Mechanism and Machine Theory*, vol. 133, pp. 417–431, Mar. 2019.

[80] Z. Cheng, K. Huang, Y. Xiong, and M. Sang, "Dynamic analysis of a high-contact-ratio spur gear system with localized spalling and experimental validation," *Machines*, vol. 10, p. 154, Feb. 2022. Number: 2 Publisher: Multidisciplinary Digital Publishing Institute.

[81] O. C. Kalay, E. Karpat, A. E. Dirik, and F. Karpat, "A one-dimensional convolutional neural network-based method for diagnosis of tooth root cracks in asymmetric spur gear pairs," *Machines*, vol. 11, p. 413, Apr. 2023. Number: 4 Publisher: Multidisciplinary Digital Publishing Institute.

[82] Z. Sun, J. Tang, S. Chen, H. Li, X. Tao, and Z. Hu, "Dynamical modeling and characteristics analysis of tooth spalling in gear system with weight reduction structure," *Mechanism and Machine Theory*, vol. 189, p. 105429, Nov. 2023.

[83] Z. Liu, C. Chang, H. Hu, H. Ma, K. Yuan, X. Li, X. Zhao, and Z. Peng, "Dynamic characteristics of spur gear system with tooth root crack considering gearbox flexibility," *Mechanical Systems and Signal Processing*, vol. 208, p. 110966, Feb. 2024.

[84] W. Zhou, R. Zhu, Z. Li, W. Liu, and J. Wang, "An improved dynamic model of spur gears considering delayed meshing out of the contact point due to root crack," *Mechanical Systems and Signal Processing*, vol. 212, p. 111325, Apr. 2024.

[85] P. Cao, Q. Li, K. Feng, and Y. Qin, "Dynamic modeling of spur gear transmission system with evolutive coupling fault of fatigue crack and wear," *Engineering Failure Analysis*, vol. 156, p. 107820, Feb. 2024.

[86] J. J. Zakrajsek, "A review of transmission diagnostics research at NASA Lewis Research Center," Technical Report NASA TM-106746, NTRS: Lewis Research Center (LRC), 1994.

[87] H. Chin, K. Danai, and D. G. Lewicki, "Efficient fault diagnosis of helicopter gearboxes," *IFAC Proceedings Volumes*, vol. 26, no. 2, Part 2, pp. 593–596, 1993.

[88] J. Zhu, T. Nostrand, C. Spiegel, and B. Morton, "Survey of condition indicators for condition monitoring systems," in *Proceedings of the Annual Conference of the PHM Society 2014*, vol. 6, p. 13, 2014.

[89] P. Večeř, M. Kreidl, and R. Šmíd, "Condition indicators for gearbox condition monitoring systems," *Acta Polytechnica*, vol. 45, pp. 35–43, Jan. 2005.

[90] A. S. Sait and Y. I. Sharaf-Eldeen, "A review of gearbox condition monitoring based on vibration analysis techniques diagnostics and prognostics," in *Conference Proceedings of the Society for Experimental Mechanics Series. Springer, New York, NY*, (New York, NY), pp. 307–324, Springer New York, 2011.

[91] V. Sharma and A. Parey, "A review of gear fault diagnosis using various condition indicators," *Procedia Engineering*, vol. 144, pp. 253–263, 2016.

[92] M. Lebold, K. McClintic, R. Campbell, C. Byington, and K. Maynard, "Review of vibration analysis methods for gearbox diagnostics and prognostics," in *roceedings of the 54th Meeting of the Society for Machinery Failure Prevention Technology, Virginia Beach, VA*, pp. 623–634, 2000.

[93] P. J. Dempsey, M. Mosher, and E. M. Huff, "Threshold assessment of gear diagnostic tools on flight and test rig data," *59th Annual Forum and Technology Display, Phoenix, AZ*, p. 20, 2003.

[94] P. J. Dempsey, J. A. Keller, D. R. Wade, U. S. Army, and R. Arsenal, "Signal detection theory applied to helicopter transmission diagnostic thresholds," *AHS 65 Annual Forum-Grapevine, Texas*, p. 16, 2008.

[95] I. R. Delgado, P. J. Dempsey, L. J. Antolick, and D. R. Wade, "Continued evaluation of gear condition indicator performance on rotorcraft fleet," Technical Report NASA/TM-2013-217876, NTRS: Glenn Research Center (GRC), Huntsville, AL, June 2013.

[96] J. J. Zakrajsek, P. J. Dempsey, E. M. Huff, M. Augustin, R. Safa-Bakhsh, P. Ephraim, P. Grabil, and H. J. Decker, "Rotorcraft health management issues and challenges," Technical Report NASA/TM-2006-214022, NTRS: Glenn Research Center (GRC), Napa, CA, Feb. 2006.

[97] R. Stewart, "Some useful data analysis techniques for gearbox diagnostics," Technical Report MHM/R/10/77, University of Southampton, July 1977.

[98] R. B. Randall, "A new method of modeling gear faults," *Journal of Mechanical Design*, vol. 104, pp. 259–267, Apr. 1982.

[99] P. D. McFadden and J. D. Smith, "A signal processing technique for detecting local defects in a gear from the signal average of the vibration," *Proceedings of the Institution of Mechanical Engineers, Part C: Journal of Mechanical Engineering Science*, vol. 199, pp. 287–292, Oct. 1985. Publisher: IMECHE.

[100] P. D. McFadden, "Detecting fatigue cracks in gears by amplitude and phase demodulation of the meshing vibration," *Journal of Vibration, Acoustics, Stress, and Reliability in Design*, vol. 108, pp. 165–170, Apr. 1986.

[101] W. J. Wang and P. D. McFadden, “Decomposition of gear motion signals and its application to gearbox diagnostics,” *Journal of Vibration and Acoustics*, vol. 117, pp. 363–369, July 1995.

[102] W. D. Mark, H. Lee, R. Patrick, and J. D. Coker, “A simple frequency-domain algorithm for early detection of damaged gear teeth,” *Mechanical Systems and Signal Processing*, vol. 24, pp. 2807–2823, Nov. 2010.

[103] W. D. Mark, M. E. Wagner, and A. C. Isaacson, “Early detection of gear-tooth bending-fatigue damage by the Average-Log-Ratio ALR algorithm,” *Mechanical Systems and Signal Processing*, vol. 171, p. 108922, May 2022.

[104] W. J. Wang and P. D. McFadden, “Early detection of gear failure by vibration analysis-I. Calculation of the time-frequency distribution,” *Mechanical Systems and Signal Processing*, vol. 7, pp. 193–203, May 1993.

[105] W. J. Staszewski, K. Worden, and G. R. Tomlinson, “Time–frequency analysis in gearbox fault detection using the Wigner–Ville distribution and pattern recognition,” *Mechanical Systems and Signal Processing*, vol. 11, pp. 673–692, Sept. 1997.

[106] W. J. Wang and P. D. McFadden, “Application of orthogonal wavelets to early gear damage detection,” *Mechanical Systems and Signal Processing*, vol. 9, pp. 497–507, Sept. 1995.

[107] W. J. Williams and E. J. Zalubas, “Helicopter transmission fault detection via time-frequency, scale and spectral methods,” *Mechanical Systems and Signal Processing*, vol. 14, pp. 545–559, July 2000.

[108] P. Loughlin, F. Cakrak, and L. Cohen, “Conditional moments analysis of transients with application to helicopter fault data,” *Mechanical Systems and Signal Processing*, vol. 14, pp. 511–522, July 2000.

[109] A. Belsak and J. Flasker, “Method for detecting fatigue crack in gears,” *Theoretical and Applied Fracture Mechanics*, vol. 46, pp. 105–113, Oct. 2006.

[110] P. D. McFadden and J. D. Smith, “An explanation for the asymmetry of the modulation sidebands about the tooth meshing frequency in epicyclic gear vibration,” *Proceedings of the Institution of Mechanical Engineers, Part C: Journal of Mechanical Engineering Science*, vol. 199, pp. 65–70, Jan. 1985. Publisher: IMECHE.

[111] J. McNames, “Fourier series analysis of epicyclic gearbox vibration,” *Journal of Vibration and Acoustics*, vol. 124, pp. 150–153, June 2001.

[112] D. G. Lewicki and J. J. Coy, "Vibration characteristics of OH-58A helicopter main rotor transmission," Technical Report NASA TP-2705 AVSCOM TR 86-C-42, NTRS: Lewis Research Center (LRC), Apr. 1987.

[113] M. Mosher, "Understanding vibration spectra of planetary gear systems for fault detection," in *Proceedings of the ASME 2003 International Design Engineering Technical Conferences and Computers and Information in Engineering Conference*, vol. 4 of *International Design Engineering Technical Conferences and Computers and Information in Engineering Conference*, (Chicago, IL), pp. 645–652, American Society of Mechanical Engineers Digital Collection, 2003.

[114] M. Inalpolat and A. Kahraman, "A theoretical and experimental investigation of modulation sidebands of planetary gear sets," *Journal of Sound and Vibration*, vol. 323, pp. 677–696, June 2009.

[115] M. Inalpolat and A. Kahraman, "A dynamic model to predict modulation sidebands of a planetary gear set having manufacturing errors," *Journal of Sound and Vibration*, vol. 329, pp. 371–393, Feb. 2010.

[116] C. G. Cooley and A. A. Hood, "Investigation of planetary gear elastic vibrations using a finite element/contact mechanics formulation," in *Proceedings of the ASME 2023 International Design Engineering Technical Conferences and Computers and Information in Engineering Conference.*, p. V012T12A024, American Society of Mechanical Engineers Digital Collection, Nov. 2023.

[117] P. D. McFadden, "A technique for calculating the time domain averages of the vibration of the individual planet gears and the sun gear in an epicyclic gearbox," *Journal of Sound and Vibration*, vol. 144, pp. 163–172, Jan. 1991.

[118] P. D. McFadden, "Window functions for the calculation of the time domain averages of the vibration of the individual planet gears and sun gear in an epicyclic gearbox," *Journal of Vibration and Acoustics*, vol. 116, pp. 179–187, Apr. 1994.

[119] P. D. Samuel and D. J. Pines, "Vibration separation methodology for planetary gear health monitoring," in *Smart Structures and Materials 2000: Smart Structures and Integrated Systems*, vol. 3985, pp. 250–260, SPIE, June 2000.

[120] A. Hood and D. Pines, "Sun gear fault detection on an OH-58C helicopter transmission," in *American Helicopter Society 67th Annual Forum*, (Virginia Beach, VA), p. 27, American Helicopter Society, Inc., 2011.

[121] A. Hood, K. LaBerge, D. Lewicki, and D. Pines, "Vibration based sun gear damage detection," in *Volume 5: 25th International Conference on Design Theory and Methodology; ASME 2013 Power Transmission and Gearing Conference*, (Portland,

Oregon, USA), p. V005T11A033, American Society of Mechanical Engineers, Aug. 2013.

[122] P. D. Samuel and D. J. Pines, "Constrained adaptive lifting and the CAL4 metric for helicopter transmission diagnostics," *Journal of Sound and Vibration*, vol. 319, pp. 698–718, Jan. 2009.

[123] W. Bartelmus and R. Zimroz, "Vibration condition monitoring of planetary gearbox under varying external load," *Mechanical Systems and Signal Processing*, vol. 23, pp. 246–257, Jan. 2009.

[124] W. Bartelmus and R. Zimroz, "A new feature for monitoring the condition of gearboxes in non-stationary operating conditions," *Mechanical Systems and Signal Processing*, vol. 23, pp. 1528–1534, July 2009.

[125] Z. Feng and M. J. Zuo, "Vibration signal models for fault diagnosis of planetary gearboxes," *Journal of Sound and Vibration*, vol. 331, pp. 4919–4939, Oct. 2012.

[126] H. Chen, Y. Lu, and L. Tu, "Fault identification of gearbox degradation with optimized wavelet neural network," *Shock and Vibration*, vol. 20, pp. 247–262, 2013.

[127] S. Xue and I. Howard, "Torsional vibration signal analysis as a diagnostic tool for planetary gear fault detection," *Mechanical Systems and Signal Processing*, vol. 100, pp. 706–728, Feb. 2018.

[128] B. Hazra and S. Narasimhan, "Gearbox fault detection using synchro-squeezing transform," *Procedia Engineering*, vol. 144, pp. 187–194, 2016.

[129] M. Zhang, M. J. Zuo, D. Wei, J. Liu, K. Wang, and Y. Wang, "Motion periods of sun gear dynamic fault meshing positions in planetary gear systems," *Measurement*, vol. 162, p. 107897, Oct. 2020.

[130] J. D. Marafona, P. M. Marques, R. C. Martins, and J. H. Seabra, "Mesh stiffness models for cylindrical gears: A detailed review," *Mechanism and Machine Theory*, vol. 166, p. 104472, Dec. 2021.

[131] S. Vijayakar, "A combined surface integral and finite element solution for a three-dimensional contact problem," *International Journal for Numerical Methods in Engineering*, vol. 31, pp. 525–545, Mar. 1991.

[132] C. G. Cooley, R. G. Parker, and S. M. Vijayakar, "A frequency domain finite element approach for three-dimensional gear dynamics," in *Volume 6: ASME Power Transmission and Gearing Conference; 3rd International Conference on Micro- and Nanosystems; 11th International Conference on Advanced Vehicle and Tire Technologies*, (San Diego, California, USA), pp. 205–215, ASMEDC, Jan. 2009.

[133] A. Singh, A. Kahraman, and H. Ligata, "Internal gear strains and load sharing in planetary transmissions: Model and experiments," *Journal of Mechanical Design*, vol. 130, p. 10, May 2008.

[134] X. Dai, C. G. Cooley, and R. G. Parker, "Dynamic tooth root strains and experimental correlations in spur gear pairs," *Mechanism and Machine Theory*, vol. 101, pp. 60–74, July 2016.

[135] Y. Lei, J. Lin, M. J. Zuo, and Z. He, "Condition monitoring and fault diagnosis of planetary gearboxes: A review," *Measurement*, vol. 48, pp. 292–305, Feb. 2014.

[136] H. Ma, Z. Li, M. Feng, R. Feng, and B. Wen, "Time-varying mesh stiffness calculation of spur gears with spalling defect," *Engineering Failure Analysis*, vol. 66, pp. 166–176, Aug. 2016.

[137] S. G. Thunuguntla, A. Hood, and C. Cooley, "Tooth mesh characterization of spur gear pairs with surface pitting damage," SAE Technical Paper 2023-01-0458, SAE International, Warrendale, PA, Apr. 2023. ISSN: 0148-7191, 2688-3627.

[138] K. Chen, Y. Huangfu, Z. Zhao, H. Ma, and X. Dong, "Dynamic modeling of the gear-rotor systems with spatial propagation crack and complicated foundation structure," *Mechanism and Machine Theory*, vol. 172, p. 104827, June 2022.

[139] S. M. Vijayakar, H. R. Busby, and D. R. Houser, "Linearization of multibody frictional contact problems," *Computers & Structures*, vol. 29, pp. 569–576, Jan. 1988.

[140] S. Vijayakar, H. Busby, and L. Wilcox, "Finite element analysis of three-dimensional conformal contact with friction," *Computers & Structures*, vol. 33, pp. 49–61, Jan. 1989.

[141] C. G. Cooley, R. G. Parker, and S. M. Vijayakar, "A frequency domain finite element approach for three-dimensional gear dynamics," *Journal of Vibration and Acoustics*, vol. 133, p. 041004, Apr. 2011.

[142] V. K. Ambarisha and R. G. Parker, "Nonlinear dynamics of planetary gears using analytical and finite element models," *Journal of Sound and Vibration*, vol. 302, pp. 577–595, May 2007.

[143] X. Dai, C. G. Cooley, and R. G. Parker, "An efficient hybrid analytical-computational method for nonlinear vibration of spur gear pairs," *Journal of Vibration and Acoustics*, vol. 141, Feb. 2019.

[144] D. G. Lewicki and R. Ballarini, "Effect of rim thickness on gear crack propagation path," *Journal of Mechanical Design*, vol. 119, pp. 88–95, Mar. 1997.

[145] R. G. Parker, V. Agashe, and S. M. Vijayakar, "Dynamic response of a planetary gear system using a finite element/contact mechanics model," *Journal of Mechanical Design*, vol. 122, pp. 304–310, Sept. 2000.

[146] H. Decker and D. Lewicki, "Spiral bevel pinion crack detection in a helicopter gearbox," in *AHS 59th Annual Forum and Technology Display*, (Phoenix, AZ, United States), p. 11, June 2003.

[147] H. Martin, "Statistical moment analysis as a means of surface damage detection,," in *Proceedings of the Seventh International Modal Analysis Conference, Society for Experimental Mechanics*, (Schenectady, NY), pp. 1016–1021, 1989.

[148] N. S. Swansson, "Application of vibration signal analysis techniques to condition monitoring," in *Conference on Lubrication, Friction and Wear in Engineering 1980, Melbourne: Preprints of Papers*, pp. 262–267, Aug. 2020. ISSN: 0858251485.

[149] J. J. Zakrajsek, D. P. Townsend, and H. J. Decker, "An analysis of gear fault detection methods as applied to pitting fatigue failure data," Technical Report 92-C-035, NTRS: Lewis Research Center (LRC), 1993.

[150] H. J. Decker, R. F. Handschuh, and J. J. Zakrajsek, "An enhancement to the NA4 gear vibration diagnostic parameter," Technical Report NASA/TM - 106553, NTRS: Lewis Research Center (LRC), Hershey, PA, June 1994.

[151] F. Honarvar and H. R. Martin, "New statistical moments for diagnostics of rolling element bearings," *Journal of Manufacturing Science and Engineering*, vol. 119, pp. 425–432, Aug. 1997.

[152] B. Tao, L. Zhu, H. Ding, and Y. Xiong, "An alternative time-domain index for condition monitoring of rolling element bearings—A comparison study," *Reliability Engineering & System Safety*, vol. 92, pp. 660–670, May 2007.

[153] J. L. Devore, *Probability and statistics for engineering and the sciences*. Boston, MA: Brooks/Cole, Cengage Learning, 8th ed ed., 2012. OCLC: 696106248.

[154] H. Li, D. Du, X. You, and Q. He, "Direct calculation method of probability density from sampled vibration signal based on linear interpolation method," *Journal of Vibroengineering*, vol. 19, pp. 5086–5103, Nov. 2017. Number: 7 Publisher: JVE International Ltd.

[155] O. D. Mohammed and M. Rantatalo, "Gear fault models and dynamics-based modelling for gear fault detection – A review," *Engineering Failure Analysis*, vol. 117, p. 104798, Nov. 2020.

[156] P. Kundu, A. K. Darpe, and M. S. Kulkarni, “A review on diagnostic and prognostic approaches for gears,” *Structural Health Monitoring*, vol. 20, pp. 2853–2893, Sept. 2021. Publisher: SAGE Publications.

[157] K. Feng, J. C. Ji, Q. Ni, and M. Beer, “A review of vibration-based gear wear monitoring and prediction techniques,” *Mechanical Systems and Signal Processing*, vol. 182, p. 109605, Jan. 2023.

[158] J. Yoon, D. He, B. V. Hecke, T. J. Nostrand, J. Zhu, and E. Bechhoefer, “Planetary gearbox fault diagnosis using a single piezoelectric strain sensor,” *Annual Conference of the PHM Society*, vol. 6, no. 1, pp. 118–127, 2014.

[159] C. Cooley, Y. Wang, and A. Hood, “Damage-induced dynamic tooth contact forces in spur gears with root cracks,” *SAE International Journal of Advances and Current Practices in Mobility*, vol. 5, pp. 57–66, Mar. 2022. Number: 2022-01-0642.

[160] S. G. Thunuguntla, A. A. Hood, and C. G. Cooley, “Evaluation of select condition indicators for detecting damage in geared transmissions using a finite element/contact mechanics model,” in *ASME 2024 International Design Engineering Technical Conferences and Computers and Information in Engineering Conference*, vol. 10, (Washington, DC, USA), p. 14, Aug. 2024.

[161] S. Braun, “The extraction of periodic waveforms by time domain averaging,” *Acta Acustica united with Acustica*, vol. 32, pp. 69–77, Feb. 1975.

[162] P. D. McFadden, “A revised model for the extraction of periodic waveforms by time domain averaging,” *Mechanical Systems and Signal Processing*, vol. 1, pp. 83–95, Jan. 1987.

[163] J. Lin and R. G. Parker, “Analytical characterization of the unique properties of planetary gear free vibration,” *Journal of Vibration and Acoustics*, vol. 121, pp. 316–321, July 1999.

[164] D. S. Shah and V. N. Patel, “A review of dynamic modeling and fault identifications methods for rolling element bearing,” *Procedia Technology*, vol. 14, pp. 447–456, 2014.